HUBERT HARAŃCZYK

ON WATER IN EXTREMELY DRY BIOLOGICAL SYSTEMS

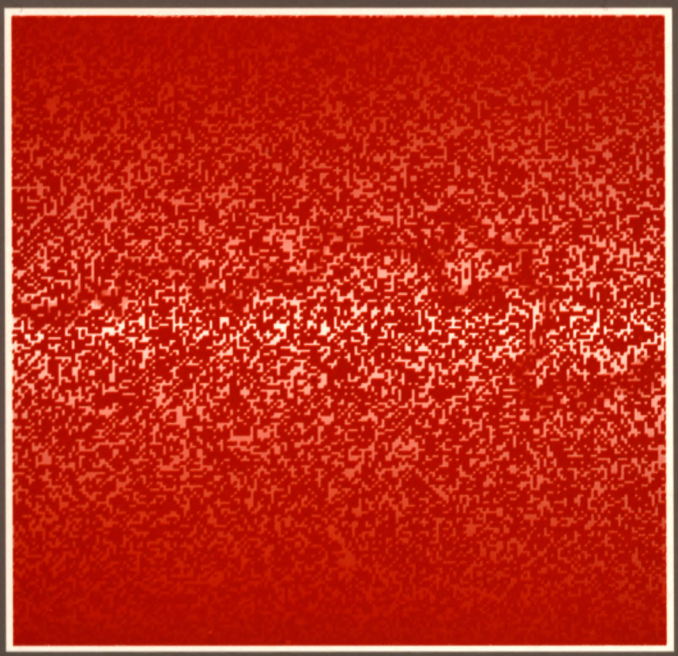

WYDAWNICTWO UNIWERSYTETU JAGIELLOŃSKIEGO

ON WATER IN EXTREMELY DRY BIOLOGICAL SYSTEMS

HUBERT HARAŃCZYK

ON WATER IN EXTREMELY DRY BIOLOGICAL SYSTEMS

WYDAWNICTWO UNIWERSYTETU JAGIELLOŃSKIEGO

Rozprawy Habilitacyjne Uniwersytetu Jagiellońskiego Nr 361

Publikacja finansowana przez Instytut Fizyki Uniwersytetu Jagiellońskiego

RECENZENT

Jerzy S. Blicharski

PROJEKT OKŁADKI

Dorota Heliasz

REDAKCJA

Jerzy Hrycyk

Wydanie I, Kraków 2003

ISBN 83-233-1713-5
ISSN 0239-782X

Wydawnictwo Uniwersytetu Jagiellońskiego
Dystrybucja: ul. Bydgoska 19 C, 30-056 Kraków
tel. (012) 638-77-83, fax: (012) 636-80-00 w. 2023, (012) 430-19-95
tel. kom. 0604 414-568, e-mail: wydaw@if.uj.edu.pl
Konto BPH BPK SA IV/O Kraków nr 10601389-320000478769

www.wuj.pl

Contents

Watson and Crick proposed the successful model of the native structure of the DNA molecule placed in vacuum. They ignored the presence of water, although, it was already known that the native form of DNA requires up to 40 wt% of water. Their success might suggest that the role of water for a complex biological system is nothing but to provide a sterical environment [116, 220, 241, 699]. On the other hand, water in a liquid state resembles a solid-like system, as hydrogen bonds of similar strength form both the structure of ice and the structure of liquid water, and melting of ice breaks only ~15% of hydrogen bonds that construct the form of the crystal [642].

In all biological textbooks sufficiently high water concentration is *implicite* assumed for the existence of biological system. At the least it is assumed that water provides the medium in which the biochemical reactions of living organisms take place. However, this assumption is violated for long cycles of biochemical reactions, e.g. photosynthetic transport of electron in light reaction of photosynthesis [255], where the reactions are realized by increased probability of vicinity of reaction substrates as a result of their location in two-dimensional structures, i.e. in planar membrane formed by the interplay of hydrophobic and hydrophilic interactions [618, 619]. This leads to the conclusion that Watson and Crick's assumption is often not sufficient to explain the final native structure taken on by biological systems. In fact, the network of hydrogen bonds in liquid water is essential for the support of any biological micro-structure.

The supportive role of water is obvious for simple biological structures and unicellular living organisms. However, the question arises whether there exist living organisms, which may dispense with (in the sense of surviving without) the long-distance "scaffolding" of water hydrogen bonds. This adaptative feature might be expected in seeds, in resting forms of living organisms, or in living organisms experiencing extreme environmental conditions. The extremely effective freezing and desiccation resistance of lichens turned this Author's attention to these organisms.

Lichens (lichenized fungi) are an excellent example of extremophilous organisms. Their unusual adaptative features are characterized: carbon dioxide concentration mechanism, resistance on desiccation, freezing tolerance,

photosynthetic activity below 0^0C, ice nucleation activity and the process of water uptake from snow.

The hydration kinetics, adsorption isotherms, static electric conductance, and proton magnetic relaxation measurements were used by the Author to study several water pools in lichen thallus: (i) water bound to 'primary' binding sites (the ones with elevated binding ability), (ii) main hydration layer (first monolayer of water, Lh), and (iii) loosely bound (or free) water. Three distinct hydration levels can be defined to describe hydration of extremely dry biological systems. Namely, with succeeding dehydration of the system: monolayer coverage, percolation threshold, and vanishing of water clusters. The Author found that the living organisms, lichenized fungi (lichens), reversibly dehydrate *in vivo* below percolation threshold (and likely below water cluster formation threshold) in the entire volume of their thalli.

The nuclear magnetic resonance experiments performed by this Author on cooling down of lichen thallus hydrated to different levels showed the presence of the two concurrent freezing protection mechanisms: (i) the enhanced ice crystallite growth in extra-cellular spaces, and (ii) the loosely bound-to-tightly bound water transfer mechanism preventing the intra-cellular spaces of thallus from the ice nucleation.

This thesis are organized as follows:

Water properties, water dynamics, and selfdiffusion are revieved in the first Chapter. The concept of the hydrogen bond is introduced and its importance for water properties, in comparison with hydrogen bonds formed by Mendeleevian neighbors of oxygen, is discussed. Liquid water in bulk and its ordering in restricted spaces of biological system is presented. The (cooperative) water freezing and (non-cooperative) immobilization of non-freezable water is described. Then, ice Ih, and ice polymorphs including vitreous ice, are discussed. Water supercooling is stressed, because of its importance and frequent abundance in biological systems. Wetting phenomena with decreasing scale are presented: breath figures and cluster formation, with the emphasis on this Author's experiment on water clustering on silica surface in vicinity of paramagnetic ions (what models bound water behavior on ultra-dry biological surface).

Then the attention is focused on the hydrophobic effect, which is essential for the existence of biological structures on the cellular scale. The so-formed structures are characterized as micelles, monolayers, lipid bilayers, and lipid phase polymorphs. Then, the structure and composition of biological membranes and several types of phase transitions in biological membranes (for example photosynthetic membranes), are described. The effect of glycerol (a common cryoprotectant in extremophilous organisms) on phase transitions in photosynthetic membranes is emphasized. Finally, the classification of several water pools – free water, loosely bound water and tightly bound water in biological system –

differentiated by the proximity to the inner surface of biological structures, is discussed.

Nuclear magnetic resonance applied to dry biological systems is addressed in the next Chapter. After brief introduction, the applicability of NMR tomography, relaxation and spectra in the investigations of dry biological systems is presented. As dry biological systems are micro-heterogeneous, the analysis of their relaxation functions using a discrete set of components (time domain two-dimensional methods of data analysis are presented) is compared with that using a continuous distribution of relaxation times. Here the results from the stretched exponential (SE) model for self-similar pore distribution with the results from modified stretched (MSE) distribution are discussed.

Effect of constant ion volume-concentration in aqueous medium filling the pores of dry biological system is considered on the example of water soluble paramagnetic impurities filling the channels of controlled pore glasses, and its influence on the NMR results discussed.

After a brief characterization of selected dry tissues: bark and bast, and wheat seed, the effect of the presence of the limited portion of water-soluble fraction on proton magnetic relaxation is discussed for bast. The proposed model yields several molecular parameters describing water soluble solid fraction. In contrast to bast, the effect of unlimited amount of water soluble fraction is discussed for the primary stages of wheat seed imbibition. (Model breaks as the seed germination starts).

The third Chapter focuses on dehydration limits of living organism.

The natural hydration scale for dry biological system is introduced: water clustering point, percolation threshold, monolayer formation. Hydration process of lichen thallus is analyzed: hydration kinetics, the analysis of water-binding sites using Dent's model, NMR relaxation experiments showing water fractions differentiated by their proximity to thallus inner surfaces, the electric conductance hydration courses showing the reversible dehydration of thallus below the two-dimensional water percolation threshold.

NMR results enabled the Author to study freezing protection mechanisms in dry biological system. In the next Chapter low temperature effect on water in lichen thallus is analyzed using NMR relaxation and NMR spectra. Separately, the effect of enhanced ice nucleation in extra-cellular spaces and the effect of loosely-to-tightly bound water fraction transfer in intra-cellular spaces are discussed. Conformational change in thallus lipids is observed. Freezing protection (freezing tolerance and freezing tolerance) of evolutionary advanced creatures, insects, are described and compared with those of lichens.

This Thesis concludes with the Summary, and a "droplet" of philosophy.

1. Water properties, its role in biological systems

Although the total mass of water present on the Earth represents only 370 ppm of the total mass of the planet, water in oceans covers 70.98% of the Earth's surface and by rainfall (or snowfall) and percolation penetrates the whole "dry" land (even "dry" dust contains up to 15% of water) [211]. Life on Earth is a surface phenomenon, as living creatures populate the space extending only ~20 km in altitude (the vast majority of living entities populate the surface of the land and the pelagic zone of oceans).

Both these observations, taken together with the fact that water was present on Earth long before the evolution of life, strongly suggest that water played an important role at the genesis of life. This critical importance of water for life maintenance, places water in the unusual position of being the only naturally ccurring inorganic liquid essential for life.

Water contents in living organisms varies between 96–97% in some marine invertebrates, 65–70% in adult human, down to 10% in some bacteria ($p/p_0 = 40\%$), 3% ($p/p_0 = 30\%$), and 6% in dry *Nostoc commune* [545].

These facts draw attention to water abnormalities, which may influence the living world. Indeed, water is probably the most studied and least understood of all known liquids, although some of its physical properties are accepted as international standards, e.g. triple point, density, mass, and viscosity [211].

1.1 Water molecule

The shape of the water molecule may be visualized (Fig. 1–1) by mapping the electron density surface using molecular modeling ([127], calculation based on [249]). Here the electron density surface of every atom is represented as

$$c \cdot \exp(-\alpha \cdot r) \ , \tag{1.1}$$

where c is a constant, α represents the steepness of the function, and r the distance between sampling point and the atom center. The parameters of the density function are chosen to provide the best qualitative representation of electron density (at $r \approx 1.7$ Å from the center of the atom). The density value (for every gridpoint p) is calculated as

$$dens(p) = \sum_{i=1}^{n} f(a_i, d) = \sum_{i=1}^{n} c \cdot Z(a_i) \cdot \exp\left[-\alpha \cdot Z(a_i) \cdot r\right], \qquad (1.2)$$

where $Z(a_i)$ is ordinal number of atom a_i, r is the distance between atom a_i and the sampling point p.

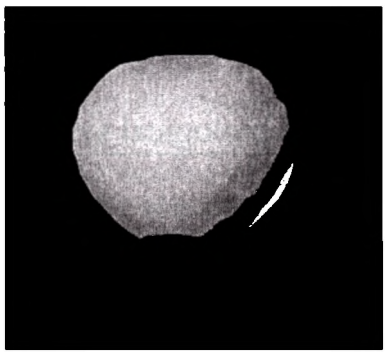

Fig. 1–1. Water molecule visualized as electron density surface, obtained using molecular modeling procedure Molcad of the program Sybil.

Although on the scale of the size of a single water molecule, quantum effects should be taken into account, the classic simplification gives surprisingly good results. The approximate shape of water may be visualized as in Fig. 1–1, with the molecular dimensions of x = 3.36 Å, y = 3.57 Å, and z = 1.40 Å. The distance O—H is equal to 0.9584 Å [33, 34].

1.2 Macroscopic anomalies of water

Although the most commonly occurring liquid on Earth, water, in contrast to other liquids, reveals numerous anomalies in macroscopic properties.

Water macroscopic anomalies may be listed (unless otherwise noted, taken from [700]): the negative volume of melting ($\Delta\rho = 0.083$ g cm^{-3}, $\Delta\rho/\rho_{ice} = 9.0\%$, at $t = 0^0$C, $p = p_{atm}$); the density maximum ($d = 1$ g cm^{-3} at $t = 3.98^0$C, which was already discussed in 1667 by the Florentine academicians of Cimento [211]); the isothermal compressibility minimum in the normal liquid range ($\chi = 44.16 \cdot 10^{-9}$ hPa^{-1} at $t = 46^0$C); several crystalline polymorphs (at least eleven, including polymorphs formed at elevated pressure, and vitreous ice); very high value of dielectric constant ($\varepsilon = 80.37$ at $t = 20^0$C); enormously high melting, boiling, and critical temperatures for a substance with low molecular weight that is neither ionic nor metallic; increasing liquid fluidity with increasing pressure; high-mobility transport for H^+ and OH^- ions (for H^+ $u_+ = 3.62 \cdot 10^{-3}$ cm V^{-1}s^{-1} and for OH^- $u_- = 1.98 \cdot 10^{-3}$ cm V^{-1}s^{-1}, both at $t = 25^0$C [184]), however, still greater in ice ($u_+ = 0.075$ cm V^{-1}s^{-1}, in ice I at $t = -10^0$C [183, 185]); very large specific heat capacity; almost universal solvent action (making rigorous purification of water extremely difficult) – nearly all chemicals dissolve in water to a slight, but detectable extent; one of the largest chemical reactivity actively interacting with ions and molecules (one of the most corrosive substances known [211]).

Although some of the anomalies are shared with other substances, possibly all of them, it is striking that so many of these abnormalities occur for one substance [642].

1.3 Hydrogen bond

The essential feature for understanding of water anomalies is the hydrogen bond. Latimer & Rodebush, [424], suggested that there is a specific attraction between electronegative atom (Y = N, O, F, Cl) and hydrogen (and deuteron), especially if hydrogen is chemically bound to an other electronegative atom (X).

The water molecule, containing two hydrogens and one oxygen in a non-linear arrangement is ideally suited for formation of hydrogen bonds. It may either act as a donor, or an acceptor of protons. The bond angle of the water molecule (104.45^0) [33, 34] is only slightly less than the ideal tetrahedral angle (104.5^0).

A hydrogen bond is strongly directional, i.e. the chemical bond X — H (containing hydrogen donated to hydrogen bond) tends to point directly towards the atom Y. Normally, the strengths of hydrogen bond (~21 kJ $mole^{-1}$) is intermediate between those of weak van der Waals interactions (~1.3 kJ $mole^{-1}$) and those of strong covalent bonds (~420 kJ $mole^{-1}$). Some authors count the hydrogen bond to the group of five so called "weak interactions" of molecular physics, namely, ionic, van der Waals, dipole-dipole, and hydrophobic interaction.

Pauling, [521], suggested that in a hydrogen bond X — H..Y the hydrogen 1s orbital can form only one covalent bond with X, so the interaction with Y (electron donor, hydrogen acceptor) is largely electrostatic in character. Then the electrostatic nature of hydrogen bond was emphasized by a few authors [554]. Lennard-Jones & Pople, proposed the point-charge model for the tetrahedral water molecule and considered the effect of the tetrahedral angle distortion on the properties of hydrogen bonds of water [428, 543]. The obtained energy of the hydrogen bond for linear water dimer was about 25 kJ $mole^{-1}$ [543].

As a major contribution to the dipole moment of water comes from the lone-pair electrons occupying the asymmetric (sp^3) orbitals of the oxygen atom [128, 129], the electrostatic effect cannot entirely explain the nature of the hydrogen bond (OH bond is much less ionic than it was assumed).

Cannon listed the conditions of the hydrogen bond X — H..Y formation [101]:

(i) the bond X — H is partially ionic; atom X is highly electronegative leading to $X..H^+$, where the orbital 1s of proton is not completely used to form the covalent bond X — H and is accessible to overlap with the orbital of the lone-pair electrons of Y;

(ii) the atom Y has a lone-pair of electrons in an asymmetric orbital;

(iii) to maximize hydrogen bond energy, bond X — H and the axis of the lone-pair electrons orbital have to be collinear.

Recently it is thought that the following forces contribute to the hydrogen bond [554]:

(i) *electrostatic term* (interaction without deformation of any charge cloud or any electron exchange);

(ii) *delocalization energy* (charge transfer: the large-scale, permanent distortion of charge clouds);

(iii) *dispersion term* (due to the small-scale, coordinated motion of the electrons);

(iv) *exchange repulsion* (due to violation of the Pauli exclusion principle).

The calculated contribution to the hydrogen bond from wave functions coming from: O_x — H O_y (covalent O_x — H bond) equals 65%, O_x^- H^+..O_y (ionic) equals 31%, and from O_x^- H — O_y^+ (fully covalent O_y — H bond with charge transfer) equals 4%. Covalent contribution to the hydrogen bond increases as the O_x — H bond length increases [130].

Lippincott & Schroeder developed a phenomenological model for the potential function of the hydrogen bond, based on the Morse function for diatomic molecules, considering [437, 438, 595]:

(i) potential function for the X — H bond;

(ii) potential function for the H..Y bond;

(iii) van der Waals repulsion between the two oxygen atoms;

(iv) the electrostatic attraction between the oxygens.

Despite the long duration of extensive research and significant progress in the investigations, strict bounds on the hydrogen bond energy have not yet been established. The reported values are varying between –13 kJ $mole^{-1}$ and –33 kJ $mole^{-1}$ [652]. Theoretical considerations relating the dielectric constant data with hydrogen bond thermodynamic properties leads to the estimates: H = –23.7 kJ $mole^{-1}$ and S = –37.2 J K^{-1} $mole^{-1}$ [652]

Averaged hydrogen bond lifetime τ_{HB} measured from depolarized light scattering experiments [114] varies from ~0.3 ps at 396 K, to ~1 ps at 252 K, whereas molecular simulations, either for the energetic bond definition ($E_{HB} < -10$ kJ $mole^{-1}$, and distance less than 3.5 Å) or geometric (O — H..O bond angle $\theta < 30^0$) supply the values about two times less [639].

Water polymers are convenient for the testing of the effect of increasing number of hydrogen bonds in well defined, small molecular system. For linear water dimer (Fig. 1–2) the dissociation energy of the hydrogen bond (E_{HB}) is about 25 kJ $mole^{-1}$, as calculated using CNDO/2 method with experimental values of structural parameters. The linear dimer is more stable than the cyclic or the bifurcated structures [244, 489].

Angular distortions of hydrogen bond are described by the values of (i) the angle, ϕ, between the O...O bond and the direction of the sp^3 lone pair orbital of the (electron) donor oxygen; (ii) the angle, θ, between the O..O bond and the direction of the O — H bond of the proton donated to the hydrogen bond (Fig. 1–2).

Undistorted linear dimer $(H_2O)_2$ was found in vapor phase; the O — O distance was recorded as equal 2.98 Å, and $\phi = 58^0$ [178]. Similar configuration of a stable water-molecule pair (r_{O-O} = 3.00 Å, $\phi = 40^0$) was obtained according to Hartree-Fock calculations [267].

However, Hartree-Fock calculations show that the energy of the dimer and E_{HB} do not vary significantly for θ varying between 0^0 and 35^0, and for ϕ between -20^0 and 60^0, although further increase of ϕ increases the dimer energy, and markedly decreases E_{HB} [245, 542]. These facts are in contrast with the suggestions that the characteristic tetrahedral orientation angles ($\phi = \pm 54.7^0$) are preferred in nature, because they align lone-pair electrons along the hydrogen bond axis.

In undistorted linear dimer, moderate rotations of water molecules around their oxygens do not require much energy, under the condition that proton donated to the hydrogen bond remains on the rotation axis. The tetrahedral angles ($\phi = \pm 54.7^0$, and $\theta = 0^0$) do not lead to pronounced energy minima. This suggests that tetrahedral orientation seems to be the only feasible way to arrange mutually repelling neighbors around a central water molecule at distances close enough to permit fully developed hydrogen bonds [642].

The CNDO/2 calculations show that the average hydrogen bond energy in water open trimer is higher than in the linear dimer [244, 321]. The average hydrogen bond energies of open tetramers and the tetrahedral pentamer are close to the value for stable trimer. E_{HB} becomes additive for polymers larger or equal to the trimer [244].

Although the cyclic trimer seems to be less stable than open trimers [244], cyclic polymers may exist; some of them may be more stable than the linear structures [154]. Cyclic polymers cannot explain the three-dimensional (3-d) networks of hydrogen bonds in liquid water, however, the possibility of the presence of isolated cyclic polymers cannot be excluded.

After the formation of the hydrogen bond, charge distribution in both water molecules changes in such a way that the proton acceptor becomes a still better donor of its proton to the next bond, than before the formation of the first hydrogen bond. Analogously, the proton donor increases its ability to accept a proton due to existence of the previous hydrogen bond.

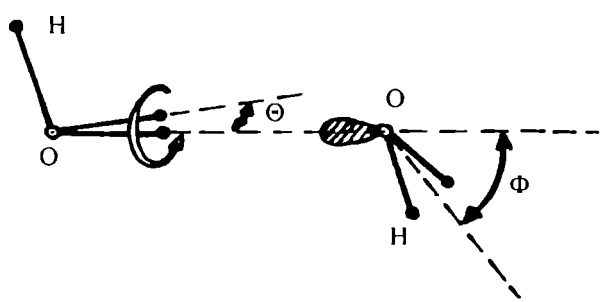

Fig. 1–2. Linear water dimer; ϕ and θ angles (see text), and rotation around O — O axis are marked.

The shortening of the O — O distance to 2.74 Å in ice, in comparison to a water dimer, may be partially explained by the attraction of non-bonded molecules. However, the hydrogen bond cooperativity contributes to the majority of this shortening [642].

1.4 Ordinary ice (Ih)

Water forms at least eleven crystalline polymorphs, however, if liquid water freezes at atmospheric pressure, the ordinary ice Ih is formed.

In ice Ih every oxygen is placed in the center of a tetrahedron, whereas its four nearest neighbors are in the apexes of that tetrahedron. The O — O distance equals 2.76 Å. Water remains as ice in its molecular form, building up four hydrogen bonds with the closest neighbors; its O — H bonds are directed towards the lone-pair electron orbitals of its two neighbors, forming two hydrogen bonds, whereas each of its two lone-pair electron orbitals is directed towards O — H bonds of two nearest neighbors, forming a third and fourth hydrogen bond. The dimensions of water molecules in ice Ih are not very different from those of isolated molecules: the O — H distance is about 1.01 Å, and the H — O — H angle is probably not much greater than the valence angle in the isolated molecule, 104.5^0 [187].

The spatial structure of Ih ice crystallite is formed from the puckered layers perpendicular to the c axis, containing the hexagonal rings in the 'chair' conformation of cyclohexane. The unit cell of Ih ice crystal contains four oxygen atoms and has a symmetry $P6_3/mmc$. The arrangement of oxygen atoms is isomorphous with the wurtzite form of zinc sulphide, and with the silicon atoms in the tridymite form of silicon dioxide [73]. An important characteristic of this structure is the presence of vacant "shafts" running both parallel and perpendicular to the c-axis. The presence of empty "shafts" accounts for floating of ice Ih on its melt [187]. The ratio c/a is only ~0.25% less than the value for a crystal built from perfect tetrahedra (1.633) [440].

Hydrogen positions are more difficult to establish, mostly because hydrogen is less effective in X-ray scattering. Pauling, [520], argued that hydrogen atoms in ice Ih are disordered, so that: (i) H_2O molecules in ice are intact (neglecting small amount of ionized molecules); (ii) each H_2O molecule is oriented in such a way that its two O — H bonds are directed approximately toward two of the four nearest neighbors; (iii) the orientation is that only one hydrogen lies approximately along every O — O axis. Under the above assumptions, the calculated, residual entropy of ice at 0K equals

$$S_0 = R \ln\left(\frac{3}{2}\right) = 3.371 \text{ J mole}^{-1}\text{deg}^{-1}, \tag{1.3}$$

which agrees well with the measured entropy of ice Ih, (3.4±0.6) J $\text{mole}^{-1}\text{deg}^{-1}$ [237, 238]. The measured residual entropy of D_2O ice Ih, (3.2±0.4) J $\text{mole}^{-1}\text{deg}^{-1}$

[441], is equal, within the experimental error to the H_2O value, confirming Pauling's hypothesis. Nagle, [495], proved that the correct calculated value, S_0, is equal to (3.409±0.0008) J $mole^{-1}deg^{-1}$ for both ice Ih and for ice Ic. Neutron diffraction (in D_2O ice) shows that Pauling's disordered structure of ice Ih is maintained down to -150^0C [528].

The outer surface of the ice crystallite consists of the hexagons of one 'puckered' layer. The oxygen atoms placed on the surface of the ice crystallite become water binding sites for approaching water molecules. Binding sites form the hexagonal lattice with the hexagon side l = 2.61 Å and with every second oxygen located 0.90 Å deep in the ice crystallite. The distance between two exposed outside neighbors equals L = 4.52 Å. The surface per one H_2O, S_{H_2O} = 17.7 Å, or 5.65 water molecules per 100 Å. The total number of water binding sites (including both exposed ones and deep ones) is 11.3/100 $Å^2$; the surface per water molecule of one 'puckered' layer equals 8.85 $Å^2$ (calculation for perfect tetrahedral structure).

1.5 Ice polymorphs

At elevated pressure and/or decreased temperature ice forms numerous polymorphs. Majority of high-pressure polymorphs may exist metastably at liquid-nitrogen temperature and at atmospheric pressure, thus, are easy to investigate (in so called *quenched* phases).

Ice polymorphs formed at moderately elevated pressure reveal several similarities (ices II, III, V, IX, and probably ice IV):

(i) Water molecule is hydrogen-bonded to its nearest four neighbors, however, the so formed tetrahedra are significantly less regular than in ice Ih.

(ii) Although the distance of nearest hydrogen-bonded neighbors equals (2.8±0.1) Å (as in ice Ih), the distance of nearest non-bonded neighbors is much shorter (3.2–3.5 Å, in contrast to 4.5 Å in ice Ih).

(iii) Tighter spatial arrangement of molecules in ice crystals arises not from shortening but from distortion of hydrogen bonds [187].

According to X-ray data, the unit cell of quenched ice II is rhombohedral and contains 12 molecules. The structure is composed of columns of puckered hexagonal rings, reminiscent of the columns in ice Ih, but linked more compactly. The columns of hexagonal rings are detached, moved up (or down) parallel, relative to axis c. The steric requirements of relinking cause the hexagonal rings in each column to twist relative to one another through an angle ca. 15^0, and alternate rings to flatten considerably. An ordered arrangement of hydrogens in ice II is suggested (entropy is roughly $R \cdot \ln(3/2)$ lower than that of neighboring phases) [348].

Unit cell of quenched ice III is tetrahedral and contains 12 molecules. Two types of oxygen may be differentiated in the structure: oxygens O_I lie on hydrogen-bonded helices having fourfold screw axis; oxygens O_2 linking these helices. Every oxygen O_2 forms hydrogen bonds with O_I oxygens in four separate helices [351].

Ice IX may be prepared by cooling of ice III to -100^0C. From entropy considerations it is suggested that hydrogens in ice IX are ordered [83, 705].

Ice V forms a monoclinic unit cell containing 28 molecules. Its structure is formed by two types of zig-zag chains of hydrogen-bonded water molecules; the chains run parallel to the a-axis of the crystal. One chain is formed from alternating O_2 and O_3 oxygens; the other from O_4 oxygens. The $O_2 — O_3$ chains are hydrogen-bonded in pairs to the $O_4 — O_4$ chains; $O_2 — O_3$ chains are joined by O_I atoms. It is thought that hydrogens are disordered in ice V [353].

Ice IV is a metastable phase found in the range of stability of ice V. Nothing is known about its structure (observed only by Bridgman, 1935).

Ices VI, VII and VIII are the densest known forms of ice. They are formed from two fully hydrogen-bonded frameworks; each of them forms cavities filled by the molecules of the other framework. The frameworks are interpenetrating, but not interconnecting [212].

Ice VI has a tetragonal unit cell containing 10 molecules. As in all other ice polymorphs, every water is hydrogen-bonded to its nearest neighbors. The molecules form chains that run parallel to the c-axis. These chains are hydrogen-bonded laterally to four neighboring chains, forming one complete framework. Every set of four chains surrounds a shaft filled by a chain of the second framework. All three types of nearest neighbor distances are about 2.81 Å. Every water molecule has eight non-hydrogen-bonded nearest neighbors at a distance 3.51 Å (belonging to the second framework). The O — O — O angles markedly differ from 109.5^0, some are 128^0, others only 76^0 [349].

Ices VII and VIII have the same crystalline structure (body-centered cubic structure), but differ in the position of hydrogens [75, 702]. The structure can be regarded as two interpenetrating ice Ic frameworks (see below). Kamb & Davis, [352], predicted that ice VII (and VIII) is the ultimate high-density polymorph, which will have the recognizable properties of ice. Every oxygen has eight nearest neighbors (at the distance 2.86 Å), but is hydrogen-bonded to four of these. As ice VII is cooled down, there is a phase transition at $+5^0$C with $S_{trans} = R \ln(3/2)$, suggesting that protons are disordered in ice VII [704]. The density of ice VIII (1.66 g cm^{-3} at $25 \cdot 10^6$ hPa) is smaller than the doubled density of ice Ic, suggesting that there is a significant repulsion between each water molecule and its four non-hydrogen-bonded nearest neighbors [350].

The vitrification of water was never obtained by extremely rapid decrease of the temperature of liquid water. The theoretical extrapolations of glass transition temperatures for binary solutions predict the temperature of glass transition for

water at $T_g = (138\pm2)$ K [8, 236, 555]. From the Vogel-Tammann-Fulcher equation (estimated for viscosity equal to 10^{12}) the temperature $T_g = (162\pm1)$ K [477], which is the temperature considerably higher than the estimate from binary solutions.

However, vitreous ice is formed when water vapor condenses on the surface cooled down to -160^0C [98]. It is a glassy form of water with not known structure. At warming vitreous ice irreversibly transfers to ice Ic (releasing 0.8–1.3 kJ mole^{-1}) [235, 171]. Differential scanning calorimetry (DSC), in water, showed a glass transition temperature at 139 K [470], whereas adiabatic calorimetry scans at 134 K [651]. Both results are in good agreement with the extrapolations from binary solutions.

McMillan & Los, [470], believe they observed a glass transformation in warmed vitreous ice at -139^0C, followed by crystallization into ice Ic at -129^0C.

Cubic ice Ic can be formed by warming of vitreous ice; by condensing of water vapor on the surface held at the temperature between -120^0C and -140^0C, or by warming any of the quenched high-pressure ice polymorphs [35, 36, 46]. At further warming ice Ic irreversibly transforms to ice Ih. This transformation was observed over a wide range of temperature (from about -130^0C [171] up to -70^0C [28]).

The structure of ice Ic evaluated from X-ray and electron diffraction is identical to the arrangement of carbons in diamond. As in ice Ih, the distance of nearest neighbors is 2.75 Å (at -130^0C), and the oxygens are arranged in puckered layers containing hexagonal rings in "chair" conformation. Unlike ice Ih, the stacking of puckered layers is such that three oxygen atoms from one layer and three, from the next one, form hexagonal ring in "chair" conformation [76]. The hydrogen atoms in ice Ic are disordered as hydrogens in ice Ih, but the O — H distance (0.97 Å) is only slightly different from 1.01 Å for O — D distances in ice Ih [318].

Summarizing, in all ice polymorphs (i) water molecules remain intact (the angles H — O — H and the distances O — H are not significantly altered as compared with isolated water molecule); (ii) water molecules are hydrogen-bonded to their nearest neighbors; (iii) approximately tetrahedral conformation of four nearest neighbors is maintained.

However, there are some characteristic features distinguishing high-pressure ice polymorphs: (i) the presence of close non-hydrogen-bonded neighbors (at a distance less than 4.5 Å); (ii) the angles of hydrogen bonds in equilibrium differ from 180^0 by more than several degrees (in Ih and Ic by only about 7^0); (iii) the O — O distances of nearest neighbors in equilibrium differ significantly from 2.76 Å.

1.6 Freezing of water

That water completely freezes at $T_m = 0^0$C (under atmospheric pressure), was contested for the first time by Faraday, who proposed the presence of a mobile

water phase on the surfaces of ice [337]. Weyl, [701], qualitatively estimated the thickness of the liquid-like layer on the ice surface at several tens of nanometers. Fletcher, [205, 206], considered quantitatively the thickness of the mobile film as a function of temperature, assuming the transition from the ordered structure of water to ice crystal.

Strong argument for the existence of mobile water phase at $T < T_m$ (and at atmospheric pressure) in polycrystalline ice is the observation of a narrow NMR line for protons of ice [30, 405]. The narrow NMR signal was explained in terms of: (i) the presence in ice of the non-hydrogen-bonded interstitial water, or the presence of impurities; (ii) the decrease of melting temperature caused by the surplus of the surface free energy on edges of ice crystallites; (iii) the presence of a semi-liquid surface layer at the water-ice interface.

To explain the nature of a narrow NMR signal, several forms of finely divided ice were tested [406]: (a) hoar-frost deposited on a Dewar flash filled with liquid nitrogen; (b) aerated ice by introduction of air bubbles into freezing water ($S \approx 1\ m^2\ g^{-1}$); (c) freezing of water containing teflon particles ($\varphi = 35$ nm, $S \approx 30\ m^2\ g^{-1}$); (d) polycrystalline ice obtained from freezing of distilled water (in ordinary polycrystalline ice the average grain dimensions are of the order of 10 μm, whereas $S \leq 0.1\ m^2\ g^{-1}$).

The magnitude of the narrow signal was found to be proportional to the ice-gas and ice-teflon interfaces, and decreased with decreasing temperature.

DSC scans performed on polycrystalline degassed ice Ih reveal the presence of non-frozen fraction with the magnitude of about 1.5% at -5^0C, subsequently decreasing with decreasing temperature down to zero magnitude at about -45^0C [78].

The disordered structure is energetically favorable in border regions between ice crystallites of polycrystalline ice. As the formation of stable crystalline structure is difficult here because of the steric mismatch of binding sites of neighboring crystallites, water molecules localized in these border regions non-cooperatively immobilize with decreasing temperature.

1.7 Hydrogen bonds in Mendeleevian neighbors of oxygen

A stable network of hydrogen bonds, responsible for several macroscopic anomalies, makes up the uniquity of water. Thus, it is interesting to consider the hydrogen binding abilities of hydrides of Mendeleevian neighbors of oxygen, namely of hydrogen fluoride (HF) and ammonia (NH_3).

Hydrogen fluoride solidifies at $t_m = -83.4^0$C. It forms slightly stronger hydrogen bonds than oxygen (FH..F length equals 2.49 Å, the F — F — F angle 120.1^0), orthorhombic unit cell contains 4 molecules (a = 3.42 Å, b = 4.32 Å, and c = 5.41 Å), and the calculated density is 1.663 g cm^{-3} at -125^0C (measured density: 1.658 g cm^{-3} at -97.2^0C). In solid HF hydrogen bonds form infinite zig-zag chains, without polygonal closures. HF can donate or accept hydrogen only once.

This is why an infinite 3-d network of hydrogen bonds is not possible. Residual entropy should be negligible, as the number of configurations equals two per every infinite chain (assuming neither F^- nor H_2F^+ ions). Coplanarity of the non-hydrogen-bonded chains may be either due to the nature of the bonding within the chain or due to ordering forces in crystalline solids [15].

Solid ammonia forms a cubic lattice (a = 5.138 Å at -102^0C), which slightly differs from perfect FCC lattice, with a unit cell (m^3) containing 4 molecules. Measured density of ammonia equals 0.817 g cm^{-3} at t = -79^0C, and 0.836 g cm^{-3} at t = -185^0C. The N — N distances are (3.349±0.003) Å, whereas the angles N — N — N are equal either to $(118.05\pm0.05)^0$ or $(71.66\pm0.16)^0$, which in both cases significantly differs from tetrahedral values. The N — H distance is 1.13 Å, which is longer than in gaseous ammonia, where it equals 1.008 Å [514].

Although ammonia could form extended 3-d network of hydrogen bonds, acting triply as hydrogen donor and triply as hydrogen acceptor, the molecular size and geometry of NH_3 are ill suited for the formation of the local arrangement of six neighbors involving formation of linear hydrogen bonds of optimal length. Hydrogen bonds formed in condensed phases of ammonia, thus, are severely strained and weakened, resulting also in a narrow temperature range of the liquid phase ($t_m = -77.7^0$C, $t_{boiling} = -33.35^0$C).

1.8 Liquid water

Melting of ice causes obvious macroscopic changes resulting from new high-temperature arrangement of molecules. Rigidity of the solid is replaced by fluidity, and the crystalline periodicity is replaced by spatial homogeneity.

Density of water increases about 9% on melting, indicating that in liquid water packing of molecules is much tighter than in periodical structure of ice. On the other hand, the ratio of melting heat (6.03 kJ $mole^{-1}$) to sublimation heat at 0^0C (46.9 kJ $mole^{-1}$) equals about 0.13, which means that the majority of chemical bonds constituting spatial structure of ice crystal is not ruptured at melting.

X-ray diffraction at 300 K reveals the existence of local tetrahedral structure in liquid water. The radial distribution function (RDF) shows the first peak at a distance of 2.9 Å (first, hydrogen-bonded neighbors) with the coordination number 3.1; the first non-hydrogen-bonded neighbors contribute to RDF peak at 3.3 Å (coordination number 1.3). The broad peaks centered at 4.5 Å and at 6.7 Å are assigned to the interactions of the second and the third neighbors, respectively. Their presence defines the size of tetrahedral structure in liquid water at room temperature. For overheated water (T = 416 K and ρ = 0.95 g cm^{-3}), the second and third peaks in RDF disappear, showing the breakdown of local tetrahedral ice-like structure of liquid water [719].

Molecular simulations yield additional information on the spatial structure of hydrogen bond network in liquid water. Although there is still room for

discussion about how well the "water-like" substance created by computer approximates real water, many of the macroscopic anomalies (such as liquid-phase density maximum, isothermal compressibility minimum, high heat capacity) and diffusive parameters obtained by computer simulations are in good agreement with experiment [642].

Monte Carlo computer simulations show that the averaged number of hydrogen bonds in liquid water equals $<n_{HB}> = 3.19$ at $T = 298$ K and at $p = 0.1$ Mpa [345], whereas neutronography supplies the value $<n_{HB}> = 3.58$ at the same conditions [631].

The averaged number of hydrogen bonds in free water decreases roughly linearly with increasing temperature [652] and in supercritical water equals $<n_{HB}> = 1.50$ ($T = 673$ K, 80 Mpa) and $<n_{HB}> = 1.68$ at $T = 573$ K and at $p = 10$ MPa (neutronography: [631]); whereas $<n_{HB}> = 0.29$ at 400^0C and at $\rho = 0.52$ g cm^{-3}, and $<n_{HB}> = 0.13$ at $t = 500^0$C and at $\rho = 0.2$ g cm^{-3} [313].

The distribution of molecules in liquid water engaged in various numbers of hydrogen bonds, n_{HB}, shows a maximum for $n_{HB} = 2.3$ ($t = 10^0$C). This result excludes "framework-interstitial" models of liquid water, for which completely non-hydrogen-bonded water molecules reside within fully hydrogen-bonded frame-works of molecules, with clathrate structure or deformed ice Ih structure (these models require a bimodal distribution, with maxima at $n_{HB} = 0$ and at $n_{HB} = 4$, which is not confirmed by molecular simulations) [643].

In liquid water at $t = 10^0$C the distribution of molecules engaging in non-short-circuited hydrogen bond polygons shows the presence of both even and odd polygons, with no notable preference for one over the other [550]. This is in contrast to ice Ih, where only non-short-circuited hexagons are possible. This result rules out "iceberg" models of water that postulate disconnected fragments of ice suspended in a sea of non-hydrogen-bonded water molecules [504].

Liquid water at room temperature (and higher) lies above the critical percolation threshold for a 3-d network of hydrogen bonds [232], which means that a macroscopic sample of liquid water has uninterrupted hydrogen bond paths running in all directions, which spans the entire volume of the sample. They provide natural routes for rapid transport of H^+ and OH^- (proton "holes") by a directed sequence of exchange hops.

To summarize: (i) in liquid water there exists a random 3-d network of hydrogen bonds; (ii) this network locally prefers tetrahedral structure with significant contribution from distorted or broken bonds (their presence enables water molecules to change the localization and the network topology); (iii) ice melting allows more tight configuration of distorted hydrogen bonds (this process dominates below 4^0C); (iv) at the same time the opposite process of hydrogen bond breaking occurs, which causes volume expansion of the liquid (dominating over 4^0C).

1.9 Self-diffusion of water

Molecules of liquids experience frequent displacements from their temporal equilibrium positions, which macroscopically manifests as "fluidity" of the liquid. The self-diffusion coefficient, D, is a measure of the rate of such itself displacements (see Chpt. 2.2.3 for more detailed discussion of diffusion equation, diffusion tensor, and diffusion coefficient).

The value of the self-diffusion coefficient of water is $D = 2.5 \cdot 10^{-5} cm^2 s^{-1}$, and does not vary depends significantly on the method of measurement; e.g. NMR spin-echo [668], isotopic tracers [342, 694, 695]. The experiments performed on isotope tracers in capillary tubes show that HDO and HTO diffuse no faster than $H_2{}^{18}O$, indicating that the mechanism of rapid H^+ transfer that accounts for the electrolytic conduction of water plays a negligible part in the self-diffusion of water. Because of its slightly higher viscosity, D_2O shows a slightly lower value of diffusion coefficient ($D = 2.11 \cdot 10^{-5} cm^2 s^{-1}$) than H_2O [442].

The temperature dependency of diffusion coefficient D is described by the Arrhenius equation [695]

$$D = A \cdot \exp(-E_a / RT) , \tag{1.4}$$

where A is a constant. The energy barrier, E_a =(9.3±1.3) kJ $mole^{-1}$ (evaluated using HDO and HTO tracers) and E_a =(18.4±1.3) kJ $mole^{-1}$(for $H_2{}^{18}O$ tracer) [694, 695], can be related to the energy of a single hydrogen bond broken to allow diffusive motion of water molecule.

The activation energies for self-diffusion, dielectric relaxation, and viscous flow of water have close values, so, that it is reasonable to assume that they are associated with the same mechanism.

Making use of these assumptions it has been shown that

$$\frac{\lambda^2}{\tau_D} = D = \frac{CkT}{\eta} , \tag{1.5}$$

where λ is the mean distance between two successive equilibrium positions of a diffusing water molecule in the direction of diffusion, τ_D is the dielectric relaxation time, η is viscosity, C is a constant depending on intermolecular separations [695]. Two observations support the validity of this assumption: (i) the quantity $D\eta/T$ is nearly independent of temperature (between 0 and at least 55^0C) [572, 695]; (ii) the values of $\tau_D T/\eta$ for H_2O and for D_2O are nearly equal [126].

1.10 Water dissociation and ion migration

The direct-current conductivity of ice Ih is equal $10^{-9}\ \Omega^{-1}\ cm^{-1}$ (at -10^0C), which is one order of magnitude smaller then the conductivity of liquid water at the melting-point. Electrolysis experiments indicate that ions (presumably protons) are

sole charge carriers in ice Ih. Thus, the conductivity is intimately related to the ionic dissociation of H_2O molecules [257, 710]. The dissociation of the water molecule may be described by the equation

$$H_2O \xleftrightarrow{k_R k_D} H^+ + OH^- , \tag{1.6}$$

where k_D is the rate constant for dissociation, and k_R is the rate constant for neutralization. Both rates, as evaluated from water electrolysis experiments, are equal to $k_D = 3.2 \cdot 10^{-9} s^{-1}$, and $k_R = 0.86 \cdot 10^{13} l\,mole^{-1}s^{-1}$.

The dissociation constant is defined as

$$K_{H_2O} = \frac{k_D}{k_R} = \frac{[H^+] \cdot [OH^-]}{[H_2O]} \tag{1.7}$$

and for ice I equals $3.8 \cdot 10^{-22}$ mole l^{-1} [185].

As compared to ice, in liquid water the values of constants describing the dissociation process decrease and are $k_D = 2.5 \cdot 10^{-5} s^{-1}$, $k_R = (1.4 \pm 0.2) \cdot 10^{11} l\,mole^{-1}s^{-1}$, and $K_{H_2O} = 1.821 \cdot 10^{-16}$ mole l^{-1} [184].

In liquid water dissociated protons hydrate forming an oxonium ion H_3O^+, or even higher complexes ($H_9O_4^+$), which are short-lived forms with the life-time of $\tau_{H^+} \approx 10^{-12}$s [183]. Thus, using the value of hydrogen ion life-time and the equation

$$\frac{\tau_{H_2O}}{\tau_{H^+}} = \frac{[H_2O]}{[H^+]} \tag{1.8}$$

one can get the average time between subsequent proton bindings for water molecule as equal to $\tau_{H_2O} \approx 5 \cdot 10^{-4}$s [187].

The hydration heat for H^+ ion equals 1.16 kJ $mole^{-1}$ (at +25°C), which is the value at least 0.419 kJ $mole^{-1}$ higher than for any other monovalent ion (e.g. for OH^- the heat of hydration equals 0.465 kJ $mole^{-1}$).

Proton and deuteron mobility in ice I (at −10°C) equals $\mu \approx 0.08$ cm^2 V^{-1}s^{-1}, and $\mu \approx 0.02$ cm^2 V^{-1}s^{-1}, respectively, which is one order of magnitude higher than in liquid water. The ion mobilities in liquid water (at t = +25°C) are $0.53 \cdot 10^{-3}$ cm^2 V^{-1}s^{-1} for Na^+ ion, and $0.79 \cdot 10^{-3}$ cm^2 V^{-1}s^{-1} for Cl^- ion [184].

This suggest that the presence of regular lattice of hydrogen bonds enables a rapid transfer of hydrogen ions along the directions of hydrogen bonds. Two mechanisms are possible: (a) one proton of the oxonium ion (H_3O^+) may jump along the line of the hydrogen bond to transfer to the nearest water molecule; (b) water proton may migrate along the hydrogen bond to recombine with OH^- ion.

In liquid water ion migration is slowed down by the breaks in the lines of hydrogen bond lattice.

1.11 Layering of water in restricted space

Although there exist considerable motional freedom of water molecule in the liquid phase, the restricted geometry of the space filled by water may induce a short-lived structural arrangement of water molecules.

Murthy & Worthington, 1991, using X-ray diffraction observed that in multilayered membranes from frog sciatic nerves the spacings between bilayers increased in discrete steps of approximately 5 Å during swelling. As myelin is hydrated, there are no intermediate hydration states between the unswollen ($d \approx 170$ Å) and minimally swollen ($d \approx 200$ Å) myelin. The 30 Å difference in thickness is probably due to changes in the charge density on the surfaces of the bilayer, which may arise from conformational changes in the membrane proteins and in the polar head-groups of the lipids. It is likely that the changes in the membrane occur in its initial (discontinuous) phase of swelling, and the repeated periods greater than approximately 200 Å have little, if any, contribution from the structural changes in the bilayer. Thus, the different repeat distances recorded from myelin swollen past the minimally swollen state reflect the differences in the widths of the fluid layers between the opposing planes of polar groups [466, 714].

From this result Murthy & Worthington could (but did not) mention that a water bilayer rather than a water monolayer is added, resembling the structure of two subsequent 'puckered' layers of distorted ice Ih. Such a mechanism of filling maintains the periodicity of the structure and allows all binding sites to be used at very similar spatial configuration as for preceding, thinner water layer.

1.12 Supercooling of water

The presence of unfrozen aqueous medium inside biological structures at the temperatures below 0^0C focuses ones attention on the process of water supercooling.

Although the measurements of supercooled water were initiated relatively early, with little progress only. Liquid water density decrease was recorded down to -9^0C [161, 162], however, the temperature range of supercooling was not extended till Mohler, 1912 (only down to -13^0C). The pressure of water vapor was measured down to -19^0C [344] and to -23^0C [560, 561]. Slow progress in increasing the degree of supercooling (for definition see Chpt. 1.12.2) intuitively suggested that the range of supercooling for water may be narrower than for other liquids.

1.12.1 Freezing of supercooled water

The measurements of water supercooling below -10^0C are difficult because the probability of avoiding the ice crystallization strongly depends on the individual sample. Specifically, such probability increases with decreasing sample size. As usually observed, the crystallization of ice does not seem to be a property of water itself, but rather a function of the solid surface in contact with water. During (i) heterogeneous nucleation of ice crystallites the surface of a very tiny 'crystal nucleus' generates the high local excess of free energy per unit volume initializing the growth of the ice crystallite [161, 162]. To observe the (ii) homogeneous nucleation at which ice is formed as a result of spontaneous order fluctuations within the pure liquid, the water sample must first be purified of all other particles [148]. The nucleation has a statistical character, thus, requires the fluctuation in space and the time needed for the growth of the crystallite.

With increasing departure from equilibrium, the tendency to reach the stable state increases and the time scale for escape from the metastable state is reduced [7]. Not very much is known on the nature of nuclei promoting crystallization, e.g. purification procedure which removes the nuclei promoting crystallization at a given temperature, fails to remove the seeds which are effective at slightly lower temperature [7]. The lowest supercooling temperature in a glass tube equal to $-30(\pm1)^0$C, was observed twice by Wylie, 1953. Within 24 hours the freezing point of this sample increased to -21.4^0C, then after next 24 hours to -13.4^0C. As the crystallization process started in the same place of the test tube, Wylie concluded that he had eliminated the suspended seeds from the water and crystallization process was initialized by the minute tridymite or other silicate crystallites placed in the wall of the glass vessel.

If the size of the sample is decreased, the lower its freezing point is likely to be, as the probability of appearance of crystallization nucleus decreases with the decrease in the sample volume. However, the probability that the nucleation event occurs at a given seed will still be dependent on random fluctuations in the arrangement of proximal water molecules, and thus, will be a function of time [246, 677, 691].

When a large number of samples is used, the distribution of freezing points observed during cooling runs at a fixed cooling rate has a characteristic form with the same 3.0^0C halfwidth distribution, irrespective of droplet size, for volumes ranging between 10^{-9} and 10 cm^3 (radii from 6 μm up to 1.3 cm) [43, 44]. Distinctly narrower distributions (only 1.3^0C, despite the presence of a distribution of sample volumes) were observed using calorimetry in the lowest freezing point ranges, i.e. near -40^0C, observed in the smallest samples of water droplets in an emulsion [118]. For extremely small and perfectly purified samples the nucleation depends on intrinsic fluctuations, which reach the critical magnitude with rapidly increasing frequencies close to the "homogeneous nucleation" temperature, T_H. This narrows the temperature range of nucleation.

In the case of heterogeneous nucleation, the freezing events will be spread over a wider range of temperature because of distribution of nuclei freezing efficiencies [7]. Every class of heterogeneous nuclei present in aqueous phase will be characterized by its own characteristic value of heterogeneous seed activity distribution, $\frac{dJ}{d\Delta T}$, where J is a nucleation rate per unit of volume, and $\Delta T = T_m - T$ defines supercooling, where T_m is the equilibrium freezing temperature. Large value of $\frac{dJ}{d\Delta T}$ implies narrow freezing ranges. It is not obvious what form such a heterogeneous seed activity distribution should have. According to the evidence summarized by Mason, 1957, (from cloud chamber experiments in which droplets are formed individually on aerosol particles), J is approximately described by

$$\ln J = \text{const} + k \cdot \Delta T . \tag{1.9}$$

Since the nucleation event is random in space and time, Eq. (1.9) implies that the volume, V, in which the nucleation event will be observed in unit time at a supercooling ΔT, will have a form

$$V = \text{const}' + k' \cdot \Delta T , \tag{1.10}$$

where parameter k' characterizes the shape of the heterogeneous nucleation activity distribution, while const′ depends on the total concentration of nuclei of all types per unit volume [7]. Eq. (1.10) allows to distinguish whether in the series of supercooling experiments heterogeneous or homogeneous nucleation process was active.

Recently, agreement was reached that water in volumes of 10^{-9} cm^3 (corresponding to a cube with 10 μm side) freezes at $-(39\pm1)^0$C (for ≈ 1–100 s observation periods) irrespective of the type of the contact surface (glass capillary wall, oil or other molecular film, or a nitrogen gas blanket) [43, 44, 109, 409]. The temperature of ice crystallization decreases from -39.1^0C [587] down to -41.2^0C [137] with an order of magnitude decrease in droplet diameter.

1.12.2 Comparison with other liquids

To quantify the supercooling ability of any given liquid, one defines the degree of supercooling as equal to $\Delta T/T_m$, where $\Delta T = T_m - T_H$ and T_m is the equilibrium freezing temperature.

The degree of water supercooling equals 0.148, which is one of the lowest values for known liquids (e.g. for P_4 it equals 0.364, for $CHCl_3$ it equals 0.33, for benzene 0.252, whereas for cyclopropane only 0.14) (data taken from [7]).

The homogeneous nucleation temperature of water decreases with increased pressure, reaching the minimum value of $T_H = -92^0C$ at $2 \cdot 10^6$ hPa [355]. At this temperature water can be supercooled by 69^0C, giving for the degree of supercooling 0.276, a value very close to the ones for other liquids.

1.12.3 Properties of supercooled water

To allow deep supercooling of water, the size of the sample is decreased (see Chpt. 1.12.1), which is realized by changing the shape of the sample:

(a) Thin layers (2-d macroscopic) allow the supercooling down to -31^0C (films of 1–2 μm thickness of diluted KI solutions placed between highly polished optically flat SiO_2) [7].

(b) Capillaries (1-d macroscopic) are preferred in measurements considering volume and/or 1-d motion.

(c) Droplet samples (0-d macroscopic) allow maximum degree of supercooling, and are usually made as a set of droplets in water emulsions. In emulsions, the sizes of droplets vary from 100 down to 0.5 μm, with the content of 50% by volume of water, e.g. in emulsion made from surfactant sorbitan tristearate (SPAN 65) in the dispersant n-heptane water supercools reversibly to -38^0C [556].

1.12.3.1 Density and expansivity

Density of supercooled water is usually measured in capillary samples. Its value decreases versus decreasing temperature. As ice Ih has the most open structure for pure (non-clathrate) system formed by four ordered water molecules, at the temperature of homogeneous nucleation of ice the local (and long-range) arrangement in liquid water should closely resemble the arrangement in ice I (either c or h). The extrapolation of density decrease with decreasing temperature gives a value of -45^0C if crystallization did not intervene, which is close to the ice nucleation temperature in cloud chamber experiments equal -41.2^0C [557, 727, 728].

The temperature dependency of (negative) expansivity,

$$\alpha = -\frac{1}{\rho}\frac{d\rho}{dT}, \tag{1.11}$$

for supercooled water is roughly exponential. The experiments at elevated pressure show that the density maximum shifts down the temperature with increasing pressure, and the maximum occurs at least up to $\approx 2 \cdot 10^6$ hPa [354].

1.12.3.2 Isothermal compressibility

Isothermal compressibility,

$$\kappa = \frac{1}{V}\frac{\partial V}{\partial T}\bigg|_T, \tag{1.12}$$

of supercooled water was measured down to -26^0C [634], showing anomalous rapid increase well described by a polynomial function

$$\kappa = a - b \cdot T + c \cdot T^2 - d \cdot T^3 + e \cdot T^4 - f \cdot T^5 \ , \tag{1.13}$$

where a, b, c, d, e, and f are fitted constants.

1.12.3.3 Heat capacity

Heat capacity of supercooled water measured for decreasing temperature (down to -38^0C) show the anomalous decrease in C_P [9]. Using the relation

$$C_V = C_P - VT \cdot \frac{\alpha^2}{\kappa} \tag{1.14}$$

the anomalously increasing part of C_P is completely compensated for by the subtractive term of Eq. (1.14), with the result that C_V remains almost constant with decrease of temperature [7].

1.12.3.4 Diffusion coefficient, viscosity

As shown on an Arrhenius plot, the diffusion coefficient of supercooled water linearly decreases with decreasing temperature. The activation energy reaches the value E_a =37 kJ mole^{-1} (at -30^0C), as observed by NMR spin-echo method [240]; or $\approx$ 46 kJ mole^{-1} (at -31^0C), as measured using polyethylene capillaries with HTO tracer [547]. The value of activation energy suggests that below 0^0C approximately two hydrogen bonds are broken at each translational step of the water molecule. The diffusion coefficient of supercooled water increases with increasing pressure [240].

Viscosity of supercooled water increases with decreasing temperature, with the activation energy increasing between -24^0C and -35^0C to the value E_a = 57 kJ mole^{-1} [515].

The temperature dependency of deuterium spin-lattice relaxation time T_1 for D_2O was recorded to the emulsion limit of -36^0C, showing that bulk data are in agreement with the data for water in emulsion. The activation energy was equal $E_a \approx 14$ kJ mole^{-1} (one bond breaking) for the temperatures roughly above 0^0C, and $E_a \approx 50$ kJ mole^{-1} (multiple bond-breaking process) for lower temperatures [305].

1.12.4 Singularity in supercooled water

The abnormal variations in κ and C_P suggest the presence of some cooperative process which dominates the behavior of supercooled water at low temperatures.

Angell, 1982, stated that the parameters for the non-equilibrium behavior of diffusion coefficient, viscosity, dielectric relaxation, rotational correlation time for dilute spin probe, proton and deuterium spin-lattice relaxation times fit consistently to the well known formula for critical phenomena:

$$Y = A_Y\left(\frac{T}{T_S} - 1\right)^{-\lambda_Y}, \tag{1.15}$$

where Y is a given thermodynamic property, and T_S is a transition temperature. He found for each Y, that $T_S = 228$ K for H_2O, and $T_S = 233$ K for D_2O.

Among aqueous systems, this anomaly may by unique for pure supercooled water, as in binary system containing 81.4% of H_2O and 18.6% of H_2O_2 there is no trace of anomalous increase in C_P preceding homogenous nucleation [511].

1.13 Wetting of surfaces

Hydration phenomena in dry biological systems deal with the problems of wetting, i.e. spreading of water on inner or outer surfaces of the system. Although essential, wetting processes are still poorly understood because [150]:

(i) all interfacial effects are very sensitive to contaminations and physical defects of the surface;

(ii) solid-liquid interfaces are much harder to explore than their solid-vacuum counterparts;

(iii) since the pioneering work of Young and Laplace, several capillary problems are not yet satisfactorily solved theoretically.

1.13.1 Young condition

When a small liquid droplet is in contact with a flat solid surface, two distinct equilibrium regimes may occur [150]: (a) partial wetting, with a finite contact angle θ_c, or (b) complete wetting with $\theta_c = 0$. The wetted portion of the solid surface is delimited by a contact line S–L–V (Fig. 1–3) of three phases: the solid S, the liquid L, and the equilibrium vapor V. Each interface has corresponding free energy per unit area: γ_{SL}, γ_{SV}, and $\gamma_{LV} = \gamma$ (a surface tension of the liquid). They well describe the energy content of the interfaces at the distance far from the line S–L–V. In the vicinity of the line S–L–V, where the situation is modified depending on the features of the system considered, a 'core region' with a radius r_c, is defined.

However, far from the line S–L–V, the contact angle θ_c may be related to far-field energies γ_{ij} without any knowledge of the core. In equilibrium, the energy of the system does not depend on any shift (dx) of the line S–L–V position (see Fig. 1–3). In such a shift the bulk energies are unaffected (as the pressure in the liquid and in vapor are the same), the core energy is unchanged (as core is only translated), the change in free energies of interfaces are related to the changes in interface areas. This leads to Thomas Young (1773–1829) condition:

$$\gamma_{SV} - \gamma_{SL} - \gamma \cdot \cos\theta_e = 0. \tag{1.16}$$

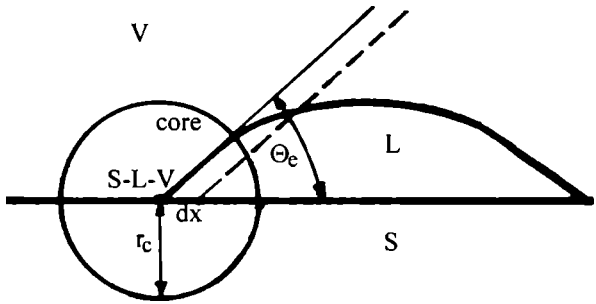

Fig. 1–3. Translation of a liquid-wedge (contact line, S–L–V) by a distance dx. S denotes a solid area, L – liquid, V – vapor, θ_e is the contact angle, r_c – the radius of the core area. The energy is unchanged in this process leading to Young condition.

The Young condition means that the contact angle is entirely defined by thermodynamic parameters. In many practical examples, the core radius $r_c < 100$ Å [539, 540], which is just a scale of wetting phenomena on dry biological surfaces.

1.13.2 Core region

Various types of core structures for the triple line are possible [150]:

(a) In presence of attractive van der Waals forces between solid and liquid, for $\theta_e << 1$, the profile of the core cross-section is hyperbolic and the height h_C of the perturbed region is of order of a/θ_e, where a is an atomic length.

(b) A form of core region which is similar to that as in case (a) occurs if a charged solid surface is wetted by salty water (with the screening length κ_D^{-1} instead h_C).

(c) At finite deformability of the solid the vapor-liquid interface may be minimized by stretching of elastic solid phase. The width of the deformed region is $r_c \approx \gamma/E$, where E is Young modulus of the solid.

(d) At thermodynamic conditions close to liquid/vapor critical point, the liquid-vapor interface becomes diffuse with the thickness ξ. Here the radius of the triple core $r_c \approx \xi$.

In experimental conditions, one finds that the triple line L is pinned, and immobile, not only for $\theta = \theta_e$, but for all angles θ:

$$\theta_r < \theta < \theta_a , \tag{1.17}$$

where angle θ_a (advancing angle) is measured when solid/liquid contact area increases, while θ_r (receding angle) is measured when the contact area decreases. The interval $\theta_a - \theta_r$ may be 10^0 or more.

Often observed pinning of the contact line S–L–V may be caused by:

(a) surface roughness. The line S–L–V can easily be trapped when parallel to a system of grooves [670]. The non-linear changes in ascending and receding angle were observed on surfaces with increasing roughness obtained by spraying of wax [163].

(b) Chemical contamination or inhomogeneities in the solid surface may pin the triple line up [150].

(c) Solutes in the liquid (surfactants, polymers, etc.) may deposit as a film on the solid surface. The presence or the absence of such a film may cause hysteresis in contact angle [112].

1.13.3 Breath figures

Deposition of water vapor on a surface is the initial stage of the hydration of dry biological system from gaseous phase. Patterns formed at the deposition process are called 'breath figures'.

Depending on wettability of the surface, condensing vapor forms a uniform film which appears dark (complete wetting case), or a set of droplets, which scatters light and appears white (partial wetting) [41]. For a long time breath figures were used as a simple and effective label to recognize the oil contamination of glass surfaces (detecting even a single monolayer of oil) [21, 476].

At complete wetting of borosilicate glass, the increase in thickness of water layer, de/dt, sprayed by vapor saturated nitrogen stream (at room temperature) on a glass plate (temperature of the glass equals T_S) is given by [41]

$$\frac{de}{dt} = \alpha \frac{w\Delta p}{RT_s} \cdot \frac{F}{A} \cdot \frac{M}{\rho}, \qquad (1.18)$$

where R is the gas constant, M is the molar mass of the liquid, ρ is its density, A is the cross-sectional area of the nozzle, F is gas flow rate, and w its percentage saturation (close to 100%).

If borosilicate glass is silanized in octadecyltrichlorosilane solution, the partial wetting case is observed. Advancing and receding angles are equal 110^0 and 95^0, respectively.

The characteristics of droplet patterns deposited on the surface can be described in terms of: the average droplet radius <R>, the polydispersity of the droplet size $g = \Delta R/<R>$, the mean distance between droplets <a>, and the surface coverage $\varepsilon^2 = (2<R>/<A>)^2$.

Depending on the duration of the experiment, three different regimes are observed [41, 392]:

(i) At short times ($t \leq 1s$), the glass surface is covered by a homogeneous pattern of small droplets with both <R> and <a> smaller than 2 μm. Intensive, coalescence caused, activity is observed.

(ii) In the intermediate time regime ($1 < t \leq 300$ s), and for $2 < \langle R \rangle \leq 300$ μm, there is well defined order: Droplets grow at almost constant polydispersity $g \approx 0.2$, and surface coverage $\varepsilon^2 \approx 0.5$. Through this time period, there are two distinct mechanisms of droplet growth. The radii of isolated droplets grow as t^n (with $n = 0.25 \pm 0.05$). When the droplets are in sufficiently close proximity, they merge rapidly to produce a step change in the radius, but the power-law growth remains unchanged between these breaks.

(iii) At very long time ($t > 300$ s), small droplets form between the large ones and the distribution of sizes becomes bimodal. The pattern of growth of large droplets remains unchanged.

Atomic force microscopy (AFM) was used to image the structures formed at room temperature by the condensation and evaporation of water on mica surfaces [323], focusing on much smaller scale of the wetting process (vertical scale was about 0.5 Å, and the lateral resolution of the order of 200 Å).

Immediately after cleavage (at $p/p_0 = 18\%$), the surface showed no contrast above the noise level. As the humidity increased monotonically, 2-d clusters formed with apparent heights of ~2 Å, and the diameter varied from 100 Å (a resolution limit) up to few thousands of angstroems. The uniform layer was obtained at $p/p_0 = 38\%$ (phase I). As the humidity continued to increase, the domains of a different phase (phase II) nucleated. They covered the surface uniformly at $p/p_0 = 40$–50%. The domains of phase II are characterized by reduction in the attractive force of several tens of piconewtons, which corresponds to a ~2 Å "lower" level than the surrounding area of phase I. The islands of phase II often have polygonal shapes (their edges often follow approximately straight lines forming angles of 60^0 and 120^0). During the drying process, holes formed in the phase II domains.

Hu et al. suggested that phase I is formed by water molecules solvating K^+ ions present on mica surface, whereas phase II of water has the crystalline structure, resembling that of an ice bilayer. However, at the temperature far above 0^0C, it is more likely that in water cluster a semi-crystalline, distorted structure is formed. Moreover, the sizes of the edges suggest strong pinning of the cluster contact line S–L–V on defects of Muscovite mica.

1.13.4 Water clustering on glass surface

Using proton spin-lattice relaxometry, this Author monitored on still finer (molecular) scale the clustering of water on silica surface. Due to high surface-to-volume ratio (S/V), the bound water contribution dominates in NMR signal recorded at low hydration level of porous system. As a model system controlled pore glasses (CPG's; for CPG parameters see Tab. 1–1) were selected.

Measurements were started with a highly hydrated system, that is, a volume of water was added equal to the calculated total pore volume. To describe the hydration state the following parameters were introduced:

(a) the volume filling factor $f_V = N/N_f$, where N is the actual number of proton spins in the sample and N_f is the calculated number of proton spins of water molecules which completely fill all the channels of the sample; and,

(b) the surface filling factor $f_S = N/N_S$, where N_S is the number of water protons which occupies all binding sites on the surface of the glass sample (one water molecule for one surface hydroxyl). The density of OH's was taken to be 4.5/100 $Å^2$ [329], which gives a geometric coverage of ~9 water protons / 100 $Å^2$.

Table 1–1. Physical characteristics of the Controlled Pore Glasses (CPG), obtained from CPG Inc., Fairfield, NY. The paramagnetic impurity content was determined by flame atomic absorption analysis.

Sample code	CPG2917	CPG548	CPG74
Pore diameter [Å]	2917	548	74
Pore distribution [±%]*	6.8	2.8	7.0
Specific pore volume [$cm^3\ g^{-1}$]	0.90	0.99	0.47
Specific surface area [$m^2\ g^{-1}$]	8.3	41.4	153
Surface / Volume [$10^6\ m^{-1}$]	9.2	42	325.5
Mn content [ppm]	< 1	< 1	1
Fe content [ppm]	40	30	30
Cr content [ppm]	< 2	5	4

* 66% of the pores' diameters are within this range of the mean.

In the high hydration regime, proton T_1's were determined using a stretched exponential (SE) fit, with the values of α between 0.9 and 1 ([149]; see Chpt. 2.3.1, 2.4, and 2.5). Single T_1 values were obtained down to a threshold value of the volume filling factor $f_V^t = (0.28\pm0.07)$ for the sample CPG74, (0.09 ± 0.04) for CPG548 and (0.11 ± 0.09) for CPG2917. For filling factors above the threshold filling f_V^t, the relaxation rate increases upon drying for all three samples.

Some external wetting of the glass beads occurs even for hydration levels below $f_V = 1$, suggesting that some pores may begin to empty before the water is released from the outer surface of the glass grains, e.g. wetting of the glass beads which results in beads being visibly "glued" together was significant in CPG548 even at $f_V \approx 0.6$.

For CPG samples dehydrated below f_V^t the proton relaxation function is no longer adequately described by a SE function. The distribution of relaxation times appears to become a sum of discrete, well-resolved peaks. The results obtained using the NMR spin-grouping analysis (see Chpt. 2.3.5–6) are shown in Table 1–2. For this range of hydration, a convenient measure of water in the system is the surface filling factor f_S.

To evaluate the effect of paramagnetic ions dissolved in water filling the CPG channels, T_1 of the water used to perfuse the CPG was first measured. There was no significant difference in proton spin-lattice relaxation time relative to bulk

water. This suggested that the dissolved paramagnetic ions (at the contamination level of 40 ppm) cannot be washed out by pure water (see Chpt. 2.5).

The hydration level for CPG74 (glass with the highest specific pore surface area) was analyzed in the broadest hydration range (Tab. 1–2). For the smallest amount of water detected, the magnetization components distinguished were the protons of the surface OH groups and protons of single water molecules tightly bound to the OH surface (presumably through two hydrogen bonds per H_2O [329]) resulting in short spin-spin relaxation times.

Upon drying f_V decreases from 1 to 0.2, the volume diffusion gradually becomes surface diffusion. Below 0.2, in the sample with 74 Å pore diameter, the pores are essentially covered with only one or two layers of water and the 2-d diffusion is within these surface layers only. In this hydration regime, the diffusion is less and less effective at averaging local differences due to more/less water and the local concentration of paramagnetic cations (Tab. 1–1). The distribution of the paramagnetic centers on the surface becomes visible, and the distribution of water droplets shows up as well. This results in an extremely non-exponential proton recovery function which cannot be accounted for by a SE model. However, it is possible to resolve the magnetization recovery into several distinct magnetization recoveries, each characterizing a combination of a specific proximity to the paramagnetic Fe ions on the surface and local water coverage.

The magnetization of the OH groups on the surface is particularly well resolved in this regime. As the sample is dried further the effectiveness of surface diffusion is slowen even more, and the spatially different protons (with different relaxation processes) become progressively more distinct. When only small clusters of water on the surface and OH groups remain, no averaging at all due to diffusion is possible. This transition from full surface coverage to water clusters can be traced through the non-exponential character of the relaxation. At $f_S < 0.03$ the diffusion is not effective any more, while between f_S's of 0.03 and 0.06 the breakdown of the surface diffusion occurs (Tab. 1–2).

The essential point of the proposed detection of percolation of water bound on glass surface is seen by comparing the 0.36 and 0.32 data (Tab. 1–2). While at $f_S = 0.36$ the longest spin-spin relaxation time T_2^* is only 320 μs, at $f_S = 0.32$ the longest $T_2^* \approx 2000$ μs is recorded. By implication, in this range of coverage, the water dynamics of the surface have changed substantially. It is proposed that the occurrence of a (7%) proton group with T_1 of 4 ms and $T_2^* \approx 2000$ μs demonstrates the formation of small droplets (which accounts for long T_2^*) situated near paramagnetic ions (which accounts for low T_1). At higher hydration of 0.36 these clusters are not yet formed, but a network of water covered these patches still allowed for averaging of OH and H_2O magnetization, both sharing the effect of paramagnetic cooling. Upon still further drying (to 0.32) this network breaks, and as a result OH magnetization (with much shorter T_2^*) and water droplets (with much longer T_2^*) can be differentiated.

Table 1–2. The results of the NMR spin-grouping analysis for the low hydration of three Controlled Pore Glasses. The samples were hydrated with redistilled and deionized water, then subsequently dried by heating to 350 K in a nitrogen atmosphere. All samples were sealed under nitrogen after this procedure. The proton spin-lattice relaxation time T_1 was measured at room temperature on a Bruker SXP spectrometer at 26 MHz using an inversion recovery sequence of r.f. pulses: $\pi - \tau - \pi/2$ —FID(t). The data were digitized using a Biomation A/D converter, then stored and processed on a Hewlett-Packard 9836 computer. To analyze the relaxation data the WATSPIN spin-grouping technique was applied.

Sample	f_S	A [%]	T_1 [ms]	T_2^* [μs]	Assignment
CPG2917	16.5	100	96	180	Diffusion averages all spins and sites
CPG548	7.00	100	110	290	As above
	4.58	100	24	140	As above
CPG74	1.71 (Near full geometric coverage of surface)	68 32	37 14	800 1500	Averaging process is not as effective, distribution of impurities and water droplets, the distribution is a characterization only
	0.93	28 72	36 9	900 1500	Mobile H_2O and OH. As above but more ions.
	0.36	62 38	65 8.0	60 330	As above, but less averaging
	"Apparent percolation transition"				
	0.32	7 86 7	1700 23 4	60 180 2000	OH, no impurities. OH and bound H_2O. Mobile H_2O near impurities
	~0*	10 79 11	2800 22 2	90 170 1200	OH, no impurities. OH and bound H_2O. Mobile H_2O near impurities

* While the stoichiometry indicated that the hydration state was close to $f_S = 0$ the assignments qouted make clear there was still a measurable quantity of water on the glass substrate.

However, by the specificity of NMR experiment, the observed "apparent percolation transition" reflects the decrease in size of water clusters detected by water diffusive properties in NMR-time-scale. Thus, it occurs for the hydration level below percolation threshold defined as creation/vanishing of infinite cluster (see Chpt. 3.2).

To summarize, the possible mechanism of changes accompanying the percolation process can be proposed (a cartoon of the above model is shown on Fig. 1–4), and ordered in steps as a function of decreasing surface hydration:

(i) For higher hydration levels the silica surface is fully covered by bound water containing paramagnetic impurities.

(ii) The bound water tends to form clusters. The uncovered areas of with separated double bound water molecules appear. The paramagnetic ions prefer the bound water clusters.

(iii) (At hydration level below percolation threshold) the "apparent percolation transition" breaks the paths between bound water clusters.

(iv) The further decrease in membrane hydration. The areas of free OH's appear; bound water clusters become smaller.

(v) The bound water clusters vanish. The paramagnetic ions remain in the regions covered by single monolayer of double bound water.

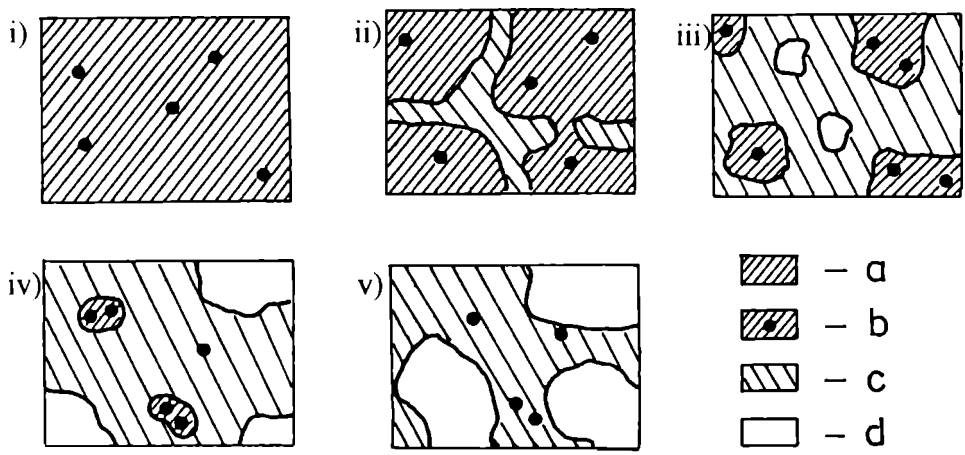

Fig. 1–4. The cartoon of the proposed model of percolation related phenomena as observed by proton nuclear magnetization. The distinguished regions: a) surface of CPG covered by bound water – fine hatching; b) paramagnetic ions – closed circles; c) separate molecules of bound water (immobilized) – coarse hatching; d) pore surface with OH's only – open area.

1.14 Hydrophobic effect

The unique solvent power of water is the effect of extreme importance for living entities, but the equally great importance is its unique lack of solvent power for many non-polar substances, enabling the formation of biological membranes, and the native conformation of biopolymers.

Hydrophobic substances are easily soluble in non-polar solvents, but poorly soluble in water, distinct from the substances that have generally low

solubility. The hydrophobic effect was for a long time explained as a "like-to-like" attraction of hydrocarbon chains (non-polar groups) [147, 460], which in fact, plays only minor role in hydrophobic effect. The effect primarily comes from strong attractive forces (hydrogen bonds) between water molecules, being isotropically arranged, which must be broken or distorted when any solute is dissolved in water. If solute is ionic or strongly polar, it can hydrogen bond to water molecules that more than compensate for breaking or distortion of hydrogen bonds in pure water.

In terms of the intermolecular bonds that are formed, the process of solution of a non-polar solute S in water may be schematically represented as [656]:

$$2\cdot(H_2-H_2O)+S-S\longleftrightarrow 2\cdot\left(H_2\overline{O-S-H}_2O\right), \qquad (1.19)$$

where the O — H bond in product of the reaction (plotted over the solute molecule) emphasizes that the hydrogen bonds tend to be maintained in distorted form [208]. The main factor driving the equilibrium in Eq. (1.19) to the left is the strength of the hydrogen bonds between water molecules.

Traube, 1891, found that the molecules consisted of long hydrocarbon chain and polar head, with measurable solubility in water, tend to migrate to the surface of the aqueous solution, what results in decrease in sufrace tension. For low concentrations of the solute (below saturation), at which the contacts between hydrocarbon chains are minimal, (and the surface is populated very sparsely), the decrease in surface tension was linear with solute concentration. The ratio of concentration at the surface layer to that in the bulk medium increases threefold with every CH_2 group added to the hydrocarbon chain ("Traube's rule"). Assuming that the attraction between alkyl chains should be responsible for the migration of the solute to the surface, the process would become cooperative at low solute concentrations (no linear dependency). Thus, the effect is caused solely by a lack of affinity between hydrocarbon and water [656].

1.14.1 Solubility of hydrocarbons

Majority of biological lipids contain hydrocarbon chains as their hydrophobic part. The hydrophobicity of the substance may be expressed in units of free energies of transfer from water to nonpolar solvent [376].

Chemical potential, μ_w, for a hydrocarbon dissolved in water is given by

$$\mu_w = \mu_w^0 + RT\cdot\ln X_w + RT\cdot\ln f_w \ , \qquad (1.20)$$

where μ_w^0 is the standard chemical potential, for infinite dilution in water, X_w is the molar concentration, and f_w the activity coefficient at concentration X_w. So defined standard chemical potential includes all interactions of an isolated hydrocarbon

molecule with the solvent water. Because of very low solubility of hydrocarbons in water, $RT \cdot \ln f_w$ can be set equal to zero. The term $RT \cdot \ln X_w$ expresses the cratic part of chemical potential, purely statistical contribution that arises from the entropy of mixing solvent and solute molecules [656].

Since the internal free energy is independent on solvent, the proper quantity to compare the effect of water and nonpolar solvent will be

$$\mu^0_{HC} - \mu^0_w , \tag{1.21}$$

where μ^0_{HC} is the standard chemical potential of hydrocarbon in nonpolar solvent.

For hydrocarbon dissolved in a nonpolar (hydrocarbon) solvent, we get for chemical potential:

$$\mu_{HC} = \mu^0_{HC} + RT \cdot \ln X_{HC} + RT \cdot \ln f_{HC} , \tag{1.22}$$

where X_{HC} is the molar concentration, and f_{HC} is the activity coefficient.

In principle, different values of μ^0_{HC} would apply to every different solvent, however, the standard chemical potentials for several nonpolar solvents differ much less as compared with $\mu^0_{HC} - \mu^0_w$, e.g. for smaller alcanes in n–hexadecane and in n–octadecane the difference equals 0.25 kJ mole^{-1} if the solute and solvent differ in chain length by 10 [465], which is (per CH_2 group) less the experimental error in determination of the chemical potential *versus* chain length. If the effect of different nonpolar solvent is negligible, the Eq. (1.20) can be applied to hydrocarbon solute itself. In this case, both $RT \cdot \ln X_{HC}$ and $RT \cdot \ln f_{HC}$ equal zero and $\mu_{HC} = \mu^0_{HC}$. Thus, we get [459]:

$$\mu^0_{HC} - \mu^0_w = RT \cdot \ln X_w . \tag{1.23}$$

For a homologous series of n–alkanes one gets:

$$\mu^0_{HC} - \mu^0_w = [-10.20\ (\pm 0.23) - 3.70\ (\pm 0.05) \cdot n_c\ ] \text{ kJ mole}^{-1} , \tag{1.24}$$

where n_C is a number of carbon atoms in hydrocarbon chain.

Eq. (1.24) can be rewritten:

$$\mu^0_{HC} - \mu^0_w = [-8.80 \cdot n_{CH_3} - 3.70\ (\pm 0.05) \cdot n_{CH_2}\ ] \text{ kJ mole}^{-1} , \tag{1.25}$$

where $n_{CH_3} = 2$ is a number of CH_3 (terminal) groups, and n_{CH_2} is the number of CH_2 groups in hydrocarbon chain. Eq. (1.25) does not describe properly the hydrophobic effect for branched hydrocarbons, e.g. for isobutane $\mu^0_{HC} - \mu^0_w = -24.5$ kJ mole^{-1} (not –26.4 kJ mole^{-1}, as predicted from Eq. (1.25)), and –25.1 kJ mole^{-1} for cyclopentane (not –18.50 kJ mole^{-1}).

As the replacement of hydrogen in CH_2 by a methyl group (in formation of isobutane from propane) causes only small increment of the contact surface with solvent molecules, $\mu^0_{HC} - \mu^0_w$ is rather proportional to the number of water molecules in contact with the hydrocarbon molecules dissolved in aqueous medium. Indeed, the dependency of $\mu^0_{HC} - \mu^0_w$ is approximately linear with the increasing surface of (or with the number of water molecules beeing in contact with) hydrocarbon molecule. The slope, obtained for nearest distance of solute surface – water molecule equal 1.5 Å, was 0.10 kJ mole^{-1} Å^{-2} [301, 563].

For aliphatic unbranched hydrocarbon with the double bonds in hydrocarbon chain one gets for n–alkenes [459]

$$\mu^0_{HC} - \mu^0_w = [-6.29\ (\pm 0.50) - 3.70\ (\pm 0.092) \cdot n_c\ ]\ \text{kJ mole}^{-1} \qquad (1.26)$$

and for n–dienes [459]

$$\mu^0_{HC} - \mu^0_w = (-3.78 - 3.60 \cdot n_c\ )\ \text{kJ mole}^{-1} \qquad (1.27)$$

with errors similar to that in Eq. (1.26).

The introduction of one or more double bonds influences the intercept but no slope of the dependency in Eqs. (1.26) and (1.27), which indicates that the hydrophobic interaction with water is of short range. The effect of unsaturation shows the decrease in hydrophobicity of unsaturated hydrocarbon as compared with saturated one. The effect of a first double bond is essentially equal the decrease in chain length equal one CH_2 group, whereas the second double bond causes little lesser effect.

Aromatic hydrocarbons are considerably less hydrophobic than cyclic aliphatic hydrocarbons with the same number of carbon atoms; e.g. for cyclohexane $\mu^0_{HC} - \mu^0_w = -28.2$ kJ mole^{-1}, whereas for benzene $\mu^0_{HC} - \mu^0_w = -19.3$ kJ mole^{-1}. If CH_3 group is added to cyclic hydrocarbon, $\mu^0_{HC} - \mu^0_w$ decreases similarly for aromatic and for aliphatic hydrocarbons, e.g. the difference between toluene and benzene equals 3.39 kJ mole^{-1}, whereas between methyl cyclohexane and cyclohexane is 3.77 kJ mole^{-1} [459].

Salts decrease the solubility of nonpolar substances in water and this effect is roughly proportional to the salt concentration. This means that μ^0 in aqueous salt solutions is higher than μ^0_w, however, when the salt concentration is ~0.3 M or less, the salt effect is no larger than the uncertainty in Eqs. (1.24–27). Thus, one can assume that the hydrophobic effect of dilute salt solutions is approximately the same as that of pure water [656].

Nonpolar solvents (like CCl_4) behave similar to hydrocarbon solvents, e.g. for ethane: $\mu^0_{CCl_4} - \mu^0_w \approx \mu^0_{HC} - \mu^0_w$. In polar solvent, however, there will be a structural ordering, which will resist the intrusion of nonpolar solute. No solvent act so effectively as water does, but glycerol and ethylene glycol effectively repel

solute molecules [656]. For aliphatic alcohols the differences in $\mu^0_{ROH} - \mu^0_w$ are relatively small and decrease with increasing hydrocarbon portion of alcohole, e.g. for butane in methanole: $\mu^0_{ROH} - \mu^0_w = 6.70$ kJ mole^{-1}, and $\mu^0_{ROH} - \mu^0_w = 4.98$ kJ mole^{-1} in ethanole [395].

1.14.2 Solubility of amphiphiles

Amphiphilic molecules consist of polar head and hydrophobic tail (in most cases of biological lipids, hydrocarbon chains). As solvent-solute interaction is of short range, the solvent-dependent part of chemical potential for amphiphiles can be treated as a sum of almost independent contributions from head and from tail of the molecule. In the point of attachement of tail to the head, the hydrophilic and hydrophobic properties are in conflict. Presumably the effect of polar head will dominate and the proximal to the head CH_2 group of hydrocarbon chain will have little if no effect on hydrophobic effect [656].

Considering the equilibrium distribution of amphiphile between hydrocarbon and aqueous solutions, from the Eqs. (1.20) and (1.22) we get

$$\mu^0_{HC} - \mu^0_w = RT \cdot \ln(X_w / X_{HC}) + RT \cdot \ln(f_w / f_{HC}) \ . \qquad (1.28)$$

For dilute solutions $f_w = f_{HC}$ and the chemical potential of transfer may be obtained just from the ratio of molar concentrations of amphiphile in aqueous medium and in hydrocarbon.

For fatty acids in equilibrium between n–heptane and aqueous buffer solutions one gets ([248], for $n \geq 16$ data corrected by [627])

$$\mu^0_{HC} - \mu^0_w = (19.3 - 3.45 \cdot n_c) \text{ kJ mole}^{-1} \ . \qquad (1.29)$$

The intercept is positive reflecting the preference of aqueous medium by highly polar group COOH. The contribution of CH_2 group (–3.45 kJ mole^{-1}) is close to the value for hydrocarbons.

If water solubility of aliphatic alcoholes is considered, the chemical potential of transfer from water to pure liquid alcohol is given by [388]

$$\mu^0_{HC} - \mu^0_w = [3.48\ (\pm 0.10) - 3.44(\pm 0.013) \cdot n_c] \text{ kJ mole}^{-1} \ , \qquad (1.30)$$

where $\mu_{ROH} = \mu^0_{ROH}$. The contribution per CH_2 group is the same as if pure hydrocarbon is a solvent. This agreement may be caused by presumed hydrogen bond formation between OH groups in pure alcohol, what exposes hydrocarbon chains to hydrocarbon parts of other molecules so efficiently as in pure hydrocarbon environment.

The contribution of CH_2 group for numerous organic compounds is equal (–3.56±0.17) kJ mole^{-1}, whereas for NH_2 group, for OH, and other polar groups it is +0.021 kJ mole^{-1} [145, 146].

The analysis of the series of amphiphiles differentiated by hydrophobic tails (either linear or non-linear) shows that the hydrophobic contribution to chemical potential linearly depends on the contact surface area with water [293].

The measurement of the temperature dependency of chemical potential of transfer from water to nonpolar environment, $\mu^0_{HC} - \mu^0_w$, allows one to separate terms coming from enthalpy and enthropy of transfer [656]:

$$\mu^0_{HC} - \mu^0_w = \overline{H}^0_{HC} - \overline{H}^0_w - T\left(\overline{S}^0_{HC} - \overline{S}^0_w\right), \qquad (1.31)$$

where $\overline{H}^0_{HC} - \overline{H}^0_w$ is the partial enthalpy, and $\overline{S}^0_{HC} - \overline{S}^0_w$ the partial entropy of transfer from water to hydrocabon (nonpolar) environment. Alternatively, the enthalpy can be measured directly by calorimetry. For hydrocarbons transferred to water either from pure liquid hydrocarbon or from nonpolar solvent (C_6H_6 or CCl_4), a decrease in partial entropy is measured [239, 656], reflecting the change of water structure towards increased ordering in presence of dissolved hydrocarbon.

The solubility measurements of amphiphiles require a very low value of X_w, to avoid micellar aggregation of amphiphile (see Chpt. 1.15). Moreover, small amphiphiles at the concentrations not sufficient to form micelles (although at higher concentrations they form micelles) reveal the minimum in partial volume. As a micellization always leads to increase in partial volume, the minimum in partial volume suggests the presence of a different form of aggregation, presumably dimerization of amphiphile [92, 213, 327, 498].

1.14.3 Molecular picture of hydrophobic effect

The structure formed at an introduction of space-filling, but essentially inert solute inside the dynamically changing network of hydrogen bonds in liquid water resembles the structure of clathrate hydrates [142].

Ice clathrates are the solid solutions of small "guest" molecules (gas and/or liquids) occupying almost spherical holes in ice-like "host" lattices made up of hydrogen-bonded water molecules.

Claussen, 1951, proposed a cubic unit cell in which 136 water molecules are arranged to form 16 dodecahedra and 8 larger hexakaidecahedra consisting of four hexagonal and 12 pentagonal faces of hydrogen-bonded water molecules (Structure II, with unit cell dimension 17.2 Å). Distinct Structure I is formed with 12-Å unit cell dimension. It contains 46 water molecules arranged to form two pentagonal dodecahedra and 6 tetrakaidecahedra, each made up of 12 pentagonal and two parallel hexagonal faces [119, 120, 121, 491, 522]. In both types of structure two types of cages for solut occur: (i) small ones (with the radius of 3.91 Å

in Structure I, and 3.902 Å in Structure II); and (ii) large cages (radius 4.33 Å in Structure I, and 4.683 Å in Structure II) [688, 689, 690].

Each water molecule has four hydrogen-bonded neighbors; the hydrogen bonds are only ≈1% stretched as compared with ice Ih; the average distortion of O — O — O angles from the tetragonal values is equal only 3.7^0 in Structure I hydrates, and 3^0 in Structure II hydrates.

Concentration of "guest" varies from the minimal value needed to form hydrate lattice up to maximum (complete filling of "host" cages). Dielectric and NMR measurements show the high degree of rotational mobility of the "guest" molecules, and the absence of any great directional dependency of the interaction with water molecules of the cage. This interaction appears to be primarily of the van der Waals type, even for polar "guests" [142].

In clathrate hydrate the distortion and the stretch of hydrogen bond is smaller than in liquid water, there is no hydrogen bonds between "host" lattice of water and "guest" molecule, all together resembles the situation of nonpolar solute placed inside hydrogen bond network of liquid water.

Indeed, molecular simulations show that an introduction of space-filling but essentially inert solute causes the network of hydrogen bonds in water to rearrange towards the formation of a clathrate-like convex cage [231]. Although the structure of the clathrate-like cage is far from perfection, there is some strengthening of the hydrogen bonds, because their distortion and stretching is still lesser than in liquid water. Negative entropy of the solution comes from this strengthening of the hydrogen bonds, and because of reduced orientational freedom of water molecules forming the clathrate-like cage. In order to preserve intact the maximum number of hydrogen bonds, water molecules next to a nonpolar solute prefer to place its tetragonal hydrogen-bonding directions in a straddling mode.

Pairs of non-polar solutes experience in water an entropy-driven attraction for one another (hydrophobic bond). If two nonpolar solut molecules are in a sufficient proximity, they tend to minimize their hydration cage, thus, decrease solvent ordering, and hence decrease entropy reduction than when these two molecules are far apart.

The ordering of water moleculues around a hydrophobic solute is accompanied by a decrease in volume, e.g. partial molar volume for n–pentanol at infinite dilution in water (at $+20^0$C) equals 101.9 $cm^3\ mole^{-1}$, whereas 108.2 $cm^3\ mole^{-1}$ in pure liquid [216].

1.15 Micelles

When amphiphiles are dissolved in water, they tend by aggregation to minimize the contact surface of their hydrophobic parts with water. The aggregates are called *micelles* (Fig. 1–5a, b).

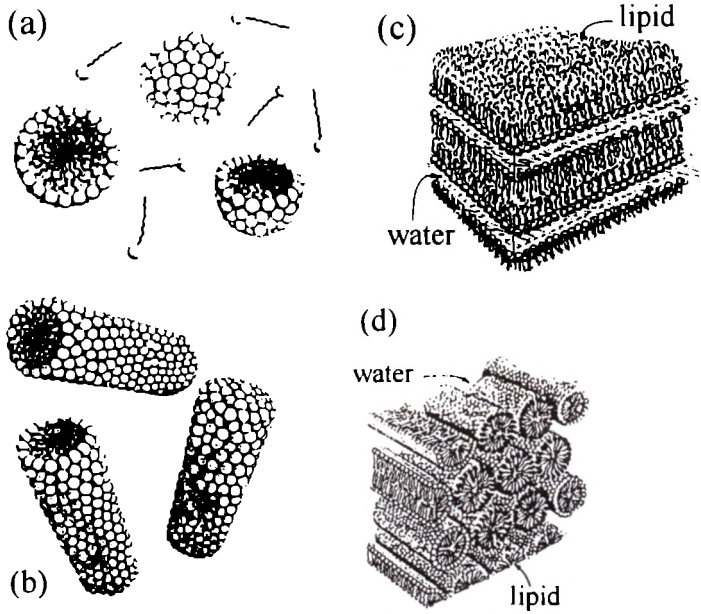

Fig. 1–5. Lipid lyotropic phase polymorphism; 0-d structures: (a) spherical and (b) rodlike micelles; 1-d structure: (c) lamellar phase; 2-d structure: (d) lyotropic hexagonal (H_I) phase.

Micelle consists of hydrophobic core containing the hydrocarbon tails of amphiphiles, and hydrophilic shell with polar head groups of the amphiphiles. The evidence that the core of micelle can be treated as a little droplet of liquid hydrocarbons comes from the measurements of the solubilities of hydrocarbons in sodium dodecyl sulfate micelles, in 0.1 M NaCl overall solvent (at the temperature varied between $+15^0$C and $+35^0$C) [709]. Assuming that the hydrocarbon within micelle constitutes an ideal solution, the standard free energy of transfer to the micelle interior from the aqueous medium is given by

$$\mu^0_{mic} - \mu^0_w = RT \cdot \ln\left(X_w / X_{mic}\right) . \tag{1.32}$$

The results at $+25^0$C give

$$\mu^0_{mic} - \mu^0_w = [-8.10\ (\pm 0.67) - 3.23\ (\pm 0.18) \cdot n_c\ ]\ \text{kJ mole}^{-1}. \tag{1.33}$$

Comparison of Eq. (1.33) with Eq. (1.24) (describing the transfer of hydrocarbon molecule to liquid hydrocarbon environment), shows their similarities, suggesting that the hydrophobic core of dodecylsulphate micelle behaves very similarly to liquid hydrocarbon. The liquid state of hydrocarbon chain in the interior of micelle differs from bulk liquid hydrocarbon (see Chpt. 1.17), however, the hydrocarbon density is not altered [562].

Water molecules can penetrate hydrophilic shell of the micelle, but they avoid its hydrophobic core. The H_2O-hydrocarbon contacts are unavoidable. The scale of such a contact is proportional to a contact surface area between hydrophilic shell and hydrophobic core. Tendency to minimization of the contact surface (and, thus, to energy decrease) determines geometry of micelles. The volume, V, of hydrophobic core of the micelle containing m' saturated hydrocarbon chains can be expressed [654, 658]

$$V = m'\left(27.4 + 26.9 \cdot n_c'\right) \ [\text{Å}^3] , \tag{1.34}$$

where n_c' is the number of carbon atoms in hydrocarbon chain, within the core of the micelle. Because of the "shading" effect of polar head group, n_c' may equal $n_c - 1$, where n_c is the total number of carbons in hydrocarbon chain. For micelles formed from di–acylo–lipids $m' = 2 \cdot m$, where m is the number of lipid molecules in micelle.

Because there is no vacuum inside micelle, one of core dimensions is limited by a maximal possible stretch of hydrocarbon chain. Tanford, 1986, estimated the maximal length, l_{max}, of hydrocarbon chain, taking 2.53 Å as a distance between subsequent carbons in hydrocarbon chain, van der Waals radius of the terminal methyl group as 2.1 Å, and half-length of the bond with the first carbon not embedded inside core as ≈0.6 Å, obtaining

$$l_{max} = 1.5 + 1.265 \cdot n_c' \ [\text{Å}] . \tag{1.35}$$

In liquid phase the hydrocarbon chain is not fully extended, its effective length, b, can be estimated for $n_c' = 11$ as [655]

$$b / l_{max} = 0.75 \tag{1.36}$$

(at room temperature). In micelle interior, every "kink" excitation decreases the chain length by 1.25 Å.

The fixed bond lengths and angles of hydrocarbon chain impose additional restrictions on form and size of micelle, e.g. hydrocarbon chains cannot be arbitrarily distorted to create perfect interface between core and hydrophilic shell [656]; moreover, the contact surface should be treated as "rough" (with peaks and troughs) being a few percent larger than its smooth time-average.

Even small micelles formed by simple amphiphiles are to large to have regular spherical form, fulfilling the requirement of Eq. (1.35). For instance, the average aggregation number of dodecyl sulphate micelle equals $\overline{m} = 62$ (in H_2O) up to 126 (in O.5 M NaCl), which exceeds the values calculated from Eq. (1.35): 23 (for $b = 0.75\, l_{max}$), or 56 (for $b = l_{max}$) [189, 493].

To increase the volume of the micelle core, with one dimension, b, remaining fixed, there are two possibilities: "disk-like", oblate shape ($a \cdot a \cdot b$), and "rod-like", prolate form ($b \cdot b \cdot a$); among them "disk-like" form offers steeper decrease in S/V with increasing aggregation number m [656].

Very large micellar aggregates have to have high asymmetry of shape. The ellipsoidal models are then probably not realistic, because too thin edges of oblate ellipsoids and to sharp ends of prolate ellipsoids. Disc models with semitoroidal ring about the edge, and capped cylinders are better representations of large micelles [333]. Extremely extended disks are in effect extended sheets, called *bilayers*. The random fluctuation of local curvature may lead to formation of *closed vesicles* with a droplet of aqueous medium trapped inside [402].

1.16 Monolayers

The hydrophobic effect causes the molecules of amphiphiles in aqueous medium to migrate towards the water surface and form there *monolayers*, in which polar head groups remain in water and hydrocarbon chains are expelled from it.

In 1770 Benjamin Franklin observed that "not more than a teaspoon" of oil spread spontaneously on a pond surface to cover an area of about half of an acre. Indeed, this was the first reasonably accurate measurement of molecular dimensions, as from his result Tanford, 1986, could calculate the film thickness (~10 Å).

The standard chemical potential, μ^0_{surf}, of amphiphile transfer from the bulk solution to the surface can be calculated using similar dependency as for other transfer processes (see Eqs. (1.28), and (1.32))

$$\mu^0_{surf} - \mu^0_w = RT \cdot \ln\left(X_w / X_{surf}\right) , \tag{1.37}$$

where X_{surf} denotes the molar concentration of the amphiphile on the surface of water. Assuming that the decrease in surface tension is proportional to X_{surf}, the values of $\mu^0_{surf} - \mu^0_w$ can be obtained from the values of X_w causing the same decrease in surface tension. Using that to Traube's results [669], Langmuir, 1917, obtained for homologic series of fatty acids, esters, alcoholes, etc.

$$\mu^0_{surf} - \mu^0_w = (const - 2.73 \cdot n_c)\ \text{kJ mole}^{-1} , \tag{1.38}$$

which was in rough agreement with Eqs. (1.24–26). The difference in value of the slope may arise from weak kohesive forces between hydrocarbon chains in aqueous medium. For amphiphiles adsorbed to the interface between water solution and liquid hydrocarbon, the slope in Eq. (1.38) equals –3.35 kJ mole^{-1} to –3.43 kJ mole^{-1} per CH_2 group [298, 299].

Amphiphile monolayers on water surface may exist in different phases, analogous to gaseous, liquid, or solid. The information on this phases and transitions between them is obtained from the measurements of surface pressure versus surface concentration defined as a surface, A, per molecule of amphiphile.

As the presence of amphiphile decreases the surface tension, surface pressure Π exerted by amphiphile monolayer is defined as

$$\Pi = \gamma_0 - \gamma \ , \tag{1.39}$$

where γ_0 is the surface tension of pure water, and γ is the surface tension in presence of amphiphile monolayer.

The following phases of monolayer can be distinguished with decreasing A [233, 234]:

(i) For extreme dilution ($A > A_i$, 'i' denotes 'ideal') the amphiphilic molecules behave like a 2-d ideal gas, obeing the analog of ideal gas equation of state

$$\Pi \cdot A = kT \ , \tag{1.40}$$

where $k = 1.38 \cdot 10^{-23}$ J K^{-1} is Boltzmann's constant, A_i is generally of the order of 50000 $Å^2$ / molecule.

(ii) For areas between A_v ('v' ='van der Waals') and A_i, the film behaves as 2-d van der Waals gas, with the equation

$$\left(\Pi + \frac{a_s}{A^2}\right) \cdot (A - A_0) = kT \ , \tag{1.41}$$

where a_S and A_0 are constants. The scope of van der Waals model applicability extends typically between 5000 – 1000 $Å^2$ / molecule.

(iii) For areas between A_v and A_C ('c' = 'condensed'), the surface pressure is independent on the area per molecule. Here coexist two discrete surface phases: a condensed film, and its 2-d vapor. The corresponding pressure Π_V may be called surface vapor pressure.

(iv) At areas less than A_C, the monolayer exists as a single homogeneous condensed phase and may form at least three different types of films: a liquid-expanded film ($A_C \approx 40$–50 $Å^2$ per aliphatic chain), liquid-condensed film ($A_C \approx 25$ $Å^2$), or a solid film ($A_C \approx 20$ $Å^2$).

Phosphatidyl cholines, PCs, which are main constituents of animal membranes form at room temperature (+22^{0}C) different phases: (i) compounds with short aliphatic chains (C_{10}, C_{14}) a liquid-expanded film; (ii) the ones having long chains (C_{18}, C_{22}) a liquid-condensed film; (iii) dipalmitoyl phosphatidyl choline, DPPC, (with both C_{16} chains) exhibits well-defined transition point from a liquid-expanded to a liquid-condensed film. At t = 6.2^{0}C DPPC monolayer is almost totally condensed (with the area per DPPC molecule equal ~42 $Å^2$). With increasing temperature, at +16.6^{0}C the liquid-expanded film appears at low pressures. The isotherms between 20.5^{0}C and 34.1^{0}C reveal a well defined transition point between both these phases. At the temperature above 41^{0}C only liquid-expanded phase is observed [5, 535].

Many cellular membranes contain cholesterol in the molar ratio of almost 1:1. Cholesterol forms a liquid-condensed monolayer with very little compressibility and A=38 $Å^2$ per cholesterol molecule, with molecules oriented perpendicularly to the interface at all pressures [99]. In binary mixtures with PC cholesterol exerts a

condensing effect on phospholipid film. This effect depends on lengths and on unsaturation degree of phospholipid acyl chains. DPPC mixes with cholesterol at all proportions, but maximal condensation effect occurs at a molar ratio 3:1 acyl chains/cholesterol (41.4 mole% cholesterol) [492].

1.17 Lipid bilayer

Lipids, in biochemical terminology, are all organic molecules of biological origin that are highly soluble in nonpolar solvents and sparsely soluble in water. They are present at high concentrations in a variety of biological systems (cell membrane, cellular organellae as chloroplasts, mitochondria, membranes, sense receptors, etc.). Membrane lipids are the amphiphiles containing hydrophilic head group and most often two hydrocarbon tails. A hydrophilic and a hydrophobic part are linked together by bonds sufficiently flexible to yield a rather independent behavior [447].

Lipid bilayer is the most important lyotropic phase for biological systems. The general structure of biological membrane, cell membrane as well as membranes of organelles, is based on bilayer made from membrane amphiphiles.

Lipid molecules in both mono-molecular layers of bilayer are placed perpendicularly to the plane of bilayer, with their polar head groups pointing to aqueous medium, thus, forming a hydrophilic shell of bilayer; and hydrocarbon chains directed to the bilayer interior (to the hydrophobic core) (Fig. 1–5c).

The liquid state of lipid hydrocarbon chain in bilayer differs from that of liquid pure hydrocarbon, because every chain is anchored to hydrophilic head group by a *backbone* group (mostly glycerol). Moreover, because of packing of hydrocarbon chains in bilayer core, there is a strong tendency to order the hydrophobic chains at physiological temperatures. Lipids form a smectic liquid-crystalline phase, a 2-d liquid with motional freedom of lipid in bilayer plane (lateral diffusion), and through the stack of lipid bilayers the crystalline periodicity of structure.

Comparing both the transition heats and the areas of transition of monolayers and bilayers, Albrecht et al., 1978, concluded that DPPC behavior in bilayer resembles that in monolayer at an external pressure $\Pi = 12.5 \cdot 10^{-3}$ N m^{-1}, however, Nagle, 1976, proposed $\Pi = 50 \cdot 10^{-3}$ N m^{-1}.

In liquid-crystalline phase the dynamic chain excitations respond for mobility of hydrocarbon chains. The discrete rotations about any of carbon-carbon bonds form the following rotational isomers (rotamers): a *trans* angle (lowest in energy), T, and two (degenerated) *gauche* angles, G^+ and G^-, turned by $+120^0$ and -120^0, respectively, which have energies ~2 kJ mole^{-1} higher. Intermediate angles have much higher energies and are therefore ignored at physiological temperatures. Close packing of hydrocarbon chains in bilayer privileges the series of rotational excitations: as kink, K, the sequence of G^+ T G^-; and jog, J, a series of two subsequent kinks in one chain [497]. The hydrocarbon chains are

disordered, as observed in plane of bilayer; the distance between hydrocarbon chains is the time average of many possible conformations and equals 5.3 Å (phase L_α, after the nomenclature by Luzzati, 1968). ^{2}D–NMR results suggest that in upper and in middle part of DPPC hydrocarbon chain kink diffusion dominates, whereas close to the terminal CH_3 groups, the contribution of free rotation around the C–C axes increases [182].

The lateral diffusion of lipids in plane of bilayer represents the degree of fluidity of lipid bilayer in a liquid-crystalline phase. Spin-labels and fluorescence photobleach-recovery measurements of lipid lateral diffusion yield the value of lateral diffusion coefficient for a head group spin-labelled phospholipid in host lipid multilayers of PC from egg yolk, as equal to $D = (1.8\pm0.6)\cdot10^{-5}$ cm^2 s^{-1} (first observation: [164], then series of experiments using photobleach-recovery technique: [611, 612, 613, 626]).

With decreasing temperature, the main gel-to-liquid crystalline phase transition in DPPC is observed at $T_m = 42^0$C ('m' denotes 'main', or 'melting'). In pure DPPC-water systems, at water content exceeding ~20 wt% the "ripple" lamellar phase (with monoclinic structure) is observed (phase $P_{\beta'}$) (Fig. 1–6) [423]. The hydrocarbon chains are packed in hexagonal lattice. For DPPC the period of distortion waves in 'ripple structure' equals $\Lambda = (205\pm5)$ Å [227]. At main transition the distance between glycerol backbones of DPPC molecules increases to 43.2 Å from 34.6 Å at the temperatures above T_m [601]. The separation of CH_3 groups from polar heads of DPPC molecules from both monolayers increases from 43.6 Å at $t = 50^0$C to 50.2 Å at $t = 28^0$C [97].

For the temperature $T_P = 33^0$C ('p' = 'pretransition') in DPPC the pretransition is observed from phase $P_{\beta'}$ to the gel lamellar phase $L_{\beta'}$ [111]. In gel phase the hydrocarbon chains are extended in *all-trans* conformation and stiffly packed in quasi-hexagonal [578] (or quasi-orthorhombic) 2-d lattice, with well defined chain-to-chain distance of 4.9 Å. ^{2}D–NMR data suggest that slow rotation of chain along its long axis is still possible [143]. X-ray diffraction shows that as temperature is further decreased, minor structural changes in gel phase, $L_{\beta'}$, occur. Namely, the hexagonal pattern of cross-section perpendicular to the hydrocarbon chains in DPPC membranes which is described at 32^{0}C, by the lattice parameters $a' = b' = 4.9$ Å, and an angle $\gamma' = 120^0$; and at 20^{0}C is described by $a' = 4.86$ Å, $b' = 4.70$ Å, and $\gamma' = 119^0$ [223].

Pretransition was observed up to now in DPPC, DMPC, and distearoyl–phosphatidylcholine (DSPC). For lower hydration, for lipids with unsaturated bonds in their hydrocarbon chains, or for lipid mixtures extracted from biological tissue, only one, main gel-to-liquid crystalline phase transition is observed.

Neutron diffraction experiments of selectively deuterated DPPC show that the three CH_3 segments of choline moiety stay at almost the same distance from the glycerol backbone (as measured from the center of bilayer) either in gel

state (t = 20^{0}C, average distance 3.2 Å, hydration: 5–6 wt% of H_2O); or in liquid crystalline phase (t = 50^{0}C, average distance 3.9 Å, hydration: 25 wt% of H_2O) [96, 97]. This means that phosphocholine group remains parallel to the surface of the membrane either below or above the main phase transition.

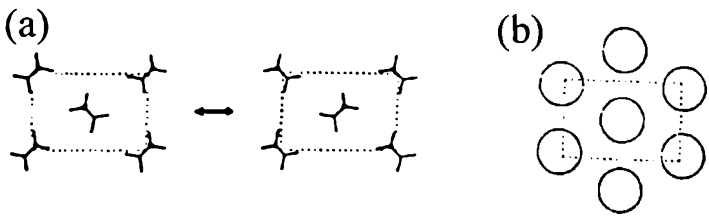

Fig. 1–6. The cross-section of the 2-d hydrocarbon lattice of the phosphatidylcholine bilayer in direction perpendicular to the direction of hydrocarbon chains: (a) orthorhombic (phase $L_{\beta'}$), at which two orientations in hydrocarbon chains are preferred; (b) hexagonal (phase $P_{\beta'}$), allowing sixfold hindered rotation of a hydrocarbon chain independently of its neighbors, which in the fast limit is equivalent to free rotation [71].

Tardieu et al., 1973, predicted non-zero tilt angle of hydrocarbon chains in phospholipid bilayer, which varied between 0 and 30^0 depending on water content in DPPC sample. X-ray diffraction shows for DPPC multilayer hydrated to (10±1) wt% H_2O the value of tilt angle equal of 12.5^0 at room temperature (phase $L_{\beta'}$) [636].

The widths of the main transition is narrow, however, it depends on the history of the sample and on the purity of lipid. The calorimetrical data show that in highly purified DPPC the peak width at half-maximal excess specific heat is only 0.067^{0}C, which clearly indicates that main gel-to-liquid crystalline transition closely approximates an isothermal first-order transition [3].

In DPPC at the temperature T_S = 18^{0}C ('s' = 'subtransition') an additional subtransition was observed, but the phase below subtransition (phase $L_{\sigma'}$) appears only after long annealing at ~0^{0}C for 3 or 4 days under atmospheric pressure [113]. ^{31}P and ^{1}H–NMR data suggest that below subtransition the rotation of the entire choline group ceases, whereas fast motions of 9 terminal protons (of choline CH_3 groups) remain [667]. The annealing time decreases gradually with increasing pressure, and finally, beyond ~$0.9 \cdot 10^6$ hPa, the sub-transition can occur without annealing [673]. Under high pressure, the sub-transition is a packing transformation from orthorhombic to quasi-hexagonal 2-d lattice through a melting-like behavior [675], whereas in the temperature range between pre- and sub-transition, hydrocarbon chain packing conformation does not have a single structure with quasi-hexagonal or orthorhombic symmetry [676].

Utoh & Takemura, [673, 674], using high pressure-DTA and high pressure-dilatometry and X-ray scattering found in DPPC (75 wt% of DPPC) at elevated pressure (~$2.0 \cdot 10^6$ hPa) s "fourth" transition at the temperature T_4

('4' = '4-th transition' after their nomenclature), below the temperature of subtransition at given external pressure. "Fourth" transition induces movement of the head group in the DPPC molecule [675].

As water content in the system is increased, the temperature of main phase transition, T_m, decreases.

For hydration up to 27 wt% at 5^0C, up to 31 wt% at 37^0C, and up to 36 wt% at 45^0C, DPPC forms a homogeneous lyotropic smectic phase from parallel stacks of lipid bilayers. For stable parallel stack of DPPC bilayers, the thickness of bilayer equals $d_L = 46.1$ Å (phase $L_{\beta'}$), and thickness of water layer $d_W = 18.1$ Å at 5^0C; whereas $d_L = 47.3$ Å (phase $P_{\beta'}$), and thickness of water layer $d_W = 22.4$ Å at 37^0C; and $d_L = 43.1$ Å (phase L_α), and thickness of water layer $d_W = 24.4$ Å at 45^0C [330]. In limit of very low lipid concentration (0.1 wt% of DPPC), the dispersion of single walled vesicles of DPPC is the thermodynamically stable state. In the intermediate concentration range, the dispersions of closed multilamellar myeline-like vesicles are formed. (At hydration level exceeding 20 wt%, the freezable water is observed, see Chpt. 1.15). For water concentration range at which parallel stacks of lipid bilayer are formed, the temperature T_m continuously decreases from the value for pure DPPC, however, for higher water concentrations remains constant [578].

The temperature of the main phase transition increases with increasing length of hydrocarbon chain. For PC, with the chain length of $n_C = 12$, $T_m = -1^0$C [680], for $n_C = 14$, $T_m = 23.0^0$C [533], for DPPC ($n_C = 16$) $T_m = 41.8^0$C [311], for DSPC ($n_C = 18$) $T_m = 58^0$C [533], and for $n_C = 22$, $T_m = 75^0$C [533]. Analogous increase is observed in phosphatidyl ethanolamine, PE, [680], in phosphatidyl glycerol, PG, [203], and in phosphatidyl serine, PS, [85].

The presence of unsaturated bonds either *cis* or *trans* decreases the temperature of main transition, T_m, e.g. for dipalmitoleoyl phosphatidylcholine (16:1c/16:1c) $T_m = -36^0$C [680]. *Cis* double bond more effectively decreases the temperature T_m than *trans* double bond, e.g. for 1–stearoyl–2–oleoyl phosphatidylcholine (18:0/18:1c), $T_m = +3^0$C, whereas for 1–stearoyl–2–elaidoyl phosphatidylcholine (18:0/18:1tr) $T_m = 26^0$C [534]. The decrease in T_m depends on position of double bond in hydrocarbon chain: for 1,2–dioctadecenoyl–sn–glycero–3–phosphocholine, with *cis*–double bond on n = 2 carbon $T_m = +41^0$C; for n = 6, $T_m = +1^0$C; for n = 9 and for n = 10, $T_m = -21^0$C; whereas for n = 13 again $T_m = +1^0$C; and finally for n = 17, $T_m = +45^0$C [24]. Moreover, double bond in sn–2 chain decreases T_m more efficiently than in sn–1 chain, as for 1–stearoyl–2–oleoyl phosphatidylcholine (18:0/18:1c) $T_m = +3^0$C [534], whereas for 1–oleoyl–2–stearoyl phosphatidylcholine (18:1c/18:0) $T_m \approx +15^0$C [151].

For phospholipids with identical, saturated hydrocarbon chains, T_m depends on polar head group increasing in the order: the lowest value for PC, and for PG; then increases for PS; finally the highest value for PE. For

instance, in phospholipids with the number of carbons in hydrocarbon chains equal $n_C = 16$, for DPPC $T_m = 41.8^0C$ [311], for DPPG (dipalmitoyl phosphatidylglycerol) $T_m = 41.5^0C$ [203], for DPPS (dipalmitoyl phosphatidylserine) $T_m = 53^0C$ [85], and for DPPE, $T_m = 63.8^0C$ [449]. Also for other chain lengths T_m value for PE is about 20^0C higher than for PC. The increased stability of disaturated PE in the gel state appears to both the smaller size of the PE as opposed to PC head group [449], and to the ability of the protonated amino group of PE to hydrogen bond to the protonated amino and negatively charged phosphate groups of adjacent PE molecules [496, 708]. At the deprotonation of the DPPE amino groups, by increasing the pH to 12, T_m decreases from 63^0C to 41^0C (the value for DPPC), what supports the latter [463]. Calorimetrical and ^{31}P–NMR results for synthetic phospholipids with polar heads ended by the group $N^+H_n(CH_3)_{3-n}$, and with one additional group CH_2 between phosphate group and nitrogen, show that for n increasing from 0 (analog of DPPC) to n=3 (analog of DPPE) the main transition temperature, T_m, increases linearly from the value for DPPC to the value for DPPE [226].

The addition of cholesterol to DPPC-water system broadens the main transition and shifts down its temperature, T_m. At cholesterol concentrations between 0 mol% and 20 mol%, two components in excess of heat capacity are recorded: a sharp and a broad one. The sharp component shifts from the T_m for pure DPPC to lower temperatures, and its area under peak (ΔH) decreases linearly with cholesterol content, falling to zero at about 20 mol% [450]. Broad component initially increases on the cost of narrow component, and then decreases with increasing cholesterol content, and finally no transition is observed with an equimolar ratio of DPPC with cholesterol in water. X-ray diffraction shows the lamellar structure of DPPC-cholesterol mixtures, however, at 50 mol% cholesterol the separation of crystalline cholesterol appears [407, 408]. Below T_m the addition of cholesterol increases the DPPC selfdiffusion coefficient, D, whereas above T_m decreases the value of D [404].

1.18 Lipid phase polymorphism

The types of the geometry of biological structures, may be approximated as one-dimensional (1-d), as well as two- (2-d) and three-dimensional (3-d).

Under this approximation, nucleic acids, proteins, polypeptides, genes are 1-d structures. The 1-d structure is especially desirable for information carriers, as the one enabling a straightforward method of sequential reading- and writing procedure. Also the process of damage repair is simpler, if structure is 1-d, because the damaged place can be easily found by simple sequence checking part-by-part algorithm.

The presence of 2-d structure allows the compartmentation of the organism, defines the inner- and the outer- space of the system. Moreover, majority

of biochemical processes has a bullet-target character, so, 2-d structure increases the probability of such a reaction by a presence of lateral diffusion. Moreover, in 2-d structures phase-like transitions occur, which affects the function of the system.

Different classification, based not on the approximated dimensionality of the structure, but on the dimensionality of the long-range order, is applied to lipid-water systems.

Indeed, lipids are the only group of biological compounds showing uniquely rich polymorphism of phases, that may be important for the functioning of the organism. For instance, the organized from bipolar lipids (in cubic phases Q^{224} and Q^{230}), very porous membrane of archaebacterium *Solfolubus solfataricus* living at $+90^0$C in acidic environment (pH 3) allows the decrease of pH gradient across the membrane to the physiological value pH 6.5 inside the cell [261, 160].

Lipids have a long-range order being not a propagation of their short-range order, but existing because of short-range disorder. The shape of lipid molecule and the properties of head-group determine the mesophase preferency of given compound, e.g. cylindrical PC prefers bilayer mesophase; conical PE and galactolipids like MGDG prefer hexagonal phase, whereas lysolipids or detergents in form of inverted cone prefer micellar organization. (A shape of molecule is understood as a geometrical space occupied by molecule including its bound water layer, thus, can be affected by inter- and/or intra-molecular interactions and the hydration level).

Except of the micellar isotropic solution (0-d ordering), lipid mesophases display a highly ordered long range organization. The type of ordering may be classified according to the long-range periodicity of the structure in n dimensions. For n = 1, 2, lipid mesophases are observed [215], whereas for n = 3 the crystalline structure is observed.

To describe the variety of lipid lyotropic phases, Luzzati, [446, 447], proposed notation using Latin letters, which specify the type of long-range structure, and Greek letters denoting the short-range ordering (the conformation of the hydrocarbon chain). With the dimensionality of long-range order, lipid lyotropic phases may be classified:

(a) *one-dimensional lattices*: lamellar phase which is a smectic liquid crystal (denoted by L). The lipids in phase L are associated in lamellae. Each lamella is filled by hydrocarbon core and is covered on both sides by hydrophilic shells consisted of lipid polar heads.

(b) *two-dimensional lattices*: hexagonal lattice, denoted H (see Fig. 1–5d), with space group p6m; and oblique or rectangular lattice (space group p2 or cmm), denoted P. The structural elements in such an arrangement are long and stiff rods, with their long symmetry axes placed in the same direction. The lateral position and the relative orientation of the rods are fixed. The length of rods is infinite (phase H) or finite in other phases. Lipid may migrate along the lateral surfaces of rods. The projection in the plane perpendicular to the rod axis defines a type of two-dimensional lattice.

(c) *three-dimensional lattices*: rectangular, T, rhombohedric, R, and cubic, C, lattices of space groups I422, $R\bar{3}m$ and Ia3d, respectively. Rectangular and rhomboedric structures consist of micellar aggregates of finite size, which are placed in a 3-d lattice. Cubic phases may be classified onto two groups: cubic structures having regions which are continuous with respect to both polar (water) and nonpolar (hydrocarbon) components ('bicountinuous phases'), e.g. Q^{224} and Q^{230} [447]; and cubic structures built up either with discontinuous hydrocarbon regions (micellar aggregates) and continuous water regions, or with discontinuous water regions (reversed micellar aggregates) and with continuous hydrocarbon regions. Although called 'bicontinuous', these phases are really 'quadricontinuous', i.e., the monolayers on each side of the minimal surface and the two water labyrinths are each distant [659].

Short range organization (Greek letters in subscript) describes the motional state of lipid hydrocarbon chains:

(a) *conformation type* α, describes disordered, liquid-crystalline phase above the main transition temperature, T_m.

(b) stiff, freely rotating hydrocarbon chains in all-trans conformation are defined as *conformation type* β *or* β'. The hydrocarbon chains are packed hexagonal or quasi-hexagonal, as observed in plane perpendicular to chain axis. In phase type β chain axis is perpendicular to the plane of the lamellae, in phase β' the tilt angle has a non-zero value.

(c) *mixed conformation type* γ *or type* $\alpha\beta$. For instance, in lipids with chemically heterogeneous chains also the conformation of chains is heterogeneous: there exist the domains of different conformation involving entire chains or parts of one chain. The proportion of chains in different domains may be fixed by the symmetry of the lattice (conformation type γ), or may vary with temperature and concentration (type $\alpha\beta$).

(d) *conformation type* δ. The hydrocarbon chains are coiled in helices, which are packed with rotational disorder to a 2-d square lattice.

In all phases, except lamellar L, the inside and outside of the structure are topologically distinguishable. Thus, two types of structure are possible, depending on water/lipid proportion in the system. Namely, structure type I (*oil-in-water*), in which lipid aggregates are embedded in aqueous medium, and structure type II (*water-in-oil*), in which the situation is just inverted. Structure of type II is often called 'reversed'.

1.19 Bound water

Lipids and polypeptides, two main constituents of biological structures, being amphiphilous, in aqueous medium organize in stable structures with their

hydrophilic parts exposed to water. On the other hand, lipid and polypeptide structures formed due to the presence of water, simultaneously influence the proximal water molecules, by changing their arrangement and motional properties. Water modified in its properties by the presence of biological structure, as compared with bulk, is called *bound water.*

Polypeptides contain amino acids with ionic and uncharged polar side chains. Polypeptide backbone itself contains the strongly hydrophilic peptide group but its effect can be nullified by formation of interpeptide hydrogen bonds. The network of hydrogen bonds appears to have comparable stability with hydrogen bonds between the peptide groups and water. Although this causes polypeptide backbones not to prefer the aqueous environment, it is intuitively clear that polypeptides (similarly to liquid crystalline structures formed by lipids) may intensively hydrate in native forms.

Indeed, variety of experimental methods [195, 196, 197, 198, 268, 300, 671] suggest that DNA and RNA are heavily hydrated. Franklin & Gosling, [209, 210], using X-ray scattering found that the crystallinity of calf thymus NaDNA fiber depends strongly on relative humidity, p/p_0, and on the past history of the specimen. Three types of patterns were distinguished by X-rays and assigned [707]: (i) highly crystalline form A ($p/p_0 \approx 75\%$, 11 base pairs per helix turn); (ii) semi-crystalline form B ($p/p_0 \approx 92\%$, 10 base pairs per helix turn); and (iii) disordered (or least crystalline) form C ($p/p_0 \approx 50\%$, 9.3 base pairs per helix turn). The A–C transition induced by variations in p/p_0 was found to be reversible, similarly to the A–B transition (at $p/p_0 = 92\%$ in unoriented samples, and at salt content: 0–4%) [190]. It is suggested that *in vivo* conformation of DNA may be of the B form [510, 707], or perhaps in same instances in the A form [660].

Water vapor sorption isotherms for nucleic acids are of sigmoidal form (with the maximum adsorption-desorption hysteresis corresponding to ~1 H_2O molecule per nucleotide). Steeply increasing segment of the isotherms (for $p/p_0 > 80\%$) comes from the condensation of water multilayers. At $p/p_0 < 25\%$ ($t = 21^0C$) ~2 H_2O molecules/ nucleotide are adsorbed (at phosphate sites) [195].

No endothermic fusion in DNA samples containing less than 10 H_2O molecules/nucleotide was detected; whereas at about -14^0C a broad endothermic peak was calorimetrically observed in samples containing more than 14 H_2O molecules/nucleotide; and a second, much more intense, peak between -1^0C and -4^0C developed when the hydration level exceeded 19 H_2O molecules/nucleotide.

Proton NMR shows that in DNA solutions, at the temperature decreasing to -35^0C, water peak linewidth is intermediate to those of ice and supercooled water, and corresponds to ~11 H_2O molecules/nucleotide [403].

To summarize, in DNA two hydration shells may be distinguished [579]:

(i) The primary shell of DNA, which is impermeable to ions, does not freeze into ice-like structure, and consists of about 20 H_2O molecules [195–198].

(ii) The secondary hydration shell formed at $p/p_0 = 80\%$, when the primary hydration shell is fully hydrated, and more water is added, causing the sample swelling. This shell resembles bulk water in sense that it is permeable to ions

and freezes into ice-like structures (as indicated by IR spectroscopy [198]). Indeed, the measurements of the sedimentation equilibrium suggest that the secondary hydration shell differs from bulk water [268].

Crystallographic studies of proteins and nucleic acids reveal that around solute molecules of a certain size water molecules organize in recurrent patterns. Pentagon is the favored pattern, because in this configuration the internal angle of 108^0 is close to the tetrahedral value. Moreover, four- and six-membered cycles may also play a role in hydration phenomena [579].

The hydration shell of DPPC bilayer contains 23 H_2O molecules/lipid [204, 581]. However, different authors suggested various distribution of total hydration pool onto subgroups: some suggested 11 H_2O molecules strongly interacting with head group [204, 672]; others propose 5 molecules in first hydration shell [259, 391, 527]; or that 4 molecules in DPPC liquid crystalline phase and 9 molecules in DPPC gel phase perform restricted motions [581]; whereas only one or two molecules are in hydration shell [204, 391].

^{2}D–NMR experiment showed either for liquid crystalline or gel phase of DPPC [225] that first five water molecules per DPPC molecule interact with DPPC phosphate group, perform restricted motions, and exchange rapidly between all binding sites. The remaining water molecules are attached to the DPPC head group, but their effective quadrupolar splittings are at least one order of magnitude lower than the effective quadrupolar splittings of the first five water molecules.

Klose & Gawrisch, 1981, proposed the detailed classification of water bound to the surface of DPPC bilayer. Water fractions are ordered with decreasing bonding (or immobilization):

(i) tightly bound water (4 – 5 H_2O molecules/DPPC molecule, with the rotational correlation time $\tau_{tb}^{(R)} \approx 10^{-7}$ s);

(ii) main hydration shell (11 H_2O molecules/DPPC molecule, $\tau_{mh}^{(R)} \approx 8 \cdot 10^{-10}$ s, selfdiffusion coefficient $D^{mh} \approx 2 \cdot 10^{-9}$ cm^2 s^{-1});

(iii) trapped water (12 H_2O molecules/DPPC molecule, $\tau_t^{(R)} = 3 \cdot 10^{-10}$ s);

(iv) free water in multilamellar phase (21–23 H_2O molecules/DPPC molecule, $\tau_f^{(R)} \approx 8 \cdot 10^{-10}$ s, selfdiffusion coefficient $D^f \approx 10^{-5}$ cm^2 s^{-1}).

The exchange time between tightly bound water and main hydration shell equals $\tau_{mh-tb}^{(EX)} \approx 10^{-4}$ s, between main hydration shell and trapped water $\tau_{t-mh}^{(EX)} \approx 10^{-5}$ s, and between free and trapped water $\tau_{f-t}^{(EX)} \approx 10^{-4}$ s,

Taking the surface per molecule in phospholipid bilayer as 41 Å for DSPC [156], or 42 Å for DPPC [535], one gets 10–12 H_2O molecules tightly bound to phosphate group, and 27 molecules of main hydration shell per 100 Å^2. The total number of bound water molecules equals 37–39 H_2O molecules/100 Å^2, which is the value exceeding that for water monolayer (~11 H_2O/100 Å^2). This is because

DPPC polar heads form extended "branches" in the hydrophilic shell of bilayer increasing water-lipid contact surface.

Freezing of water in phospholipid-water binary system significantly affects the phase behavior of lipids. Below 25 wt% of H_2O no freezing of DPPC/water system is observed at 0^0C. Lowering the temperature leads to further freezing [111]. In PE (with 18:1/18:1) containing 50 wt% of water, marked supercooling is observed: ice formation occurs between about -10^0C and -20^0C. Under supercooled condition, on cooling, the $H_{II} \rightarrow L_\alpha$ transition is observed at -4^0C, and then the $L_\alpha \rightarrow L_\beta$ (liquid crystalline to gel) transition at -10^0C; at reheating, the $L_\beta \rightarrow L_\alpha$ transition is completely reversible, showing no hystheresis, whereas the $L_\alpha \rightarrow H_{II}$ transition occurs at $+16^0$C. In the sample, which was frozen to -20^0C and then reheated to -2^0C, at cooling run the onset of the $L_\alpha \rightarrow L_\beta$ transition is recorded at -6.5^0C. This increase in T_m temperature is caused by the presence of ice and reflects the osmotic dehydration of the sample at freezing [583].

Although proposed for water hydrating lipid bilayer, the classification of water fractions may be extended on water in other biological systems distinguishing:

(i) *tightly bound water* to the "hot" binding sites of the surface;

(ii) *main hydration shell*, mainly consisted of the first monolayer of bound water;

(iii) *trapped water*, localized between the "branched" structures of the surface; and

(iv) *free water* pool which, in fact, is not uniform and may be divided onto bulk water, and water experiencing (during the time of experiment) in its diffusion the restricted geometry (planar or cylindrical) of environment.

In proximity of smooth surfaces the trapped water pool may be significantly reduced, compared to that in proximity of branched lipid hydration shell.

There exists also other, commonly used classification of water present in biological system distinguishing:

(i) *tightly bound* fraction, including water bound to the "hot" binding sites of the surface together with main hydration shell; and

(ii) *loosely bound* fraction, including mostly trapped water;

(iii) *free water*.

1.20 Biological membrane

The concept that the structure of biological membrane is based on lipid bilayer is a consequence of Gorter & Grendel classic experiment from 1925 [250]. They found that the surface of monolayer formed from the total lipid extract per erythrocyte is twice higher than the surface of the cell. The next investigations revealed several weaknesses of this experiment: (a) the red blood cell surface area was underestimated by about 30%; (b) lipids were extracted using acetone without

checking whether all lipid fraction is removed; (c) the monolayer area was measured at arbitrary low surface pressure ($\sim 9 \cdot 10^{-3}$ N m^{-1}) (see Chpt. 1.17), whereas phospholipase action recorded versus surface pressure suggest that lipid are packed in erythrocyte membrane comparably with a lateral surface pressure $(31 - 34.8) \cdot 10^{-3}$ N m^{-1} [157, 730]. Nevertheless, the recent models of biological models are based on the conclusions from Gorter & Grendel experiment.

Danielli & Davson, 1935, proposed a model of membrane formed from a lipid bilayer, in which the membrane proteins are placed on the membrane surface, and do not penetrate the interior of the membrane. The weakness of Danielli-Davson model was that the expected thickness of protein layer on the membrane surface allowed only β–sheet conformation of protein, which had to expose to many hydrophobic groups towards aqueous medium.

Sjöstrand, 1968, basing on electron micrography data, proposed a model of membrane structure formed by extended network of protein molecules with embedded lipid micelles or small liposomes. However, the grains seen in the micrograms came from the artefacts produced by sample preparation not from micelles.

Finally, Singer & Nicholson, 1972, proposed the recently accepted fluid-mosaic model of biological membrane, in which lipids form a bilayer in liquid-crystalline phase (above T_m), and membrane proteins are classified onto two groups:

(a) *Extrinsic proteins*, mostly globular, which in native conformation have their polar amino acids localized on the surface of protein and hydrophobic amino acids placed inside the molecule. Extrinsic proteins are electrostatically bound to the membrane surface and easily dissociate at extreme values of pH, or of ionic strength.

(b) *Intrinsic proteins*, which may be removed from the membrane after the destruction of membrane structure by use of detergents. Their hydrophobic amino acids are exposed on the outer surface of globular protein constituing the hydrophobic area which anchors the protein to hydrophobic core of lipid bilayer. Intrinsic proteins can either penetrate across the membrane; or can form complexes penetrating the whole membrane thickness, e.g. forming ion channels; or can be asymmetrically anchored exposing their hydrophilic surface to one side of the membrane; or can be exclusively localized in hydrophobic core of bilayer.

It is assumed that extrinsic proteins show the specific affinity to the hydrophilic segments of intrinsic proteins exposed to aqueous medium.

Membrane carbohydrates are bound either to membrane lipids, forming glycolipids or to proteins forming glycoproteins. Beyond their biological role (recognition processes, cell adhesion), their presence increases the volume of the bound water layer covering the membrane surface (trapped water and main hydration shell) (see Chpt. 1.19).

Singer-Nicholson model emphasizes the fact that biological membrane is a 2-d liquid above T_m, in which either lipids or proteins may diffuse laterally enabling the sequences of biochemical reactions. The lateral diffusion of

membrane proteins was observed for the first time in fluorescence marked antigenal proteins of super-cells obtained by merging mouse cells with human cells. The obtained value of lateral diffusion coefficient was $D = 2 \cdot 10^{-10}$ cm^2 s^{-1} [217]. However, the diffusion coefficient value varies for different proteins, e.g. for retinal rodopsin equals $D = 4 \cdot 10^{-9}$ cm^2 s^{-1} [541], whereas for proteins from mouse fibroblasts $D = 1.4 \cdot 10^{-11}$ cm^2 s^{-1} for the direction parallel, and $D = 3.8 \cdot 10^{-12}$ cm^2 s^{-1} for the direction perpendicular to the stress filaments [462].

In contrast to lateral diffusion, the process of lipid transfer across bilayer (called "flip-flop" mechanism) is extremely slow. Hubbel & McConnell estimated the probability of transfer of the spin-labelled lipid molecule from the inner surface to the outer surface of the liposome as 0.07 h^{-1} per molecule (at +30^{0}C). However, the mechanism of "flip-flop" process as an exchange of only two molecules is much less probable because of high energy barrier for lipid polar head group in hydrophobic core of bilayer. Electron microscopy and ^{31}P–NMR suggest that the lipid transfer across the membrane starts from the domain separation of conical phospholipids (PE), which form the invaginations in bilayer surface, then converting to inverted micelles (or hexagonal H_{II} phase cylinders) placed in bilayer hydrophobic core, and subsequently bond to the opposite surface of bilayer. The small micelles ("lipidic particles") were observed in the interior of model lipid membranes [153, 683] and of natural membranes [134, 135, 152]. Also the process of cell fusion may be explained in terms of local formation of non-lamellar lipid phases, as at use of fusogenic agents the cylinders of hexagonal H_{II} phase are formed [136].

Several experimental parameters of biological membrane reveal discontinuities and/or breaks in slope of their temperature dependencies suggesting the presence of phase transitions.

(i) The temperature dependency of the enzymatic activity of some membrane proteins show breaks in slope [331, 334, 507, 588].

(ii) The fluorescence intensity, the fluorescence anisotropy of fluorescent dyes [516, 681], and the delayed fluorescence [334] show breaks or rapid changes as measured versus temperature.

(iii) Calorimetric data reveal the presence of phase transition in the membranes of *Acholeplasma laidlawii* [641], several phase transitions in thylakoid membranes of spinach [133], and two phase transitions in purple membranes of *Halobacterium halobium* (at +80^{0}C the transition in membrane lipids, and at +100^{0}C the denaturation of bacteriorhodopsin) [335]. Inner membranes of beef heart mitochondrion show phase transition at –10^{0}C [48]. In contrast, because of high cholesterol content the erythrocyte [407] and myelin [408] membranes show no cooperative transition.

(iv) Circular dichroism in the membranes of *Halobacterium halobium* shows the rapid change at +78^{0}C [312].

(v) The temperature induced gathering of lipids and of proteins is observed on membrane electron micrographs [715].

(vi) NMR spectra recorded for *Acholeplasma laidlawii* show a broad phase transition [144, 644].

The presence of phase transitions in biological membrane strongly supports the Singer-Nicholson model of membrane.

1.21 Phase transitions in photosynthetic membranes

The contained in chloroplast photosynthetic membranes (*thylakoid* membranes) are arranged in lamellar stacks of bilayers (*grana*), in which the light reaction of photosynthesis takes place. Photosynthetic membranes differ in composition from animal membranes, because the dominant lipid fraction consists mostly of polyunsaturated monogalactosyl-, di-, and sulphoquinovosyl-diacylglycerols (MGDG, DGDG, and SQDG, respectively), whereas the content of phospholipids in significantly reduced. For example, total polar lipid extract of broad bean (*Vicia faba* L.) chloroplast consists of 50.7 mol% (of total lipid) of MGDG, 27.4 mol% of DGDG, 14.4 mol% of SQDG, 4.1 mol% of PG, and only 3.4 mol% of PC [253].

The composition and the function of thylakoid membranes is reflected also in their phase behavior. They reveal a variety of phase transitions, which may be ordered with increasing temperature:

(i) gel-to-liquid crystalline transition of several lipid fractions; gel domains in liquid-crystalline phase;
(ii) melting of gel lipid domains still present;
(iii) the denaturation of some proteins leading to the inactivation of light reaction of photosynthesis;
(iv) formation of non-lamellar lyotropic liquid crystalline phases;
(v) irreversible denaturation of temperature-resistive membrane proteins.

1.21.1 Gel-to-liquid crystalline phase transitions in photosynthetic membranes

Due to the domination of lipids with polyunsaturated hydrocarbon chains in plant membranes [253, 648], their gel-to-liquid crystalline transition temperatures are very low. Model lipid membranes formed from MGDG of pelargonium leaves show the transition at -30^{0}C, whereas the ones formed from synthetic MGDG at -50^{0}C [616]. In soybean lecithin the transition was recorded for the temperature between -30^{0}C and -20^{0}C [549]. Spin-labelled mobility in liposomes from spinach lipid extract shows a discontinuity at -30^{0}C and a change in slope of the temperature dependency at -40^{0}C [339]. The temperature dependency of fluorescence intensity shows breaks at -29^{0}C for lipids isolated from tomato chloroplasts (value averaged for heating and for cooling of the sample), at -25^{0}C (also averaged value) for lipids from chloroplasts of *Mimulus cardinalis*, at -21^{0}C (for sample cooling only) lipids of a pepper chloroplast [207].

In contrast to isolated spinach lipids, no breaks in temperature dependency of the mobility of spin-labels bound to spinach chloroplast membranes are observed within the range of between -10^0C and -60^0C [339]. Also in tomato and in *Mimulus cardinalis* no breaks in fluorescence intensity are observed between 0^0C and -60^0C [207].

The absence of the phase transition 'i' in some photosynthetic membranes, as compared with the behavior of lipid extracts, is not explained, however, may be caused by stabilizing role of proteins. On the other hand, X-ray scattering for bean (*Phaseolus vulgaris*) chloroplast suggest the presence of semi-liquid crystalline arrangement even at -30^0C [468]. Thus, the role of membrane proteins in photosynthetic membranes may, to some extent, resemble the cholesterol action in animal membranes, i.e., smoothening and broadening of the phase transition.

Several methods give an evidence of the transition 'ii' either in extracts of polar membrane lipids, or in photosynthetic membranes.

DSC scans of lipid extracts from bean leaves (*Vigna radiata*) show a broad exotherm between $+12^0$C and -8^0C at sample cooling. Only ≈7% of lipids forms gel domains, whereas the rest remains in liquid crystalline phase (transition 'ii'). In chilling-resistant pea the exotherm is observed between 0^0C and -10^0C, whereas in chilling-resistant wheat the transition starts at -3^0C. The addition of 1% DPPC shifts the transition to higher temperatures [552]. Lipids of chilling-sensitive bean chloroplasts show the phase transition with the maximum at $+15^0$C (at heating), whereas the lipids from chilling-resistant pea chloroplasts show no transition in this range of temperature [343].

The temperature dependency of the fluorescence intensity of chlorophyll a shows breaks in slope (or local maxima) for chloroplasts of maize at 19^0C and at 16^0C, for pepper at 16^0C and at 13^0C, for tomato at 13^0C and at 9^0C, for *Mimulus cardinalis* at 25^0C and at 0^0C, and for water hyacynth (*Eichhornia crassipes*) at 18^0C and 12^0C, respectively for heating and for cooling the samples down; for total lipid extracts of maize at 16^0C (only at cooling down), for tomato at 9^0C (only at cooling down), for pepper at 16^0C (heating) and at 12^0C (cooling down), for *Mimulus cardinalis* at 2.5^0C (heating) and at 0^0C (cooling down), and for *Eichhornia crassipes* at 19^0C (heating) and at 16^0C (cooling down) [207].

Spin-label study shows the fluidity change in bean (*Phaseolus vulgaris*) chloroplast membrane at 13^0C [343], in spinach chloroplasts at $+18.5^0$C [665], whereas in spinach thylakoids suspended in 50% glycerol at -10^0C and at $+15^0$C [339].

The effect of transition 'ii' on chilling resistivity of plants is widely discussed, however, the correlation between the transition temperature and the chilling resistance or chilling sensitivity, although suggested by some authors, is questioned by others [343, 444, 549].

1.21.2 Phase transition at inactivation of photosynthetic membrane

With increasing temperature the structural changes of the photosynthetic membrane occur between +30°C and +50°C (transition 'iii'), which are connected with the denaturation of photosystem II light harvesting complex (LHC) proteins.

The inactivation of Hill reaction occurs between 41°C and 46°C for maize, 37°C and 46°C for bean (*Vigna radiata*), 37°C and 43°C for pea [509], between 40°C and 48°C for spinach [133], and between 38°C and 42°C for barley [508, 623]. Heating of oleander (*Nerium oleander*) thylakoid membranes from 42°C up to 56°C causes not only the inactivation of the chlorophyll a/b – LHC complex, but also the dissociation of this complex [12]. The heat-induced physical dissociation of PS II LHC was observed also in spinach chloroplasts [593].

The increase in ionic strength decreases the temperature of transition 'iii' from 44°C down to (42±2)°C in spinach thylakoids. Similar change in temperature of transition 'iii' is observed in thylakoids of pea, tomato, *Cucumis melo*, and in bean (*Phaseolus vulgaris*) [133].

The transition 'iii' is irreversible, for spinach chloroplasts its enthalpy equals ≈18.4 mJ mg^{-1} Chl. At the transition the manganese ions migrate from water splitting complex of PS II to aqueous medium (100% of Mn at 50°C) [133].

The temperature dependency of proton spin-lattice relaxation time for wheat 0.8 M Tris washed (deprived of loosely bound non-functional and functional manganese pool) photosynthetic membranes show a discontinuous change at 49°C, whereas for native wheat thylakoid, the increasing exposition of manganese ions to aqueous medium (between 55 and 70°C) is recorded [55].

1.21.3 Non-lamellar phases in photosynthetic membrane lipids

Main lipid constituents of photosynthetic membrane differ in phase behavior from the major lipids of animal membranes. MGDG when dispersed in water forms hexagonal H_{II} phase [604], whereas DGDG a lamellar phase [616].

In freeze-fractured replicas prepared from thermally quenched (from about 20°C) sonicated dispersions of MGDG and DGDG mixtures (2:2 mole ratio) 10–12 nm particles were observed, corresponding to inverted micelle structures, i.e., 'lipidic particles' [153, 683]. The diameter of observed particles depend on the ionic strength of the suspending medium, i.e. for the lipids suspended in electrolyte solutions (100 mM monovalent or 10 mM divalent cations) the average particle diameter reduces to 8–10 nm. Often a large number of the small-diameter particles is ordered into close-packed array in the lamellar structure. The micrographs show the series of transitioning states between a phase separated state in which MGDG is localized predominantly in inverted micelles to one in which the two lipids are mixed in a uniform lamellar phase. The increase only few degrees in temperature (above 20°C) is sufficient to shift the balance towards the former, and a similar decrease towards the latter state [605].

The replicas of broad bean (*Vicia faba* L.) galactolipid water dispersions quenched from the elevated temperature (50°C) or mixed with cryoprotectant (ethylene glycol) show the enhanced formation of inverted lipid micelles. The lipids tend to form quasi-crystalline structures consisting of sheets of 8–9 nm diameter particles organized in orthorhombic lattice. The orientation of alternate sheets varies giving rise to "herring bone" pattern. In contrast, ethylene glycol-treated samples form more regular structures consisting of 13–16 nm particles. Lowering of the temperature from which the samples are quenched and/or decreasing the concentration of ethylene glycol decreases the occurrence of such structures [603].

In presence of 30 wt% glycerol, increasing concentration of polyvalent (but not monovalent) cations leads to further structural rearrangements involving the formation of para-crystalline arrays of tubular and spherical inverted micelles. The cylindrical inverted micelles resemble the H_{II} structures seen in replicas prepared from pure MGDG. The diameter of the cylinders is about 10–11 nm as opposed to 5–6 nm in pure lipid. The cylindrical micelles in polar lipid extracts appear to be sandwitched within individual lipid bilayers, and to pack on a cubic or orthorhombic, rather than hexagonal lattice. At low salt concentrations (< 2 mM) the frequency of non-bilayer structures was lower and the diameter of particles was reduced [253].

The native MGDG (with both acyl chains: C_{18}, and the average number of double bonds per lipid molecule equal 5.44) shows a characteristic H_{II} organisation (if quenched from +20°C), whereas hydrogenated samples with average numbers of double bonds per molecule below 4.5 show lamellar structures (characteristic for fully saturated distearoyl derivatives [604]). MGDG promotes the formation of non-bilayer structures in total polar lipid extracts of broad bean (*Vicia faba* L.). The effectiveness of this process depends on degree of unsaturation of MGDG. The disappearance of non-bilayer structures in accompanied by decrease in the fluidity of lipid matrix [252].

Unlike DGDG whose overall shape approximates a cylinder, MGDG molecule resembles cone [45, 488]. This facilitates greatly the formation of hexagonal configuration of this lipid in model systems [45, 616, 635]. Although MGDG is the major lipid constituent of thylakoid membrane (see Chpt. 1.21), in spite of its great tendency to the formation of hexagonal phase cylinders, such structures are not detectable in native photosynthetic membranes at physiological temperatures. It is believed that part of MGDG pool occupies the inner leaflet of highly curved marginal regions of grana [487], whereas the existence of these molecules localized in the planar regions of thylakoid membrane in bilayer form may be stabilized by interaction of this lipid with membrane proteins [386].

1.21.4 Non-lamellar phases in photosynthetic membranes

The existence of the thermally induced non-lamellar phases in the thylakoid membrane freeze-fractured replicas was postulated by Gounaris [251]. They found

that photosynthetic lamellae the hexagonal phase tubulae formation dominates over the process of small membrane vesicle formation in replicas of the preheated and then thermally quenched thylakoid membranes. However, freeze-fracture technique does not supply data on the native system, but only its thermally-quenched replica. Thus, the technique-dependent artifacts can influence the results.

^{31}P–NMR is well suited to determine the lyotropic phase of a phospholipid-water system, as the spectra can easily distinguish between the lamellar phase, the cylinders of hexagonal phase, and the spherical vesicles [385, 386]. In contrast to freeze-fracture technique, as an non-invasive method, ^{31}P–NMR supplies data on the structure of the sample at the temperature investigated, not on the structure of the sample rapidly quenched from the investigated temperature far below zero Celsius (in strong believe that the lyotropic phase of the membrane was conserved during the time of freezing). Unfortunately, the phospholipids are only minor fraction in lipids of photosynthetic membranes [549], what causes the significant difficulties in obtaining ^{31}P–NMR spectra of photosynthetic membranes. In fact, first recorded ^{31}P–NMR spectra were obtained by this Author for the photosynthetic membranes freeze-dried and subsequently resuspended in aqueous medium [285, 286]. This procedure allowed the sufficient increase in concentration of the membrane. However, signal to noise ratio remained the most important problem of those experiments. Further discussion is needed on the degree of correspondence of photosynthetic membranes reconstituted after lyophilization to the native state.

1.21.4.1 Non-lamellar phases in native photosynthetic membranes

This Author recorded the first ^{31}P–NMR spectra of wheat thylakoid membrane sediment (previously suspended in D_2O and the centrifuged) [287]. At heating from the room temperature the spectra show for the temperature below 55^{0}C the superposition of a broad anisotropic line characteristic for lamellar phase of phospholipids (in this particular case phospholipids localized in large thylakoids) and a narrow isotropic line, typical for the inorganic phosphorus in the solution or from small membrane particles with increased isotropic mobility (Fig. 1–7a). The low field shoulder of the lamellar anisotropic line does not appear, which means that the observed line is a superposition of lamellar lines reflecting the size distribution of thylakoid vesicles [95, 88]. At least two factors can determine the motional averaging of ^{31}P–NMR spectra of photosynthetic membranes, namely the vesicle tumbling and phospholipid lateral diffusion. Superposition of these effects on the lineshape as a function of temperature, should be fully thermally reversible. However, the estimated averaged diameter of the thylakoid was equal to about 0.2–0.4 μm [649], which is sufficiently large to avoid the vesicle tumbling effects on the lineshape at the room temperature [95].

The estimated proportion of the isotropic line is visualized in Fig. 1–7b. For the temperatures lower than 35^{0}C the proportion of isotropic line seems to be constant but for the temperatures higher than 40^{0}C it increases. This increase is irreversible, as the sample is cooled down. The lamellar line component is no

longer observed at the temperature 55°C and 60°C. However, the asymmetric lamellar line component appears again after cooling down the sample containing up to 60% of the signal.

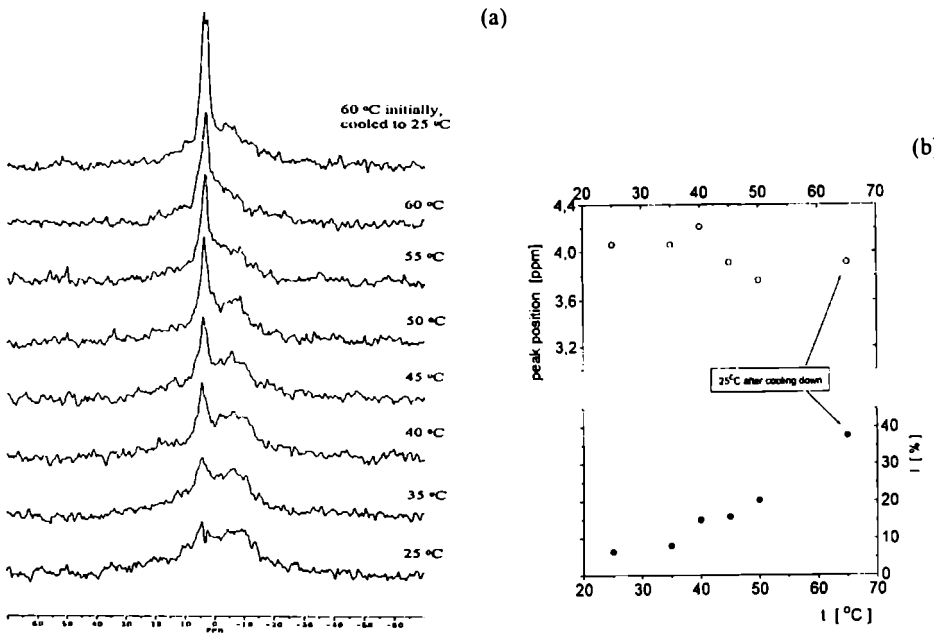

Fig. 1–7. The temperature dependency of the ^{31}P–NMR spectra at 162 MHz for the wheat thylakoid membranes suspended in D_2O. The spectra were recorded for temperature increasing from 25°C to 60°C, and then for the sample cooled down from 60°C to 25°C. Number of scans was 10000 and the line broadening 100 Hz. Part (a) shows the phosphorus spectra; part (b) the spectral parameters: the isotropic line peak position (in ppms) (open circles) and the isotropic line contribution I [%] (full circles) calculated for the temperature in which the presence of hexagonal line is not observed (except 55°C and 60°C).

For the temperatures 55°C and 60°C (see Fig. 1–8) the spectrum is similar to that one recorded for inverted hexagonal phase in model phospholipid system (DLPE, at t = 37°C, pH 5.0) [696]. The temperature dependency of the isotropic line intensity shows the plateau beginning at 40°C, also at 40°C the position of the isotropic peak begins to shift (Fig. 1–7b). These two facts suggest that at 40°C in thylakoid membranes a phase transition begins.

The spectrum cooled from 60°C down to room temperature does not show the line contribution from hexagonal phase, whereas the isotropic peak is significantly increased. This suggest that the decay of photosynthetic lamellae does not end on hexagonal phase cylinders, but the cylinders are further disassembled to small spherical micelles.

Thus, the 2-d lamellae structures decay to 0-d (macroscopically) micelles requires the intermediate step of 1-d hexagonal tubulae. The lamellar-to-hexagonal liquid crystalline phase transition (transition 'iv') is correlated with the transition 'iii',

PS II LHC denaturation and, thus, the irreversible lack of photosynthetic activity of thylakoid membrane.

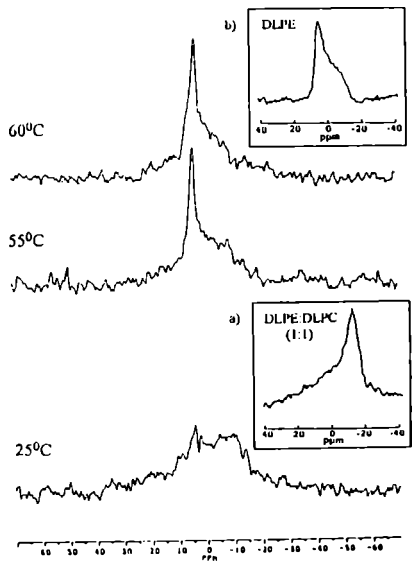

Fig. 1–8. The comparison of the recorded ^{31}P–NMR spectra at 162 MHz for wheat thylakoid membranes suspended in D_2O with the phosphorus spectra of DLPC:DLPE (1:1) mixture in lamellar phase (Inset a) and DLPE in inverted hexagonal phase (Inset b); both spectra recorded at 37°C and at pH 5.0) (taken from [696]).

1.21.4.2 Glycerol effect on the non-lamellar phase formation in photosynthetic membrane

Glycerol present in the sample medium acts as a cryoprotectant [54, 288]. Glycerol as well as the other cryoprotectant, ethylene glycol, were shown to influence the phase behavior of photosynthetic membrane lipids as observed using freeze-fractured membrane replicas [252, 253, 603]. Phosphorus NMR supplies data on the effect of glycerol on the phase behavior of the intact photosynthetic membrane.

This Author recorded the temperature dependency of the ^{31}P–NMR spectra for the wheat thylakoid membranes suspended in D_2O/glycerol mixture (57 wt% glycerol) at the temperature increasing from 25°C to 60°C and again after cooling the sample down to 25°C [287]. For the temperatures lower than 45°C spectra contain two components only: the anisotropic lamellar and the isotropic. For the temperatures higher than 45°C one cannot exclude the presence of an anisotropic hexagonal line (Fig. 1–9a). However, this contribution is very small if any. Fig. 1–9b shows the temperature dependency of relative isotropic component contribution to the ^{31}P–NMR spectra. This contribution increases linearly for the temperatures between 25°C and 60°C and this change is generally thermally irreversible. After

cooling the sample no more than ≈35% of the original lamellar anisotropic signal remains. As for the thylakoid sample suspended in D_2O, the plateau in isotropic line intensity I associated with the plateau in isotropic line position temperature dependency begins at 40^0C.

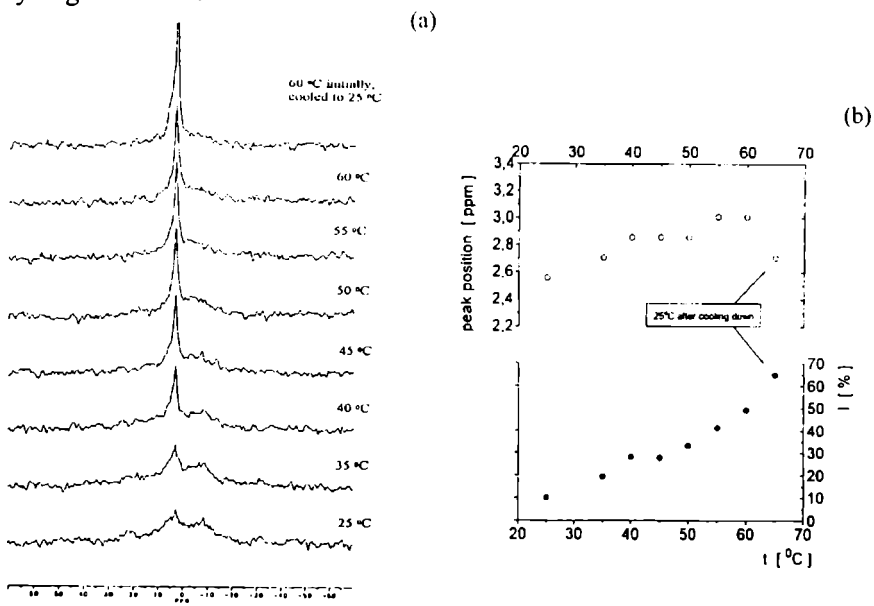

Fig. 1–9. The temperature dependency of the ^{31}P–NMR spectra at 162 MHz for the wheat thylakoid membranes suspended in D_2O/glycerol mixture (57 wt% glycerol). The spectra were recorded in the temperature range from the 25^0C to 60^0C, and for the sample cooled down from 60^0C to 25^0C. Number of scans was 12248 and the line broadening 100Hz. Part (a) contains the recorded spectra; part (b) the spectral parameters: the isotropic line position [in ppms] (open circles) and the isotropic line contribution I [%] (full circles).

Thus, at transition 'iii' glycerol presence in aqueous medium promotes the direct formation of small micelles ('lipidic particles') omitting the intermediate stage of hexagonal phase cylinders.

1.21.4.3 Non-lamellar phases in photosynthetic membranes reconstituted after lyophilization

There is still discussed, how far the photosynthetic membranes reconstituted after lyophilization (freeze-drying) resemble a native membrane. There are several reports (e.g. [132, 397]) that freeze dried and subsequently reconstituted thylakoid membranes retain photosynthetic activity.

The first ^{31}P–NMR spectra recorded have shown that the reconstituted membrane forms at 27^0C lamellar phase, whereas heated up to 55^0C irreversibly disasembles to small spherical micelles. However, even at low temperature where the lamellar phase is observed, still high contribution of phosphorus isotropic line is detected (coming from small micelles and/or membrane fragments) [285, 286].

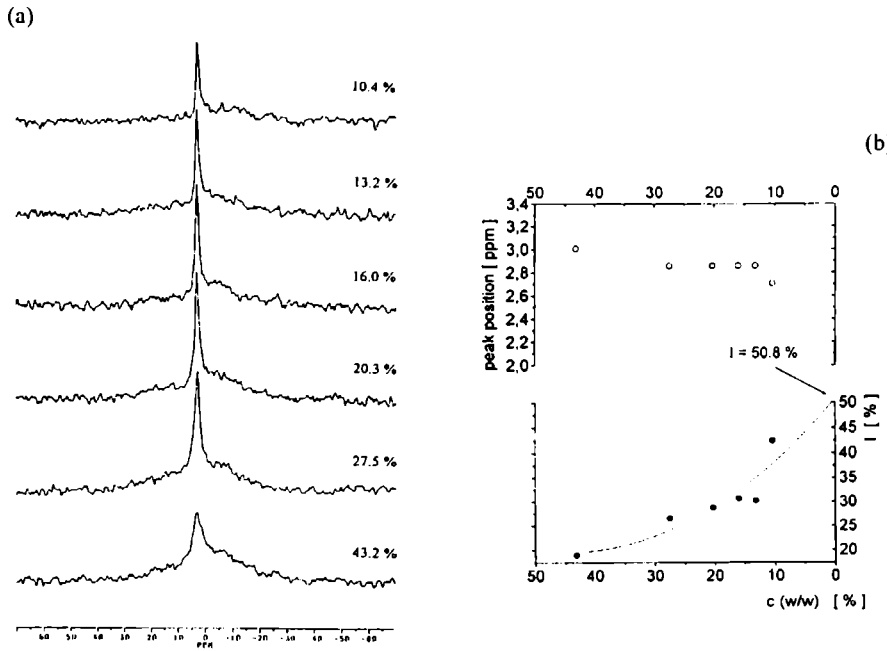

Fig. 1–10. The ^{31}P–NMR spectra at 162 MHz for the wheat thylakoid membranes freeze-dried and subsequently diluted in D_2O. The temperature was stabilized at 25^{0}C; number of scans was 8360. Part (a) shows the spectra (dry masses of the samples are annotated at the spectra); part (b) the spectral parameters: the isotropic line position [in ppms] (open circles) and the isotropic line contribution I [%] (full circles); solid curve obtained by polynomial fit gives the value I = 50.8% for the membrane dry mass extrapolated to 0%.

To observe the contribution to ^{31}P–NMR spectra of small membrane fragments, in reconstituted by suspension of freeze-dried thylakoid membranes, the Author recorded the ^{31}P–NMR spectra as a function of membrane dry mass [287]. D_2O suspension of the thylakoid membranes with the dry mass of 43.2 wt% was prepared and portions of D_2O were added step by step followed by sample homogenization (stirring than centrifugation at about 500 g for 1') and incubation (for 3 h at 4^{0}C).

Fig. 1–10a shows the room temperature ^{31}P–NMR spectra for decreasing membrane concentrations in the sample. The spectrum obtained was a superposition of both anisotropic lamellar and isotropic line components with varied proportion of both line components (Fig. 1–10b) and no evidence of hexagonal phase cylinders. In Fig. 1–10b the isotropic line component contribution I as a function of membrane dry mass is shown. The above dependency seems to be a smooth function of membrane dry mass and the extrapolated to 0 wt% – dry mass (infinite dilution case) isotropic line component contribution $I_{0wt\%} = 50.8\%$, whereas the isotropic line contribution extrapolated to 100 wt% equals $I_{100wt\%} \approx 20\%$. This means that the thylakoids at

reconstitution from lyophilizate by addition of D_2O mostly retain their lamellar structure.

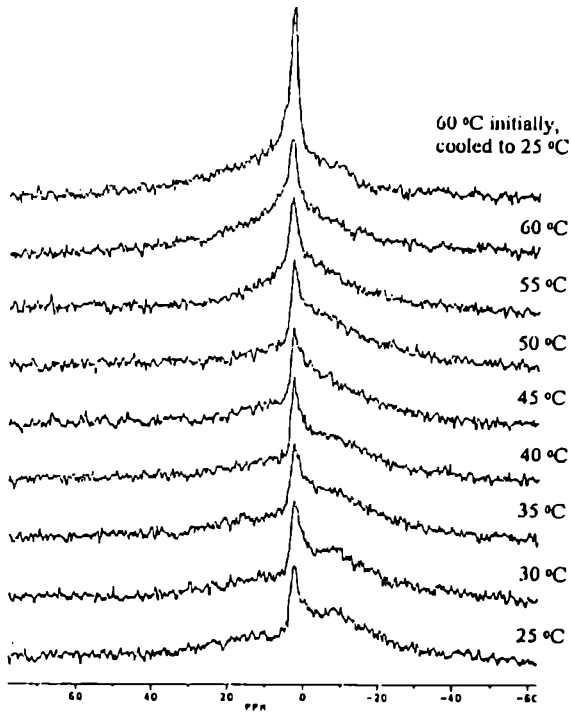

Fig. 1–11. The temperature dependency of the ^{31}P–NMR spectra at 162 MHz for the wheat thylakoid membranes freeze-dried and subsequently suspended in D_2O. The temperatures are annotated at the spectra. Number of scans was 8000.

If the temperature is increased, at 35^{0}C the ^{31}P–NMR spectrum of reconstituted from lyophilizate thylakoid membranes is a superposition of two components: an anisotropic lamellar one and an isotropic one arising from phospholipid particles present in membrane and from inorganic phosphorus (see Fig. 1–11). For the temperature 40^{0}C and higher (especially for spectra recorded at 45^{0}C and at 50^{0}C) one cannot exclude the presence of anisotropic hexagonal line component. For the ^{31}P–NMR spectrum recorded at the temperature 60^{0}C the isotropic line component dominates over the contribution of lamellar or hexagonal anisotropic line components. The isotropic line increase remains after cooling the sample down to 25^{0}C. The observed thermal hysteresis of the spectra suggests that the changes of the ^{31}P–NMR lineshape are accompanied by the irreversible changes of the membrane structure rather than by increased mobility of the small membrane fragments. Moreover, one cannot exclude that the hexagonal component of the spectrum partially remains.

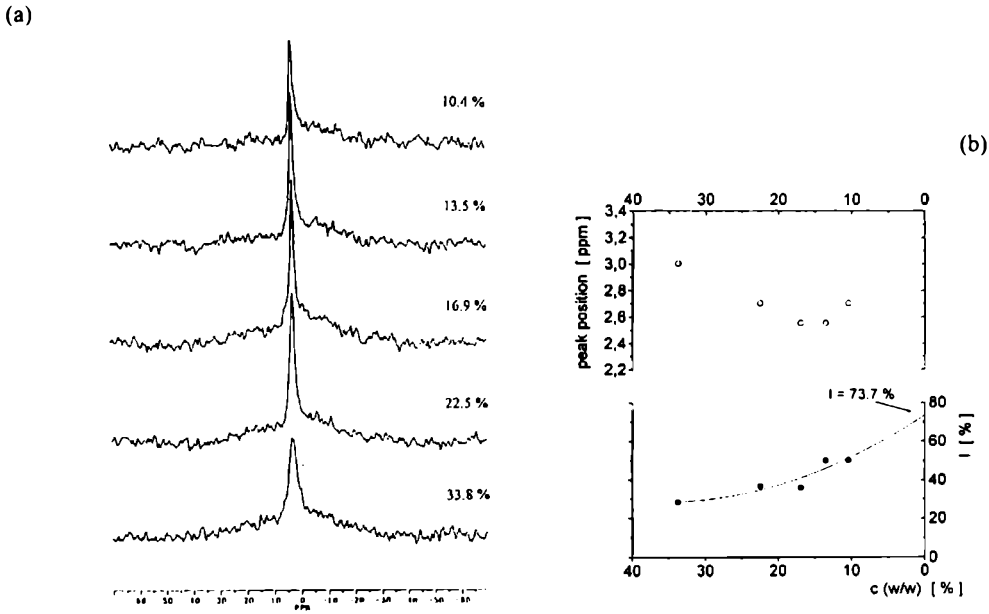

Fig. 1–12. The ^{31}P–NMR spectra at 162 MHz for the sample of the wheat thylakoid membranes freeze-dried and subsequently suspended in D_2O/glycerol mixture. The temperature was stabilized at 25^{0}C; number of scans was 8360. Part (a) shows the phosphorus spectra (dry masses of the samples are annotated at the spectra); part (b) – spectral parameters: the isotropic line position [in ppms] (open circles) and the isotropic line contribution I [%] (full circles). Solid line obtained by polynomial fit gives the value I = 73.7% for the infinite dilution case (at 0wt% membrane dry mass).

1.21.4.4 Glycerol effect of non-lamellar phases in photosynthetic membranes reconstituted after lyophilization

To observe the effect of glycerol containing aqueous medium on photosynthetic membranes reconstituted after freeze-drying this Author recorded the room temperature ^{31}P–NMR spectra versus the membrane concentration in the sample (up to ~33% of dry weight) [287].

Fig. 1–12a shows the membrane concentration dependency of the ^{31}P–NMR spectra for the wheat thylakoid membranes suspended in the D_2O/glycerol mixture (57 wt% glycerol). The observed spectra are the superpositions of broad anisotropic component (most likely due to lamellae) and isotropic one with its contribution increasing versus decreasing membrane dry mass content. Fig. 1–12b shows the dependency of contribution of isotropic component I versus decreasing membrane dry mass. The value I measured was for all concentrations significantly higher than the one for the membrane suspended in D_2O, and may reach, if smoothly extrapolated to 0% – dry mass, even 73.7%.

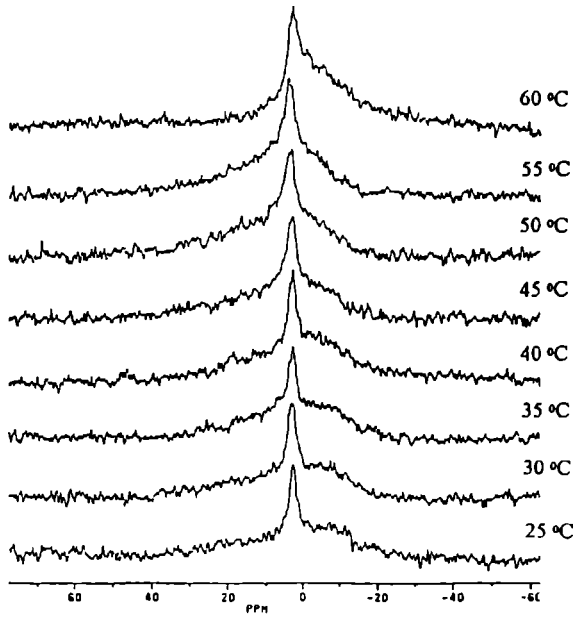

Fig. 1–13. The temperature dependency of the ^{31}P–NMR spectra at 162 MHz for the wheat thylakoid membranes freeze-dried and subsequently suspended in D_2O/glycerol mixture (52wt.% glycerol). The temperatures are annotated at the spectra. Number of scans was 8000.

At membrane heating (Fig. 1–13), for the temperature lower than 40^{0}C the phosphorus line can be resolved to superposition of two components only: an anisotropic lamellar one and an isotropic one. In the contrast to native membranes suspended in D_2O/glycerol mixtures at the temperatures higher than 35^{0}C one cannot exclude a contribution of the hexagonal component, however, to a much smaller extent than in the case of glycerol absence. The most probable contribution of the presumed hexagonal line component was found in the spectrum recorded at 60^{0}C, however, to much smaller extent than in native membranes.

1.21.5 Denaturation of temperature-resistant membrane proteins

For the temperatures above the temperature of the thylakoid biological inactivation and their spatial decomposition, several denaturations of temperature-resistant membrane proteins are recorded (transition 'v').

Calorimetric experiments performed for photosynthetic membranes show series of exotherms for the temperature above +40^{0}C; also proton spin-lattice relaxation times temperature dependency recorded by this Author shows the discontinuities (Tab. 1–3).

The observed in spinach thylakoids transition +65^{0}C changes after using of tripsine or with decreasing the ionic strength of the aqueous medium. The ATP

synthesis inhibition is observed in chloroplast extract after heating to 65°C for 2 min, whereas the ATP–ase activity remains [679]. The same effect was recorded in CF heated to 65°C [200, 201]. These functional changes may be connected with the conformational changes in CF. Thus, the transition at 65°C can be quite probably attributed to changes in CF.

In contrast to the transition at 65°C, other denaturation-caused-transitions recorded either by DSC or by NMR are not yet attributed to given protein fractions.

Table 1–3. The temperatures t [°C] of protein denaturation caused phase transitions in photosynthetic membranes. The accuracy of transition temperatures equals ±1°C except for lowest transition in spinach (measurement A), where it is ±2°C.

Species	t [°C]	Ref.
Spinach [A]	42, 54, 65, 72, 79, 84	[133]
Spinach [B]	44, 61, 66, 70, 78, 83	[133]
Spinach [B]	45, 60, 62, 65, 70, 79, 83	[444]
Pea	49, 60, 65, 72, 77, 85, 92	[444]
Soybean	67, 75, 82, 88	[444]
Cucumis melo	52, 62, 70, 76, 83, 86	[444]
Tomato (*Lycopersicon esculentum*)	54, 61, 69, 82, 91	[444]
Tomato (*Lycopersicon hirsutum* LA 1361)	50, 61, 65, 80, 92	[444]
Bean (*Phaseolus vulgaris*)	51, 66, 74, 82, 88	[444]
Wheat [C]	49, 59, 81	[55]

A = medium with high ionic strength;
B = medium with low ionic strength;
C = proton relaxation data.

2. Nuclear magnetic resonance applied to dry biological systems

As a volume-sensitive method, i.e. where the detected signal is proportional to the total number of nuclei in the sample, NMR seems not to be designed for observation of surface effects, such as behavior of water bound to the surfaces of biological system.

Poor sensitivity of NMR for surface phenomena can be overcome by use of the systems which are nothing but surface (systems with high S/V). This may be solved in two ways: (i) by monitoring the hydration of porous system, e.g. controlled pore glasses with homogeneous distribution of mass and pore sizes [430]; or (ii) by suspending in water high number of small solid objects (glass beads or macromolecules), because the splitting of the suspended solid onto n parts, increases its total surface at least $n^{1/3}$ times.

The aggregation and/or gelation, and dynamics of the glass beads and (even more) of the macromolecules shade in NMR experiment the bound water effects, in contrast to the solid matrix of porous system not depending so sensitively on hydration level (still immobilized with not changed spatial arrangement).

The measurement of nuclear magnetic relaxation, as no other method, supplies precise information on stoichiometry and dynamics of hydrogen atoms in non-transparent system. Proper stoichiometry is obtained from NMR data under two requirements: (i) dead time of the spectrometer detection channel is short in comparison to free induction decay (FID) time, T_2^*; (ii) the concentration of paramagnetic ions in the examined system does not eliminate the significant part of protons by the enormous shortening of proton relaxation times of the signal (e.g. for solidifying concrete [574]).

2.1 Elements of nuclear magnetic relaxation

2.1.1 The dynamics and relaxation of nuclear spin systems

The dynamics of isolated nuclear spins may be sufficiently described in terms of the motion of classical magnetization vectors [191]. However, in case of coupled

spins, a quantum mechanical formalism describing the state of the system should be considered. Then, the density operator σ permits the most convenient description of the quantum mechanical system dynamics. From the time-dependent Schrödinger equation one gets the equation of motion for the density operator σ. This differential equation is called Liouville-von Neumann equation and plays the leading part in calculating the dynamics of quantum mechanical systems

$$\frac{d\sigma(t)}{dt} = -i \cdot \left[H(t), \sigma(t)\right] = -i \cdot \hat{L}(t) \cdot \sigma(t), \tag{2.1}$$

where $\hat{L}$ is a Liouvillian and H is an effective Hamiltonian of the spin system in angular frequency units.

In further considerations a semi-classical approach will be used, in which spin variables are treated quantum-mechanically; whereas lattice variables are treated classically. This approach, was developed in series of papers by Bloch, Wangsness, Redfield and Hubbard, and is called BWRH-theory [324, 559, 697]. It may be presented either in an operator formalism or in a matrix formalism for a density matrix elements $\sigma_{\alpha\alpha'} = \langle\alpha|\sigma|\alpha\rangle$.

Here the spin system is described by a reduced density operator: $\sigma = Tr_L \rho$, where $Tr\sigma = 1$, and an effective spin Hamiltonian

$$H_{eff} = H_0 + H'(t), \tag{2.2}$$

which is a sum of static Zeemanian interaction, H_0, and time-dependent perturbation, $H'(t)$. The use of an operator formalism leads to the following equations

$$\frac{d\sigma(t)}{dt} = -i \cdot \hat{L}_0 \cdot \sigma + \hat{\Gamma} \cdot \left(\sigma - \sigma^{eq}\right), \tag{2.3}$$

where

$$\hat{L}_0 \cdot \sigma = \left[H_0, \sigma\right], \tag{2.4}$$

$$\hat{\Gamma} \cdot \sigma = -\frac{1}{2} \cdot \int_{-\infty}^{+\infty} \left\langle \left[\tilde{H}'(t+\tau), \left[\tilde{H}'(t), \sigma\right]\right] \right\rangle \cdot d\tau, \tag{2.5}$$

and $\tilde{H}'(t)$ is the Hamiltonian of the system expressed in interaction representation

$$\tilde{H}'(t) = e^{iH_0 t} H(t) e^{-iH_0 t}. \tag{2.6}$$

The expectation value of any spin operator Q, and its time evolution can be calculated from the density operator in the form

$$\langle Q \rangle(t) = \left\langle Q | \sigma(t) \right\rangle = Tr\left\{Q^+ \sigma(t)\right\}. \tag{2.7}$$

Using Fano expansion for the density operator

$$\sigma(t) = \sum_{k=1}^{n^2} c_k(t) \cdot \hat{T}_k \tag{2.8}$$

for $Q = \hat{T}_j$ one gets:

$$\left\langle \hat{T}_j \right\rangle(t) = c_j(t), \tag{2.9}$$

where $\hat{T}_k$ are orthogonal and normalized operators in a n^2–dimensional Liouville space (n is a dimension of Hilbert space).

From Eqs. (2.3–2.9) one gets

$$\frac{d\left\langle \hat{T}_j \right\rangle}{dt} = -\sum_k A_{jk} \left\langle \hat{T}_k \right\rangle - \sum_k R_{jk} \left(\left\langle \hat{T}_k \right\rangle - \left\langle \hat{T}_k \right\rangle^{eq} \right) \tag{2.10}$$

with

$$A_{jk} = i \cdot Tr\left\{ \hat{T}_j^+ \left[H_0, \hat{T}_k \right] \right\}, \tag{2.11}$$

and with

$$R_{jk} = +\frac{1}{2} \int_{-\infty}^{+\infty} Tr\left\{ \left[\hat{T}_j, \tilde{H}(t) \right] \cdot \left[\hat{T}_k, \tilde{H}(t+\tau) \right]^+ \right\} \cdot d\tau, \tag{2.12}$$

where A_{jk} is a spin dynamics matrix and R_{jk} is a relaxation matrix.

From Eq. (2.12) one can evaluate the relaxation times $T_j = R_{jj}^{-1}$, and cross-relaxation times $T_{jk} = R_{jk}^{-1}$ for multispin systems.

For instance, taking for the operators $\hat{T}_j = \hat{T}_k = I_z \Big/ \sqrt{Tr(I_z)^2}$, and $I_x \Big/ \sqrt{Tr(I_x)^2}$, one gets the expression for spin-lattice and for spin-spin relaxation times, T_1 and T_2, respectively.

In presence of dipole-dipole interaction described by dipolar Hamiltonian

$$H'(t) = \sum_{i<j} \sum_{M=-2}^{+2} A_{2M} \frac{C_{2M}\left(\theta_{ij}(t), \phi_{ij}(t)\right)}{r_{ij}^3(t)}, \tag{2.13}$$

the spin-lattice and spin-spin relaxation times for identical spins I–I and for non-equivalent spins I–S, where spin S may denote either nuclear or electronic spin, can be expressed in the compact form

$$\left(\frac{1}{T_L}\right)_I = \sum_{K=I,S}\sum_{\lambda=R,T}\left(\frac{1}{T_L}\right)_{I,K}^{(\lambda)} = \left(\frac{1}{T_L}\right)_{I,I}^{(R)} + \left(\frac{1}{T_L}\right)_{I,S}^{(R)} + \left(\frac{1}{T_L}\right)_{I,I}^{(T)} + \left(\frac{1}{T_L}\right)_{I,S}^{(T)}, \quad (2.14)$$

where K denumerates spins I and S; λ denumerates type of diffusion influencing the relaxation process: R rotational diffusion, T translational diffusion; L = 1 stands for spin-lattice relaxation, and L = 2 for spin-spin relaxation.

For identical spins I, from Eqs. (2.13) and (2.14) we get

$$\left(\frac{1}{T_1}\right)_{I,I}^{(\lambda)} = A_{I,I}^2\left[J_1^{(\lambda)}(\omega_I) + 4\cdot J_2^{(\lambda)}(2\omega_I)\right], \quad (2.15)$$

$$\left(\frac{1}{T_2}\right)_{I,I}^{(\lambda)} = \frac{1}{2}A_{I,I}^2\left[3\cdot J_0^{(\lambda)}(0) + 5\cdot J_1^{(\lambda)}(\omega_I) + 2\cdot J_2^{(\lambda)}(2\omega_I)\right], \quad (2.16)$$

whereas for non-equivalent spins I–S

$$\left(\frac{1}{T_1}\right)_{I,S}^{(\lambda)} = \frac{1}{3}A_{I,S}^2\left[J_0^{(\lambda)}(\omega_I - \omega_S) + 3\cdot J_1^{(\lambda)}(\omega_I) + 6\cdot J_2^{(\lambda)}(\omega_I - \omega_S)\right], \quad (2.17)$$

$$\left(\frac{1}{T_2}\right)_{I,S}^{(\lambda)} = \frac{1}{6}A_{I,S}^2\left[4\cdot J_0^{(\lambda)}(0) + J_0^{(\lambda)}(\omega_I - \omega_S)\right] + \\ + \frac{1}{6}A_{I,S}^2\left[3\cdot J_1^{(\lambda)}(\omega_I) + 6\cdot J_1^{(\lambda)}(\omega_S) + 6\cdot J_2^{(\lambda)}(\omega_I + \omega_S)\right]. \quad (2.18)$$

For K = I, S, $A_{I,K}^2$ is equal

$$A_{I,K}^2 = K(K+1)\gamma_I^2\gamma_K^2\hbar^2\left(\frac{\mu_0}{4\pi}\right)^2. \quad (2.19)$$

See that $A_{I,K}^2\left\langle r_{I,K}^{-6}\right\rangle = d_{I,K}^2$, where $d_{I,K}^2$ is the square of the dipolar constant for spins I and K.

In case of isotropic rotational and translational diffusion (see Chpt. 2.1.2) the spectral density functions are expressed by

$$J_M^{(R)}(\omega) = \frac{\left\langle r_{I,K}^{-6}\right\rangle}{5}\frac{2\tau_c}{1+\omega^2\tau_c^2}, \quad (2.20)$$

and

$$J_M^{(T)}(\omega) = \frac{4\pi N}{5d^3\omega}f(\alpha, x), \quad (2.21)$$

respectively. Here N is the number of spins per unit volume, τ_c^2 is correlation time, and d denotes the minimal distance of intermolecular spin pair ij, which, in principle, may be less than the diameter of the molecule, a. Function $f(\alpha,x)$ is defined [666, 531] in the following way

$$f(\alpha,x)=\frac{2}{x^2}\left\{v\cdot\left[1-\frac{1}{u^2+v^2}\right]+\left[v\cdot\left(1+\frac{1}{u^2+v^2}\right)+2\right]\cdot e^{-2v}\cos 2u\right\}+$$
$$+\frac{2}{x^2}\left\{u\cdot\left[1-\frac{1}{u^2+v^2}\right]\cdot e^{-2v}\sin 2u\right\} \qquad (2.22)$$

with the parameters u and v defined as

$$u=\frac{1}{2}\sqrt{\frac{q(1-q)}{\alpha}}\text{, and } v=\frac{1}{2}\sqrt{\frac{q(1+q)}{\alpha}}\text{,} \qquad (2.23)$$

where

$$q=\frac{\alpha\cdot x^2}{\sqrt{1+\alpha^2x^4}}. \qquad (2.24)$$

The variables of the function $f(\alpha,x)$ are defined as

$$\alpha=\frac{\langle r^2\rangle}{12d^2}\text{, and } x=\sqrt{\frac{\omega\alpha^2}{D}}. \qquad (2.25)$$

In the limiting case $\langle r^2\rangle >> d^2$, Eq. (2.22) simplifies to

$$J_M^{(T)}(\omega)=\frac{8\pi N}{15d^3\omega}\frac{\tau}{1+\left(\frac{\omega\tau}{2}\right)^2}\text{,} \qquad (2.26)$$

while for $\langle r^2\rangle << d^2$ and for $\tau << \omega^{-1}$

$$J_M^{(T)}=\frac{8\pi N}{15d^3\omega}\left\{\frac{1}{x}-\frac{2}{x^3}+\frac{e^{-x}}{x}\cdot\left[\left(1-\frac{2}{x^2}\right)\sin x+\left(1+\frac{4}{x}+\frac{2}{x^2}\right)\cos x\right]\right\}\text{,} \qquad (2.27)$$

where $x=\sqrt{\frac{\omega d^2}{D}}$.

The correlation time for rotational selfdiffusion, and for translational selfdiffusion (see Chpt. 2.1.2.1) at $\langle r^2\rangle >> d^2$ is defined as [531]

$$\tau_c^{(T)} = \frac{\langle r^2 \rangle}{12 \cdot D} . \tag{2.28}$$

However, for continuous translational diffusion the correlation time may be defined on different way [1]

$$\tau_c^{(T)'} = \frac{d^2}{2 \cdot D} . \tag{2.29}$$

In such a case

$$x = \sqrt{\frac{\omega d^2}{D}} = \sqrt{2\omega\tau} . \tag{2.30}$$

Although here the considerations are restricted to the dipolar interaction, several other interactions may, in general, contribute to relaxation processes, namely, quadrupolar interaction, spin-rotational interaction, and the anisotropy of the electronic screening. Their contributions and the interference effects between these interactions (and dipolar interaction) were thoroughly discussed for multispin systems by Blicharski [49, 50, 51, 52, 53, 57, 58, 59, 60]. If interferences between interactions take place, they give additional contribution to the relaxation matrix and in consequence a non-exponential time dependency of the nuclear magnetization may appear.

2.1.2 Diffusion equation

Let's consider a particle randomly moving in a medium. At t = 0 the particle is placed in the beginning of the Cartesian reference frame, in point (0,0,0). Particle interacts with the other particles by collisions randomly changing the direction of its motion, whereas the speed of the particle remains unchanged. The position of particle after M collisions may be expressed as a function of time

$$\vec{r}(t) = [x, y, z] = \sum_{j=1}^{M} \vec{r}_j , \tag{2.31}$$

where $\vec{r}_j$ is the displacement between j'th and j+1'th collision.

For so described process, the elements of the diffusion tensor $\hat{D}$ are defined

$$D_{\alpha\beta} = \lim_{t \to 0} \frac{\langle x_\alpha \cdot x_\beta \rangle}{2t} , \tag{2.32}$$

where $\alpha, \beta = 1, 2, 3$ (= x, y, z), and x_α, x_β = x, y, z. Here the averaging is over the ensemble of particles and over the number of collisions.

For short time t $(t \to 0)$, the mean square displacement may be expressed as

$$\langle x^2 \rangle = 2 \cdot D_{xx} \cdot t \ , \tag{2.33a}$$

$$\langle y^2 \rangle = 2 \cdot D_{yy} \cdot t \ , \tag{2.33b}$$

$$\langle z^2 \rangle = 2 \cdot D_{zz} \cdot t \ , \tag{2.33c}$$

For isotropic diffusion $D_{xx} = D_{yy} = D_{zz} = D$, and D is called diffusion coefficient. Thus, knowing that $(\bar{r})^2 = x^2 + y^2 + z^2 = r^2$, and from Eqs. (2.33a), (2.33b), and (2.33c), for 3-d case one gets

$$\langle r^2 \rangle = 6 \cdot D \cdot t \ . \tag{2.34}$$

Eq. (2.34) describes diffusion process starting from any immobilized point (here the center of coordinates frame).

2.1.2.1 Selfdiffusion

If two mobile particles (denoted "1" and "2") move in continuous medium, the relative mean square displacement of one mobile particle from the other one is

$$\Delta\bar{r}_{1,2} = \bar{r}_1 - \bar{r}_2 \ . \tag{2.35}$$

The averaging over the ensemble of the particles and over the number of collisions gives

$$\langle \Delta\bar{r}_{1,2} \rangle^2 = \langle \bar{r}_1 - \bar{r}_2 \rangle^2 = \langle \bar{r}_1 \rangle^2 + \langle \bar{r}_2 \rangle^2 \tag{2.36}$$

and yields the formula for selfdffusion

$$\langle \Delta\bar{r}_{1,2} \rangle^2 = 12 \cdot D \cdot t \ . \tag{2.37}$$

Taking for t the value τ_c, which is the correlation time characterizing the motion considered (for translational diffusion it is time needed to diffuse on the distance of the size of a molecule), one gets

$$\langle \Delta\bar{r}_{1,2} \rangle^2 = a^2 = 12 \cdot D \cdot \tau_c \tag{2.38}$$

and

$$\tau_c^{(T)} = \frac{a^2}{12 \cdot D} \ . \tag{2.39}$$

For the specifity correlation times used in (defined for) NMR method, see Chpt. 2.1.1.

2.1.2.1.1 Translational selfdiffusion

For translational diffusion the friction force of viscous medium is given by

$$\vec{F} = -\hat{\xi} \cdot \vec{v} \text{, and } F_\alpha = -\sum_\beta \xi_{\alpha\beta} v_\beta \text{,} \tag{2.40}$$

where $\xi_{\alpha\beta}$ is frictional tensor.

For isotropic environment (i.e. bulk H_2O) we get

$$\vec{F} = -\xi \vec{v} \text{.} \tag{2.41}$$

Here $\hat{\xi}^{(T)} = \xi^{(T)} \hat{I}$, thus, $\xi_{xx} = \xi_{yy} = \xi_{zz} = \xi^{(T)}$ and for diffusing sphere is

$$\xi^{(T)} = 6\pi\eta a \text{.} \tag{2.42}$$

Index (T) denotes the translational diffusion.

The temperature dependency is given by

$$\hat{D}^{(T)} = k_B T \cdot \left(\hat{\xi}^{(T)} \right)^{-1} \text{,} \tag{2.43}$$

which implies the value of translational diffusion coefficient for isotropic processes

$$D^{(T)} = \frac{k_B T}{\xi^{(T)}} \text{.} \tag{2.44}$$

2.1.2.1.2 Rotational selfdiffusion

For rotational motion, the friction torque, $\vec{N}$, should be considered

$$\vec{N} = -\hat{\xi}^{(R)} \cdot \vec{\omega} \text{,} \tag{2.45}$$

where $\hat{\xi}^{(R)}$, is rotational friction tensor. Similarly to translational diffusion

$$\hat{D}^{(R)} = k_B T \cdot \left(\hat{\xi}^{(R)} \right)^{-1} \text{.} \tag{2.46}$$

If the rotational diffusion is isotropic, one gets

$$D^{(R)} = \frac{k_B T}{\xi^{(R)}} \text{,} \tag{2.47}$$

where $D^{(R)}$ is rotational diffusion coefficient, and $\xi^{(R)}$ is rotational friction coefficient.

2.1.3 Correlation times

For translational motion, the correlation time $\tau_c^{(T)}$ is given by

$$\tau_c^{(T)} = \frac{a^2}{12Dt} = \frac{a^2}{12}\frac{6\pi\eta a}{k_B T} = \frac{\pi\eta a^3}{2k_B T} \,. \tag{2.48}$$

The rotational correlation time, $\tau_c^{(R)}$, is given by

$$\tau_C^{(R)} = \left(6D_R\right)^{-1} = \frac{4\pi\eta a^3}{3k_B T} \,. \tag{2.49}$$

From Eqs. (2.45) and (2.46) we get the ratio of rotational to translational correlation times equal to

$$\frac{\tau_c^{(R)}}{\tau_c^{(T)}} = \frac{8}{3} \,. \tag{2.50}$$

2.1.4 Chemical shift

Nuclear spins $\vec{I}$ placed in external magnetic field $\vec{B}_0$ experience, except Zeemanian interaction, also the interactions with the internal magnetic fields induced by $\vec{B}_0$ in the place of a given nuclear spin. The sources of these interactions are the orbital electronic currents induced in atom, in its closer or more distant surrounding, in molecule or in its neighborhood.

The above interaction is called chemical shielding and its Hamiltonian may be expressed in terms of external magnetic field $\vec{B}_0$, and nuclear spin $\vec{I}$, as

$$H_S = \gamma \cdot \vec{I}\hat{\sigma} \cdot \vec{B}_0 \,, \tag{2.51}$$

where γ is nuclear gyromagnetic coefficient and $\hat{\sigma}$ is chemical shielding tensor.

In presence of chemical shielding the static Hamiltonian may be rewritten in form

$$H_0 = H_Z + H_S = -\gamma \cdot \vec{I}\left(1 - \hat{\sigma}\right)\vec{B}_0 \,, \tag{2.52}$$

where $H_Z = -\gamma \cdot \vec{I} \circ \vec{B}_0$ is Zeemanian term of Hamiltonian.

In case of fast molecular motions the second rank tensor interactions are averaged out. Thus, only the trace of chemical shielding tensor contributes to spin Hamiltonian

$$H = -\gamma \cdot \left(1 - \sigma\right)\vec{I} \circ \vec{B}_0 \,, \tag{2.53}$$

where σ is a trace of chemical shielding tensor

$$\sigma = \frac{1}{3}\mathrm{Tr}\{\sigma_{\alpha\beta}\} = \frac{1}{3}\sum_{\alpha}\sigma_{\alpha\alpha} \ , \tag{2.54}$$

If, in addition, the external magnetic field, $\vec{B}_0$, is parallel to the z-axis of laboratory frame of reference, the equation (2.53) may be written in simpler form

$$H_0 = -\omega_0 \cdot I_z , \tag{2.55}$$

where

$$\omega_0 = \gamma \cdot (1-\sigma) \cdot B_0 \tag{2.56}$$

is Larmor frequency of nuclear spin in effective magnetic field $B_{eff} = (1-\sigma)B_0$.

2.1.5 Why not NMR-tomography?

Recently, NMR-tomography is the most trendy branch of NMR. It provides the spatially resolved distribution of proton density and/or of proton relaxation times in the sample. Indeed, it would be very tempting to observe separately the layers of bound water covering its surface, and free water in the vicinity of biological system.

Nowadays, the resolution of NMR microscopes is of about 10 μm for liquids ($4 \cdot 4 \cdot 30$ μm) and 50 μm for solids, which is still 4 to 5 orders of magnitude more than the water monolayer thickness. If voxel size is diminished n times, its volume (and, thus, the signal-to-noise ratio, S/N) decreases n^3 times. The observation of single water monolayers using NMR-microscopy requires the increase in the equipment sensitivity of the order 10^{12} up to 10^{15}, which is unrealistic. Moreover, the lower limit of the NMR-microscopy resolution is defined by the diffusion of water at the time of the experiment, which may blur the tomographical picture. As the experiment duration is of the order of tenth ms, the diffusion displacement is given by

$$\langle x^2 \rangle = 8Dt \tag{2.57}$$

(from Eqs. (2.33, 2.34), and Eq. (2.57) in 2-d case), where $D = 2.5 \cdot 10^{-5} cm^2 s^{-1}$ (at $t = 25^0C$) is the diffusion coefficient of water, $\langle x^2 \rangle$ is the mean square displacement of the molecule and t is the time of the NMR experiment (at least, ~50 ms). Thus, the resolution limit for the NMR microscopy equals ~10 μm (close to the minimal sizes of voxel recently achieved for liquids).

On the other hand, NMR-tomography promises of the direct observation of the density profile of proliferating liquid (in case, if macroscopic diffusion is slow in NMR-experiment-time-scale) for water in dry biological system.

2.2 NMR relaxation function analysis

Spin-subsystems present in micro-heterogeneous biological systems, namely: solid matrix, mobile molecular groups, bound water and free water pools, are often differentiated by relaxation times (T_1, $T_{1\rho}$, T_{1D}, T_2 or T_2^*) and relative magnetization fractions. In case of intermediate or slow exchange, and for limited number of subsystems, the observed relaxation function of such systems is well approximated by the set of discrete components (usually exponential or Gaussian functions) with specific relaxation times [517, 524, 526, 629], whereas for high number of subsystems the continuous distribution of relaxation times better approximates the reality. For instance, in controlled pore glass [4, 170, 329] a continuous distribution well models the spin-lattice relaxation function if pores are completely filled with water [117, 630], whereas if pore hydration is comparable to the mono-molecular coverage, the relaxation function is a superposition of discrete components (see Chpt. 1.13.4) [283].

2-d analysis in time domain significantly improves the decomposition of relaxation data. The spin-grouping technique [523, 525] based on a correlated analysis of spin-lattice and spin-spin relaxation functions, was successfully used to determine relaxation parameters for the samples, where the 1-d approach gave no satisfactory results [523, 629]. However, the used algorithm, based on the weighted least-square fitting of the straight lines, diminished the effectiveness of that method. Thus, employing Marquardt's non-linear least squares fitting routine, and the spin-grouping approach, CracSpin computer program was developed for 2-d relaxation data analysis in time domain [703].

Porous rock containing liquid fraction may model a dry biological system, in which solid (here mineral) matrix is not observed, and proton signal comes solely from liquid fraction filling the pores of rock. Then, the relaxation function is a sum of a series of functions coming from the liquid embedded in set of pores. Proton relaxation data allow to evaluate porosity [591, 663], permeability [443, 606, 663]; content of water, solid and liquid hydrocarbons [302, 389, 505, 571]; and to search the kinetics of the hydration process [574].

Continuous distributions of components are routinely applied to analyze relaxational data of porous rock [260, 292, 467]. Although data inversion algorithms finding continuous distributions of the relaxation times without any knowledge on the form of the relaxation function were developed [70, 84, 396, 706], often the distribution of relaxation times is modeled by stretched exponential (SE) function [61, 499, 553] or by modified stretched exponential (MSE) function [530].

Regarding high "numerical capacity" of SE function, one should keep in mind that it may successfully fit the relaxation function which, indeed, is a superposition of discrete single exponentials. It is suggested, that for any given micro-heterogeneous biological system, independently on agreement obtained for

SE fits, the multiexponential fits are made, to find with sufficiently high dose of credibility a real form of relaxation function.

2.2.1 Stretched exponential (SE) and modified stretched exponential (MSE) function

Commonly used SE function may reflect the relaxation function for a real self-similar (fractal) distribution of pore sizes [149] or may be just used as an easy to fit function supplying the average 1/e value of the relaxation function [117]

$$F(\tau) = F_{SE} \cdot e^{-\left(\frac{\tau}{T_{SE}}\right)^{\alpha}} \tag{2.58}$$

Indeed, fractal approximation may not extend below the minimal pore size, at least implied by the molecular structure of porous material, and in consequence the shortest non-zero value of relaxation time T_0. The discrepancy between real and fractal distribution is clearly seen, as the first derivative of SE function for $\tau \to 0$ is

$$\frac{dF(\tau)}{d\tau} \to -\frac{\alpha F_{SE}}{T_{SE}^{\alpha}}\left(\frac{1}{\tau}\right)^{1-\alpha} \to -\infty. \tag{2.59}$$

In multi-component relaxation function the infinite value of the first derivative causes the overestimation of SE component amplitude, F_{SE}. Thus, Peyron et al., 1996, proposed MSE function

$$F(\tau) = F_{MSE} \exp\left[-\frac{\tau}{T_0}\left(1+\frac{\tau}{T_C}\right)^{\beta-1}\right]. \tag{2.60}$$

For $\tau << T_C$, the MSE function has the single exponential asymptotic form

$$F(\tau) \to F_{MSE} \exp\left(-\frac{\tau}{T_0}\right), \tag{2.61}$$

whereas for $\tau >> T_C$ the form of SE function

$$F(\tau) \to F_{MSE} \exp\left[\left(-\frac{\tau}{T_{MSE}}\right)^{\beta}\right], \tag{2.62}$$

where $T_{MSE} = T_0^{1/\beta} T_C^{1-1/\beta}$.

Parameter T_C defines the short-time limit for SE behavior, as required by the MSE model (Eq. 2.60), and can be evaluated from the shortest, T_0, and the effective, T_{MSE}, relaxation time describing porous system.

To compare the reliability of the analyses based on SE and MSE function, this Author tested porous rock, oil-containing Węglowicki sandstone, for which proton spin-lattice relaxation function was not fitted with sufficient accuracy neither by single exponential function nor by double exponent [291], whereas either SE function (Fig. 2–1a) or MSE function (Fig. 2–1b) fitted well the relaxation data.

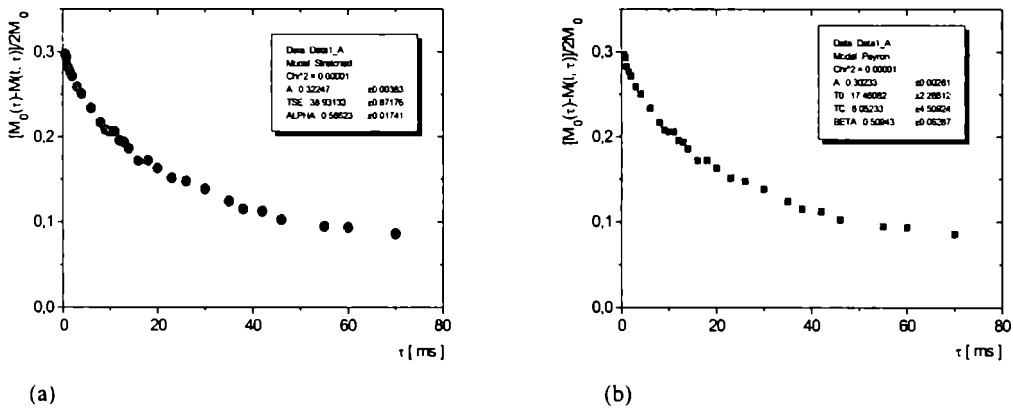

Fig. 2–1. The normalized proton spin-lattice relaxation for Węglowicki sandstone recorded at 99 μs after π/2 pulse and (a) the SE function (full circles) and (b) MSE function (full squares) fitted to the data. Proton spin-lattice relaxation time was measured using the π/2 — τ — π/2 — FID(t) sequence of pulses.

The overestimation of the signal amplitude by SE model compared to MSE was defined as

$$\delta = \frac{F_{SE} - F_{MSE}}{F_{MSE}}. \tag{2.63}$$

Fig. 2–2 shows the dependency of δ versus time t after π/2 pulse for Węglowicki sandstone. The effect of the amplitude overestimation was not large even at the value of fractal exponent meaningfully different from $\alpha = 1$ (Tab. 2–1). The mean value of the overestimation was $\delta = 0.035$ with $\sigma_\delta = 0.020$.

Table 2–1	α	σ_α	β	σ_β
t < 30 μs	0.501	0.021	0.513	0.020
t > 30 μs	0.617	0.032	0.592	0.054

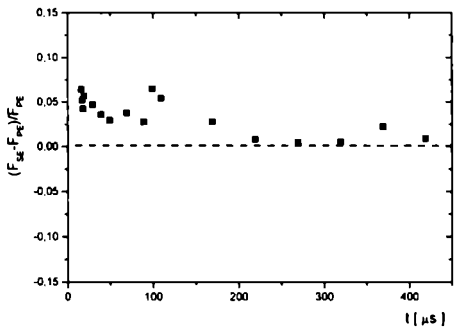

Fig. 2–2. The relative amplitude overestimation δ for Węglowicki sandstone expressed versus time distance of FID sampling point t from the π/2 pulse.

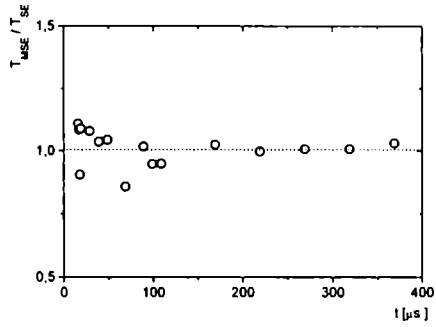

Fig. 2–3. The time constants ratio T_{MSE}/T_{SE} versus time t for Węglowicki sandstone.

Value of minimal relaxation time T_0 is a parameter correlated with T_C, thus, its value is not approximated with sufficient quality, although time, T_{MSE}, is accurately fitted.

To compare the values of effective relaxation times T_{SE} and T_{MSE}, the coefficient χ was defined as

$$\chi = \frac{T_{MSE}}{T_{SE}} \quad . \tag{2.64}$$

Due to the sample features, the effective spin-lattice relaxation time differs for solid ($t < 30$ μs) and for liquid ($t > 30$ μs) region of FID function, however, the values obtained from both SE and MSE models are very close (Fig. 2–3). Mean value of the χ coefficient equals 1.011 with $\sigma_\chi = 0.069$, which means that MSE model does not alter the value of effective relaxation time compared to SE model.

Fig. 2–4 presents the dependency of fractal exponents on time t. Although fractal exponents α and β vary for solid and liquid parts of FID, their values obtained from both SE and MSE models do not differ much (see Tab. 2–1).

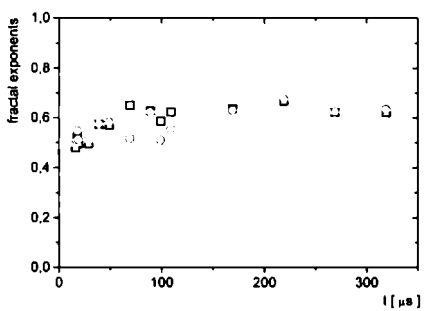

Fig. 2–4. The values of fractal exponent α fitted for SE model and β for MSE model versus time t after π/2 pulse for Węglowicki sandstone sample.

2.2.2 Spin-grouping technique

Spin subsystem relaxing with a single relaxation time is called *spin-group* [523]. In most micro-heterogeneous systems the assignment of spin-groups requires 2-d analysis of relaxation data (spin-grouping technique), in which data are stored in a 2-d matrix with the indices p and r denoting:

(i) t_p – time pointing along FID (p = 1 .. m); and

(ii) τ_q – time (q = 1 .. n), which for T_1 experiment is time period between two r.f. pulses (π and $\pi/2$ for inversion recovery, or two $\pi/2$ pulses for saturation recovery sequence); for $T_{1\rho}$ experiment, τ is the length of a spin-locking pulse; whereas for T_{1d} measurements it is the time distance between $\pi/4$ pulses (see Fig. 2–5).

For each value of t, the normalized magnetization (expressed as a function of τ) is presented on semilogarithmic plot. Then the superposition of straight lines is fitted, starting from the longest component. Each following component is fitted to the difference between the data and the best fitted superposition of longer components [523, 525]. Fitting yields $m \cdot N_{T1}$ values of the spin-lattice relaxation times, $T_{1,p,i}$, and m values of the component's magnitudes ($M_{p,i}$) at $\tau = 0$ for every magnetization component, where N_{T1} is the number of components with different T_1's. Subsequent averaging of $T_{1,p,i}$ over the range of t improves the accuracy of $T_{1,i}$. Magnitudes, $M_{p,i}$, expressed as a function of t form FID of i-th component. Their decomposition supplies spin-spin relaxation times, T_2^*, and magnitudes for every component. The normalized magnitudes define the apparent magnetization fractions of the spin-groups distinguished by values of the spin-lattice and spin-spin relaxation times, T_2^*.

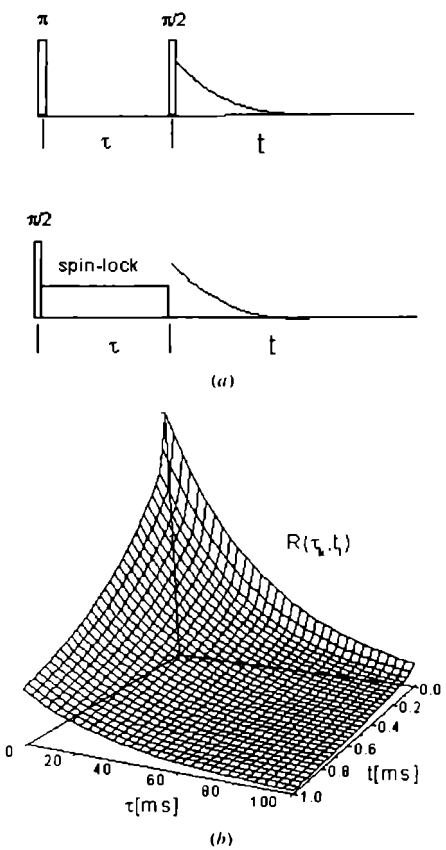

Fig. 2–5. (a) Pulse sequences for T_1 inversion recovery, and for $T_{1\rho}$ experiments. (b) The corresponding 2-d data matrix.

The spin-grouping approach was applied to resolve complex relaxation data [523, 526, 629]. However, user's arbitrary decisions undertaken during fitting might influence the results for data of poor quality. Moreover, if spin-groups are not differentiated in their spin-lattice relaxation times, they are not resolved.

2.2.3 Functions fitted to the relaxation data

The 2-d nuclear relaxation function R may be described by

$$R(\tau,\vec{a}_1,t,\vec{a}_2) = A_0 + \sum_{i=1}^{N_{T1}} \sum_{j=1}^{N_{T2}} R_{1,i}(\tau,\vec{a}_1) R_{2,i,j}(t,\vec{a}_2) \ , \qquad (2.65)$$

where: A_0 is a baseline level, R_1 and R_2 are spin-lattice and spin-spin relaxation functions respectively, $\vec{a}_1$, $\vec{a}_2$ are vectors of parameters (i.e. relaxation times and magnetization fractions). The functions R_1 and R_2, used to fit the spin-lattice relaxation functions or Carr-Purcell (CP) decay are defined as

$$R_1(\tau_q,\vec{a}) = \sum_{i=1}^{N_{T1}-N_{T1,SE}} A_i \cdot \exp\left(-\frac{\tau_q}{T_{1,i}}\right) + \sum_{j=1}^{N_{T1,SE}} B_j \cdot \exp\left(-\left(\frac{\tau_q}{T_{1,j}}\right)^{\alpha}\right) \qquad (2.66)$$

while for FIDs R_2 equals

$$R_2(t_p,\vec{a}) = \sum_{m=1}^{N_{Gauss}} C_m \cdot \exp\left(-\left(\frac{t_p}{T^*_{G,m}}\right)^2\right) + \\ + \sum_{i=1}^{N_{Exp}-N_{T2,SE}} A_i \cdot \exp\left(-\frac{t_p}{T^*_{2,i}}\right) + \sum_{j=1}^{N_{T2,SE}} B_j \cdot \exp\left(-\left(\frac{t_p}{T^*_{2,j}}\right)^{\alpha}\right) \ , \qquad (2.67)$$

where $N_{SE,T1}$ is a number of SE components of spin-lattice relaxation function, N_{Gauss} is a number of Gaussian components, and $N_{SE,T1}$ is the number of SE components in FID, whereas A_i, B_j, C_m are fractions of the signal with relaxation times T_{1i}, T_{1j}, (or T^*_{2i}, T^*_{2j}, T^*_{Gm}) respectively. In general, $N_{SE,T2}$ not necessarily equals $N_{SE,T1}$.

2.2.4 Non-linear least squares fitting

NMR experiment supplies Ndata = n·m values of sampling times t and τ, and equal number of values of nuclear magnetization M. The relaxation parameters are found by minimizing the sum of squares

$$S(\vec{a}) = \sum_{k=1}^{Ndata} \frac{\left(R(t_k,\vec{a}) - M_k\right)^2}{\sigma_k^2} \ , \qquad (2.68)$$

where $\vec{a}$ is a vector of parameters, $R(t_k,\vec{a})$ is a value of the fitted relaxation function, and σ_k is the standard deviation of the measured value M_k. The fitting

procedure, commonly Marquardt's algorithm [454, 546], varies the parameters $\vec{a}$ iteratively, until $S(\vec{a})$ reaches a minimum. If data errors σ_k are normally distributed, the minimum values of $S(\vec{a})$ are governed by a χ^2 distribution with ν = Ndata – Npar degrees of freedom, where Npar is the number of fitted parameters. For $\nu >> 1$ the expected value of the sum of squares in minimum is $\cong\nu$, and its standard deviation $\cong \sqrt{2\nu}$ [39].

2.2.5 The selection of sampling times

The quality of data depends on S/N and on the selection of sampling times. Although the increase in the number of acquisitions improves S/N, it is time-consuming. The proper selection of sampling points improves the quality of the fits not increasing total duration of experiment.

For single-exponential dependence the sampling points should gather at the beginning of the decay ($t_k \approx 0$), then close to the relaxation time ($t_k \approx T_n$), and at the end of the decay ($t_k >> 5T_n$), however, the results are weakly influenced by this [20]. An other selection (22% of data points at $t_k \approx 0$ and the rest at ~1.28 T_n) was suggested elsewhere [341].

For SE fits data points should be grouped near $t_k \approx 0$, 0.2÷0.4 T_n, 1.5÷2.5 T_n and >>5T_n [499].

In case of multi-exponential decay or continuous distribution of relaxation times, a choice of sampling points may alter the results of the analysis. To obtain the results closest the reality, a comparable number of data points should be collected for decay range of every component of the signal. However, if the components are not known *a priori*, time distances τ should be logarithmically spaced [84].

The values of the sampling times t (in FID measurements) usually are gathered in two or three groups with different spacing. The first group of points covers short-time component dominated by solid-like (approximately Gaussian) decay.

2.2.6 Selection of the best-fitted model

An effective test of the fit quality supplies the sum of squares in minimum, divided by number of degrees of freedom

$$\chi^2_N = \frac{S(\vec{a}_{min})}{\text{Ndata} - \text{Npar}} \quad . \tag{2.69}$$

The closer χ^2_N is to 1 the better is quality of the fit. Values significantly higher than 1 suggest a poor model. New parameters added to the model decrease the

value of χ^2_N, until the fitted function becomes overparametrized, when further addition of parameters no longer decrease χ^2_N (even may increase it), and the values of the estimated errors of the fitted parameters and non-zero cross terms of the covariance matrix are high [39].

The residual function, r_k, supplies additional hint on the fit quality

$$r_k = R(t_k, \vec{a}_{min}) - M_k \ , \tag{2.70}$$

where $R(t_k, \vec{a}_{min})$ are the values of fitted relaxation function. When the proposed function describes data properly, residuals versus time randomly distribute around zero. The systematic positive or negative deviation suggest the application of another model.

2.2.7 Computer program CracSpin

We proposed the following improvements of the spin-grouping method:

(i) The use of Marquardt's non-linear least squares fitting algorithm [454] providing user-independent results instead of the "line stripping" algorithm used in spin-grouping. A user can fix some parameters and select the appropriate range of data points for analysis, which may help for data partially distorted by spectrometer dead time or by B_0 inhomogeneity.

(ii) The the quality of the fit is tested by the residual function and the covariance matrix.

(iii) The 2-d procedure of CracSpin may initially proceed with the data analysis either in function of τ, (as in spin-grouping) or in function of t. The second approach is used, if the spin-lattice relaxation times for several spin-groups are similar, whereas the T_2's significantly differ.

This was realized in CracSpin program performing either 1-d or 2-d analysis of the relaxation function [703].

Although, for the SE function the parameter α varies between 0 and 1, CracSpin allows the values of α in the range between 1 and 2, as for Weibullian function, being intermediate between an exponential and Gaussian, and used to characterize FIDs in solid polymers [377].

The relaxation time for Gaussian component is defined, as the time at which signal decreases to 1/e of its initial value, as for exponential and for SE function [see Eq. (2.67)]. The second moment, M_2, which is commonly used to characterize the solid FID, equals here $2 \cdot T_2^{-2}$. The value defined as a halfwidth of the Gaussian line may be calculated by dividing by $\sqrt{\ln 2}$. Fukushima, [219], also suggests the 1/e value of complicated FIDs as a convenient measure of the decay time.

2.2.7.1 One-dimensional data analysis

CracSpin performs 2-d data analyses by analyzing 1-d cross-sections of relaxation matrix. Therefore the 1-d analyses were tested using the simulated data resembling the multiexponential relaxation function observed in hydrated bark [290]. Similar approach (two or three exponential decays, non-linear least squares fitting) was presented elsewhere [122].

In presented tests, the effect of fitted baseline, the resolution of two components with close values of the relaxation times, and the resolution of minor component with long relaxation time are discussed.

Tested FIDs consisted of Gaussian component ($T_G^* = 20$ μs) and three exponential components: short one ($T_2^* = 100$ μs), long one ($T_2^* = 2500$ μs; and the intermediate one with T_2^* changed in the range from 200 μs to 1600 μs (100 μs step). Gaussian and middle exponential made up from ~60 to 90% of total magnetization, in the aim to test the resolution of minor components, i.e. magnetization fraction below 10% of the total signal.

A random noise (normal distribution, S/N ranging from 4 to 1024) was added, covering S/N range encountered in NMR measurements. The noise level was defined as equal to the three standard deviations of the normal distribution. Each decay consisted of 120 points, grouped in two equal subsets (60 points equally spaced), and began at 10 μs (the dead time of the spectrometer). The sampling range covered the times for which the signal amplitude exceeded ~1% of initial amplitude.

2.2.7.1.1 Effect of S/N and overparametrization of model

In tests reported here, fitted functions consisted of Gaussian and the increased number of exponents. The baseline was either fixed or fitted. For comparison, the SE function was fitted to each data set.

CracSpin fits of the 4–component to four-component FID (the relaxation times: 20 μs, 100 μs, 400 μs, 2.5 ms; and component's fractions: 0.658, 0.066, 0.263, 0.013, respectively), as a function of S/N, shows that the quality and the stability of fits significantly depend on the S/N and the value of the component fraction. The major, Gaussian component is well fitted for all S/N. The relaxation time and the component fraction of intermediate exponential are fitted acceptably even for S/N < 10. The short exponential (100 μs, 6.6%) is resolved for similar range of S/N, however for S/N < 32 the estimated errors of the fitted parameters may exceed 100%. The long exponential (2500 ms, 1.3%) is resolved within estimated errors for S/N ≥ 64. If S/N varies between 16 and 64 the longest component is still resolved, but the errors of the parameters are large. For S/N < 16 only three components are found, with relaxation times corresponding roughly to the real valuses of the three major components.

Table 2–2. The χ^2_N values for different n-component models fitted to 4-component (Gauss + 3 exponents) relaxation function, versus S/N.

S/N	n = 5	n = 4	n = 3	n = 2	n = 2 + SE
4	–	0,959	1,019	1,093	1,033
8	–	1,141	1,211	1,254	1,225
16	0.966	0,969	1,028	1,181	1,029
32	0.959	0,938	1,036	2,026	1,079
64	1.185	1,165	1,379	3,958	1,316
128	1.001	0,985	1,964	14,824	2,468
256	1.125	1,104	4,106	46,954	5,594
512	1.041	1,021	13,378	181,052	17,579
1024	0.957	0,959	49,215	721,080	69,712

χ^2_N smoothly decreases to about 1 (for 4-component model) with increasing number of fitted parameters (Tab. 2–2). The range of the changes depends on S/N.

According to Brown, [84], for confident distinguishing between 3 and 4 component models, for such a data set (120 data points, 8 fitted parameters), the difference in χ^2_N values should be at least ~20%, which is here fulfilled for S/N ≥ 64. For S/N = 128, the ratio of χ^2_N for 3– and 4–component model is ~2, while for S/N = 256 equals ~4.

To observe the overparametrization effect, the values of χ^2_N for 5–component fit (Gaussian + 4 exponentials) are calculated. The overparametrization manifests in mostly value χ^2_N higher than that for a 4–component fit, except few cases where χ^2_N is no more than 0.3% lower (S/N = 16).

The 3–component fit does not describe data properly for S/N > ~60. For S/N = 32 and 16 the comparison of the χ^2_N values for 3, 4 and 5 components fits still suggests that the 4–component model is the most probable. However, the relative differences between χ^2_N of 3– and 4–component models are smaller than 10% and only the comparison with results for the 5–component model leads to choosing the 4–component one as the most reasonable. For S/N < 16 the procedure failed to find a minimum of χ^2_N for the 5–component model.

2.2.7.1.2 Effect of baseline and sampling range

Non-zero baseline is the equipment effect and thus can be eliminated by proper experimental setup. If not corrected during experiments, non-zero baseline alters fits.

For fixed baseline, minimal S/N necessary to obtain satisfactory fits may be up to 6 to 8 times lower (~50 times shorter experimental time) than if baseline is fitted. The difference in fit quality between fitted and fixed baseline is most pronounced for longest component (T_2 = 2.5 ms) and minor amplitude, while for

the Gaussian component it is negligible. This is because the sampling range (3 ms) only slightly exceeds the longest T_2, although it covers the signal decrease below ~1% of the initial amplitude. Increase in sampling range is sole way to decrease the distortion of fits with fitted baseline. The increase in the sampling range from 3 ms to 6 ms significantly improves the fits for fitted baseline.

Quality of fit and stability of obtained parameters strongly depend on S/N and relation between the values of the relaxation times. A proper (fixed) value of the baseline in most cases significantly improves fits. The comparison of the results with a fixed and a fitted baseline gives hint to selection of a proper model.

2.2.7.1.3 Resolution limits for time constants

It is thought that in multiexponential decay the resolution of components differentiated in time constants by factor of less then ~3 is not possible [122]. However, in some cases CracSpin resolves the components with the relaxation times different by less than factor 3.

Fig. 2–6 shows the results of the 4–component fit (Gaussian + 3 exponents) to data for which the relaxation time of intermediate exponent (200 μs) was only two times longer than that for short component (100 μs). For S/N > 100, all components are unambiguously resolved within estimated errors. For 100 > S/N > 20 the components are resolved, but ranges of parameter errors overlap, which may hinder the identification of components. For S/N < 20, the fitting of a 4–component model is not successful. The fitting procedure indicated overparametrization, and/or estimated errors of the fitted parameters overlapped in broad range. Only the Gaussian component was fitted with satisfactory accuracy. The values of χ^2_N and the residual function suggest that the 4–component model is preferred for S/N > ~20. However, the errors of the fitted parameters overlap for some components at S/N < ~100. For lower S/N, 3–component fit is more stable, but the results diverge from the real values, except for the Gaussian component.

To test the case of two relaxation times close to the upper limit of sampling range, T_2^* of intermediate exponent was set to 1600 μs, similarly to the value for long component (2500 μs). The sum of the relative fractions of two close components was kept constant (56.6%), while the relative fraction of the long exponential was set to 30%, 15%, 10%, 5% and 1%. The sampling range was 3 ms, then 6 ms, and finally 9 ms. For S/N > ~60 two close components are resolved, while for lower S/N only one average component is fitted. This result does not depend on the sampling range, for the relative fraction of the long component at least 5%. The long exponential with relative fraction equal to 1% is not detected. The differences of the fitted parameters from the real values for two resolved components depend on S/N, on the component relative fractions, and on the sampling range. Decrease in the real contribution of the long component from 30% to 5% decreases the fitted values of the relaxation times of both components. The longer component is more affected, and the contributions of components tend to equalize (Fig. 2–7).

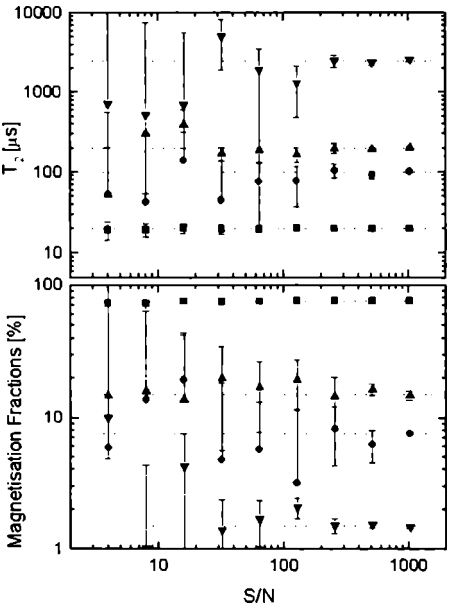

Fig. 2–6. The results of the fitting of the four–component model to a four–component FID as a function of S/N in case of relaxation time ratio ~2. The dotted lines correspond to the true values of the relaxation times (i.e. 20 μs, 100 μs, 200 μs, 2.5 ms) and component's fractions (i.e. 0.758, 0.076, 0.151, 0.015).

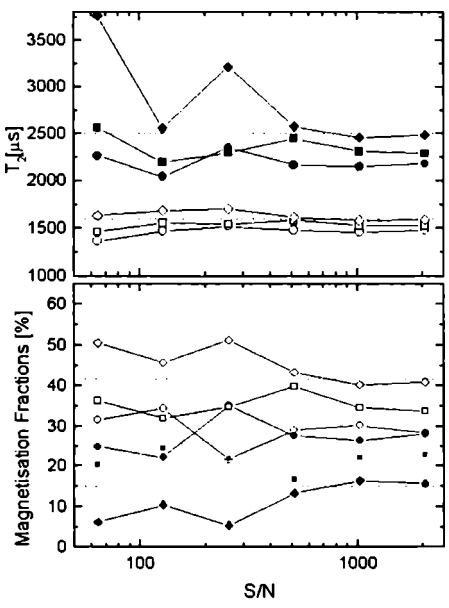

Fig. 2–7. The fitted values of the relaxation times and component's fractions of the two components with close values of the relaxation times (1.6 ms and 2.5 ms) as a function of S/N and sampling range for 15% contribution of the long exponential. The four–component model is fitted to the data with true values of the relaxation times equal to 20 μs, 100 μs, 1.6 ms, 2.5 ms. The dotted lines correspond to the true values of the parameters.

The < 10% difference of the fitted values of the relative fractions from the real ones occurs for the S/N > ~500. Moreover to get the longest T_2 within 10%–difference, the sampling range of 9 ms, 6 ms and 3 ms is required for the component fraction equal 10%, 15% and 30%, respectively. The sampling range of 9 ms and 6 ms enables to fit the relative fraction of the longest component equal to at least 15% and 30% within 10% difference. A smaller fraction of the long component (2500 μs) is detectable even for S/N < 100, but the values of the fitted parameters are biased.

To summarize, at component fractions ≥ 10% of the total signal and S/N ≥ 100 CracSpin may resolve the FID components with the ratio of the relaxation times equal 2 or even less. If the ratio of component relaxation times is higher then ~3, satisfactory decomposition is possible for S/N > 10, even if component abundance is about 1%. The algorithm fails for the ratio of relaxation times less than 2 and difference in relative abundance exceeding one order of magnitude.

2.2.7.2 Two dimensional data analysis

In some cases Cracspin enables a resolution of the spin groups with similar relaxation times. This is for the spin groups having similar spin-lattice relaxation times, but differ in values of the spin-spin relaxation time (or *vice versa*). CracSpin analysis may start with T_1 decomposition or with T_2 decomposition. To test both approaches the analyzed data consisted of a matrix of 50·50 sampling points. S/N was set to 128. First, the relaxation function was a superposition of three components with different T_1's. Two of them consisted of two sub-components with different T_2's. The total FID consisted of four spin groups (Tab. 2–3).

Table 2–3. True and fitted (in parentheses) values of the parameters used in simulated 2-d relaxation data in the case of 3–component recovery function and 4–component FID.

T_1 [ms]	T_2^* [μs]	Amp[%]
4	800	5
(4.1±0.1)	(824±36)	(5.08± 0.25)
30	20	30
(30.4±0.8)	(20.1±0.6)	(30.6±1.6)
	300	25
	(293±21)	(25.3±1.8)
100	20	30
(102.5±2.7)	(19.9±0.7)	(29.3±2.1)
	110	10
	(107±10)	(9.7±0.9)

For 2–component model of the magnetization recovery function, fitted parameters depend on t, while for the 3–component model they do not, giving an additional hint to estimate the reliability of the fitted model. Relative errors of the parameters are < 3%.

For three resolved components, all component fractions as well as relaxation times fit well. Errors of fitted parameters are < 4% (see Tab. 2–3). For comparison, the 1-d decomposition of the total FID resolves all components, but relative errors of some parameters exceed 50%.

If the investigated system has less T_2 components than T_1 components, or if the T_1 values for different components are so close that they are not clearly resolved by the analysis of the recovery function (τ dependence), the decomposition of the FID should be used. Tab. 2–4 shows fits for a recovery function containing five components. Two of them have spin-lattice poorly separated relaxation times, i.e. 140 ms and 150 ms. The next one has a relaxation time equal to 70 ms. Proper T_2 decomposition of this data is easy to perform. 3–component results are τ–independent. The analysis of the reconstructed recovery functions leads to parameters matching the true values (Tab. 2–4). Relative errors do not exceed ~8% but are much lower for most of the parameters.

Table 2–4. True and fitted (in parentheses) values of the parameters used in simulated 2-d relaxation data in the case of 5-component recovery function and 3-component FID.

T_1 [ms]	T_2^* [μs]	Amp[%]
10	1000	10
(9.8±0.4)	(1014±18)	(9.8±0.4)
70	20	10
(68.1±5.8)	(19.9±0.2)	(10.0±0.5)
	300	10
	(305±11)	(9.5±0.9)
140	1000	15
(139±4)	(1014±18)	(14.6±0.6)
150	20	15
(150±11)	(19.9±0.2)	(15.3±1.2)
	300	15
	(305±11)	(16.1±1.5)
500	20	25
(504±17)	(19.9±0.2)	(24.8±3.0)

In contrast, the analysis starting from the recovery function (τ dependence) is more composed. In 3–component model, T_1 depends on t. The T_1 value for the middle component, as estimated for short t values ("solid region"), is shorter than that estimated from the region with t > ~50 μs ("liquid region"). This indicates that the recovery function contains the unresolved components with different T_2^*'s. The use of 4–component model gives T_1 values of 9.9 ms, 71 ms, 143 ms and 535 ms, which are not very far from the true values (Fig. 2–8, Tab. 2–4). However, it is not possible to resolve the components with T_1 equal to 140 ms and 150 ms, and only the average value is obtained.

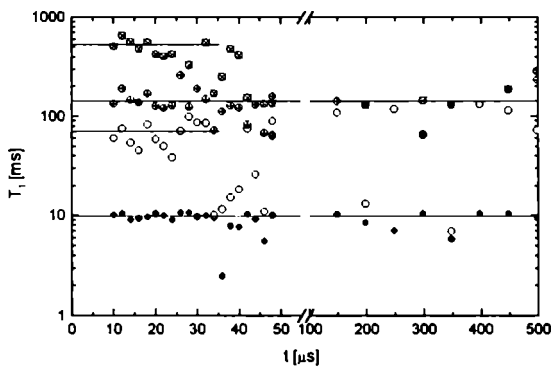

Fig. 2–8. The fitted values of the spin-lattice relaxation time (4–component model) as a function of t (position of the data point on the FID) for the same data set as shown in Tab. 2–4.

To summarize, the tests of 2-d analysis show the advantage of the correlated decomposition, especially in case of numerous components or close values of the relaxation times. The resolution is enhanced if decomposition is started from the cross-section of the 2-d relaxation data containing less components or with the component relaxation times better separated.

2.3 Multiexponential or SE relaxation function in pores of dry biological system?

In many cases, either SE function (Eq. 2.58) or multiexponential one successfully fit NMR relaxation data. In fact, there is no free choice of the form of a fitted function, as relaxation function reflects the physical properties of the system. This difficulty should be overcome, at least because proton magnetic relaxation is widely applied to evaluate the several parameters of porous system.

2.3.1 Analysis of simulated data

CracSpin effectiveness in fitting of SE function was tested on the superposition of Gaussian ($T_G^* = 20$ μs, intensity equal 62.5% of total) and SE function ($T_{SE}^* = 800$ μs, intensity 37.5%, and $\alpha = 0.8$) was fitted. The SE and multiexponential fits are compared.

For the whole range of S/N, the relaxation times, relative fractions, and α values of the fitted superposition of Gaussian and SE are estimated properly (Fig. 2–9).

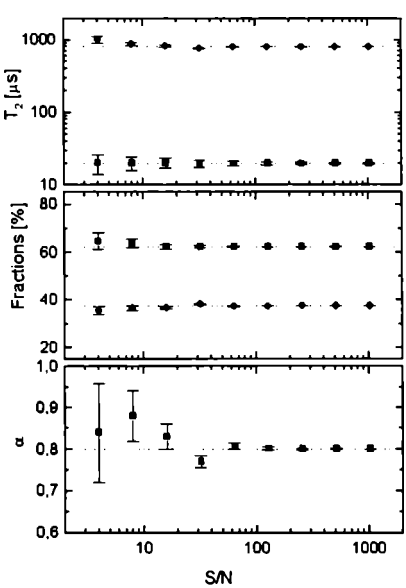

Fig. 2–9. The results of the fitting of the 2–component model (Gauss+SE) to the simulated FID being a superposition of Gaussian (amplitude = 0.625, $T_G^* = 20$ μs) and SE (0.375, $T_{SE}^* = 800$ μs, $\alpha = 0.8$) versus S/N.

Residual function and χ^2_N show that for S/N > 16 the model with Gaussian and SE functions describes data better than the combination of Gaussian and single exponential, however for S/N < 16 none of the models is preferred.

For S/N $\geq$ 64, the superposition of Gaussian with SE describes data better than Gaussian with two exponents, whereas for S/N $\geq$ 512 it gives better fit than Gaussian with 3 exponents (Tab. 2–5).

Table 2–5. The χ^2_N values for n-exponential models fitted to 2-component (Gauss + SE) relaxation function, versus S/N.

S/N	True: Gauss+SE	n = 4	n = 3	n = 2
4	1,055	1,033	1,035	1,060
8	1,229	1,233	1,211	1,247
16	1,027	1,017	1,021	1,323
32	0,927	0,940	0,986	2,968
64	1,151	1,155	1,235	6,568
128	0,933	0,954	1,185	24,866
256	1,077	1,095	2,031	91,813
512	1,000	1,120	5,064	355,495
1024	0,954	1,544	16,385	1417,3

The number of fitted parameters for single SE function equals 3 (time constant, abundance and parameter α) in comparison to 2, 4 or 6 for single, double and triple exponentials, respectively. Thus, for similar χ^2_N values, the models with 2 or 3 exponents may be eliminated, as they need more free parameters.

2.3.2 SE versus multiexponential fits of data for porous rocks

This Author compared the effectiveness of SE fits with multiexponential ones decomposing relaxation functions of liquid fraction filling the pores of rock. Two oil-containing porous rocks with different pore distributions were used as models: the Węglowicki sandstone and the limestone (Ca_2).

The samples were characterized by low S/N due to low content of hydrocarbons in pores, e.g. total content of hydrocarbons in oil-containing limestone varied from 7.8 mg to 10 mg HC/g rock, with (67.1±0.6)% contribution of mobile hydrocarbon fraction and with (32.9±0.6)% contribution of resident hydrocarbons [292]. The proportion of mobile-to-resident hydrocarbon fraction may vary within the core.

Proton FID for hydrocarbons trapped in pores of Węglowicki sandstone and in limestone is described by a superposition of solid fraction (Gaussian with the T_2^* value defined as a time needed for the signal to relax to the 1/e of its initial magnitude) and mobile liquid fraction (exponential component). Meaningful contribution of

Gaussian component ("1") comes from the solid hydrocarbons present in porous rock, ie. mineral wax, as well as from OH groups and crystallization water trapped in pores of mineral matrix. The fitted values of T_2^* are shown in Tab. 2–6a.

Table 2–6. Proton FIDs for Węglowicki sandstone (a) and for limestone (b) recorded at room temperature. For limestone samples the intermediate component ("2") was fitted as Gaussian, however, the exponential fit did not differ very much in amplitude and the time constant. The amplitudes A_i are normalized to the total amplitude of the signal.

(a)	Component "1"		Component "2"	
Sample	A_1	T_2^* [μs]	A_2	T_2^* [μs]
„wc1"	31.7%	24.26	69.3%	100.0
„wc2"	30.5%	28.84	69.5%	119.4
„wc3"	60.2%	24.02	39.8%	88.6

(b)	Component "1"		Component "2"		Component "3"	
Sample	A_1	T_2^* [μs]	A_2	T_2^* [μs]	A_3	T_2^* [μs]
'71'	55.0%	15.3	29.4%	55.6	15.5%	297
'72'	60.4%	14.3	28.9%	30.22	16.6%	163

FID signal from oil-containing limestone (Fig. 2–10) reveals beside the Gaussian component coming from the solid fraction and the exponentially decaying signal from the mobile liquid fraction, also an intermediate signal, which may be fitted either by very broad Gaussian or by an exponent. The obtained fits of T_2^* and amplitude values are shown in Tab. 2–6b. As in sandstone, the solid signal may come from solid hydrocarbons, i.e. mineral wax, or from OH groups and crystallization water trapped in pores or protons bound inside rocky matrix of limestone. The "intermediate" signal fraction ($T_2^* \cong 45$ μs) most likely comes from the solid protons.

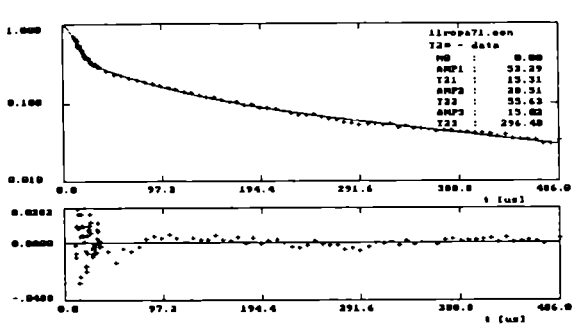

Fig. 2–10. Proton FID for oil-containing limestone, sample '71' (+) recorded at 30 MHz. Transmitter power was 400 W; pulse lengths π/2=3.4 μs, repetition time 5 s; data averaged over 2000 accumulations; t = 25°C, stabilized in a gaseous nitrogen stream. The superposition of Gaussian, "intermediate" component (Gaussian) and single exponent is fitted (solid line) using the program CracSpin [703]. The residual function is presented on lower plot.

Although proton high power FIDs record the total proton signal, B_0 field inhomogeneities (for water $T_2^* \cong 12$ ms) cause that proper fit of mobile liquid components is not possible [663]. The measured T_2^* is given by:

$$\frac{1}{T_2^*} = \frac{1}{T_2} + \frac{\gamma \Delta B_0}{2}, \tag{2.71}$$

where the contribution of B_0 inhomogeneities overwhelms the observed effect for the components relaxing with long T_2.

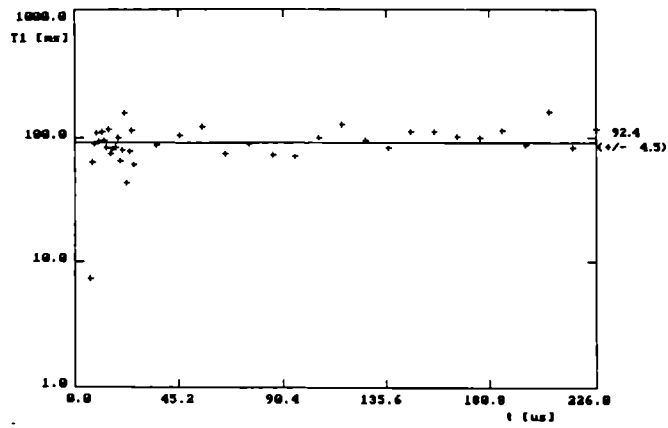

Fig. 2–11. Proton spin-lattice relaxation times for limestone sample '71' calculated as a function of time t for FID signal. The saturation method was applied ($\pi/2$ — τ — $\pi/2$ — FID(t)); resonance frequency was 30 MHz; transmitter power 400 W; pulse lengths $\pi/2$=3.4 μs, repetition time 5 s; data averaged over 400 accumulations; t = 25°C, stabilized in a gaseous nitrogen stream. Fits were obtained using the spin-grouping program CracSpin [703].

Table 2–7. Proton spin-lattice relaxation times measured for oil-containing limestone. Decreased number of accumulations per FID (400) excluded the detailed analysis of FID (see Tab. 2–6b) Tab. 2–7a shows the single-exponential fits; Tab. 2–7b fits of SE function.

Tab. 2–7a	T_1 [ms]	A_1	T_2^* [μs]	A_2	T_2^* [μs]
Sample 71	92.4	70.9%	12.9	29.1%	92.4
Sample 72	186.4	79.3%	17.2	20.7%	186.4

Tab. 2–7b	α	T_{SE} [ms]	A_1^{SE}	T_2^* [μs]	A_2^{SE}	T_2^* [μs]
Sample 71	0.90	88.8	70.9%	12.9	29.1%	145
Sample 72	0.90	214	79.4%	17.4	20.6%	114

Proton magnetization recovery for limestone samples was well fitted by single exponential function. (Fig. 2–11; fitted parameters in Tab. 2–7a). Also the SE function (Eq. 2.58) was fitted to these data (Tab. 2–7b). Either the values of T_1, T_2^* or the amplitude values are close to the ones fitted using single exponential fits.

The fractal exponent α is close to 1. Similar value was observed for water in controlled pore glasses, reflecting the narrow distribution of pore sizes and the narrow range of the system self-similarity [117, 630]. Single exponential proton magnetization recovery for oil-containing limestone suggests the presence of fast proton exchange between the pores or the narrow distribution of relaxation times for protons in isolated pores of similar size.

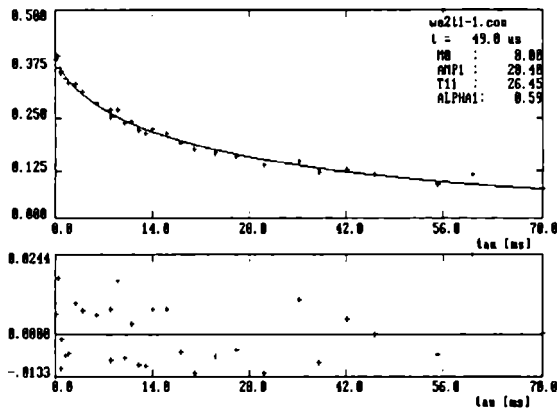

Fig. 2–12. The normalized proton spin-lattice relaxation for Węglowicki sandstone sample 'wc2' (+) recorded at t = 49 μs after π/2 pulse. The saturation method was applied (π/2 — τ — π/2 — FID(t)); resonance frequency was 30 MHz; transmitter power 400 W; pulse lengths π/2=1.2 μs, repetition time 5 s; data averaged over 400 accumulations; t = 25°C, stabilized in a gaseous nitrogen stream. Fits were obtained using the spin-grouping program CracSpin [703]. The SE function (solid line) was fitted to the data. The lower plot shows the residual function.

Magnetization recovery function for Węglowicki sandstone is fitted neither by single exponential function nor by double exponential. Fig. 2–12 shows proton magnetization recovery for Węglowicki sandstone (sample 'wc2') recorded at t = 49 μs after π/2 pulse and fitted using SE function. SE dependency fits well the spin-lattice relaxation function. The fractal exponents α versus time t is shown on Fig. 2–13, whereas the Tab. 2–8 presents the obtained averaged values of α and t. Fitting of MSE (Eq. 2.60) [530] to Węglowicki sandstone proton relaxation functions yields the values of parameters similar to obtained from SE fit (see Chpt. 2.2.1).

Table 2–8. Proton spin-lattice relaxation times T_1 measured for Węglowicki sandstone. In our system, the inversion recovery method requires that the circuit of shortening the spectrometer dead time is not used. Thus, the artificial broadening and the increase in magnitude of fitted Gaussian function was observed.

α	T_1 [ms]	A_1^{SE}	T_2^* [μs]	A_2^{SE}	T_2^* [μs]
0.61±0.02	37.6±4.5	49.5%	33.5	50.5%	138.1

The obtained value of fractal exponent significantly differs from 1 and is $\alpha = (0.61 \pm 0.01)$ for times $t > 30$ μs, whereas for shorter times t $\alpha = (0.51 \pm 0.01)$, which is the effect observed in presence of broad distribution of pores of oil-containing rock. The differentiation of mobile and immobilized liquid fraction should be understand not as a signal coming from two well defined groups of pores but coming from different spin subsystems from every given pore.

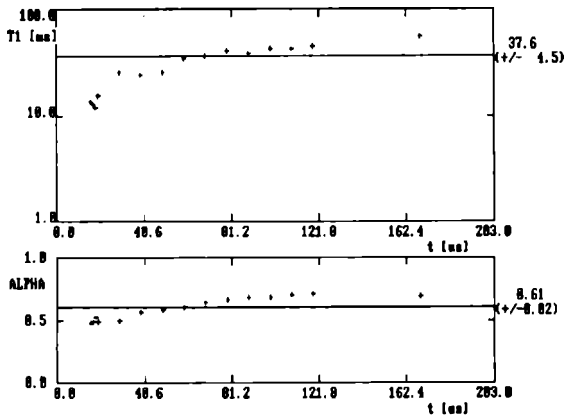

Fig. 2–13. The fitted values of relaxation times T_1 and fractal exponent α of the SE function fitted to the proton spin-lattice relaxation function for Węglowicki sandstone, sample 'we2', expressed as a function of the time t after $\pi/2$ pulse. The saturation method was applied ($\pi/2$ — τ — $\pi/2$ — FID(t)); resonance frequency was 30 MHz; transmitter power 400 W; pulse lengths $\pi/2$=1.2 μs, repetition time 5 s; data averaged over 400 accumulations; t = 25°C, stabilized in a gaseous nitrogen stream. Fits were obtained using the spin-grouping program CracSpin [703].

CracSpin yields either multiexponential or SE fits. This allows one, with high dose of credibility, to recognize the real form of relaxation function. In case of Węglowicki sandstone, high quality of fits clearly suggests that the proton spin-lattice relaxation function is in SE form, whereas for oil-containing limestone it was well described by a single exponential function.

2.4 Paramagnetic ion behavior in wet porous silica glass

Paramagnetic ions are present in biological systems. They play significant role in numerous biochemical reactions, e.g. in photosynthetic water splitting and in oxygen evolution [379, 380]. The content of manganese in photosynthetic lamellae of spinach equals 5.3 M of Mn/400 M of chlorophyll [47], and in wheat 9 M of Mn/400 M of chlorophyll [536], which is a low value in absolute numbers. However, the lack of manganese ions in thylakoid membrane inhibits the light reaction of photosynthesis (first reported in [538]). Moreover, manganese cannot

be replaced by cobalt, iron, magnesium, and zinc in concentrations equal to, or even almost one order of magnitude higher than that needed for the optimal level of the photosynthetic oxygen evolution [115].

The presence of electron paramagnetics enormously enhances the dipolar relaxation of proton because the electron gyromagnetic ratio is three orders of magnitude greater than gyromagnetic ratio of proton (Eq. 2.19). In case of photosynthetic membranes, paramagnetic effect overwhelms proton relaxation [54, 56, 254, 288, 381, 568, 569, 570, 609, 716, 717]. By decreasing the hydration level of the system, the concentration of paramagnetic ions increases, and the paramagnetic relaxation may dominate the relaxation processes. Thus, their effect should be analyzed prior to molecular dynamics considerations.

This Author analyzed the effect of the paramagnetic ions present in channels of controlled pore glasses (CPG), which due to their high S/V (Tab. 1–1) and their natural paramagnetic ion contamination [242], well model a low-concentration ion behavior in aqueous medium placed in small compartments [117, 630]. Borosilicate glass forms solid porous structure, no effects of aggregation occur (as for glass beads), thus, only the effects of limited pore size influence bound water behavior.

Relaxation measurements of a liquid filling the pore space of porous silica glasses supplies the information on pore internal geometry [170, 243, 264, 591]. Furthermore, the effect of restricted geometries, well defined for CPGs, has been studied by NMR measurements of diffusion coefficient of an aqueous fraction filling pore channels [218, 374]. The porosity of these systems gives them increased tortuousity, therefore lowering the effective diffusion. Also the surface chemistry of silica and the adsorption of water molecules to the surface of porous silica glass were observed by NMR [23, 77, 180, 199, 393]. Paramagnetic ions reveal affinity for the surface of CPG. Furthermore, CPG act as an ion exchanger for organic and inorganic cations [479, 480].

It is generally assumed that water relaxation in porous system (and in porous glass) can be described by a two-site model involving a free solvent and a water bound on the pore surface with an increased correlation time [4, 87, 169, 170, 243, 264, 270, 394, 591, 637, 638, 664]. These two phases are in fast exchange with each other and as the result, the observed relaxation becoming a function of the S/V of the pore.

Given a pore with surface area S, containing a volume V of water one can consider the water as exchanging between the bound water, which is confined to a surface layer of thickness λ, and a fraction of free, bulk water in the volume. The observed relaxation rate can then be expressed as [729]

$$R = R_0\left(1 - \frac{\lambda S}{V}\right) + R_S\left(\frac{\lambda S}{V}\right), \tag{2.72}$$

where R_0 is the relaxation rate of free water depending on water purity (in reported case water was deoxigenated, $R_0 = (0.39 \pm 0.3)\ s^{-1}$), and R_S is the relaxation rate of

protons bound in the surface layer due to the moderation of water by the silica surface, R is the average relaxation rate of water in pores.

Under the following assumptions one can now introduce relaxation due to paramagnetic ions in the low concentration limit:

(i) the concentration of paramagnetic ions dissolved in the volume of a pore remains constant over a range of hydration;

(ii) the paramagnetic ions on the pore surface can be approximated as acting within a layer of thickness D with an equivalent rate of relaxation; and

(iii) the surface ions are evenly distributed on a plane Euclidean surface.

In this model, there are three regions with distinct relaxation rates: (I) a bulk region in which proton relaxation occurs due to dipolar interactions as in free water, as well as due to paramagnetic ions dissolved in the volume, (II) a region with additional relaxation due to the influence of surface paramagnetics, within a layer of thickness D and (III) the bound water surface layer with further relaxation due to water moderation on the glass surface. The relaxation rate becomes

$$R = \left(1 - D\frac{S}{V}\right)R_I + \left((D-\lambda)\frac{S}{V}\right)R_{II} + \left(\lambda\frac{S}{V}\right)R_{III} , \tag{2.73}$$

where R_I , R_{II} , and R_{III} are relaxation rates in layers I, II, and III, respectively. Explicitly, one can write

$$R_I = R_0 + \frac{N^{pv}}{V}A , \tag{2.74a}$$

$$R_{II} = R_0 + \frac{N^{pv}}{V}A + \frac{N^{ps}}{S}B , \tag{2.74b}$$

$$R_{III} = R_S + \frac{N^{pv}}{V}A + \frac{N^{ps}}{S}B , \tag{2.74c}$$

where N^{pv}/V and N^{ps}/S are, respectively, the number of paramagnetic ions dissolved in the pore water and the number of ions bound on the pore surface; while A and B are, respectively, the relaxation rate per number concentration in a volume and on a surface. For the purposes of this model, A and B are constant for a particular ionic species at constant temperature. The effective surface area S is taken to be constant – so long there is enough water, all surface will be wetted (complete wetting case).

By assumption (1) above, N^{pv}/V is a constant c^{pv}. The total number of paramagnetic ions within a pore, N^{pt}, remains constant, thus, $N^{ps} = N^{pt} - N^{pv}$ and Eq. (2.73) can be written

$$R = \left[R_0 + c^{pv}\cdot(A - DB)\right] + \left[(R - R_0)\frac{\lambda S}{V_0} + \frac{N^{pt}}{V_0}BD\right]\cdot\left(\frac{V_0}{V}\right) . \tag{2.75a}$$

Here, V_0 is the volume of the pore; thus, V/V_0 is a measure of the hydration level; expressed as the amount of water scaled to the volume of a particular pore, allowing comparison between samples of different pore size. Note that Eq. (2.75a) also gives the relaxation rate in a sample containing identical pores if all the extensive parameters refer to the entire sample instead of one pore. V_0, therefore, becomes the total pore volume and V describes the total volume of water present in the sample.

Up to here, it was taken that $D > \lambda$, however, this constraint is immaterial. For Eq. (2.75a) is the same for D greater than or equal to λ. If we simplify the above situation and assume that only the surface layer is affected by surface paramagnetics ($D = \lambda$) and the paramagnetic ions dissolved in the volume not enter the surface layer, then Eq. (2.75a) simplifies to

$$R = \left[R_0 + c^{pv}\cdot(A - \lambda B)\right] + \left[\left(R - R_0 - c^{pv}A\right)\frac{\lambda S}{V_0} + \frac{N^{pt}}{V_0}B\lambda\right]\cdot\left(\frac{V_0}{V}\right), \quad (2.75b)$$

which differs from Eq. (2.75a) only by a constant term in the slope. The interpretation of data through this simplified model parallels that for Eq. (2.75a), and the conclusions are identical for either model. For convenience, only Eq. (2.75b) will be discussed.

Note that if, in contrast with the assumption of constant volume concentration, one assumes that all the paramagnetic ions are dissolved in the volume, one obtains

$$R = R_0 + \left[\left(R_s - R_0\right)\frac{\lambda S}{V_0} + A\frac{N^{pt}}{V_0}\right]\cdot\left(\frac{V_0}{V}\right). \quad (2.75c)$$

Or, assuming all ions are bound on the pore surface, one obtains

$$R = R_0 + \left[\left(R_s - R_0\right)\frac{\lambda S}{V_0} + \frac{N^{pt}\cdot B}{V_0}(D - \lambda)\right]\cdot\left(\frac{V_0}{V}\right). \quad (2.75d)$$

Assuming some combination of a constant number of ions dissolved in the volume and on the surface, one gets

$$R = R_0 + \left[\left(R_s - R_0\right)\frac{\lambda S}{V_0} + \frac{N^{ps}}{V_0}BD + A\frac{N^{pv}}{V_0}\right]\cdot\left(\frac{V_0}{V}\right). \quad (2.75e)$$

If one now considers relaxation in the entire sample, the additional possibility arises that in the case of high hydration level, V exceeds V_0. In this instance the amount of water outside the pore channels may become significant. This case can be modelled by introducing the two additional assumptions:
(a) the paramagnetic ions do not diffuse outside the pore channels; and

(b) if V does not greatly exceed V_0, since the CPG grains are of typical dimension ~70 μm, the water outside the glass grains remains in fast exchange (on the time scale of the spin-lattice relaxation time) with the water inside the pores. This is equivalent to saying that the dimension of the diffusion cell is on the order of glass grain size (~50 μm).

The relaxation rate can then be expressed as:

$$R = \left(1 - \frac{V_0}{V}\right) \cdot R_0 + \frac{V_0}{V} \cdot R_p \,, \tag{2.76}$$

where R_p is the relaxation rate within the pore channels, as given by Eq. (2.75a) or (2.75b). Substituting Eq. (2.75a) for R_p one obtains

$$R = R_0 + \left[c^{pv} \cdot (A - DB) + (R_s - R_0)\frac{\lambda S}{V_0} + \frac{N^{pt}}{V_0} BD \right] \cdot \left(\frac{V_0}{V}\right) . \tag{2.77}$$

At low values of V/V_0, the discrete site approximation for the surface paramagnetic effect in Eq. (2.77) does fail and the nonexponential relaxation of proton magnetization becomes visible (see Chpt. 1.13.4).

As the ion concentration of paramagnetic ion is low, its adsorption, and especially a constant concentration regime can be predicted from the low pressure limit of Langmuir adsorption isotherm ([420], see also Chpt. 3.4)

$$\theta = \frac{b(T)p}{1 + b(T)p} \,, \tag{2.78}$$

where p is the pressure, θ is the ratio of the surface coverage of the adsorbate to full monolayer surface coverage, and b is some function of the temperature T. Eq. (2.78) can be applied to the adsorption of ions on the surface of silica by letting θ be proportional to the surface concentration of ions N^{ps}/S, and the pressure with the volume concentration of ions N^{pv}/V (at constant temperature). One can absorb these proportionality constants into b(T), redefining it to be $b_p(T)$, and Eq. (2.78) becomes

$$\frac{N^{ps}}{(S/\sigma_0)} = \frac{b_p(T) \cdot \left(N^{pv}/V\right)}{1 + b_p(T) \cdot \left(N^{pv}/V\right)} \,, \tag{2.79}$$

where σ_0 is the area needed for one ion to bind to the surface. From Eq. (2.79) one gets in the low pressure limit at constant temperature

$$\frac{N^{ps}}{(S/\sigma_0)} = b_p\left(N^{pv}/V\right) \,. \tag{2.80}$$

If one solves Eq. (2.80) for the volume concentration

$$N^{pv}/V = \left[\frac{N^{pt}}{b_p(S/\sigma_0)}\right]\cdot\left[1+\frac{\sigma_0 V}{S\cdot b_p}\right]^{-1} \tag{2.81}$$

Since $b_p(T)$ is constant at constant temperature, the volume concentration is constant if $\sigma_0 V/Sb_p$, is small compared to 1; that is, for large S/V.

The proton spin-lattice relaxation time experiments were performed CPG with three pore sizes 74, 548, and 2917 Å contaminated by 40 ppm iron.

In order to determine the effect of washing out the paramagnetic ions, samples were incubated in a small excess of distilled and deionized water. After 24 h, water was extruded and the supernatant measured. In no case was T_1 of the supernatant different from the T_1 of the deionized water beyond the accuracy of the experiment (±3%). Therefore, the small Fe contamination could not be reduced by flushing the CPG with water. (However, it can be removed to a large degree by repeating five times the washing cycle of hydration with 1 mM EDTA solution and by subsequent rinsing with water).

The spin-lattice relaxation rate R plotted as a function of V_0/V is shown in Fig. 2–14. Due to slight non-exponential character of a magnetization recovery curve, spin-lattice relaxation times T_{SE} were determined from fitting the magnetization recovery function to a SE function (Eq. 2.58). The characteristic exponents of the distribution, α, are shown versus V_0/V in Fig. 2–15. In the range of the volume filling factor V/V_0 equal to 1.3 to 0.5, the nonexponentiality is barely visible with a exponent $\alpha \geq 0.9$. Outside of this filling factor range the nonexponentiality increases progressively, with $\alpha \approx 0.8$ and smaller.

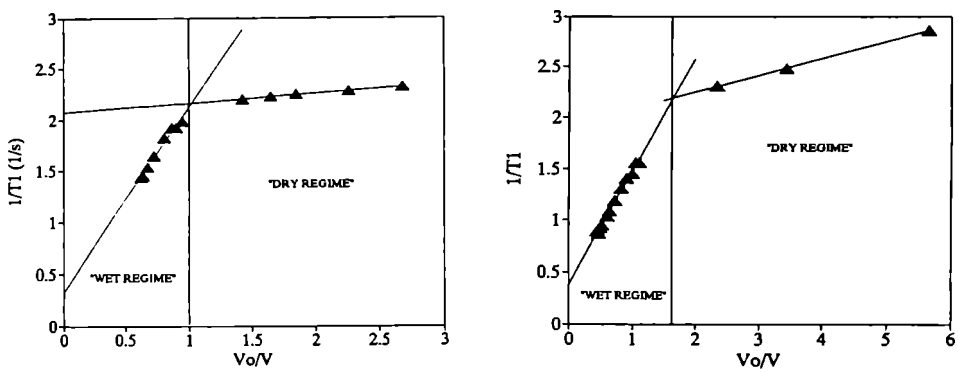

(a) (b)

Fig. 2–14. Proton spin-lattice relaxation rate versus V_0/V for the CPG with the average pore diameters (a) 2917 Å, and (b) 548 Å. The samples were hydrated with redistilled and deionized water, then dried by heating to 350 K in a nitrogen atmosphere and subsequently sealed under nitrogen. The volume of water lost in the dehydration process was accounted for by gravimetry. The proton spin magnetization recovery function was measured at 26 MHz using an inversion recovery sequence of pulses (π — τ — $\pi/2$ — FID(t)).

Proton spin-lattice relaxation of water in CPG contaminated by a small amount of Fe ions cannot be expressed as a linear function of the S/V. For all three pore sizes, the relaxation rates show two regions of linearity when plotted against V_0/V, the two regions being more distinct the larger the pore size. The two regions of linearity are most visible in the largest pores in Fig. 2–14a (the break between them sharply defined at V_0/V equal to one), supporting the concept of the two dehydration regimes given by Eqs. (2.75a) and (2.78); that is, a "dry" regime where water is entirely within the pore channels ($V_0/V > 1$), and a "wet" regime in which water exceeds the total pore volume ($V_0/V < 1$) (see Tab. 2–9). In "dry" regime, the observed relaxation rates extrapolate to an intercept larger than R_0.

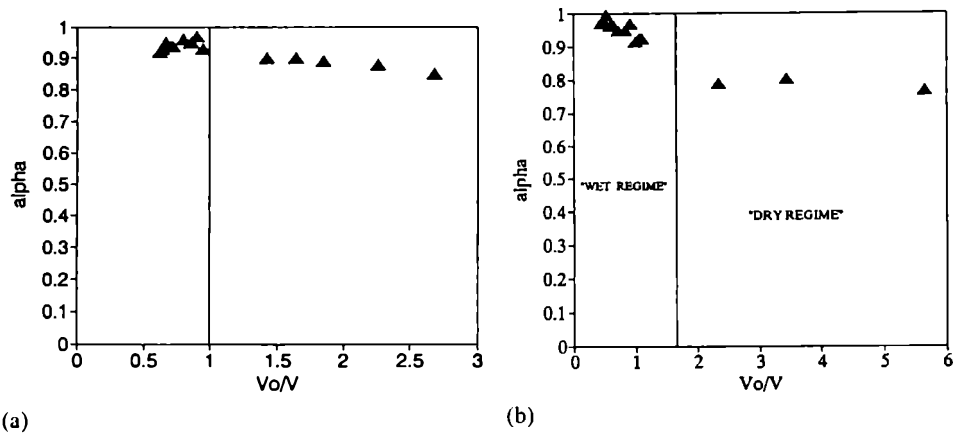

(a) (b)

Fig. 2–15. The fractal exponent α for SE function fitted for water filled porous glass with the average pore diameter (a) 2917 Å, and (b) 548 Å, versus V_0/V.

Note that this relaxation enhancement is not predicted from any of the Eqs. (2.75c) through (2.75e). Therefore, the models in which all the ions are dissolved in the volume or all glued to the surface are not consistent with the experiment. The data are consistent with the assumption of constant volume concentration. This suggests that the two CPGs studied satisfy the limit of large silica surface to water volume ratio [see Eq. (2.81)]. This relaxation "intercept" enhancement is, as expected about the same for both pore sizes, since the same ionic species are involved, and the geometries are very similar. However, the comparison has to be considered with care as the diffusion cells in CGP 2917 and CPG 548 must be substantially different.

The slopes of the dependencies are not dependent on the pore size. The conventional analysis of clean pores [Eq. (2.72)] predicts that the slopes are proportional to the S/V of the pore. These differ by a factor 6. Tab. 2–11 shows clearly that the slopes are not proportional to the S/V. This can be explained by referring to Eqs. (2.75a) and (2.75b), where the leading term in the slope is of paramagnetic origin. It does not dependent on the S/V. It is worth noting that a number of investigators have used Eq. (2.72) to characterize the geometry of porous materials. These techniques involve solving Eq. (2.72) for the S/V in terms of parameters λ, R_0,

and R_S, which could be determined for a particular solvent filling the pore space. Eqs. (2.75a) and (2.75b) show however that in the presence of paramagnetic impurities, the relaxation rate cannot be solved for S/V.

Table 2–9. Parameters from least-square fit of R on V_0/V dependencies. Accuracy is better than, or equal 10%.

Pore diameter [Å]	Hydration	Intercept [s^{-1}]	Slope [s^{-1}]
2917	dry	2.07	0.093
	wet	0.32	1.8
548	dry	1.91	0.17
	wet	0.38	1.10
548*	dry	1.91	0.29
	wet	0.38	1.89

* The values for the sample CPG 548 obtained if the kink in the R of V_0 /V dependence is set to 1.6 (see text).

To determine whether the paramagnetic iron ions are Fe^{3+} or Fe^{2+}, the paramagnetic rates of water protons contributed by both paramagnetic species, when diluted to 1 mM, are compared. For Fe^{3+}, the paramagnetic rate is 3.20 s^{-1}, while the latter at 1 mM contributes to proton relaxation a paramagnetic rate 0.33 s^{-1}. Thus, in contaminated pores both Fe^{3+} and Fe^{2+} ions contribute to the paramagnetic enhancement of the water proton spin rate. A simple linear analysis gives Fe^{3+} molarity of 0.49 mM and Fe^{2+} molarity as 0.31, their sum being 0.8 mM.

Eq. (2.77) applies for $V_0/V < 1$ (water resides both inside and outside the pore channels). For both pore sizes (CPG2917 and CPG548), the effective relaxation rates are again linear functions of V_0/V, with slopes and intercepts clearly distinct from those in the regime $V_0/V > 1$. On the basis of the Eq. (2.77), an intercept equal to the free water rate is expected and indeed observed in this hydration regime. For both pores, the intercept rates are very close to the free water rate $R_0 = (0.39 \pm 0.3)\ s^{-1}$.

Of course, the above discussion is applicable to a small range of hydration levels only. In the very high hydration limit, for example, the fast exchange between the inside and outside of the pore channels should clearly fail. In this case, the nonexponentiality of magnetization recovery function should increase. As can be seen, the values of α, are not much smaller from its maximum value (of ~0.95) at $V_0/V = 1$. In the sample CPG548, the increase of the nonexponentiality at high hydration is not at all noticeable (Fig. 2–15). This could be due to the highest specific pore volume of CPG 548 (Tab. 2–9), which therefore has the least tortuous internal geometry and largest diffusion cell. Diffusion within a restricted geometry is expected to be a monotonic function of porosity, increasing with increasing porosity, thus, would be more effective for CPG 548 than CPG 2917 [218, 374].

At the other end of hydration, this model should fail near the surface percolation, when the amount of water is insufficient to cover the pore surface.

Before this limit is reached, however, the three site approximation will also break down (see Chpt. 1.13.4, [283]).

In conclusion, in full to about quarter full (of water) contaminated porous glass the paramagnetic impurities do not wash out of the pore sample with distilled water; and porous glass maintains, while dehydrated, a constant volume concentration of paramagnetic ions in the bulk water within the pore as predicted by the Langmuir isotherm; i.e. a constant "ion pressure".

2.5 Water soluble solid fraction in dry biological system (bast and seed)

The quantitative analysis of hydration process in ultra-dry biological system should consider the effect of water soluble solid fraction. So long as water soluble solid fraction remains in solid phase, the hydration process results in surplus of liquid fraction of the signal. As a model to search for the effect of water soluble fraction on proton relaxation data three following systems were selected:

(i) pine (*Pinus silvestris* L.) and horse chestnut (*Aesculus hippocastanum* L.) bark was used as a control sample without water soluble fraction;

(ii) horse chestnut (*Aesculus hippocastanum* L.) bast is the system with limited amount of water soluble fraction, hydrophilic part of extractive fraction, which may be washed out from the sample;

(iii) wheat (*Triticum aestivum* L.) seed with the large volume of the soluble fraction coming from gel-like starchy endosperm.

The initial phases of hydration processes may be observed here using very mild hydration performed from gaseous phase. (Seed is here an exception because the initial phases of seed imbibition occur relatively slow, thus, the hydration procedure can be performed either from gaseous or from aqueous phase). At low hydration level of the system the solid (S) as well as the liquid (L) proton NMR signal component can be easily evaluated from the relaxation function.

2.5.1 Bark and bast composition

Bark builds up an outer shell of tree, external to cambium surrounding the stem, branches, and roots (Fig. 2–16). Bark consists of 10–15% of the total mass of the tree. The name 'bark' is often reserved for outer bark, *rhytidome*, whereas inner bark, which differs in structure and composition from outer layer, is called 'bast'.

Both these tissues consist of two groups of compounds differentiated by their technical properties, among them is cellulose, the most abundant organic compound occurring on Earth [647]:

(i) non-extractive components, including: polysaccharides (30% of tissue dry mass), suberins (20–40%, absent in bast), lignin (15–30%), and inorganic compounds (2–5% of dry mass);
(ii) extractive components, which are washable by non-polar or by polar solvents and by water (20–40% of dry mass).

The hydration properties of bast and bark significantly differ from those of wood. Bark contains more waxes and suberins which change the pore surface, whereas bast contains more hydrophilic extractive fraction than wood (and bark) [347, 621].

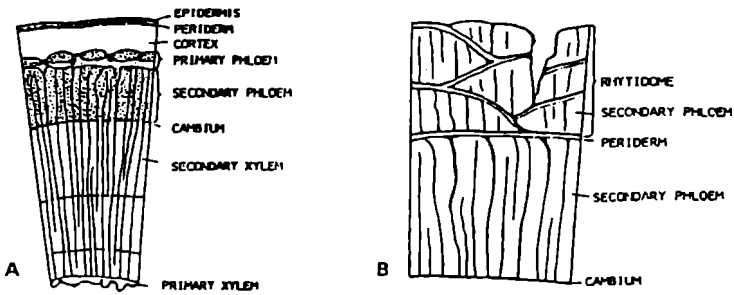

Fig. 2–16. Schematic cross-section of stem (A) and of mature bark (B): *phloem* – living bast, *rhytidome* – dead (outer) bark.

2.5.1.1 Polysaccharides

Cellulose is a basic constituent of wood and one of most important constituents of bark. Cellulose is a linear homo-polysaccharide consisted of β–D–glycopiranose units [$(C_6H_{10}O_5)_n$, n = 2500–12000] bound by glycoside bonds (Fig. 2–17). Cellulose molecules tend to aggregate in *microfibrils*, in which ordered (crystalline) regions (micelles) are separated by amorphous areas. Bunches of microfibrils form *fibrils*, which subsequently are arranged in *cellulose fibers*. Fibrillar structure and strong hydrogen bonds make cellulose a non-soluble and very stable polymer, which supports the structure of wood cell walls. Cellulose crystallizes forming tetragonal unit cell (a = 8.35 Å, b = 10.3 Å, c = 7.9 Å) containing four sugar units per one unit cell, stabilized by hydrogen bonds between O(3) and O(6) (see Fig. 2–17). In natural cellulose there are no hydrogen bonds between layers, but only a weak van der Waals interactions. Glucose radicals are bound by 1,4 β–glycoside bonds (210 kJ $mole^{-1}$); O(3) – O(6) bridges (by hydrogen bonds) have 63 kJ $mole^{-1}$. Cellulose occurs also in other polymorphs, namely, cellulose II formed by dilution in alkaline medium and subsequent sedimentation (with hexagonal unit cell); and cellulose III, and IV, obtained from celluloses I and II by chemical treatment and/or by heating.

Hemicelluloses are heteropolysaccharides built from D–glucose, D–mannose, D–xylose, L–arabinose, L–ramnose, D–glukuronic acid, 4–O–methylo–D–glukoronic

acid units. Hemicelluloses have branched structure from usually no more than 200 units. They are water soluble polymers [621].

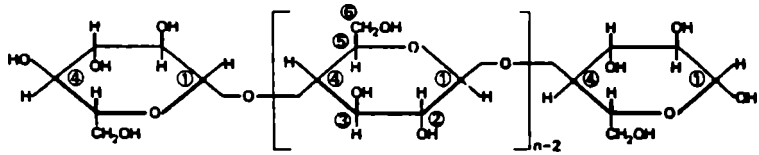

Fig. 2–17. The cellulose chain with the numbering of the carbons indicated. The chain direction is positive from right to left.

Galactoglucomannan forms a linear or slightly branched chain consisted of β–D–glucopyranosyl and β–D–mannopyranosyl units bounded by (1–4) bond. The α–D–galactopyranosyl units form side chains by (1–6) bond. The galactose:glucose:mannose proportion equals 1:1:3 for galactose–rich species; and 0.1:1:4 for galactose–poor species.

Guar galactomannan is a branched polysaccharide obtained from the seed endosperm of *Ciamopsis tatragonolata* consisting of a main chain of (1–>4)–linked β–D–mannopiranosyl units with α–D–galactopyranosyl side chains O–6–linked to alternate mannose residues. In aqueous medium, at the concentration exceeding 3 wt% guar galactomannan shows the change in bulk water motional properties (by saccharide chain contact), as indicated by proton T_1/T_2 ratio [82].

In glucomannan, which is a linear polymer, the ratio of β–D–glucopyranosyl to β–D–mannopyranosyl units varies between 1:2 to 1:1.

Glucoronoxylane is a basic hemicellulotic constituent of sapwood. It forms O–acetyl–4–O–methylglucorono–β–D–xylane chain built of β–D–xylopyranosyl units (1–4) bound, with attached by (1–2) bond the 4–O–methylo–α–D–glucoronic acid radical at every 10 units.

Arabinoglucoronoxylane is a linear (with some branches) polymer of two glucoronic acid units per every 10 xyloses. Moreover, by (1–3) bond the branched α–L–arabinose is bound (1.3 arabinoses per 10 xyloses).

Arabinogalactan forms a chain of β–D–galactopyranosyl units bound by (1–3) bond, with almost at every unit bound (at 6) the side groups of β–D–galactopyranose (or L–arabinose).

Araban is a carbohydrate specific for bark and bast. Main chain is formed from α–L–arabinose units, bonded by (1–3) or (1–5) bond. Side groups contain usually α–L–arabofuranose radicals.

Bast contains relatively high amount of pectins, which are acidic derivatives of galactan. They consist of 80% of poly–D–galakturonic acid chain with most carboxyl groups estrified by methanol. Remaining 20% of pectin mass consists of arabans and galactans. The molecular mass varies between 25,000 and 360,000. Among pectins there are water soluble species, and other ones not soluble in water. As the plant ages the contribution of soluble fraction decreases and the contribution of non-soluble fraction increases. Water soluble species

form gel in a process involving the formation of infinite networks in which extended junction-zones between macromolecules are established. At high cosolute (ethanol, t–butanol, dioxane) concentration the two-exponential relaxation function indicates a phase separation of solid amorphous phase and liquid phase, both appearing with cosolute caused gel disruption [79].

Other polysaccharide constituents of bark and bast are starch, and callose, (1–3)– β–D–glucan, which is contained in tubulae of siew aparatus of bast.

2.5.1.2 Suberins

The occurrence of suberins is characteristic for dead cork cells. Suberins are the heterogeneous complexes of exotic organic acids and poly–phenols, which have character of tannins. Suberins contain 60% of tannins. Main acidic constituents of suberins are:

$HO–CH_2–(CH_2)_{20}–COOH$, fellonic acid;

$HOOC–(CH_2)_{24}–COOH$, fellogenic acid;

$HOOC–(CH_2)_7–CH(OH)–(CH_2)_7–COOH$, floinic acid;

$HOOC–(CH_2)_8–CH=CH–COOH$, traumatinic acid.

The length of their chain varies, but the majority has 16 or 18 carbon atoms. Suberins tend to form composed polymeric structure, which reveals chemical and biological stability.

2.5.1.3 Lignin

Lignin is a heterogeneous, branched polymer with dominating number of phenyl–propyl units. The precursors of lignin synthesis are non-saturated alcoholes: p–kumarilic, koniferilic, synapilic (produced from D–glucose).

There exist bonds between lignin and suberins. Lignin is very resistive on chemical and on biological agents, and differentiated depending on the wood species. Lignin from bark is not yet sufficiently investigated [621].

2.5.1.4 Extractive components

Extractive components can be classified as lipophilic, i.e. extracted by use of non-polar solvents as ethyl ether, or ethyl alcohol; and as hydrophilic components, extractable with water alone or with polar organic solvents (acetone, ethyl alcohol, etc.).

Lipophilic components are:

(i) alifatic compounds as n–alcanes, $CH_3–(CH_2)_n–CH_3$, $n = 8 \div 30$; alcohols, $CH_3–(CH_2)_n–OH$, $n = 16 \div 22$; fatty acids, $CH_3–(CH_2)_n–COOH$, $n = 10 \div 24$ (mostly linoleic, oleinic, linolenic); glycerol esters, $(CH_2–OR)–(CHOR')–(CH_2–OR'')$, where R, R', R'' are fatty acid groups; and waxes, $RO–CH_3$, RO–sterol, or RO–trepenic alcohol, where R is fatty acid group; and

(ii) terpenes and terpenoids. In resin canals of wood appear resins contained mostly of resine acids, which are terpenes, described by a general formula: $(C_{10}H_{16})_n$. Usually they are monoterpenes (n = 1), sesquiterpenes (n = 1.5), and biterpenes (n = 2). Bark is reach in terpenoids and sterides.

Hydrophilic components are:

(i) tannines, which hydrolyze on gallic acid (elagic acid) and sugars;

(ii) flavonoids, based on $C_6C_3C_6$ skeleton (as chrysidine, or taxyfoline);

(iii) carbohydrates, proteins and vitamins present in bark; and

(iv) starch, pectins, oligosaccharides (rafinose, stachiose) in bast.

The content of extractive components in bark is higher than in wood, varying in wide range (20–40% of dry mass).

2.5.1.5 Mineral components

There is significantly more mineral components in bark than in bast (and in wood). Metals occur as salts (phosphates, silica). Predominant metal constituents are: calcium, and potassium. Bark contains traces of boron, copper, and manganese.

2.5.2 Bark and bast structure

Inner and outer bark is composed of several types of cells and its structure is more composed compared to wood.

The main components of bast (inner bark) are *sieve elements*, *parenchyma* cells, and *sclerenchymatous* cells. The sieve elements, which may be divided on narrower *sieve cells*, and thicker and cylindrical *sieve tubes*, perform the transportation of liquids and nutrients. The average diameter of pores in sieve tubes usually equals ~1 μm, but in some plants exceeds this value up to 10 μm. The sieve tubes are ordered in longitudinal cell rows, with sieve cells between. After 1–2 years the activity of the sieve elements ceases and they are replaced by new cells. Seasonal changes cause that solidifying callose seals the pores, what blocks the transport function of sieve elements and isolates single sieve cylinders. In aged cells the sealing of pores by callose is often irreversible.

Parenchyma cells store nutrients. They are located between the rows of sieve elements.

Sclerenchymatous cells support the structure of bast tissue. Two types of sclerenchymatous cells are distinguishable: the *bast fibers* (0.3–3 mm in length) often arranged in tangential rows; the *sclereids* (or *stone cells*), which are short and rounded.

Bark (outer bark) consists mainly of *periderm* or cork layers. It protects the wood tissues against damage and variation of external conditions. Cork cells, consisted of three thin layers and only rarely pitted, are arranged in radial rows and die at an early stage. They are glued together to a tight tissue resistive for water and gases.

2.5.2.1 Cell wall

Plant cells are surrounded, except the cellular membrane, by a cell wall [621]. Primary wall (0.1–0.2 μm) surrounds growing cells. In mature cell, on its inner side may develop secondary wall consisted of outer layer (0.2–3 μm); the thickest one, middle layer (1–5 μm); and inner layer (~0.1 μm). Walls of neighboring cells are glued together by pectin pellet (0.2–1 μm).

Cell wall is formed from elastic, strong cellulose skeleton and filling materials. The mechanical resistance of cell wall is higher than that of its constituents separately. In mature and dead cells, cell walls are incrusted (inside the wall structure) by lignin, tannins, waxes, and mineral constituents. The most important incrusting constituent is lignin, which mostly deposit in primary wall. Lignin strengthens the cell wall structure and decrease its permeability. In bark cell wall contains hemicelluloses causing its swelling with hydration. Suberins, kutines, waxes, and other lipophilic compounds adcrust the cell wall surfaces of cork cells. This results in increased elasticity and water resistance of cork cells present in bark.

The presence of regular network formed by cell walls of dead cells makes bast and bark a pretty uniform model porous systems.

2.5.3 Hydration kinetics of bark and bast

The hydration kinetics of bark and bast of horse chestnut (*Aesculus hippocastanum* L.) performed by the Author at room temperature from the gaseous phase over the surface of H_2O (at the relative humidity, $p/p_0 = 100\%$) is well fitted by a two-exponential function (Fig. 2–18)

$$\frac{\Delta m}{m_0} = A_0\left[1 - A\exp\left(-\frac{t}{T_a}\right) - (1-A)\exp\left(-\frac{t}{T_b}\right)\right]. \qquad (2.82)$$

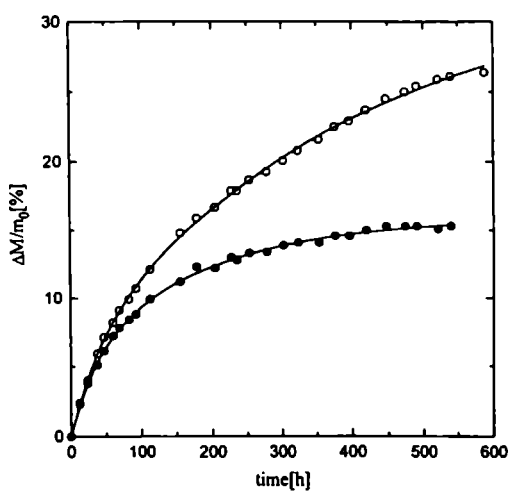

Fig. 2–18. The hydration kinetics for horse chestnut (*Aesculus hippocastanum* L.) bark and bast expressed as the time dependence of the relative mass increase, $\Delta m/m_0$

Saturation hydration was $A_0 = (15.9\pm0.3)\%$ for bark, and $A_0 = (32.1\pm0.8)\%$, for bast. Faster hydration step is characterized by a time constant $T_a = (34\pm7)$ h causing the relative mass increase $\Delta m/m_0 = (4.9\pm0.1)\%$, which is common for bark and bast samples; and a slower one with characteristic times $T_b = (177\pm20)$ h and $T_b = (361\pm28)$ h for bark and bast, causing additional mass increase of $(11.1\pm0.2)\%$ for bark, and $(27\pm0.7)\%$ for bast.

Such a behavior suggests the presence of well defined pool of water binding sites in the low hydration range common for both tissues. To avoid a non-uniform water distribution across the sample volume, the sealed sample was stored after each hydration step for about 2–3 hours.

2.5.4 EPR observation of paramagnetic ions contained by bark and bast

As the paramagnetic impurities have a significant influence on the relaxation of NMR signals (see Chpt. 2.4) the samples were examined for their possible presence by ESR spectroscopy.

EPR spectra of the bark of *Pinus silvestris* recorded at room temperature (Fig. 2–19a,a') showed a complex signal composed of a narrow ($\Delta B_{pp} = 0.6$ mT) line at 2.0034, a broader ($\Delta B_{pp} = 4$ mT) dominant pseudo–singlet centered at 2.03, two low field components of a hyperfine structure with the splitting of 8 mT, and a broad feature at $g = 2.3$. Registration of the spectra at 77 K additionally revealed a distinct sextet with the splitting of 9.2 mT as well as the remaining hyperfine lines of the multiplet signal centered at $g \sim 2.0$ (Fig. 2–19a"). The signal at $g = 2.03$ prevailing at room temperature was practically undetectable at 77 K.

The room temperature EPR spectra of the bark of *Aesculus hippocastanum* showed three types of resonance (Fig. 2–19b). Two very broad signals at $g = 4.3$ and $g = 2.3$ and the narrow 2.0034 line (the same as that detected in the pine bark). In the corresponding bast sample the EPR signals were apparently weaker (Fig. 2–19c,c'). The dominant ones except of the $g = 2.0034$ signal appeared at $g = 3.2$ ($\Delta B_{pp} \sim 10$ mT) and $g = 1.98$ ($\Delta B_{pp} = 3.5$ mT).

Due to poor resolution of the spectra caused by the micro-heterogeneity of the samples and partial overlap of some the signals their assignment can be only approximate. Generally, the detected signals correspond to two types of centers: organic radicals (narrow lines with g values closed to free-electron g_e value) and metal containing paramagnetic impurities (broader lines with g values significantly deviated from g_e). The large spin-orbit coupling constant of metals results in a distinct shift of g values and a relatively short relaxation time of the latter.

The g value of 2.0034 lies well within the range specific for heteroatomic organic radicals containing oxygen [168]. Such radicals may originate from photodegradation of the bark cellulose weathered by sunlight, as the presence of Fe^{3+} (detected by ESR in all investigated samples) has a great sensitizing effect on this process [315]. Indeed, alkoxy radicals produced by rupture of the glucosidic

linkage at the C_1 and C_4 positions exhibit a singlet spectra at this g value which is stable at room temperature but with a line width of 1.5 mT [316]. Both the g value and the linewidth of this signal, however, compares favorably with that found for quinone radical [607]. In fact, quinone radicals are often found in many biological systems, as needles of cornifers, lichens, or in humus [439].

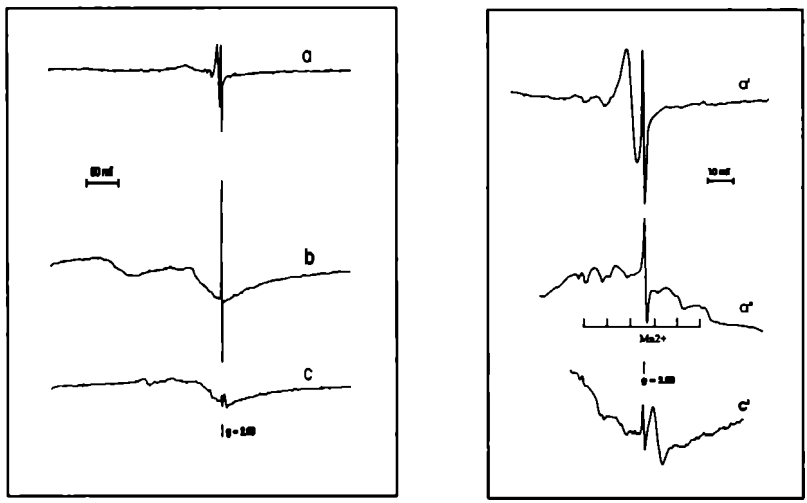

Fig. 2–19. The EPR spectra of the bark of *Pinus silvestris* (a) taken at 295 K, scan range 500 mT, (a') at 295 K, scan range 200 mT, (a") at 77 K, scan range 200 mT; (b) the bark of *Aesculus hippocastanum* taken at 295 K with the scan range 500 mT and the bast of *Aesculus hippocastanum* (c) taken at 295 K, scan range 500 mT, (c') at 295 K, scan range 200 mT. Spectra were recorded on a ESR 300 (Bruker) and ESR 220 (Adlershof) spectrometers both working at X-band with 100 kHz field modulation. A MJ-111 NMR teslameter (Radiopan) was used for magnetic field calibration. To avoid distortion of the spectra by power saturation, the measurements were carried out at a microwave power of 2 mW.

Both the g value and the linewidths of the dominant signal at 2.03 suggest that it may be associated with a metal containing center. For such radicals deviation (Δg) of the g value from g_e can be approximated as $\Delta g = \Sigma_i \rho_i \xi_i / \Delta E_i$. Thus, larger shifts can be expected if the spin density (ρ_i) increases on atoms with large spin-orbit coupling constants ξ_i. Since the spin-orbit coupling constants generally increase with increasing atomic number, larger deviations from free-spin value will be observed for radicals containing heavy atoms like metals [168]. On the other hand, the deviation is too small to be accounted for by unpaired electron localized directly on a d^n metal center (positive shift of g implies $n > 5$). Thus, this signal most likely comes from paramagnetic complexes formed by ligand radicals (like quinone, polynuclear constituents of lignin or humic acid) coordinated to metal ions. Such complexes are readily formed with divalent and trivalent ions [421]. Similar signals can be also produced by the interaction of transition metals with humic acid.

As this signal is completely altered at 77 K, presumably these complexes are localized in bound water pools (see Chpt. 2.5.5).

The broad resonances at g = 4.3, 3.2 and 2.3 are characteristic of high spin Fe^{3+} iron (S = 5/2) in various environments. Such spectra can be described in terms of the following spin Hamiltonian: $\mathcal{H} = g\beta BS + D[S_z^2 - 1/3S(S+1)] + E(S_x^2 - S_y^2)$ (plus other higher order terms). Depending on the values of the fine structure parameters D and E and the symmetry of the site, trivalent iron can give rise to numerous resonances over the wide range of the effective g values. The signal at g = 4.3 (so called 30/7 signal) corresponds to isolated Fe^{3+} ions in cubic symmetry of strong rhombic distortion E/D = 1/3 [448]. The signal at g = 3.2 (10/3 signal) is produced for particular combinations of fine structure parameters in various lower symmetry environments [448]. The iron signal at g = 2.3 may correspond to cubic Fe^{3+} provided that zero field splitting is small or to antiferromagnetically coupled clusters [179]. Following the literature the signals at 3.3 and 2.3 can be associated with highly dispersed airborne [693] limonite ($FeO(OH)\cdot nH_2O$) and hematite (Fe_2O_3) particles respectively [328]. Iron was already detected in pine bark collected from various sites in Poland [138] and in Finland [653].

While the sextet signal with splitting of 9.2 mT detected in the pine bark can be readily assigned to Mn^{2+} ions, attribution of the second multiplet signal is rather difficult. The eight line structure and $g > g_e$ may suggest cobalt complex.

The relatively weak 1.98 signal observed in the horse chestnut bast points to $d^{1(3)}$ ions. The lack of a clear hyperfine structure indicates that practically only Cr^{3+} or Ti^{3+} ions should be taken into account. As the latter species are unstable in aqueous media, this signal should be assigned to trivalent chromium centers. The ground state of Cr^{3+} in octahedral symmetry is an orbital singlet $^4A_{2g}$ which is connected through the spin-orbit coupling to excited T_{2g} state only. For this reason, the g value is very nearly isotropic, even in highly distorted environments. As all excited states are much higher in energy, the relatively long spin-lattice relaxation time give rise to narrow ESR absorption lines, even at room temperature [464] which is consistent with the behavior of the experimental signal.

Summarizing, paramagnetic impurities are present in the all investigated samples. Their concentration in the bark is distinctly greater than in the bast, which may be explained by an additional contribution of the airborne origin (adsorption of Fe–containing dust particles on the surface of bark). The iron(III)(hydr)oxides adsorbed on the surface of bark can be then partially transferred into bound water pools, e.g. via (photo)reductive dissolution process [650]. However, the resultant Fe(II) species though paramagnetic (S = 1) are EPR silent since the spin-lattice relaxation time is quite short and the zero-field splitting very large [464].

2.5.5 Proton free induction decay of bark and bast

Until now, most of the attention in nuclear magnetic relaxation investigations of timber products was paid to wood [11, 86, 296, 322, 474, 475, 565], including the

observation of water clustering on the surface of pores in biological systems [295]. This Author applying proton NMR to bast, discussed the effect of water soluble solid fraction and obtained for this fraction the upper dissolution threshold $\Delta M/m_0$ (the amount of water necessary to dissolve the whole water-soluble fraction), saturation concentration c_s of soluble fraction, thus, $\Delta M_c/m_0$, the content of solid soluble fraction, and moreover the effective (scaled to water) proton densities of bark solid and water soluble fractions of bark, *in situ* (see Chpt. 2.5.7–8).

Fig. 2–20 shows the FID for protons in hydrated ($\Delta m/m_0$ = 11.5%) horse chestnut bark. FID is composed of a solid contribution (S) coming from the immobilized protons of the solid part of the bark; and of two liquid components (L_1 and L_2) coming from water bound on a pore surface of the bark and/or from the chemical groups of the bark cellulose, mobilized in the vicinity of the water layer. The liquid components are easily fitted by the superposition of two exponential functions (the short-live component has the amplitude L_1 = 28.8 arbitrary units (a.u.) and the time constant $T_2^{L_1}$ = 170 μs; while the long-living component has the amplitude L_2 = 3.53 and $T_2^{L_2}$ = 573 μs.

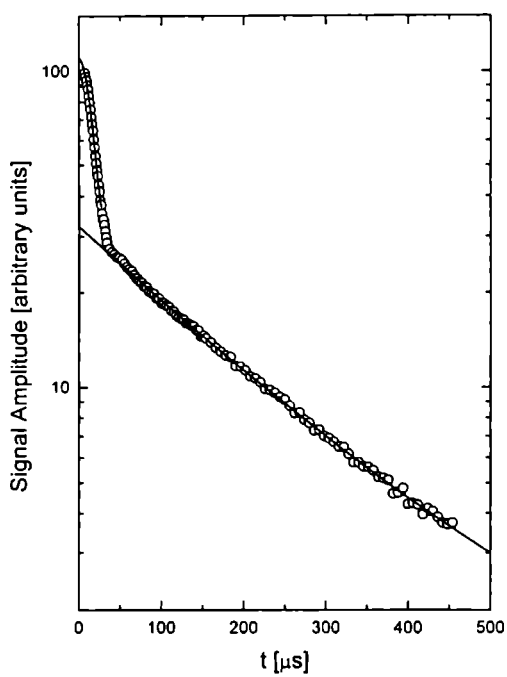

In case of bast, water soluble fraction in solid phase contributes to S signal, whereas in liquid phase to L_i components of proton FID.

Fig. 2–20. The semi-logarithmic plot of the proton free induction decay (FID) for the horse chestnut (*Aesculus hippocastanum* L.) bark hydrated to $\Delta m/m_0$ = 11.5 %. FIDs were recorded at 30 MHz; output power was 400 W; the pulse length $\pi/2$ = 1.1 μs; the spectrometer dead time was of about 6 μs. All FIDs were recorded starting 10 μs after $\pi/2$ pulse; t = 25^{0}C, stabilized in a gaseous nitrogen flow. Data were averaged over 800 accumulations. FIDs were analyzed using the spin-grouping program CracSpin [703]. The function fitted according to Eq. (2–91).

2.5.5.1 Solid component of the free induction decay signal

In rigid lattice approximation, the solid contribution to FID function is given by [1]

$$F(t) = \sum_n M_{2n} \frac{(-1)^n t^{2n}}{(2n)!}, \tag{2.83}$$

where M_{2n} is 2n-th moment of the NMR line.

However, for several biological solid tissues the solid FID component is usually expressed by Gaussian function. If one expands Gaussian function in moments, one gets

$$e^{-\left(\frac{t}{T_g}\right)^2} = e^{-\frac{M_2 t^2}{2}} = e^{-\frac{t^2}{2\sigma^2}} = \sum_n (-1)^n \frac{t^{2n}}{n!\left(2\sigma^2\right)^n}, \tag{2.84}$$

where

$$M_2 = \frac{1}{\sigma^2} = \frac{2}{T_G^2} \tag{2.85}$$

and T_G, the effective spin-spin relaxation time is usually called T_2^*.

Thus, for Gaussian function one gets

$$M_{2n}^G = \frac{(2n)!}{n!2^n\sigma^{2n}}. \tag{2.86}$$

Knowing that

$$(2n)! = 2^n n!(2n-1)!! \tag{2.87}$$

one gets

$$M_{2n}^G = \frac{(2n-1)!!}{\sigma^{2n}}. \tag{2.88}$$

From Eqs. (2.85) and (2.88) one obtains the formula of practical use to check the agreement of the form of any given solid signal with the Gaussian function

$$\frac{M_{2n}}{(M_2)^n} = (2n-1)!! \tag{2.89}$$

which equals for

$$\frac{M_4}{M_2^2} = 3, \quad \text{and for} \quad \frac{M_6}{M_2^2} = 15. \tag{2.90}$$

The moment expansion of horse chestnut bark proton FID solid component (after subtraction of the liquid ones from the total signal) gives the amplitude: S = 77.4±0.4 and the values of the moments: $M_2 = 5.08 \cdot 10^9\ s^{-2}$; $M_4 = 6.0 \cdot 10^{19}\ s^{-4}$ and $M_6 = 6.2 \cdot 10^{29}\ s^{-6}$. Thus, in this approach, the overall form of the FID was given by

$$f(t) = S\left(1 - \frac{M_2}{2!}t^2 + \frac{M_4}{4!}t^4 - \frac{M_6}{6!}t^6\right) + L_1 \exp\left(\frac{-t}{T_2^{L_1}}\right) + L_2 \exp\left(\frac{-t}{T_2^{L_2}}\right) \quad (2.91)$$

Fitting the superposition of solid (Gaussian) component and two liquid exponential decays yields the solid signal amplitude S = 76.7 and time constant $T_2^* = 18.61$ μs (T_2^* calculated from the 1/e value of the Gaussian signal) and two liquid components: L_1 = 28.8 a.u. with and $T_2^{L_1}$ = 170 μs and L_2 = 3.44 with $T_2^{L_2}$ = 585 μs. Though the solid line deviates slightly from the Gaussian shape ($\frac{M_4}{M_2^2}$ = 2.31), the amplitude of the solid line calculated from the Gaussian approximation differs from the value obtained from the moment expansion by less then 1.0%. The model yielding the molecular parameters for the bark and bast hydration deals mainly with amplitudes of liquid and solid components. Thus, Gaussian fit provides sufficient accuracy of the solid amplitude determination.

The value of $T_2^* \approx 20$ μs is close to those obtained for many biological dry matrices such as the solid part of wheat seed [289], lichen thallus [272, 273], dental enamel [221], dentine [222, 275] or wood [296]. This correspondence observed in a wide range of biological systems comes from general congeniality of proton chemical environments over angstrom dimensional scales [537].

2.5.5.2 Liquid components of the free induction decay signal

The two liquid components (see Fig. 2–20) of horse chestnut proton FID signal come mainly from water subsystems distinguished by the proximity to solid matrix and therefore by the strength of the chemical bonding differentiating motional states of protons and reflected in distinct relaxation times. As the B_0 homogeneity of our magnet gives the $T_2^* \cong 16$ ms for bulk water the T_2^* value for shortest, L_1, component is close to its real T_2 value [290]. At dehydration of the horse chestnut bast sample, the L_1 component is the last one to vanish while it remains the sole liquid component in horse chestnut and pine bark dehydration. Thus, the L_1 signal component comes from a tightly bound water fraction. A single T_2 value indicates a relative uniformity of motional state. The value $T_2^* \approx 100$ μs is close to that recorded for separated water molecules bound on the surface of CPG [283].

The component L_2 (and, observed at extremely low hydration, L_3 – see below) comes from protons of loosely bound water or from bulk aqueous medium.

Because their T_2 values are much longer than the maximum value allowed by B_0 inhomogeneities (see Eq. (2.71), a detailed resolution was not possible.

2.5.5.3 Hydration of bark and bast observed using proton FID

Bark and bast of horse chestnut (*Aesculus hippocastanum* L.) and bark of pine (*Pinus silvestris* L.) were harvested from living trees in fall (before first chill), and hydrated at the room temperature from the gaseous phase (in the atmosphere with gradually increased humidity over the supersaturated solutions of H_3PO_4, p/p_0 = 9%, $CaCl_2$ – 32%, $Na_2Cr_2O_7$ – 52%, $Na_2S_2O_3$ – 76%, K_2CrO_3 – 88%, Na_2SO_4 – 93% and H_2O, 100%). The incubation time was 72 hours. The highest hydration levels were obtained over the water surface at prolonged incubation; in two cases elevated temperatures (30°C and 35°C) were applied.

Fig. 2–21 shows the hydration dependence of the proton spin-spin relaxation times T_2^* for horse chestnut bark (2–21a) and bast (2–21b). For both samples, T_2^* of the solid component remains almost unchanged over the whole hydration range, which means that the hydration, beside dissolution, does not significantly change the solid matrix of bark and bast. Taking into account the good stability of the time constant of solid component, solid signal amplitude (S) as a standard for liquid component amplitudes (L_1, L_2 and L_3) calculation was used.

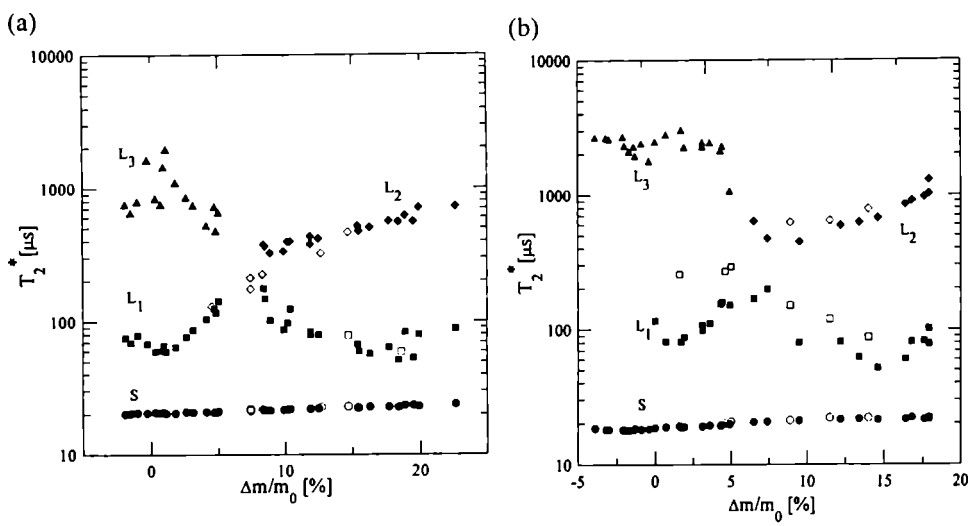

Fig. 2–21. The proton relaxation times T_2^* (calculated from FIDs) as a function of sample hydration (relative mass increase $\Delta m/m_0$) for horse chestnut bark (a) and bast (b) sample recorded at room temperature. The T_2^*'s of solid component S are showed by circles, liquid L_1-component – squares, liquid L_2 – diamonds and liquid L_3 – triangles (open symbols – at hydration, close symbols at dehydration).

The tightly bound water signal, L_1, is well resolved for the whole hydration range covered by both horse chestnut bark and bast samples, except for the hydration level close to $\Delta m/m_0 \approx 5\%$ at which the loosely bound water pool, L_2, vanishes. This causes the numerical procedure to give a mixed value of the time constant for the L_1 fraction and for the remnants of the loosely bound L_2 fraction.

For even lower hydration, the loosely bound pool L_3 is detected. The T_2^* value of L_3 is approximately twice that of L_2 and has substantially smaller contribution to the FID signal. Therefore, since L_2 comprises the largest component of the signal in the bark or bast sample (at higher hydration), the L_3 component is masked by it and not resolved from total FID signal. It is not removed from the bark and bast sample even at lowest hydration level obtained.

Fig. 2–22 shows the relative contributions of the observed liquid component amplitudes expressed in units of solid component S. For the whole hydration range of the bark chestnut sample, the liquid component L_1 with $T_2^* \approx 100$ μs is observed. The similar L_1 component (with $T_2^* \approx 100$ μs) is observed in horse chestnut bast, remaining constant for higher hydration levels (at which L_2 signal component is resolved). However, at $\Delta m/m_0 \approx 4\%$ the L_1 component starts to decrease linearly and finally vanishes at $\Delta m/m_0 \approx 0\%$.

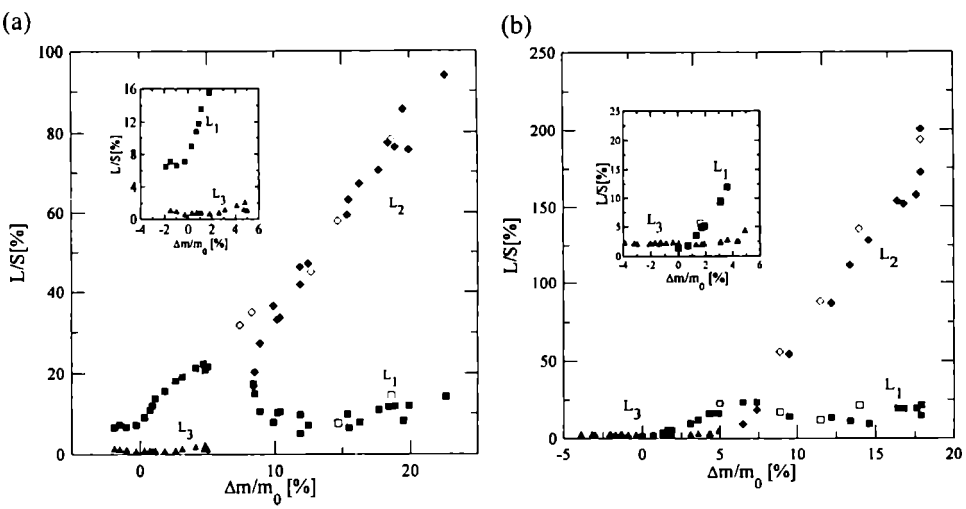

Fig. 2–22. The hydration ($\Delta m/m_0$) dependence of proportions of liquid proton FID decay components: L_1 (squares), L_2 (diamonds) and L_3 (triangles), expressed in units of solid S component for horse chestnut bark (a) and bast (b). (The open symbols represent measurements for sample hydration, the shaded ones – sample dehydration). Negative $\Delta m/m_0$ was obtained for drying at slightly elevated temperature. In case of bast, the L_1 component appears above zero hydration; in case of bark, the L_1 component is constant as the sample is dehydrated.

At hydration level higher than $\Delta m/m_0 > 0\%$ for horse chestnut bark and $\Delta m/m_0 > 5\%$ for horse chestnut bast the liquid component L_2, characterized by the T_2^* value of several hundreds of μs is observed. This component increases as the hydration is raised. For bark the L_2 hydration dependence is almost linear. At dehydration, the L_2 component vanishes nearly at the hydration, at which the L_1 starts to decrease (in bast sample) which confirms its interpretation as the one coming from solvent (water and, in case of bast, water soluble fraction) loosely bound to the solid matrix of plant tissue (bark or bast).

The decrease in resolution at $\Delta m/m_0 \approx 5\%$ occurs also on L/S data for bark, causing an artificial increase of L_1 for a couple of data points. (For the bast sample the L/S data were not substantially altered by mixing of L_1 and L_2 contribution).

The liquid component L_3 observed in all horse chestnut samples at very low hydration (at which L_1 decreases and L_2 is no longer present), requires further explanation. It is not numerically resolved (by the fitting procedure) from the total FID signal at higher hydration because of its residual magnitude (see Fig. 2–22). Its T_2^* seems to be substantially longer than T_2^* for the L_2 component, which suggests that L_3 comes from the proton spin subsystems different from that giving contribution to the L_2 signal. The interesting point is that the contribution of the L_3 component to the total proton FID signal remains unchanged, as the hydration is changed. Therefore, it may come from mobile chemical groups of the solid matrix of chestnut bark and bast, however, in this case it should somehow depend on hydration. On the other hand, its long T_2^* (~2 and ~3 ms, respectively) suggests that it may come from water trapped in completely sealed solid matrix pores which are not dried by dehydration at low aerial humidity or at mild sample heating. Drastic preheating (150°C), at which waxes and other hydrophobic components may desorb, opening the cavities sealed at lower temperatures, removed the component L_3, confirming that L_3 component comes from sealed water.

2.5.6 The absence of water soluble solid fraction

If the water soluble solid fraction is absent in the sample of micro-heterogeneous system hydrated by addition of Δm mass of water, the intensities of the liquid L and the solid S signal component are

$$L = L_0 + \alpha_{H_2O}\rho_{H_2O}\Delta m \,, \tag{2.92a}$$

$$S = S_0 \,, \tag{2.92b}$$

where ρ_{H_2O} is the proton density of water, α_{H_2O} is the proportionality coefficient describing the effective contribution of a given proton pool to the total signal. Coefficient α_{H_2O} may be decreased in the presence of paramagnetic in

solution [1]. L_0 and S_0 are the initial liquid and solid FID signal components. The liquid L_0 is the signal fraction coming from all mobile molecular groups of solid matrix and/or liquid fraction present in the sample, which cannot dissolve any solid portion of protons (e.g. localized in completely sealed pores of the structure). Thus L_0 and S_0 are given by

$$L_0 = \alpha_m \rho_m \left(m_0 - m_{S_0} \right) , \tag{2.93a}$$

$$S_0 = \alpha_S \rho_S m_{S_0} , \tag{2.93b}$$

where ρ_m and ρ_S are proton densities of mobile (liquid-like) chemical groups and/or residual water, and of the solid non-soluble fraction, respectively; α_m and α_S are effectiveness coefficients for these proton pools; m_0 is the minimal mass of the sample obtained after drying, and m_{S_0} is the mass of solid non-soluble fraction (the difference is equal to the mass of mobile chemical groups).

Hence, the ratio of L to S expressed in terms of the relative mass increase $\Delta m/m_0$ is given by

$$\frac{L}{S}\left(\frac{\Delta m}{m_0}\right) = \frac{\beta_m}{\beta_S}\left(\frac{1}{p_{S_0}} - 1\right) + \frac{1}{\beta_S p_{S_0}}\left(\frac{\Delta m}{m_0}\right) , \tag{2.94}$$

where $p_{S_0} = \dfrac{m_{S_0}}{m_0} \le 1$ is the weight proportion of the immobilized proton fraction that contributes to the solid proton signal, β_S and β_m are effective, (scaled in units of water) proton densities of solid non-soluble and mobile fractions, respectively, which are given by

$$\beta_S = \frac{\alpha_S \rho_S}{\alpha_{H_2O} \rho_{H_2O}} , \tag{2.95a}$$

$$\beta_m = \frac{\alpha_m \rho_m}{\alpha_{H_2O} \rho_{H_2O}} . \tag{2.95b}$$

If part of the solid signal is lost because of a non-zero spectrometer dead time or if the sample contains paramagnetic centers which can completely switch the signal from neighboring protons off, the constants α for both fractions may not be equal, and thus the coefficients β_S and β_m may differ from the ratio of proton densities for non-exchangeable solid (or liquid) and water. This may happen, also, if α_{H_2O} is altered by paramagnetic ions present in solution only.

Pine bark is an example of biological dry system in which no water soluble solid fraction is detected. The hydration process visualized as a total liquid signal

component of proton FID dependency on relative mass increase, $\Delta m/m_0$ (Fig. 2–23) is linear (Eq. 2.94). Proton density of solid mobile fraction, β_S, is a weighted average over several chemical groups present in solid matrix of lichen thallus. However, it varies in a range between 0.3 (lower limit for solid components), then 1 (as for water) and finally 1.8 (CH_3 group) (Tab. 2–11a). The values of β_S and p_0 calculated for this range of β_m do not change significantly, with their mean values equal $\beta_S = (0.33\pm0.01)$ and $p_0 = (0.977\pm0.01)$. In the absence of paramagnetic centers and a completely immobilized proton fraction, the signal effectiveness ratios α/α_{H_2O} are equal to 1, then the fitted values of β_S's should agree with those calculated directly from the chemical formulas (stoichiometry) relative proton density ρ_S/ρ_{H_2O} of solid non-soluble fraction. As compared with calculated values of relative proton densities for major bark solid constituents (see Tab. 2–10), the fitted value of β_S is noticeably lower than the calculated one. This probably reflects the effect of endogenous paramagnetic centers present in the solid matrix of the pine bark (see Chpt. 2.5.4).

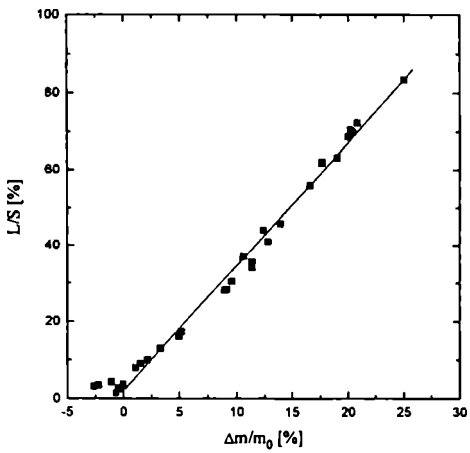

Fig. 2–23. The liquid-to-solid ratio L/S as a function of relative mass increase at hydration ($\Delta m/m_0$) for pine bark.

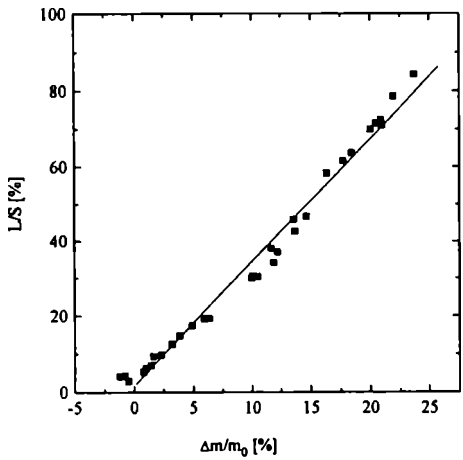

Fig. 2–24. The liquid-to-solid ratio L/S as a function of $\Delta m/m_0$ for horse chestnut bark.

Also in horse chestnut bark the hydration dependency on relative mass increase is linear with low value for χ^2 per degree of freedom (Fig. 2–24). As in the case of pine bark, β_S and p_0 change only slightly as calculated for the wide range of β_M values. The averaged values of $\beta_S = (0.31\pm0.01)$ and $p_0 = (0.99\pm0.01)$ are close to those obtained for the pine bark, underestimating the proton density of solid fraction calculated from the stoichiometry. The weight content of the movable fraction ($1 - p_0$), which is not removed by drying, is much less than the

weight content of the CH_3 groups suggesting that it belongs to a water pool present in the bark pores which are sealed by waxes and suberins.

Table 2–10. Relative (scaled to water) proton densities for common bark or bast components calculated directly from the chemical formula of given compound.

Substance	β (total)	β (without CH_3 groups)
cellulose	0.556	–
lignin	0.554	0.403
suberins	1.16	–
sucrose	0.579	0.429*
callose	0.56	–
Lipophilic extractive components:		
n–alkanes	1.35	1.28
fatty alcohols	1.27	1.24
fatty acids	1.14	1.10
Hydrophilic extractive components:		
gallic acid	0.318	–
catechin	0.763	–
pinoresinol	0.572	0.507

*Without CH_2OH groups.

Table 2–11a. The fitted values of the effective proton density β_S and relative contribution p_0 of solid non-soluble fraction for bark of horse chestnut and of pine. The calculated values for horse chestnut bast washed out of the water soluble solid proton fraction.

β_M	β_S	p_0
Pine bark		
0.3	0.34±0.01	0.953±0.010
1	0.33±0.01	0.986±0.003
1.8	0.33±0.01	0.992±0.002
Horse chestnut bark		
0.3	0.31±0.01	0.984±0.010
1	0.31±0.01	0.983±0.003
1.8	0.31±0.01	0.997±0.002
Horse chestnut bast		
	0.196	0.996

2.5.7 Presence of limited amount of water soluble solid fraction

If a soluble fraction of protons occurs in the sample, as in the case of bast [347, 621], Eq. (2.94) is no longer obeyed. The signal of the proton soluble fraction is at least partially transferred from the solid to the liquid signal

component, during the hydration of the sample. Then, the liquid L and the solid S components are

$$L = L_0' + \alpha_{H_2O}\rho_{H_2O}\Delta m + \alpha_{cd}\rho_c m_{cd} \,, \tag{2.96a}$$

$$S = S_0' - \alpha_{cu}\rho_c m_{cd} \,, \tag{2.96b}$$

where m_{cd} is the mass of soluble fraction in liquid phase, ρ_c is its proton density, α_{cd} and α_{cu} are proportionality coefficients for the solid soluble fraction in the dissolved and the non-dissolved phase, respectively. In general, they may not be equal. The initial solid and liquid components of the signal are now redefined as

$$S_0' = \alpha_S\rho_S m_{S_0} + \alpha_{cu}\rho_c\Delta M_c \,, \tag{2.97a}$$

$$L_0' = \alpha_m\rho_m\left(m_0 - m_{S_0} - \Delta M_c\right) . \tag{2.97b}$$

For S_0' the first term describes the solid non-soluble fraction and the second term the contribution to the signal coming from the soluble fraction in the solid phase, ΔM_c is the total mass of the soluble fraction in the sample.

The dissolved portion m_{cd} may be obtained from

$$c_s = \frac{m_{cd}}{m_{H_2O} + m_{cd}} \,, \tag{2.98a}$$

where m_{H_2O} is the actual mass of water added, and c_s is the saturation concentration of the water soluble fraction. Then for given ΔM, the portion of water necessary to dissolve the whole soluble proton pool, we get the ΔM_c value

$$\Delta M_c = \frac{c_s}{1 - c_s}\Delta M \,, \tag{2.98b}$$

which due to its linearity, is in general fulfilled for any mass of water added, Δm, giving the mass of soluble fraction in liquid phase Δm_c.

According to Eqs. (2.96–98), the liquid-to-solid component ratio is given by the rational function of $\Delta m/m_0$

$$\frac{L}{S}\left(\frac{\Delta m}{m_0}\right) = \frac{\beta_m\left(1 - p_{S_0} - \dfrac{c_s}{1-c_s}\dfrac{\Delta M}{m_0}\right) + \left(1 + \beta_{cd}\dfrac{c_s}{1-c_s}\right)\left(\dfrac{\Delta m}{m_0}\right)}{\beta_S p_{S_0} + \beta_{cu}\dfrac{c_s}{1-c_s}\left(\dfrac{\Delta M}{m_0} - \dfrac{\Delta m}{m_0}\right)} \,, \tag{2.99}$$

where β_{cd} and β_{cu} are, measured in units of water, effective proton densities of solid soluble fraction in liquid and solid phase, respectively

$$\beta_{cd} = \frac{\alpha_{cd}\rho_c}{\alpha_{H_2O}\rho_{H_2O}}, \qquad \beta_{cu} = \frac{\alpha_{cu}\rho_c}{\alpha_{H_2O}\rho_{H_2O}}. \tag{2.100}$$

They may differ if α's are different for soluble fraction in liquid and in solid phase.

Knowing that ΔM of water dissolves the whole solid soluble fraction, the liquid-to-solid signal intensity (expressed as a function of relative mass increase for $\Delta m > \Delta M$) becomes linear again

$$\frac{L}{S}\left(\frac{\Delta m}{m_0}\right) = \frac{1}{\beta_S p_{S_0}}\frac{\Delta m}{m_0} + \frac{\beta_m\left(1-p_{S_0}\right)+\left(\beta_{cd}-\beta_m\right)\dfrac{c_s}{1-c_s}\dfrac{\Delta M}{m_0}}{\beta_S p_{S_0}}. \tag{2.101}$$

If a wide range of hydration is recorded, covering the range of applicability of both Eqs. (2.99) and (2.101), then most of the parameters may be fitted with acceptable accuracy.

In the case of horse chestnut bark and pine bark hydration, any attempts to fit the composed non-linear dependence given by (2.99) and (above the $\Delta M/m_0$) by (2.101) fail; the procedure diverges giving no reasonable values of β_S and p_{S_o}.

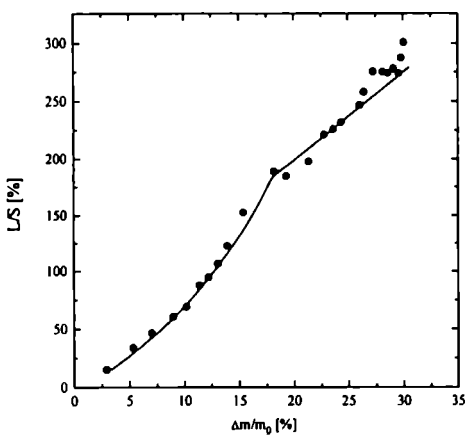

Fig. 2–25. The ratio of total liquid L to solid S ratio expressed as a function of relative mass increase at sample hydration ($\Delta m/m_0$) for horse chestnut bast (native sample).

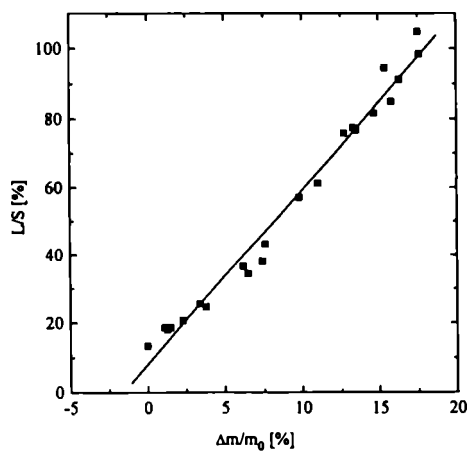

Fig. 2–26. The ratio of total liquid L to solid S ratio expressed as a function of relative mass increase at sample hydration ($\Delta m/m_0$) for horse chestnut bast sample with the hydrophilic part of extractive fraction washed out.

A horse chestnut bast is an example of biological system (tissue) in which the existing water soluble solid fraction [347, 621] is limited in mass and the effect of dissolution is not accompanied by other processes as it is in case of primary stages of seed imbibition (see Chpts. 2.5.9, 2.5.12).

The hydration ($\Delta m/m_0$) dependence of relative liquid component contribution (L/S) is non-linear (see Fig. 2–25), meaning that the solid component signal intensity S is no longer a simple standard for liquid component estimation. To evaluate the parameters describing the sample with water soluble fraction one can use the following. From the Fig. 2–22b one may read the contribution of non-removable liquid portion, which is $L_3/S = 0.02$. To calculate the relative mass contribution of this proton fraction one should apply the hydration dependence of liquid signal in horse chestnut bast washed out from the water soluble fraction (Fig. 2–26). The slope is 5.128 which gives the fraction of protons in non-removable liquid fraction as $1 - p_0 = 0.004$, which is the value close to the values obtained for horse chestnut and pine bark (Table 2–11a). Thus, if $p_0 = 0.996$ the Eq. (2.94) gives the relative proton density of the solid matrix as $\beta_S = 0.196$. From the Eqs. (2.94) and (2.101) one can get p_{S_0}, the fraction of solid matrix non-soluble protons

$$p_{S_0} = \frac{w}{u} \cdot p_0 , \tag{2.102}$$

where u and w are the slopes of the L/S hydration dependencies in horse chestnut bast sample containing the water soluble fraction and the one washed out from the water soluble fraction, respectively. We get for horse chestnut bast $p_{S_0} = 0.672$. Thus, we can calculate the relative mass of the water soluble fraction

$$\Delta M_c/m_0 = 1 - p_{S_0}/p_0 = 0.325 . \tag{2.103}$$

Taking into account the mass of water necessary to dissolve the whole water soluble solid fraction ($\Delta M/m_0$=0.18), we get the saturation concentration of the water soluble fraction in horse chestnut bast as $c_S = 0.643$.

The relative proton density of the water soluble solid fraction may be easily (with low χ^2 per degree of freedom) fitted using a rational function (Eq. 2.99) for $\Delta m < \Delta M$ and a linear function, Eq. (2.101) above ΔM. The obtained values are shown in Tab. 2–11b.

Table 2–11b. The fitted values of the relative proton densities for the water soluble solid proton fraction in solid, β_{cu}, and liquid, β_{cd}, phase. Fits were done for $p_{S_0} = 0.672$, $c_S = 0.643$, $\Delta M/m_0 = 0.180$ and $\Delta M_c/m_0 = 0.325$ (see text). The coefficient $\eta = \frac{\beta_{cu}}{\beta_{cd}}$.

β_M	β_{cd}	β_{cu}	η
Horse chestnut bast			
0.3	0.224±0.010	0.465±0.066	2.08
1	0.215±0.010	0.476±0.067	2.21
1.8	0.206±0.010	0.489±0.067	2.37
(absolute signal intensity vs. Δm)			
1	0.254	0.549	2.16

2.5.8 Absolute NMR signal measurement of water soluble solid fraction in bast

If the amplification of the NMR spectrometer is stable in time and kept constant over the whole time range of bast hydration experiments, the fitted values obtained from Eqs. (2.99) and (2.101) may be compared with the parameters directly calculated from Eqs. (2.96–97) from the absolute liquid and solid NMR signal. Fig. 2–27 shows the hydration dependency of FID intensity for total (L+S) signal and its liquid (L) and solid (S) components.

The relative proton density of water soluble fraction in the solid phase may be expressed by

$$\beta_{cu} = \frac{\left|\frac{\partial S}{\partial m}\right|_{\Delta m<\Delta M}}{\left.\frac{\partial L}{\partial m}\right|_{\Delta m>\Delta M}} \left(c_S^{-1} - 1\right) . \tag{2.104}$$

For horse chestnut bast in solid phase we get $\beta_{cu} = 0.549$, which matches with the relative proton density for carbohydrates (with a dominant sucrose part) calculated from the chemical formula (Table 2–10).

The relative proton density of the water soluble fraction in liquid phase differs from the value in solid phase if the ratio, $\eta = \frac{\beta_{cu}}{\beta_{cd}}$, differs from 1. One can get this ratio from

$$\eta = \frac{\beta_{cu}}{\beta_{cd}} = \frac{\left|\frac{\partial S}{\partial(\Delta m)}\right|_{\Delta m<\Delta M}}{\left.\frac{\partial L}{\partial(\Delta m)}\right|_{\Delta m<\Delta M} - \left.\frac{\partial L}{\partial(\Delta m)}\right|_{\Delta m>\Delta M}} . \tag{2.105}$$

For horse chestnut bast $\eta = 2.16$, which gives (2.104) the effective proton density of the water soluble fraction in a liquid phase as $\beta_{cd} = 0.254$.

Comparing the values of the relative proton densities of water soluble solid fraction in liquid and in solid phase fitted from equations (2.99) and (2.101) to the values obtained from absolute signal intensity, one can see that the fits give the values underestimated roughly about 20%.

The fraction of solid matrix non-soluble protons, p_{S_0}, may be independently calculated from

$$p_{S_0} = \frac{S|_{\Delta m>\Delta M}}{m_0 \left.\frac{\partial L}{\partial(\Delta m)}\right|_{\Delta m>\Delta M}} \beta_S^{-1} . \tag{2.106}$$

The obtained from Eq. (2.106), $p_{S_0} = 0.671$, is very close to the one evaluated from Eqs. (2.102–103).

The difference between the effective proton density for the solid soluble fraction in dissolved (β_{cd}) and solid (β_{cu}) phase may be caused by two reasons: (i) the presence of paramagnetic impurities in the system and (ii) the composition of the soluble fraction in the solid phase, in a gel-like molecular network which bonds water so tightly that the water signal resembles that for solid.

If the second case occurs, bast dehydration should result in water being squeezed from the gel-like structure, and this should be manifested as a flat or constant dependence of the liquid signal versus mass of water added ($\Delta m/m_0$).

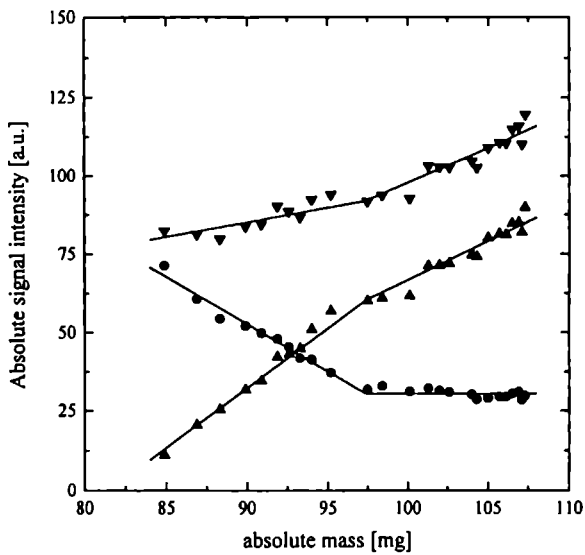

Fig. 2–27. The hydration dependence of the absolute (in arbitrary units) FID signal (L+S) and its liquid (L) and solid (S) components measured versus mass increase for hydrated horse chestnut bast. The mass of the sample at which the L_1 component disappeared at dehydration was $m_0 = 82.4$ mg, the mass of water at which the change of the slopes of L and S hydration dependencies occurs is $\Delta M = 14.818$ mg, thus the threshold hydration is $\Delta M/m_0 = 0.180$. For $\Delta m < \Delta M$ the total solid signal S is fitted by the function: $S(m) = (294\pm12)+(-2.71\pm0.13)\cdot m$, whereas the liquid signal L by the function: $L(m) = (-327.5\pm15.3)+(3.995\pm0.168)\cdot m$. For $\Delta m > \Delta M$, the solid signal was constant: $S = 29.7\pm0.4$, and the liquid signal L was fitted by the function: $L(m) = (-209\pm21)+(2.74\pm0.20)\cdot m$.

If paramagnetic species, transported from the solid to the liquid phase, are responsible for the dependence $\beta_{cd} < \beta_{cu}$, this means that their efficiency in quenching the NMR signal is much higher in the hydrated phase. Similar magnification of paramagnetic relaxation, was observed when the paramagnetic

manganese ion migrated from a thylakoid membrane to aqueous medium [55, 381]. Also in hydrating Portland concrete paste the paramagnetic impurities transformed to liquid phase drastically increase their effect resulting in quenching of proton signal [451, 574, 594]. The content of metal ions in bark is relatively high, i.e., manganese makes up to 0.1% of outer bark dry mass [202]. If the observed effect is due to paramagnetics, for hydration above upper dissolution threshold $\Delta M/m_0$, at which point the whole paramagnetic pool present in the water soluble fraction is transferred to aqueous phase and no external paramagnetic fraction is added, one should observe an increase in the slope of the plot of total NMR signal versus mass of water added. The upper curve on Fig. 2–27 shows that this is the case.

The EPR measurement directly revealed the presence of paramagnetic centers in all samples investigated (see Chpt. 2.5.4).

The saturation concentration $c_s = 64.3\%$ calculated for water soluble fraction is little lower than that for a sucrose (66.8% at $+20^0$C [721]), however, it is the mean value for all carbohydrate soluble fractions present in chestnut bast. The solubility of each varies over a wide range, starting, for example, from poorly soluble callose [192] up to readily soluble sucrose. The measured value suggests, however, that the sucrose pool dominates in water soluble solid fraction. On the other hand, the value of the relative proton density cannot differentiate the carbohydrates as is close for several carbohydrate pools.

2.5.9 Seed structure and composition

The seeds of most species during the last stage of maturation lose almost all their water. Being desiccated, seeds can withstand harsh environmental conditions and remain viable for prolonged periods of time. After rehydration seeds recover their metabolism and start germination processes. In contrast, desiccation of other plant tissues and organs leads to death [247, 624]. The ability of deep dehydration and rehydration focuses ones attention on a seed as a system approaching some molecular limits of life.

Wheat seed is consisted of *embryo*, starchy *endosperm* and *pericarp*. The proportions of these constituents remain close independently whether seed is air-dry or hydrated (see Tab. 2–12).

Table 2–12. Weight contribution of selected wheat seed fractions in dry and hydrated ($\Delta m/m_0 = 0.42$) forms, calculated as the average over 20 randomly selected seeds [289].

Wheat seed:	Embryo	Starchy endosperm	Pericarp
Air-dry	1.8%	73.2%	25.0%
Hydrated	2.0%	73.9%	24.1%

Seed contains proteins, nucleic acids, fats and carbohydrates. The major carbohydrate constituents are starch and cellulose. Starch, $(C_6H_{10}O_5)_n$, is main constituent of endosperm and may consist up to 80% of seed dry mass. Pericarp contains majority of seed cellulose, which forms cell walls. Other seed components are alcaloids, glycosides, tannins, etc.

Although wheat seed dehydrates to very low level during storage in an air-dry state ($\Delta m/m_0 = 0.095 \pm 0.005$), water distribution in seed is highly non-uniform. Whereas the starchy endosperm and pericarp are dehydrated, the embryo is still hydrated to relatively high level, and in macroscopic observation it seems to be 'oily' [289]. The macro-observations correlate with the seed micro-scale behavior. The 'oil-lake' component of EPR signal drastically decreases with drying of embryo cells of nonviable seeds, while dried samples from viable seeds retain the 'oil-lake' EPR signal (due to spin-label molecules located in liquid crystalline lipid domains, including so-called lipid bodies) [247].

Also at seed imbibition the spatial distribution of the hydration caused effects is observed. EPR imaging with natural spin probes (soil humic substances) performed on wheat seed imbibed and germinated in moist soil samples for two days, and then subsequently dried at 60^0C for about 10 h, show the non-uniform density of deposited spin probes, with the maxima near the germ and vascular bundle [625].

2.5.9.1 Initial stages of seed imbibition

The seed in primary stages of imbibition (consisting of water uptake and subsequent swelling of seed volume) shows a snap-shot of a living system activating from anabiosis [40]. As the enzymatic activities require the presence of sufficient amount and arrangement of proximal water, the initial stages of seed imbibition are thought to have a 'physical' or 'semi-physical', passive nature. If so, the water absorption process plays the triggering role for the chain of biochemical reactions, and that is why the exact analysis of water uptake at initial phases of seed imbibition is necessary in the understanding of all processes of life activation from anabiosis in seed. It is also understandable that the processes occurring in grain at extremely low hydration will have at primary stages a 2-d character.

The hydration stages of seed are characterized by [2]:

(i) the appearance of active metabolism at low hydration level;

(ii) complex multistage process of imbibition;

(iii) the long duration of the 'physical stage' during the imbibition;

(iv) the presence of 'physical stage' during the maturation of seeds.

Autoradiography data show that water penetrates whole volume of wheat seed for 6–8 hours.

Assuming that whole seed dehydrates to extremely low level, Simon, [617], has suggested that in dehydrated state cell membranes are unable to function as selective permeability barriers, which is a consequence of a membrane lipid phase transition from a lamellar to a hexagonal phase upon dehydration. Thus, seed imbibion involves a phase transition which in turn leads to reconstitution of

cellular membranes. However, X-ray diffraction and ^{1}H–NMR spectra for soybean (*Glycine max* L.) seed did not confirmed this hypothesis. Polar lipid extract as well as cotyledon membranes retain the bilayer organization when dehydrated [602].

However, there exist a strong effect of dehydration on seed membranes. The comparative EPR spin label study of dried and hydrated wheat embryos of viable (germination index equal 90%) wheat seeds and ones with low extent of germination after long-term storage (germination index 0%) shows that loss of seed viability correlates with the loss of external membrane integrity [247]. DSC data show that seed viability correlates with the reduction of the energy of the lipid melting, which may be caused either by the alteration of lipid chemical composition, or change in lipid physical arrangement during storage of the seed [685].

2.5.9.2 Kinetics of wheat seed imbibition

The effectiveness of initial stages of seed imbibition depends on the wetting conditions. It differs in mass increase and the rate of the process. This Author tested the effectiveness of following methods of hydration on wheat seeds [289]:

(a) for the wheat seed soaked (at active gas exchange, between two layers of blotting-paper placed in closed Petri dish), which is the closest simulation of natural conditions;

(b) completely immersed in water; and

(c) placed over the water surface (relative humidity $p/p_0 = 100\%$).

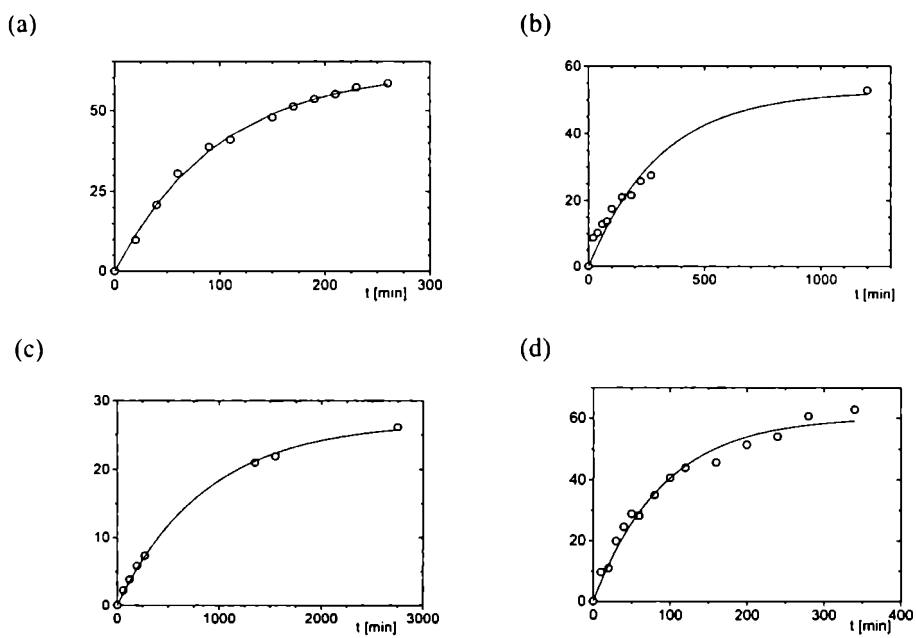

Fig. 2–28. Wheat (cv."Jara") seed hydration expressed as relative mass increase ($\Delta m/m_0$) versus time t: (a) – seed soaked between two layers of blotting paper; (b) – seed completely immersed in water; (c) – seed hydrated over the water surface (at p/p_0=100%); (d) – seed soaked in D_2O (procedure as (a)).

The isotope effect on imbibition kinetics was tested for wheat seed hydrated in D_2O according to protocol (a).

The hydration dependence of wheat seed with sufficient accuracy may be fitted by a single exponential function (see Fig. 2–28)

$$\Delta m / m_0 = A \cdot \left(1 - e^{-t/T}\right), \tag{2.107}$$

where T is characteristic time (here $k = T^{-1}$ is kinetic constant), and A maximal mass increase. However, one cannot exclude the very fast component which may cause initial rapid mass increase of about $\Delta m/m_0 \approx 5\%$, but two-exponential fits of mass increase time dependence diverged. Tab. 2–13 shows the results of fits to hydration courses. One sample (sample (2) hydrated from gaseous phase) showed deviations from single exponential form of hydration function for long times of hydration, which may be caused by individual specificity or triggered germination. In fact, maximal mass increase, A, should by treated only as a potential one, as for sufficiently long times normal growth of plant starts.

Table 2–13. Wheat seed hydration kinetics [fitted from Eq. (2.107)] for various hydration protocols.

Sample		A	T [min]	$k \cdot 10^3 [min^{-1}]$
Seed wetted on blotting paper				
(H_2O)	sample (1)	0.62±0.02	98±5	10.20±0.52
	sample (2)	0.39±0.02	108±12	9.26±1.03
Seed immersed in H_2O				
	sample (1)	0.58±0.02	357±29	2.80±0.23
	sample (2)	0.55±0.02	315±29	3.17±0.29
	sample (3)	0.45±0.02	254±25	3.94±0.39
	sample (4)	0.52±0.02	300±31	3.33±0.34
Seed hydrated over H_2O surface				
	sample (1)	0.268±0.005	862±42	1.16±0.06
	sample (2)	0.22±0.02	474±53	2.11±0.24
Seed wetted on blotting paper				
(D_2O)	sample (1)	0.35±0.01	78±5	12.82±0.82
	sample (2)	0.60±0.02	90±7	11.11±0.86

The most effective hydration (high A and k) is obtained from aqueous phase and simultaneous air contact with the hydrated seed when the gas exchange is not hindered by the aqueous medium fully covering the grain. The seed hydrated from gaseous phase ($p/p_0 = 100\%$) increases its mass, however, with lower rate and to a low level which is not sufficient to trigger the living processes and growth of the seed. Worth mentioning is the high effectiveness of hydration in D_2O, for some cases even faster than hydration in H_2O. Additionally, Tab. 2–13 shows that water uptake is equally effective for starchy endosperm, pericarp and embryo of wheat

seed. For long times and the high hydration level ($\Delta m/m_0 > 0.60$) the germination process may interfere with the observed imbibition effects [400].

The hydration courses recorded for several wheat seeds (within the same variety "Jara") show significant individual differences of relative mass increase $\Delta m/m_0$ (and also of the proton spin-spin T_2^* values, see Chpt. 2.5.11). Therefore, it seems that more convenient parameter describing the hydration phenomena is not the time t of imbibition but the relative mass increase $\Delta m/m_0$.

Other gravimetric and NMR experiments show that either hydration in H_2O or D_2O show the presence of a very fast component in wheat seed hydration kinetics [398, 399]. Also EPR spin label spectra of prepared wheat embryo (initially hydrated to $\Delta m/m_0 = 0.13$) suggest two-exponential kinetics of spin label transport, if the embryo was taken from a seed soaked for 5h prior to preparation. However, without soaking period, spin-label transport process interferes with the initial stages of seed imbibition, which results in more complicated form of the dependency. Moreover, this experiment required relatively high concentration of ferricyanide (80 mM), which may additionally influence the initial stages of hydration [624].

2.5.10 Water bound in seed

Basing on DSC studies performed on pea (*Pisum sativum*) and soybean (*Glycine max*) cotyledons, Vertucci, [684], suggested the following classification of hydration levels of cotyledon:

hydration level '1' in the range between 0 and 0.12 for pea cotyledons, and 0–0.08 for soybean, as expressed in $\Delta m/m_0$ units;

hydration level '2' in the range 0.12–0.24 for pea, and 0.08–0.21 for soybean;

hydration level '3' in the range 0.24–0.35 for pea, and 0.22–0.33 for soybean;

hydration level '4' in the range 0.35–0.58 for pea, and 0.33–0.55 for soybean; and

hydration level '5' above 0.58 for pea, and above 0.55 of $\Delta m/m_0$ for soybean cotyledon.

Hydration level '1' and '2' are distinguished from the other hydration levels because here water does not freeze or melt. Water in '1' has an apparent heat capacity less than that of pure water, but greater than that of ice, whereas water in '2' reveals heat capacity greater than that of liquid water.

Water is first observed to melt in hydration level '3', although no freezing exotherms are recorded during cooling runs. It is suggested that the thermal behavior of water differs in '3' for pea and soybean. This may be caused by differences in freezing resistance of pea, which reveals no reduction in germination after cooling down to -80^0C at $\Delta m/m_0 = 0.36$; and of soybean, which survives exposition to -30^0C but is killed by freezing down to -50^0C, at the respective hydration level.

Thermal properties of water in seeds at the hydration level '4' are similar to those of pure water. However, water in '4' is still distinguishable from bulk water in that the apparent energy of the melting is less than that of pure water.

The apparent thermal properties measured at '5' resemble those of water in diluted solutions. Although cotyledons still take up water, the properties of water do not change substantially, which suggest that seed is in '5' fully hydrated.

2.5.11 Proton NMR of seed hydration

The NMR measurements of cowpea seed imbibition [80, 81, 166, 167, 453] were performed using low power spectrometer designed for liquid signal detection (Carr-Purcell-Meiboom-Gill train of pulses [108]). This method is useful for water compartmentation in tissue [10, 17]. Pulsed gradient spin echo technique in ears prepared from germinated (14 days) wheat seed detected the volume water flow of about $0.06 \cdot 10^{-3}$ mm^3 s^{-1}, *in situ* [338]. Pulsed field gradient NMR supplied the values of self-diffusion coefficient, equal $D = (6.1 \pm 0.2) \cdot 10^{-10}$ m^2 s^{-1} for wheat seed endosperm hydrated from gaseous phase at relative humidity, $p/p_0 = 98\%$, but rapidly decreasing below $D = 2 \cdot 10^{-10}$ m^2 s^{-1} at relative humidity equal $p/p_0 = 88\%$ [100].

However, in these measurements solid protons, and at extremely low hydration single layer of immobilized water were not observed, but protons of liquids only. Moreover, the restrictions of low power spectrometers made impossible the proper explanation of unusual increase of liquid proton signal (observed in hydrated cowpea by Di Nola et al., 1991). This Author applied the high power relaxometry, which allowed the direct observation and proposed a quantitative model to describe the effect of solid water soluble fraction [289].

2.5.11.1 Proton free induction decay of wheat seed

Fig. 2–29 shows the typical FID for a wheat seed, consisting of two components: a Gaussian one (S) due to protons of the solid matrix of the seed and an exponential one (L) coming from protons of liquid components of the seed. The liquid signal components with T_2 longer than ~1ms are not differentiated by the measurement of T_2^* from FID [see Eq. (2.71)]. However, the T_2^* value of the solid component (halfwidths) is not changed; also the proportion of liquid and solid signals is equal to the proportion of protons in both proton pools (in the absence of paramagnetic impurities).

Fig. 2–30 shows the hydration ($\Delta m/m_0$) dependence of T_2^* for solid signal component of a wheat seed. For every type of hydration the value of T_2^* changes only weakly with mass increase, which means that the solid matrix of the seed (mostly starch body) is not much affected by water added in regions which are not digested or dissolved. Thus, the amplitude of the solid S component was used as an unit to measure the liquid proton fraction L.

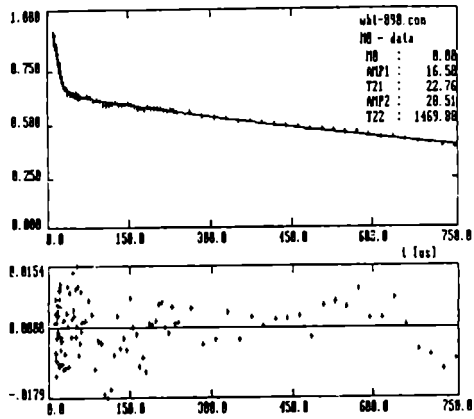

Fig. 2–29. a) Proton FID for wheat (*Triticum aestivum* L.) seed hydrated for 90 min (protocol (a), see text) to $\Delta m/m_0$ = 38.7%. The resonance frequency was 30 MHz; output power 400 W; the detection mode: phase sensitive; $\pi/2$ length was 1.05 μs; the temperature stabilized in gaseous nitrogen flow at 25°C. Data analyzed using the FID analyzing procedure of CracSpin [703]. The values of fitted parameters are given in inset, the fitted function was

$$M(t) = M0 + Amp1 \cdot \exp\left[-(t/T_{21})^2\right] + Amp2 \cdot \exp(-t/T_{22}).$$

(b) The residual function calculated as a difference between the fitted and recorded values of FID signal, which in any recorded point does not exceed 1.54%.

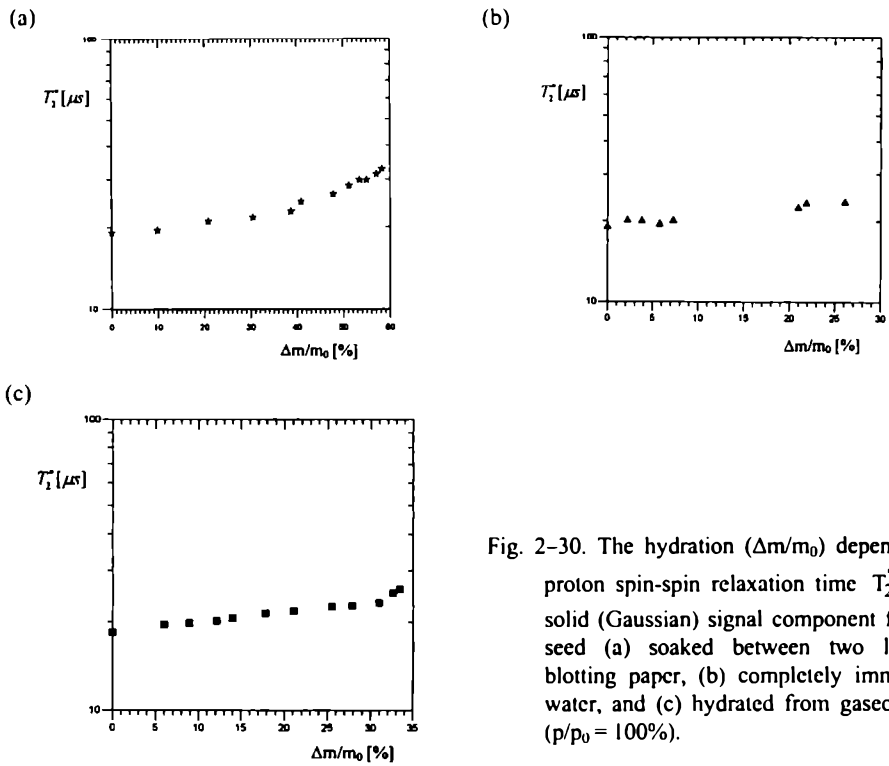

Fig. 2–30. The hydration ($\Delta m/m_0$) dependence of proton spin-spin relaxation time T_2^* for the solid (Gaussian) signal component for wheat seed (a) soaked between two layers of blotting paper, (b) completely immersed in water, and (c) hydrated from gaseous phase (p/p_0 = 100%).

Fig. 2–31 shows the hydration dependence of the spin-spin relaxation rate $R_2^* = \left(T_2^*\right)^{-1}$, for the liquid FID component. The R_2^* continuously decreases for hydration increased up to $\Delta m/m_0 \approx 0.20$; then it reaches a plateau suggesting that the new hydrated state was reached and only the amount of hydrated substance increases as the hydration is further increased. This hydration level correlates with that needed to appearance of freezable water in pea and in soybean cotyledon [684].

At $\Delta m/m_0$ = 0.30–0.50 (for wheat seed hydrated on blotting paper) R_2^* rapidly decreases, which may reflect the germination starting in the wheat seed; as so high hydration is reached after a relatively long time, and because this threshold is observed at individually different hydration levels.

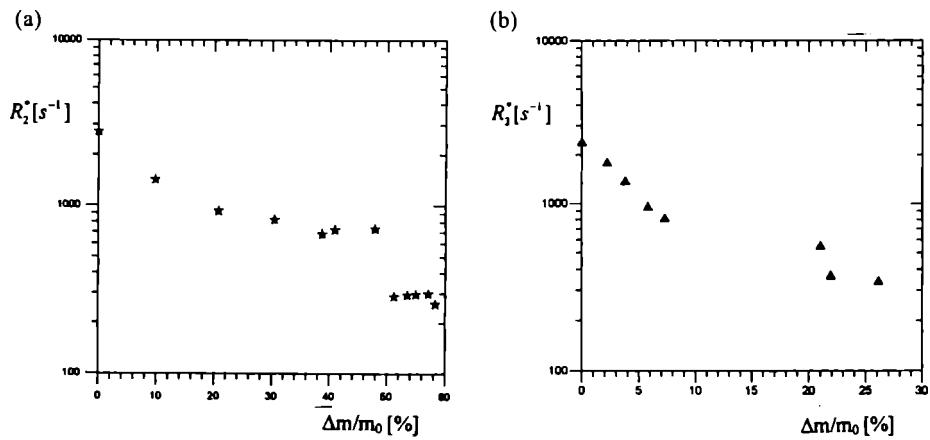

Fig. 2–31. The hydration ($\Delta m/m_0$) dependency of the spin-spin relaxation rate R_2^* of liquid (L) FID signal component for wheat seed hydrated (a) at air access or in atmosphere of (b) saturated water vapor (at p/p_0 = 100%).

In no case was the decomposition of the liquid FID component on subsystems possible, which is in contrast to results obtained for other ultra-dry biological systems such as lichen thallus [272, 273], bark and bast [290], shell of molusc [281], or the surface of porous glass [283], where the short liquid component ($T_2^* \approx 100$ μs) due to the first water layer may be separated. This makes the gel-like starchy endosperm of wheat seed similar rather to the other systems without a well defined rigid surface in which one averaged relaxation time for liquid protons is observed (as for the gel medium of eye lenses).

2.5.12 Presence of high amount of water soluble fraction

The rational function from Eq. (2.99) fits very well the sets of wheat seed hydration data either at hydration from aqueous phase under the access of air (on blotting

paper) or by placing in atmosphere of saturated water vapor (at $p/p_0 = 100\%$) (Fig. 2–32). However, the number of parameters and their interdependencies exclude practically unambiguous determination of all of them. Assuming that all liquid protons in the dry seed are water protons (localized mostly in embryo and pericarp), the initial seed hydration may be derived from L/S at $\Delta m/m_0 = 0$, remembering that relative proton densities for both solid proton pools should be of about $\beta_S \approx \beta_{cu} \approx 0.56$ (as for polysaccharides, see Tab. 2–10). The obtained initial water content: $\Delta m/m_0 = 0.10$, 0.095 and 0.09 for wheat seed hydrated at $p/p_0 = 100\%$, under the access of air and immersed in water, respectively, was equal air-dry hydration level for the respective seeds.

In developing seed the process of dissolution of water soluble solid is accompanied by enzyme action and by starting of germination process, which limits the data obtained from the proposed model.

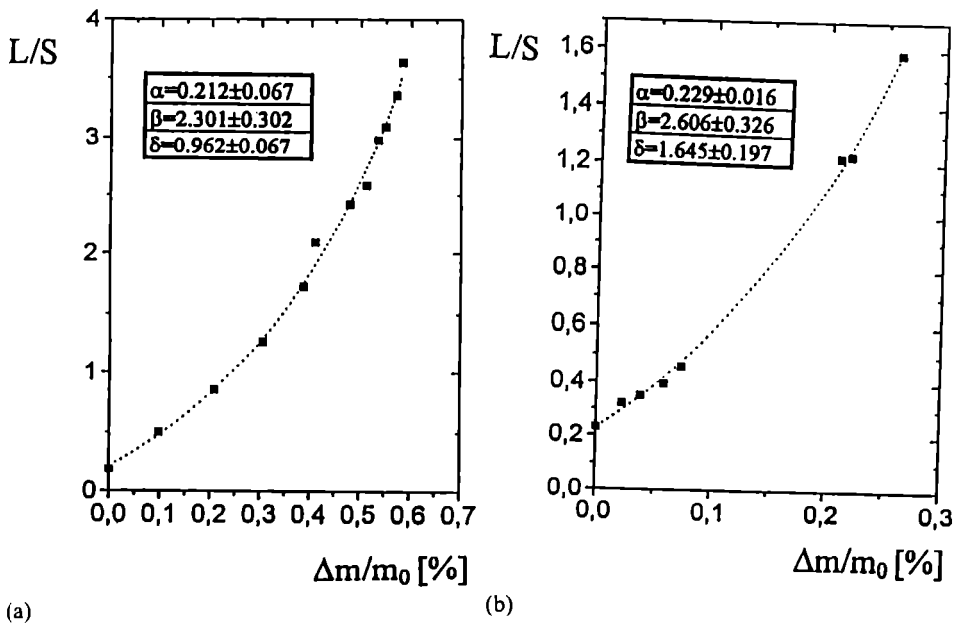

Fig. 2–32. The hydration ($\Delta m/m_0$) dependence of liquid (L) proton signal expressed in units of solid (S) component for wheat seed hydrated (a) on blotting paper and (b) by placing in atmosphere of saturated water vapor (at p/p_0=100%). The solid lines were obtained by fitting the rational function: $\frac{L}{S} = \frac{\alpha + \beta \cdot \frac{\Delta m}{m_0}}{1 - \delta \cdot \frac{\Delta m}{m_0}}$.

The values of parameters fitted are given in insets.

2.5.13 Hydration in D_2O in presence of water soluble solid fraction

The dilution of the system in D_2O enables the analysis of the soluble fraction of solid matrix present in the system. If the system is hydrated from aqueous phase, the "parasitic" H_2O contribution is significantly reduced. The convenient quantity to analysis will be S/(L+S) hydration dependence, as the total proton signal of the seed is, in first approximation, constant. Thus, the relative contribution of solid signal S/(L+S) versus the hydration of the sample is shown by the following dependency

$$\frac{S}{L+S}\left(\frac{\Delta m}{m_0}\right) =$$

$$= \frac{\beta_S p_{S_0}(1-\alpha) + \beta_{cu}\frac{c_S}{1-c_s}\frac{\Delta M}{m_0} - \frac{\beta_S p_{S_0}\alpha}{1-p_{S_0}-\frac{c_S}{1-c_s}\frac{\Delta M}{m_0}}\frac{\Delta m}{m_0} - \beta_{cu}\frac{c_S}{1-c_s}\frac{\Delta m}{m_0}}{\left(1+(\beta_S-1)p_{S_0}+(\beta_{cu}-1)\frac{c_S}{1-c_s}\frac{\Delta M}{m_0}\right)}, \quad (2.108)$$

where α is the proportion of exchangeable groups in the solid non-solvable part of seed, and

$$\frac{\frac{\Delta m}{m_0}}{1-p_{S_0}-\frac{c_S}{1-c_S}\frac{\Delta M}{m_0}}$$

expresses the ratio of water deuterons to water protons.

Fig. 2–33 shows the S/(L+S) versus relative mass increase for a wheat seed hydrated from aqueous phase of D_2O with access to air. S/(L+S) decreases linearly, according to Eq. (2.108). The linear form of the solid component magnitude decrease means that the processes of starch decomposition in endosperm occur as functions of the mass of water absorbed, depending less on the time interval of the decomposition, meaning that the concentration of product slows down the process.

Di Nola et al., 1991, measured the time course of proton liquid signal arising after immersion the cowpea seed in D_2O. The proton signal increased from zero as a function of time. Their measurements were done using the NMR spectrometer designed for measurements of the signal for liquids only. Therefore, the tightly bound water pool which is usually present in native samples could not be detected. However, the qualitative conclusion of part of solid signal transferred to the liquid signal pool was right. As the hydration was performed at excess of water they could monitor the kinetics of the process. However, they could not monitor the quantitative dependence of the amount of the solid signal transferred to the liquid proton pool as a function of the mass of water added. Thus, their results

did not give quantitative values of parameters as they have no internal meter-stick (solid signal) to scale the amplitude of liquid signal.

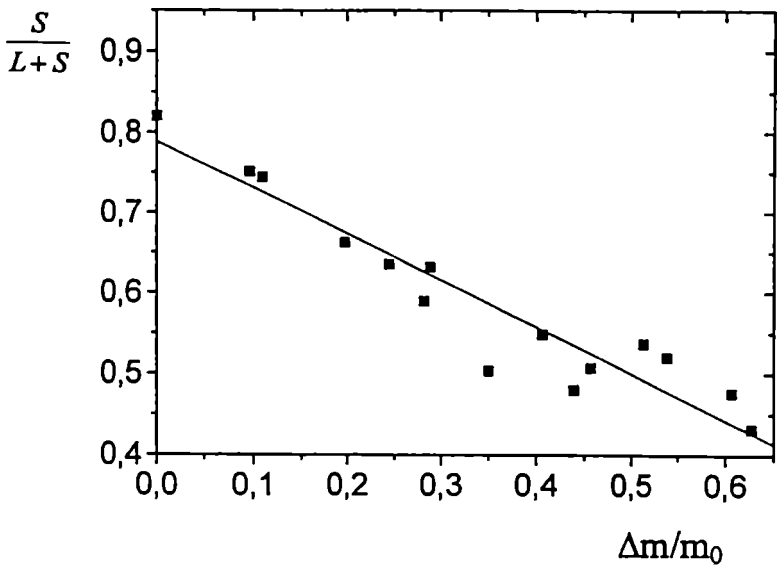

Fig. 2–33. The hydration ($\Delta m/m_0$) dependence of solid (S) signal expressed in units of total (L+S) proton signal for the wheat seed hydrated in D_2O between two layers of blotting-paper. The fitted linear function was: $S/(L+S) = A+B\cdot(\Delta m/m_0)$, at $A = (0.789\pm0.019)$, $B = -(0.578\pm0.04)$ and correlation coefficient equal $\gamma = -0.95$.

However, from the finding that the amount of solid matrix transferred to liquid pool is a linear function of mass of water taken up the by seed, allowed to obtain from Di Nola's data characteristic times for native and cooked cowpea immersed in D_2O, which is $T = 27$ min for native and $T = 67$ min for cooked (at 105^0C for 12 h) sample. The value for native sample differs from the one obtained by gravimetry for wheat seed. The difference may come from the different envelope constitution for both species. The difference between the cowpea samples came most probably from the irreversible structural changes of cowpea seed surface due to drastic preheating. These fits of Di Nola's data suggested the presumed non-zero contribution of the liquid signal at zero-time which may suggest the presence of fast process at beginning of hydration. The fast component consists of 18% of total liquid signal after hydration for native cowpea and 16% for cooked cowpea sample. Most likely Di Nola et al. used improper method to calculate the amount of water actually taken in by seed, because there is no evidence that the preheated cowpea seed hydrates to the same level as native one.

3. The dehydration limits of living organism

In search for dehydration limits of living creatures, the attention is focused on microorganisms, seeds, and other species which populate Earth areas experiencing the extreme conditions of low hydration and/or decreased temperature.

Indeed, some bacteria dehydrate to $\Delta m/m_0 = 0.10$ at $p/p_0 = 40\%$, and to $\Delta m/m_0 = 0.03$ at $p/p_0 = 30\%$ [545]. Desiccated colonies of cyanobacterium *Nostoc commune* dehydrate at freeze-drying to $\Delta m/m_0 = 0.06$ [545]. These low values suggest that there may exist living organisms dehydrating below the coverage of single water monolayer. Beside experimental difficulties in preparation of the samples of bacterial spores, one may expect several pecularities differentiating bacterial structures from other organisms even on molecular level.

Among macro-organisms, seeds should be taken into account. However, for two reasons seed also is not the best system for investigations of extremes of life. (i) They are juvenile forms of living creatures, what may limit the conclusions obtained from the observations of their dehydration and freezing protection properties. (ii) Although wheat seed dehydrates to a very low level in anabyotic form, water distribution in dry seed is non-uniform. Whereas starchy endosperm and pericarp are dehydrated, embryo still retains a measurable hydration level (see Chpt. 2.6.9).

The lichens, mostly Antarctic and Arctic species, have been chosen, because in contrast to freezing tolerant vascular plants, which stop their photosynthetic activity during winter, lichen species can be photosynthetically active and productive even if the tissue is frozen. Photosynthetic CO_2 exchange can be activated during frost by snow, however, strong light on clear days may inhibit their photosynthetic apparatus.

To emphasize the scale of lichen adaptation, in following Chapters the detailed description of their abilities is presented: freezing tolerance and freezing protection (Chpt. 3.1.3); photosynthetic activity performed at the temperatures below 0^0C (Chpt. 3.1.4), and below the ice heterogeneous nucleation point of thallus fluids (Chpt. 3.1.5); stimulated ice nucleation in thallus resulting in increased water deposition; resistance to acute water stress (Chpt. 3.1.7); effective intake of water from gaseous phase; spontaneous dehydration to gaseous phase to the hydration level significantly lower than that needed to stop living processes in

thallus; ability to take up water directly from snow (Chpt. 3.1.6). As a comparison, freezing protection mechanisms (Chpt. 3.1.2) and methods of photosynthesis level enhancement (Chpt. 3.1.1) of free living algae are discussed.

3.1 Lichens

Lichens are symbionts of a heterotropic fungal partner (majority of them belonging to *Ascomycotina* and some to *Basidiomycotina*) and a photosynthetic autotroph, that may be either a microalga, a cyanobacterium or in some cases both [317]. The fungal partner is often called *mycobiont* and algal partner *photobiont*. The names given to lichens refer to mycobiont; photobionts may have then a separate scientific name. Fungus forms a structure of the lichen organism (*thallus*), whereas photobiont supplies carbohydrates for both partners (Fig. 3–1). Recently, lichens are not treated as distinguished taxonomic group, but involved in fungal kingdom as *lichenized fungi*.

Dry thallus resembles porous system. The porosity of lichen thalli family *Umbilicariaceas*, as estimated using mercury intrusion porosimetry, varied between 30% for *Lasallia hispanica* Frey, down to 10% for *Umbilicaria cinereorufescens* (Schaer.) Frey [678].

Different photobionts of the same mycobiont reveal another behavior, e.g., the green algal and the cyanobacterial photobionts of *Placopsis contortuplicata* within the same thallus differ in response of PS II photochemical efficiency to hydration [596].

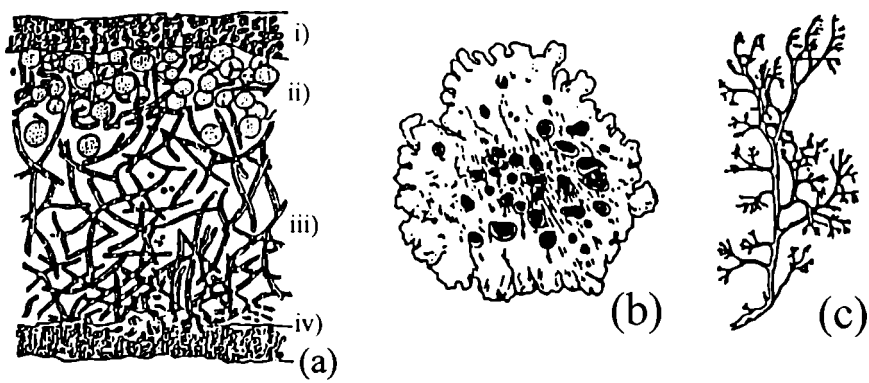

Fig. 3–1. Scheme of lichen structure: (a) crossection of thallus, (i) upper cortex, (ii) algal layer (photobiont cells embedded in fungus body), (iii) medulla, (iv) lower cortex; main types of structure of lichens investigated: (b) foliose, (c) fruticose.

A question arises, whether a lichen is a mutualistic system with both partners equally benefiting from each other or is a system that results from a parasitic nature of the mycobiont. Indeed, the analysis of the lichen's water

relations, CO_2 exchange, and response to strong light suggest that photobiont derives minor benefits from the mycobiont. In lichen reduction of the photobiont may never reach the level of chloroplast. However, the mycobiont supresses sexuality of photobionts, thus, restricting their evolutionary progress, and controls its productivity and biomass [363].

Indeed, lichenization is a very successive method of fulfilling by fungi their requirement for carbohydrates. The scale of the success of their strategy is that about 20% of all fungi species are lichenized (13,500 species) [297]. The symbiosis increases the ability of the lichenized organisms to exist in extremely difficult environmental conditions as low temperature, acute water stress, low level of light irradiance (for example, inside eroded rock), or in combination of these environmental stress factors.

The absence of roots (for water uptake) and of epidermis and cuticula (as a water-preserving protection layer) means that lichen metabolic activity (i.e. respiratory and photosynthetic CO_2 exchange) fully depends on external moisture conditions. This primitive organization characterizes lichens as poikilohydrous organisms. However, this combined with their resistance to acute water stress, makes life strategy of lichens advantageous in extremely harsh environmental conditions [360]. The *fruticose* thalli of the genus *Usnea* form shrublets of up to 20 cm length in Antarctica; the *foliose* plate-shaped *Umbilicaria* may reach a diameter of 20 cm in the maritime Antarctic [372]. Thus, very retarded growth of lichens which is the consequence of their organization seems not to be high price for their populational success.

3.1.1 Carbon dioxide concentration mechanism

Many free-living algae and most cyanobacteria have a CO_2 concentrating mechanism (CCM) which operates under conditions of low CO_2 availability in the environment. The CCM is driven by photosynthetic electron transport [614, 633] and functions to accumulate an internal pool of inorganic carbon, which is subsequently used to increase the CO_2 carboxylating enzyme, Rubisco. CCM results in increased affinity of intact cells for CO_2 as photorespiration is suppressed [18, 125, 356]. In microalgae the mechanism of inorganic carbon transporting system has not been conclusively determined [18, 125, 483].

Since the resistance to CO_2 diffusion in the hydrated fungal matrix may be high [131, 416, 417, 628] the CCM significantly participates in the photosythetic process of lichenized algae and cyanobacteria [19, 518], e.g. the hydration dependency of photosynthetic CO_2 uptake in *Ramalina maciformis* indicates the presence of CCM occurring in lichen photobiont [258]. However there are some exceptions, e.g., although cyanobacterial (primary photobiont: *Nostoc* sp.) lichen *Lobaria scrobiculata* shows the operation of CCM, in the closely related tripartite lichen *Lobaria pulmonaria* (green alga *Dictyochloropsis reticulata* Tschermak-Woess, as primary photobiont) the CCM is either missing or only present with lower activity [519].

3.1.2 Freezing protection and freezing tolerance of free living algae

Numerous species of algae are well adapted to acute water stress, elevated or decreased temperature, extreme pH values or to starvation by formation of stress resistant cells. Some species develop by sexual reproduction resistant zygotes [124, 314, 436], whereas others develop akinetes from vegetative cells [124, 141, 332, 482, 506].

Akinetes are characterized by thick cell walls and presence of the reserve substances. The formation of akinetes was experimentally induced by starving (prolonged culture of vegetative cells without reneval of culture medium) in one species from the genus *Zygnema* [469], in four species from the genus *Heterococcus* isolated from the Antarctic soil [141], and in *Tribonema missouriens* [506]. In a nitrate-deficient medium *Tribonema bombycinum*, *Tribonema minus* and *Tribonema yamadanum* formed akinetes [332]. Dessication was a factor causing the akinete formation in *Klebsormidium rivulare* [482].

Akinetes show tolerance to acute water stress [332, 469]. Many algae species able to form akinetes occur in areas of high latitude including polar regions [188, 458, 610, 687], which suggests that akinetes of these algae may present a freezing tolerance. Indeed, in starvation-induced akinetes of *Tribonema bombycinum* (*Xanthophyceae*) the freezing tolerance (defined as temperature that caused 50% leakage of electrolytes, thus, 50% injury) is far below -30^0C whereas it is only -3^0C for vegetative cells. So obtained akinetes have many small vacuoles and oil droplets in the protoplasm and thick cell walls, in contrast to vegetative cell which have a large central vacuole and thin cell walls [494].

3.1.3 Freezing tolerance of lichens

Although there are extremely frost tolerant (-40^0C and lower) vascular plants (i.e. trees of boreal forest and of the arctic region and/or evergreen coniferous species) populating the most extended to the North areas of Canada and Siberia, only two taxa are present as far South as Antarctic Peninsula. As latitude increases, the domination of non-vascular plants, particularly lichens, is more pronounced. Lichens are superior to vascular plants when summer season is very short and cold [362].

Freezing tolerance of lichens manifests in their resistance to low temperature as well as to the long duration of the low temperature period.

The prolonged frozen storage (3.5 years at -60^0C) of air-dry *Alectoria ochroleuca* (Hoffm.) Massal. does not change its basic photosynthetic and respiratory responses to temperature, light intensity, and thallus hydration level after defreezing (for 12 h in distilled water at $+6^0$C), as compared with freshly collected lichen [422]. Also after prolonged (96 and 110 weeks) freezing at -15^0C *Cladonia foliacea* (= *Cladonia alcicornis*) thallus recovers its control level of CO_2 uptake after 20 h incubation at $+10^0$C [411].

The unusual survivality of freezing down to the extremely low temperatures independently on freezing rate by lichens (Tab. 3–1) cannot occur without mechanisms controlling freezing of water bound in tissue. It is thought that in freezing tolerant plants occurs extracellular water freezing and the lethal process of intracellular formation of hexagonal ice crystal is avoided [93].

The molecular mechanisms of lichen freezing protection are not yet fully explained, although, sugars and polyols are thought to play a role in cryoprotection of the tissue [375]. On the other hand, in Antarctic bryophytes the repeated freeze-thaw cycles (up to n = 16) increase rates of carbohydrate loss, which is not significantly correlated the DSC-detected freezing temperature of tissue [472].

Table 3–1. Freezing tolerance of lichens (from: [362], after: [413, 500, 501]).

			No injury if frozen t [^{0}C]	
Species	Region	Month	Rapidly	Slowly
Caloplaca elegans	Antarctica	Nov.	–196	–196
Rhizoplaca melanophthalma	Antarctica	Nov.	–196	–196
Xanthoria mawsoni	Antarctica	Nov.	–78	–196
Buellia frigida	Antarctica	Nov.	–78	–196
Umbilicaria decussata	Antarctica	Nov.	–78	–196
Usnea capillacea	New Zealand	Nov.	–78	–196
Lobaria pulmonaria	Central Europe	Sept.	–78	–196
Cladonia rangiferina	Central Europe	Sept.	–78	–196
Ramalina maciformis	Negev Desert	Nov.	–78	–196
Umbilicaria vellea	Central Europe	Dec.	–50	–196
Cladonia convoluta	Mediterranean region	Mar.	–50	–50
Sticta marginifera	New Zealand	Nov.	–30	–50
Roccella fucoides	Mediterranean region	Apr.	–10	–20
Dendrographa minor	California	Jun.	–	–12

3.1.4 Photosynthetic CO_2 uptake below 0^{0}C

As a result of adaptation, the temperature of net photosynthesis maximum and the level of net photosynthesis in maximum changes with the lichen habitat, eg. the Mediterranean population of *Umbilicaria nylanderiana* shows increased level of net photosynthesis as compared to Antarctic population of *Umbilicaria nylanderiana*, whereas the temperature of a net photosynthesis maximum occurs at +15^{0}C instead of +3^{0}C for Antarctic population [582].

Many of lichen species show the photosynthetic activity at the temperatures significantly lower than 0^{0}C. *Usnea sphacelata* (= *Usnea sulphurea*) shows the positive net photosynthesis at –5^{0}C (*light* form) and at –3^{0}C (*shade* form) [357]. Lange & Kappen, [413], detected the positive net photosynthesis in lichens at –18^{0}C. Fixing of ^{14}C labeled CO_2 was observed in *Stereocaulon alpinum*, *Cladonia foliacea* (= *Cladonia alcicornis*) and in *Peltigera subcanina* at –10^{0}C [415].

Table 3–2. Lowest recorded temperatures for photosynthetic activity of lichens.

Species	t [^{0}C]	Method	Provenance	Ref.
A) Laboratory measurements				
Cladonia foliacea (=*Cladonia alcicornis*)	–24	IRGA closed cycle	Southern Germany	[410]
Cladonia convoluta	–22	IRGA closed cycle	Southern France	[410]
Xanthoria parietina	–18	IRGA closed cycle	Southern Finland	[346]
Cetraria nivalis	–20	IRGA closed cycle	Kevo, Finland	[346]
Usnea acromelanea (=*Neuropogon acromelanus*)	–18.5	IRGA closed cycle	Antarctic continent	[413]
Xanthoria mawsonii	–16.5	IRGA closed cycle	Antarctic continent	[413]
Rhizoplaca melanophtalma (=*Lecanora melanophthalma*)	–16.5	IRGA closed cycle	Antarctic continent	[413]
Stereocaulon alpinum	<–10.9	^{14}C fixation	Southern Germany	[415]
Cladonia foliacea (=*Cladonia alcicornis*)	<–10.7	^{14}C fixation	Southern Germany	[415]
Peltigera subcanina	<–10.6	^{14}C fixation	Southern Germany	[415]
Cryptoendolithic lichen*	<–4.2	IRGA open cycle	Antarctic continent	[365]
sample 790/47	~ –6		(Southern Victoria	
sample 790/50	–8		Land)	
Usnea sphacelata (=*Usnea sulphurea*)		IRGA open cycle	Antarctic continent (Southern Victoria Land)	[357]
light form	<–6			
shade form	<–3			
Leptogium puberulum	–2	IRGA	South Shetlands	[590]
B) Field measurements				
Umbilicaria aprina	–17	IRGA, minicuvette	Antarctic continent	[597]
Usnea antarctica	<–5	IRGA open system	King George Island, South Shetlands	[598]
Usnea aurantiaco-atra (= *Usnea fasciata*)	–6	IRGA	King George Island, South Shetlands	[368]
Himantormia lugubris	–5	IRGA	King George Island, South Shetlands	[368]
Caloplaca regalis	–5	IRGA	King George Island, South Shetlands	[368]
Usnea sphacelata	<–10	IRGA open system	Antarctic continent	[361]
Usnea submollis	–10	Ivanov-method CO_2 absorption & $Ba(OH)_2$ titration	Sinaia Mts., Rumania	[13]
Ramalina farinacea	–9	Ivanov-method	Sinaia Mts., Rumania	[14]
Letharia vulpina	–9	Ivanov-method	Sinaia Mts., Rumania	[14]
Hypogymnia physodes	–6	IRGA open system	Solling, Germany	[600]

IRGA – infrared gas analysis.
* Identified as *Buellia*.

Schroeter et al., 1994, measured the CO_2 exchange rates of *Umbilicaria aprina* in its natural habitat (Cape Geology, Antarctica). They recorded the net photosynthesis down to -17^0C (which is the lowest temperature of photosynthesis recorded in field conditions), whereas the dark respiration significantly decreased at -7^0C and ceased at -11^0C. The light dependence of maximum photosynthetic rate showed the decrease of light saturation with decreasing temperature (from 400 $\mu Em^{-2}s^{-1}$ at above -6^0C down to 150 $\mu Em^{-2}s^{-1}$ at -17^0C). Also the light compensation point of net photosynthesis decreased with decreasing temperature (from 35 $\mu Em^{-2}s^{-1}$ at $+1^0C$ to 20 $\mu Em^{-2}s^{-1}$ at -5^0C), vanishing with the ceasation of dark respiration. Maximum net photosynthesis declines with temperature in two phases: first, rapidly, between -1^0C and -9^0C to about 10% of the rate at $+1^0C$. second, slower but steady, to very low rates at -17^0C. These might be the result of increase of CO_2 diffusion resistance, possibly by the ice nucleation which occurs in water saturated thalli of *Umbilicaria aprina* at -5.4^0C [599].

Tab. 3–2 sets up the lowest recorded temperatures of photosynthetic CO_2 uptake during laboratory measurements and during field measurements.

3.1.5 Ice nucleation activity of lichens

Numerous lichens display biological ice nucleation activity (INA) in thallus extracts at the temperatures much higher than the low temperature limit of their photosynthetic activity [382, 383, 384, 500, 599]. At slow cooling down the saturated thalli of *Umbilicaria aprina* Nyl. (from continental Antarctica), INA occurs at -5.4^0C (detected using DTA method), which is above the temperature of metabolism initialization detected by CO_2 exchange. Low-temperature scanning electron microscopy reveals the extracellular ice formation, which leads to cytorrhysis in the photobiont cells and to cavitation in the mycobiont cells. Both processes are reversible with the re-warming of thalli [599].

Other biological systems which act as active ice nucleators at "high" temperature are certain strains of epiphytic bacteria [431, 432, 433]. "High" temperature for INA is frequently considered -5^0C [434, 435] and the nuclei active above this temperature are termed Type I nuclei [532, 720]. As ice nucleating bacteria were not isolated from lichens, it is thought that one or both lichen symbionts are sources of ice nuclei [382].

Nuclei of Type I are present rather in fungal than in algal partner of lichen. In contrast, there are lichen symbionts which show INA only at low temperature (mycobiont *Cladonia bellidiflora* shows INA at -8.3^0C whereas *Cladonia rangiferina* at -5.0^0C) [383].

Nuclei isolated from *Xanthoparmelia* collected in the sites from ~2300 m (N. Mexico) were active above -3^0C, whereas for *Xanthoparmelia* collected from ca. 1600 m the nuclei were active at lower temperature [382].

Biological ice nuclei (active at ~ -4^0C) extracted from *Rhizoplaca chrysoleuca* are stable for heating at 60^0C (for 10 minutes) and active from pH 1.5

to pH 12 [384]. They appear to be proteinaceous, as they are sensitive to proteases and the treatment with either guanidine hydrochloride or urea with high concentration (2 M and 5 M, respectively) completely abolished INA above -10^0C, whereas there was no effect on their INA after treatment in chloroform (used as delipidator). Kieft & Ruscetti, [384], suggested that in thallus protein monomers aggregate to form warm-temperature ice nuclei.

In *Usnea aurantiaco-atra* small sized particles (diameter < 120 μm) were active at higher temperature (at -5.1^0C first freezing event for *Usnea aurantiaco-atra*, and 75000 g^{-1} nuclei at -7^0C) than both larger sizes (particles 160 μm reveal 1400 g^{-1} nuclei at -7^0C and particles 240 μm – first freezing event at -8.3^0C). The comparative study of lichens, mosses and higher plants, samples from sub-Antarctic South Georgia and the maritime Antarctic, showed that at -7^0C the mean number of nuclei per gram were lichens>mosses>higher plants and ranged from 257000 g^{-1} to 16220 g^{-1} [712].

The selective advantage of lichens from the presence of Type I ice nuclei may result either from the INA caused enhancement of moisture uptake from the gaseous phase by inducing deposition of ice in lichen thallus, or from the promotion of freezing at relatively warm temperature lessening frost damage by early formation of smaller, possibly extracellular ice crystals [382].

3.1.6 Water uptake from snow

Higher plants may easily exist under snow cover if they are not frozen [662]. Snow reduces temperature extremes, provides moist environment and allows the light transmission sufficient to photosynthetic activity on moderate level [364, 452]. It is not known whether the developmental processes observed in higher plants under snow (growth, leaves production or germination from seed) [580] are accompanied by photosynthetic production, however, it is thought that photosynthesis occurs only when the snow covering plant is mostly gone (*Claytonia lancelota* leaves) [387]. A lack of the full complement of enzymatic activity for photosynthesis in Arctic herbaceous plants was observed before snow melt [661].

Lichens populating Antarctic continent experience during their photosynthetically active period the temperatures rarely exceeding 8^0C when moist [359] and snow is almost the only source of water. Covering snow layer of the thickness of 1–4 cm does not stop lichen photosynthetic activity. However, during a period of strong light (irradiance higher than 600 $\mu Em^{-2}s^{-1}$) net photosynthesis is reversibly depressed (for several hours) in snow covered *Usnea sphacelata* [369]

Several lichen species are often strongly injured by prolonged snow cover [31, 32], whereas others (chionophilous species, e.g. crustoce lichen *Carbonea assenties* (= *Lecidea sciatrapha*) from the maritime Antarctic) are physiologically adopted to snow cover presence [371]. *Usnea antarctica* appears mainly in windblown and snow-free sites in the maritime Antarctic, however, besides that it is found in snow-covered habitats of continental Antarctic [266].

Cetraria nivalis hydrates to $\Delta m/m_0$ = 1.40–2.20 (presumably ±0.05) under snow depth 10–20 cm, and to 1.70–2.05 under 1–5 cm of snow, whereas *Usnea sphacelata* up to $\Delta m/m_0$ = 0.50–1.10 (m_0 is the dry mass, determined after heating of thallus to constant mass usually at t = 80°C) and to 0.50–1.95, respectively [373]. The hydration level of *Usnea antarctica* induced by snow cover varies between $\Delta m/m_0$ = 0.75 and 1.65 [364].

Umbilicaria aprina showed the net photosynthesis and dark respiration down to –4°C when a lichen thallus was rehydrated only from snow [599]. In *Usnea sphacelata* and in *Umbilicaria aprina* snowfall can activate photosynthetic CO_2 uptake below 0°C (down to –10°C and to –17°C, respectively) [361, 597].

Air-dry thallus of *Umbilicaria aprina* covered with snow in the darkness for 16 hours or more increased its water content from $\Delta m/m_0$ = 0.09 for air-dry sample to 0.56 in –4.5°C, to 0.50 in –6°C and to 0.25 in –14°C. No INA in hydrated from snow *Umbilicaria aprina* thallus was observed. The hydration level obtained by water uptake from snow, although high, is still four times lower than the hydration level of thalli hydrated from liquid phase (> 2.00). In *Umbilicaria aprina* rehydration conducted from snow at –4°C, the photosynthetic CO_2 exchange was monitored, however, the functional response of the thallus on hydration was not directly proportional to $\Delta m/m_0$. Namely, with hydration level increase up to $\Delta m/m_0$ = 0.20 no significant rates of CO_2 exchange were found. At $\Delta m/m_0$ = 0.30 CO_2 release indicated respiratory activity in the thallus, and at 0.40, positive gas exchanges were monitored. An equilibrium was reached after 20h at $\Delta m/m_0 \approx 0.60$ with a photosynthetic rate of +1.1 μM $CO_2\,kg^{-1}$ [599].

Obviously, water uptake from snow at freezing temperatures occurs from gaseous phase, from vapor sublimating from snow. It requires a water potential gradient between dehydrated lichen thallus and surrounding snow.

3.1.7 Resistance of lichens on dessication

Lichen thallus may hydrate to relatively high level. For instance, *Usnea sphacelata* (= *Usnea sulphurea*) takes to a maximum level of $\Delta m/m_0$ = 1.60 [357]; rain water-soaked *Usnea fasciata* hydrates to $\Delta m/m_0$ = 1.64, whereas *Ramalina terebrata* to $\Delta m/m_0$ = 2.63 [359]. During the daylight period in Antarctica, *in situ* hydration level of *Lasalia pustulata* varies between $\Delta m/m_0$ = 0.5 and 4.0, whereas between 1.0 and 5.0 for *Umbilicaria spadochroa* [370].

The maximal thallus hydration level and the drying rate change with adaptation to conditions of habitat. In the circumpolar Arctic lichen, *Cetraria nivalis*, the maximal thallus hydration level increases from ~2.9 to ~4.0 with increasing latitude of habitat, whereas the drying rate decreases with increased latitude [589]. *Mastodia tesselata* populating the exposed rock surfaces in the supralitoral maritime Antarctic sprayed with see-water hydrates to significantly higher level than when sprayed with fresh-water [325].

At low hydration levels net photosynthesis almost linearly depends on $\Delta m/m_0$, whereas highly hydrated thalli show depression in net photosynthesis.

In epiphyte lichens, *Dendrographa minor* Darb. and *Ramalina menziesii* Tayl., the gradual decline in CO_2 rates with decreasing water potential was recorded either at dehydration to the gaseous phase at controlled relative humidity, p/p_0, or osmotic stress caused by incubation of the thalli in sea salt or sorbitol solutions. The CO_2 fixation occurred at the relative humidity p/p_0 = 77–85%. Photosynthesis in *Pseudocyphellaria anthrapsis* Magn., a species with a cyanobacterial photobiont, strictly depends on thallus wetting with liquid water. Net photosynthesis was detectable to water potential equal –3.5 Mpa in sorbitol and salt solutions, but no CO_2 uptake in moist air [502]. The re-hydration characteristics for some green algal and cyanobacterial lichens were recorded, with the latter associations requiring liquid water to reactivate photosynthesis [417, 418].

The presence of maximum in net photosynthesis may be caused by increased thallus CO_2 diffusion resistance at high hydration levels [258]. Field measurements show that in *Ramalina terebrata* net photosynthesis is lower in thallus hydrated to $\Delta m/m_0 = 1.12$ than in thallus hydrated to < 0.92 (with the maximum at 0.87) [367]. The maximum of CO_2 exchange occurs for *Usnea sphacelata* (= *Usnea sulphurea*) and for *Usnea aurantiaco-atra* (= *Usnea fasciata*) at $\Delta m/m_0 = 0.70$ [359]. For *Umbilicaria decussata* the optimal net photosynthesis is recorded at $\Delta m/m_0 = 1.0$, for *Umbilicaria aprina* at $\Delta m/m_0 = 1.2$, whereas for *Usnea antarctica* and for *Usnea sphacelata* at $\Delta m/m_0 = 0.85$ [364]. In laboratory conditions ($t = +5^0C$), the maximum of CO_2 exchange was recorded at $\Delta m/m_0 = 1.50$ for *Lasalia pustulata*, and at $\Delta m/m_0 = 0.90$ for *Umbilicaria spadochroa* [370]. The photobiont of *Mastodia tesselata*, the green alga *Prasiola crispa* ssp. *antarctica*, reveals the optimum level of net photosynthesis at $\Delta m/m_0 = 5.20$, compared to $\Delta m/m_0 = 3.00$ for the thallus of *Mastodia tesselata* [325]. Net photosynthesis for fruticose lichens populating semiarid Iberian Peninsula shows a maximum at $\Delta m/m_0 \approx 1.05$ for *Teloschistes lacunosus*, and at $\Delta m/m_0 \approx 1.15$ for *Ramalina bourgeana*. For higher hydration level net photosynthesis rapidly decreases to 20% of maximal level at $\Delta m/m_0 \approx 2.3$ for *Teloschistes lacunosus*, and at $\Delta m/m_0 \approx 2.6$ for *Ramalina bourgeana* [155].

Mild desiccation to gaseous phase (often happening in natural conditions) may completely remove the loosely bound water fraction and significantly reduce the tightly bound water fraction. The life activity of lichen stops for very low hydration level, recovering as lichen is rehydrated to $\Delta m/m_0 \approx 0.2$ for *Teloschistes lacunosus*, and to $\Delta m/m_0 \approx 0.25$ for *Ramalina bourgeana* [155], to $\Delta m/m_0 = 0.2–0.3$ for *Usnea aurantiaco-atra* (= *Usnea fasciata*) [359], to $\Delta m/m_0 = 0.3$ for *Cetraria nivalis* [373], to $\Delta m/m_0 = 0.3–0.4$ for *Ramalina terebrata* [359]; and for *Usnea sulphurea* to $\Delta m/m_0 = 0.4$ [357, 359], at relative humidity $p/p_0 = 70\%$ for *Dendrographa minor*, $p/p_0 = 80\%$ for *Ramalina menziesii* and $p/p_0 = 85\%$ for *Pseudocyphelaria antraspis* [502], as measured from photosynthetic activity or dark respiration.

Aerophilic green algae and lichens [37, 38, 412, 502] restart photosynthetic activity at p/p_0 = 77–85%. The recovery of life activity after rehydration occurs relatively fast, e.g. air-dry *Usnea sphacelata* (= *Usnea sulphurea*) restores net photosynthesis up to 50% and dark respiration up to 60% after 60 h of exposition to humid air ($p/p_0 > 96\%$). The rehydration level depends on light intensity, e.g. at 6^0C *Usnea sphacelata* (= *Usnea sulphurea*) hydrates to $\Delta m/m_0 = 0.70$, in darkness, whereas exposed to light (360 $\mu Em^{-2}s^{-1}$) only to $\Delta m/m_0 = 0.55$ [357].

The accumulation of large quantities of monosaccharides (glucose, fructose, mannitol, and arabitol) in lichen mycobionts (in *Evernia esorediosa* (Müll. Arg.) Du Rietz, in *Ramalina subbreviuscula* Asah., and in *Ramalina sublitoralis* Ash.) may be an adaptative feature for growing in dry conditions [265].

On the other hand, thalli of *Umbilicaria decussata* (hydrated to $\Delta m/m_0 \approx 2.0$) collected from wet habitats of Clark Peninsula, Windmill Islands, East Antarctica, did not differ in total level of low molecular weight carbohydrates (and in pigment level) from thalli collected from dry habitats ($\Delta m/m_0 \approx 0.17$). However, in the samples from wet habitats the proportion of algal products (ribitol) relative to fungal products (arabitol and mannitol) was greater. They also showed slightly elevated tissue freezing point (–13^{0}C, determined by DTA), compared to –16^{0}C in thalli from dry habitats [473].

3.2 Natural scale of the biological system hydration

In attempt to model the surface of dry biological system, lets consider an infinite 2-d square lattice, the limited fragment of which may be represented by an empty chessboard. Every square of sixty four is called *site*; every site models a water binding site of dry biological system. Here there is no distinguishing between water binding sites with increased water affinity, i.e. "hot binding sites", and other water binding sites. The line joining every pair of vicinal squares is called *bond* (even on the empty chess board).

Than act as a bad chessplayer preparing his chessboard to game, thus, placing randomly n chessmen on the chessboard. Let us assume that all chessmen are equivalent, say, they are all pawns. The number n of pawns divided by sixty four is p, the probability of site population. For a large fragment of lattice (N sites) and the population probability p, the number of occupied sites is pN. Every pawn models a water molecule bonded to the surface of dry biological system. Bonds between pawns on chessboard resemble hydrogen bonds between water molecules. Indeed, this model is too simplified as in two dimensions the network of hydrogen bonds resembles rather honeycomb lattice.

The groups of occupied sites are called *clusters* (single site is not considered as a cluster). The bounds between sites in cluster are the hydrogen bonds between water molecules forming a cluster (droplet). As the probability of site population, p, increases, the number of clusters, the size of clusters and the number of occupied sites increase. Assuming that every cluster forms a pathway

(from any given occupied site of the cluster to another one), the lengths of pathways increase with increasing p.

The fragment (200x200) of 2-d square lattice occupied with the increasing probability p is presented in Fig. 3–2.

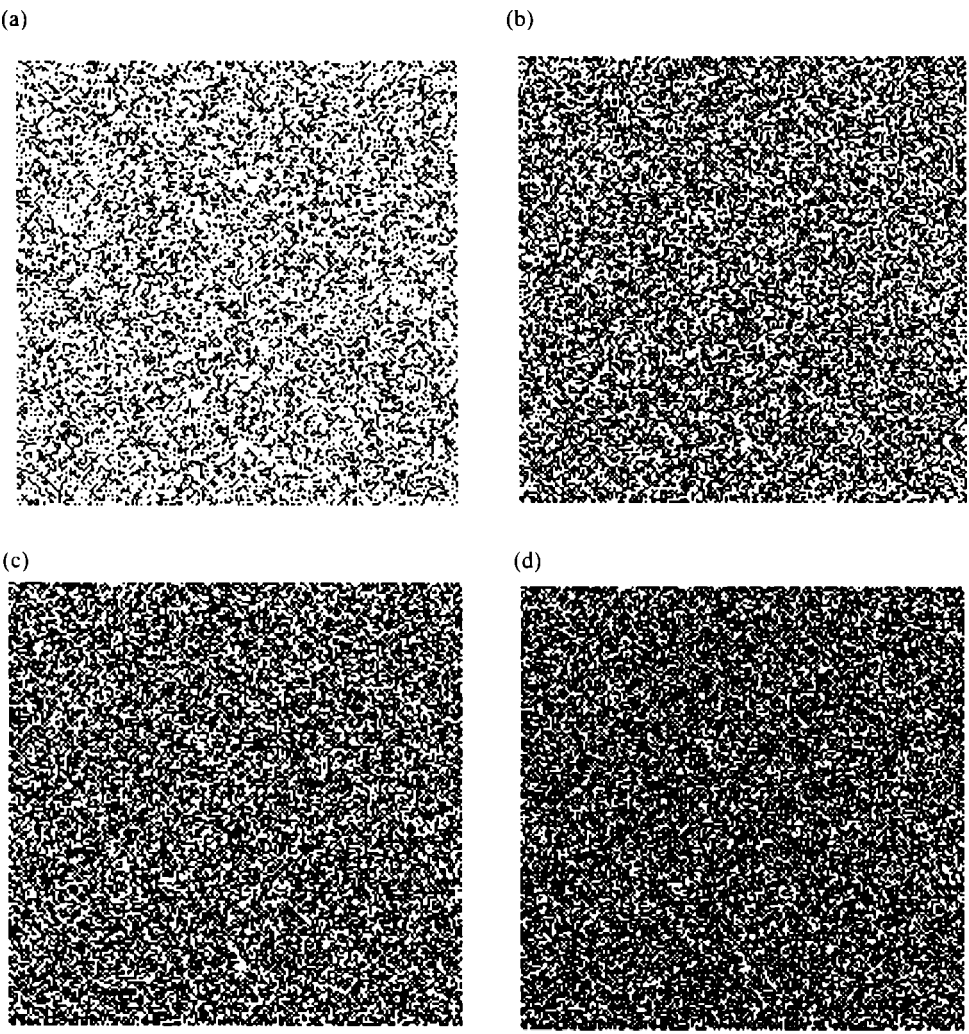

Fig. 3–2. The fragment of the square lattice (200x200 sites) occupied with varied probability p. (a) p = 0.30, (b) p = 0.50), (c) p = 0.60, (d) p = 0.70.

At given, well defined for every lattice, probability $p = p_c$, the pathway leading from infinity to infinity appears. (The infinite cluster appears). The probability p_c is called *percolation probability* and the transition occurring with increased probability is called *percolation threshold* (Fig. 3–3). To calculate the

value of percolation threshold usually the limited fragment of any given lattice is taken for computer calculations. However, the sufficiently large fragment of the lattice is required, in the aim to exclude the accidental alignment of occupied sites which may alter the results.

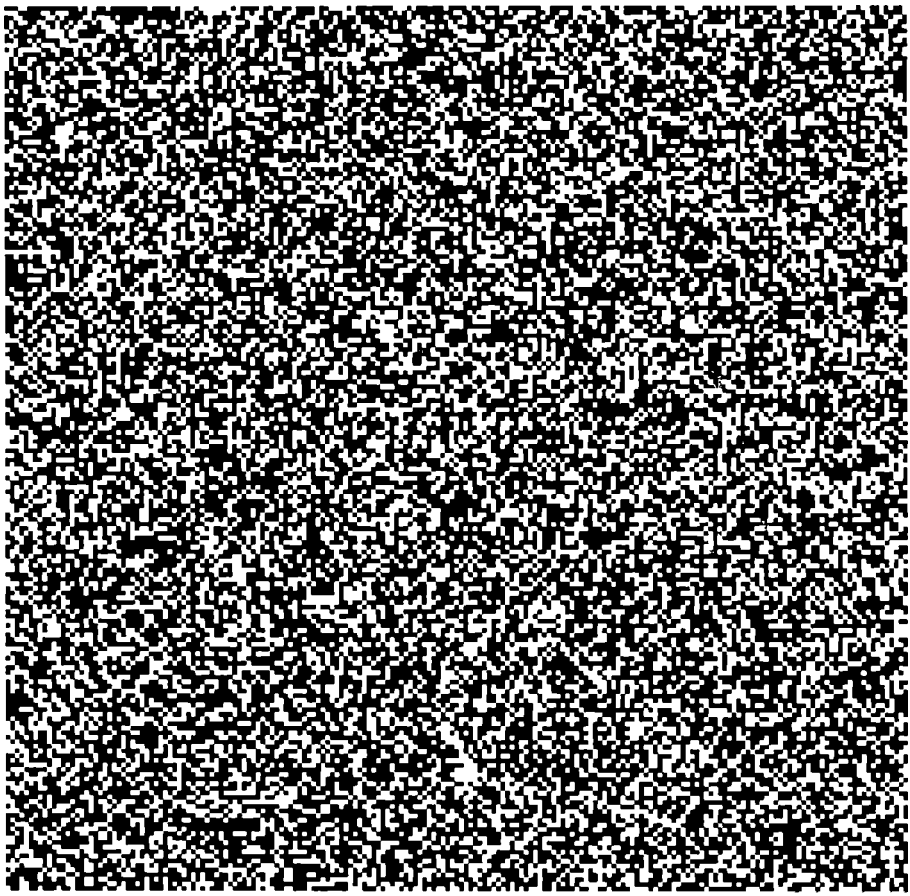

Fig. 3–3. The square network with p = 0.60 (Fig. 3–2c. copied and magnified). The percolation pathway is shaded. (Although the percolation threshold (site percolation) for square lattice is p = 0.592746, the Author cheated and added one missing populated point, because due to the finite size, the generated set of points was below percolation threshold...).

In general, percolation in n-dimensional lattices is considered, however, the network of hydrogen bonds of bound water molecules may be modeled by the one of 2-d lattices with the number of bonds $n \leq 4$ (as the number of hydrogen bonds formed by one water molecule cannot exceed four). The percolation thresholds for the possible 2-d regular lattices shows the Tab. 3–3. The lattices with the number of bonds $n = 4$ are not very much probable, although the additional hydrogen bond may be accidentally formed in 3-d space of free liquid water.

At very low hydration level the probability of 3-d cluster on the organic matrix surface is negligible. In bulk water the averaged number of hydrogen bonds equals n=2.4 [642], with dynamically changed spatial localization of the bonds.

Although the angles of hydrogen bonds may be distorted, there is negligible probability that all four hydrogen bonds may contribute to 2-d lattice of water monolayer on the surface of dry biological system. Moreover, one bond is in most cases used to bind to the surface of biological matrix. Thus, for water monolayer only $n \leq 3$ should be take into account.

Further increase in population of occupied sites lead to full coverage of the lattice at $p = 1$, which in case of dry biological system is a single monolayer coverage.

Table 3–3. Percolation thresholds for bond or site percolation selected for the 2-d lattices with the number of bonds, n, up to 4 [640], for kagomé: [726]. The errors of the numeric values of percolation thresholds are comparable to the last digit [640].

Type of lattice	n	p_c^{bond}	p_c^{site}
Square	4	0.50000	0.592746
Kagomé	4	0.45	0.6527
Honeycomb	3	0.65271	0.6962
Bethe	n	1/(n-1)	1/(n-1)
Bethe	3	0.50000	0.50000
Bethe	4	0.33333	0.33333
Bethe	2.4	0.71429	0.71429

Basing on the percolative model, this Author suggests the natural scale of hydration for ultra-dry biological system, arranged in following stages with increasing hydration level:

(i) dry surface;

(ii) water molecules bound to binding sites with high affinity, i.e. "hot binding sites";

(iii) water clustering point, at which the separated molecules of bound water start to group in molecular clusters (micro-droplets); (it is distinguished if it is a separated proces succeding pt. (ii), but not occuring paralelly);

(iv) 2-d percolation threshold of water bound on the surface of biological system, at which the infinite cluster is formed;

(v) monolayer formation, at which the hydration of the system is sufficient to cover full monolayer of water molecules.

3.2.1 Percolation of liquid water in bulk

Molecular simulations of percolation of water aqeous solutions require, by finite size of simulation box, proper identification of percolation threshold [513]. The following cryteria are used:

(i) the probability to find water molecule in an infinite (spanning across the periodical simulation box) cluster is 50%;
(ii) the Hausdorff dimension of the infinite cluster equals d = 2.53 [336];
(iii) the mean cluster size has a maximum (the largest cluster is excluded from the sums);
(iv) the cluster number distribution obeys a power law with the universal exponent $\tau = 2.19$ [640].

At room temperature and under atmospheric pressure liquid water is above the percolation threshold [642]. However, Monte Carlo computer simulations show that, except for the highest density states, supercritical water water is always below the percolation threshold which is equal $\langle n_{HB} \rangle = 1.6$ [345].

Percolative behavior is more complicate in binary water-solute systems.

Water-hydrofuran binary mixture at 325 K reveals a wide region of immiscibility extending from ~30% to ~70% of water. Molecular (Monte-Carlo) simulations show percolation of water in the concentration range from 100% of water down below the organic-rich branch of the coexistence curve. The 2-d percolation threshold occurs at 18.3% of water, then Hausdorff dimensionality of spanning water clusters continuously increases; and finally 3-d percolation cluster (Hausdorff dimension $d \cong 2.5$) is formed at the organic-rich branch. In whole region of immiscibility gap either water or hydrofuran percolate [513].

In completely miscible binary systems the infinite water hydrogen bond network breaks at water mole fraction equal 0.17 in methanol [585], 0.10 in ethanol [584], 0.09 for propanol [586], and between 0.1 and 0.2 in 1,4–dioxane [455], whereas for higher concentrations of solute water attaches to the hydrophilic sites of solute arranged in chain-like structures [584, 585, 586].

3.3 Air-dry thalli

Lichen thallus reversibly dehydrates to air-dry hydration level during storage in herbary at room temperature and at room humidity.

Air-dry hydration level equals for *Cladonia mitis* Sandst. [= *Cladonia arbuscula* (Wallr.) Flot ssp. *mitis* (Sandst.) Ruoss], collected in Spitsbergen in summer of 1985, $\Delta m/m_0 = (8.9 \pm 0.1)\%$, (sample CM85); and $\Delta m/m_0 = (9.3 \pm 0.2)\%$, for *Cladonia mitis* collected in Iceland, in summer of 1998 (sample CM98). For *Himantormia lugubris* (Hue) Lamb collected on Jersak Hills, hillside exposed to East, altitude 180 m over sea level on December 16th, 1995, air-dry hydration level equals $\Delta m/m_0 = (10.2 \pm 0.2)\%$, whereas for *Usnea aurantiaco-atra* (Jacq.) Bory, collected from the site on Jersak Hills (≈200m over sea level) at December 16th, 1995, $\Delta m/m_0 = (8.5 \pm 0.2)\%$. Ornito-coprophilic lichen *Caloplaca regalis* (Vain.) Zahlbr. collected near to the penguin nesting sites on Antarctic Peninsula, hydrates to $\Delta m/m_0 = (7.8 \pm 0.7)\%$ in air-dry state, whereas foliose *Umbilicaria antarctica* Frey

et Lamb, collected in the region of Antarctic Peninsula, Cuverville Island on February 21st, 1996, to $\Delta m/m_0 = (10.2 \pm 0.9)\%$ [271].

Although air-dry hydration level is not sufficiently high to initiate photosynthetic activity (see Chpt. 3.1.7), the vitality tests performed using the fluoresceine biacetate and etidine bromide show in so stored thalli that in *Cladonia mitis* thallus 50–60% of cells reacted positively, in *Himantormia lugubris* 40–50% of cells and in *Usnea aurantiaco-atra* 80% [278].

3.4 Sorption isotherm of lichens

Obviously, the most important role in initial stages of the biological system hydration plays bound water. It remains in the system after the free water fraction is completely removed from the system and leaves it as the last water subsystem. Bound water differs from water in bulk, remaining in non-icelike form at temperatures below actual eutectic point for solution present in tissue [159], and revealing the differences in molecular dynamics (see Chpt. 1.19). The analysis of sorption isotherms gives an insight to bound water behavior, its affinity to water binding sites, and to wetting conditions of lichen thallus (full wetting case or non-zero value of wetting angle).

The mechanism of attachment and detachment (or loss) of molecules from the sorbed material was first quantified by Langmuir, 1918, leading to his basic theory for monolayer sorption (and to Langmuir isotherm). Although most of sorption data can be fit to Langmuir isotherm for low level of relative humidity ($h \leq 0.1$, where h is p/p_0 expressed as fraction) they are sigmoidal in form. Brunauer, Emett and Teller, 1938, extended the theory for multilayer sorption at limited and unlimited number of layers (BET isotherm). BET equation usually fits to real data for relative humidity up to $h = 0.4$.

This Author recorded the sorption isotherms for fruticose (*Cladonia mitis*, samples CM85, and CM98, *Himantormia lugubris*, *Usnea aurantiaco-atra*, and *Caloplaca regalis*), and foliose (*Umbilicaria antarctica*) lichen thalli hydrated (or dehydrated) directly from air-dry state over silica gel ($p/p_0 = 0\%$), over H_3PO_4 ($p/p_0 = 9\%$), over the surfaces of supersaturated solutions of several compounds, and over the water surface ($p/p_0 = 100\%$) (as in Chpt. 2.6.5.3). Silica gel was dried in 120°C, which is enough to remove weakly bound water; drying in 600°C was not used, as it increases formation of siloxane bridges, even if it leads to further dehydration [692].

The relative mass increase was calculated after 7–day incubation and subsequently after next 7 days. As no further mass increase was recorded, the 14–day value was taken as equilibrium value for a given humidity.

For every lichen investigated the sorption isotherm revealed the sigmoidal form (Fig. 3–4, open circles). To describe the sigmoidal form of sorption isotherms, Dent, 1977, modified the multilayer model considering the sorption to two

distinguished specific binding sites. Namely the "primary" sorbed molecules which than form (or expose) "secondary", usually weaker, sites for further sorption.

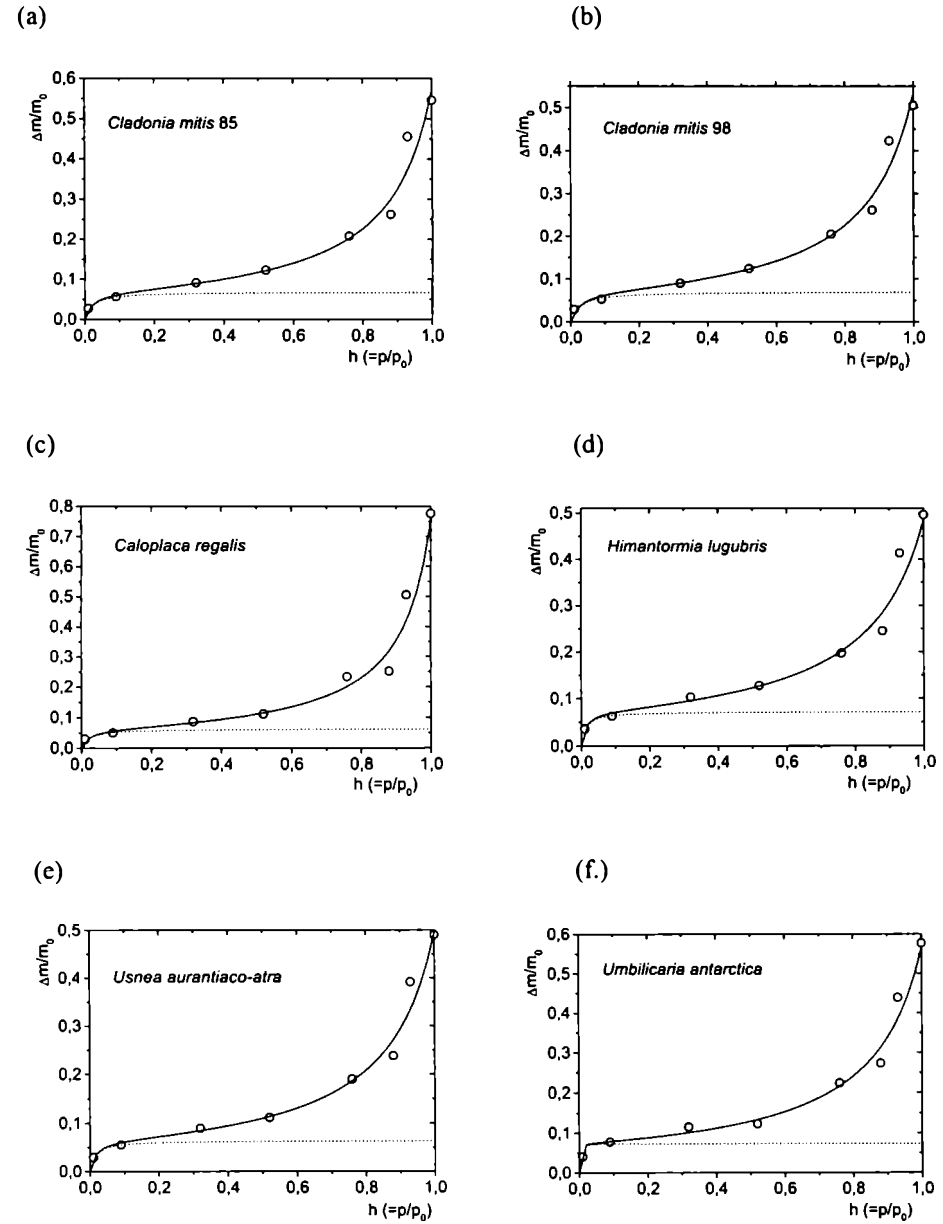

Fig. 3–4. The sorption isotherms recorded at room temperature for (a) *Cladonia mitis* 86, (b) *Cladonia mitis* 98, (c) *Caloplaca regalis*, (d) *Himantormia lugubris*, (e) *Usnea aurantiaco-atra*, and for (f) *Umbilicaria antarctica*. Solid line shows total sorption, dotted line the population of monolayer sorption, both predicted by Dent isotherm (see text); h is relative humidity expressed in absolute units.

Although Dent derived his isotherm under the assumption of layering of adsorbed molecules, as his model does not differentiate among the molecules adsorbed in second and any next layer, the binding constant b describes binding either in bulk or binding on the surfaces of water droplet if no sorbate layering takes place. In their model, Heilwood & Horrobin, 1946, also discussed three subsystems: dry matrix, hydration water, and free water, interacting as ideal solution. They obtained the same equation as Dent (Eq. 3.4), however, the parameters of their model are differently defined. Here Dent model is used, as the one being the generalization of BET formula.

Dents model needs only the escape rate constant for primary binding sites, C_0, and the escape rate for all other layers of sorbate, C. It yields for total number of water molecules per binding site, y/y_m

$$\frac{y}{y_m} = \frac{b_1 h}{(1-bh)\cdot(1+b_1 h-bh)}, \tag{3.1}$$

where $h = p/p_0$ expressed as ratio, $b_1 = \frac{a}{C_0} p_0$ and $b = \frac{a}{C} p_0$. The constant a is an attachment rate constant per unit pressure and is assumed to be the same for all layers (as in BET model). Constant b_1 is a relative surface coverage for first monolayer at given h; b is the coverage of n-th layer expressed in units of coverage of (n–1)-th layer.

If b = 1, one gets from Eq. (3.1) the formula of BET isotherm

$$\frac{y}{y_m} = \frac{b_1 h}{(1-h)\cdot(1+b_1 h-h)}. \tag{3.2}$$

For b = 0 (monolayer coverage) one gets

$$\frac{y}{y_m} = \frac{b_1 h}{1+b_1 h}, \tag{3.3}$$

which is the Langmuir sorption isotherm.

Very useful, easy for fitting, form of Dent sorption equation is

$$\frac{h}{y} = A + B\cdot h - C\cdot h^2. \tag{3.4}$$

Where the new constants are

$$A = \frac{1}{b_1 y_m},\quad B = \frac{b_1 - 2b}{b_1 y_m} \text{ and } C = \frac{b\cdot(b_1 - b)}{b_1 y_m}. \tag{3.5a, b, c}$$

Thus, the parameters of isotherm may be easily calculated [622]:

$$b = \frac{\sqrt{B^2 + 4AC} - B}{2A}, \tag{3.6a}$$

$$b_1 = \frac{B}{A} + 2b, \tag{3.6b}$$

and

$$y_m = \frac{1}{Ab_1}. \tag{3.6c}$$

Although Dent wrote his equation in terms of relative population of binding site, it is more convenient to rewrite the isotherm in terms of $\Delta m/m_0$. Thus, we get for isotherm

$$\frac{\Delta m}{m_0} = \frac{\Delta M}{m_0} \cdot \frac{b_1 h}{(1 - bh) \cdot (1 + b_1 h - bh)}, \tag{3.7}$$

where $\Delta M/m_0$ is the mass of full monolayer expressed in units of dry mass.

The sorption isotherm for $\frac{h}{\Delta m/m_0}$ expressed as a function of h is

$$\frac{h}{\Delta m/m_0} = A' + B' \cdot h - C' \cdot h^2, \tag{3.8}$$

from which we get

$$b = \frac{\sqrt{B'^2 + 4A'C'} - B'}{2A'}, \quad b_1 = \frac{B'}{A'} + 2b, \text{ and } \Delta M/m_0 = \frac{1}{A' \cdot b_1}. \tag{3.9a, b, c}$$

The sorption data in form of Eq. (3.8) are well fitted by square function (Fig. 3–5) for all lichens investigated.

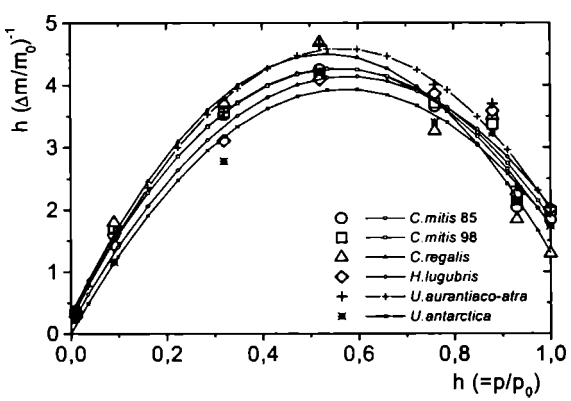

Fig. 3–5. The sorption data expressed in terms of Eq. (3.8) (see text).

Applying Dent sorption isotherm to lichen thallus, one should take into account that it does not predict the residual hydration level at h = 0. The residual hydration level is observed in other biological systems as bark and bast [290], and in wheat seed [289]. To use the data obtained at h = 0 to Dent isotherm, this point was treated as h = 0.01, assuming accidental hydration, caused by non-perfect conditions of experiment. The parameters from Dent model fitted to the sorption data for lichen thalli are set up in Tab. 3–4.

Fitted values of b, which are the ratios of populations of (n+1)-th layer to populations of n-th layer, at h = 1:

$$\left.\frac{S_{n+1}}{S_n}\right|_{h=1} = b, \tag{3.10}$$

do not differ much for all thalli investigated and is equal to 0.879±0.02, as averaged over all lichens.

According to Dent, the reciprocal of b_1 is the number of empty binding sites at h=1:

$$S_0/N|_{h=1} = 1/b_1 \tag{3.11}$$

This value differs for the lichens investigated (Tab. 3–4b), reflecting the difference in wetting properties (the "strength" of water bonding). For *Umbilicaria antarctica* the wetting at h = 1 is almost complete, whereas for other lichen species the contribution of empty water binding sites varies up to 2.44% for *Cladonia mitis*.

Table 3–4. The values of parameters obtained from Dent isotherm fitted to lichen sorption data from Eqs. (3.7) and (3.8).

Table 3–4a.	A′	B′	C′
Cladonia mitis 86	0.305±0.235	14.30±1.21	12.86±1.16
Cladonia mitis 98	0.356±0.218	13.96±1.12	12.44±1.08
Caloplaca regalis	0.315±0.375	15.70±1.94	14.70±1.86
Himantormia lugubris	0.156±0.27	13.75±1.39	11.85±1.34
Usnea aurantiaco-atra	0.232±0.244	15.43±1.26	13.65±1.21
Umbilicaria antarctica	0.013±0.271	13.69±1.40	11.94±1.34

Table 3–4b.	b	b_1	$S_0/N\|_{h=1} = 1/b_1$	$\Delta M/m_0$
Cladonia mitis 86	0.883	48.65	2.06%	0.067
Cladonia mitis 98	0.871	40.96	2.44%	0.069
Caloplaca regalis	0.919	51.68	1.93%	0.061
Himantormia lugubris	0.854	89.85	1.11%	0.071
Usnea aurantiaco-atra	0.873	68.25	1.46%	0.063
Umbilicaria antarctica	0.871	1055	0.09%	0.073

Full coverage of monolayer (the mass of water bound to the water binding sites on thallus surfaces), $\Delta M/m_0$, shows the values close for all six thalli. As averaged over the lichen samples investigated $\Delta M/m_0$ = 0.0675±0.0045. This

reflects the high affinity of water to the thallus binding sites, as majority of them is populated at relative humidity close to 0%.

Dent isotherm, yields the fractions of total sorption at various h, thus, the fraction of empty sites per total number of binding sites is given by

$$\frac{y_0}{y_m} = \frac{1 - b_1 h}{1 + (b_1 - b)h} \,. \tag{3.12}$$

Fig. 3–6 shows the fraction of empty binding sizes as a function of relative humidity h. The elevated affinity of water binding sites in *Umbilicaria antarctica* is manifested as significantly decreased population of empty binding sites compared to other lichen species. The dependency for another foliose species investigated, *Caloplaca regalis*, matches with the fruticose thalli.

The monolayer coverage is equal to:

$$\frac{\Delta m}{m_0} = \frac{\Delta M}{m_0} \cdot \frac{b_1 h}{1 + (b_1 - b)h} \,, \tag{3.13}$$

and is shown on sorption isotherms (Fig. 3–4) as a dotted line.

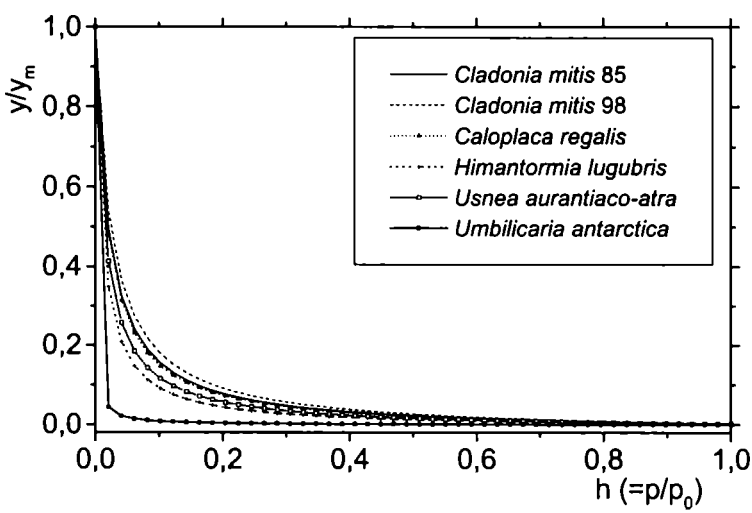

Fig. 3–6. The predicted by Dent isotherm contribution of empty water binding sizes in units of total number of binding sizes expressed as a function of h.

The value obtained as monolayer coverage, $\Delta M/m_0$, although do not necessary is a real monolayer (because of the separation of water binding sites on thalli surface) may, however, be used as lower limitation of the surface accessible for water molecules bound in lichen thallus.

3.5 Hydration and dehydration kinetics of lichens

The hydration of lichen thallus from from air of high humidity stimulates CO_2 exchange to the high values of net photosynthesis, without exposing the lichens to liquid water. However, lichen species differ in the length of the reactivation time. Several fruticose and foliose species (e.g. *Parmelia hypoleucina*, *Ramalina fenestrata*) reach 50% of maximum photosynthesis after about 5 h hydration from the gaseous phase (p/p_0 = 96.5% at +15^{0}C), whereas *Cladonia mitis* after 9.75 h; Antarctic *Umbilicaria antarctica* 16.5 h, and *Caloplaca regalis* after 34 h [414].

In maritime Antarctica during a period of rain, the rate of water uptake ranged from 0.15 h^{-1} (presumably expressed as relative mass decrease during first hour of hydration [326]) for *Usnea antarctica* to almost 0.90 h^{-1} for *Mastodia tesselata*. Loss rates after the rain ceased were lower than uptake rates and ranged from 0.085 h^{-1} in *Umbilicaria decussata* to 0.39 h^{-1} in *Mastodia tesselata*. The maximum water content ranged from $\Delta m/m_0 = 0.67$ in *Usnea antarctica* to 3.91 in *Mastodia tesselata* [326].

The hydration of *Ramalina terebrata*, *Usnea aurantiaco-atra* and *Himantormia lugubris* performed from aqueous phase (water spread on the thallus surface) showed the presence of very fast component occurring in the time scale of tenths of minutes. The hydration after one hour was close to saturation point which was about M/m_0 = 1.7±0.4 for *Himantormia lugubris*, M/m_0 = 1.9±0.2 for *Ramalina terebrata* and $\Delta M/m_0$ = 1.7±0.3 for *Usnea aurantiaco-atra* (calculated from [366]).

The hydration courses performed from the gaseous phases give systematically lower saturation values than hydration courses performed from aqueous phase. The hydration of *Usnea sulphurea* performed from the gaseous phase (p/p_0 > 96%) was described by averaged hydration time T_h = 16 h (1/e value) and saturation hydration, $\Delta m/m_0$ = 0.70 (calculated by this Author from [357]). For *Usnea aurantiaco-atra* hydrated in moist chamber the saturation value M/m_0 = 0.85±0.03, the hydration time T_h = 30 h; for *Ramalina terebrata* M/m_0 = 1.2±0.05 and T_h = 40 h; and for *Himantormia lugubris* M/m_0 = 0.85±0.05 and T_h = 30 h (all calculated by Author from [366]).

All numbers given above were obtained assuming that the hydration courses were single exponential. This assumption was to some extent arbitrary because of the poor quality of some data [357], and needs confirmation. To test the form of hydration and dehydration function of lichen thallus, this Author performed the hydration time courses in two series. Namely, the samples incubated at p/p_0 = 0% were placed over the water surface (p/p_0 = 100%), whereas the samples dehydrated at p/p_0 = 9% were placed over the surface of supersaturated Na_2SO_4 (93%).

The dehydration time courses were also performed to two different levels of relative humidity. The samples incubated for 96 h at $p/p_0 = 93\%$ (used before in sorption isotherm measurement at $p/p_0 = 100\%$: *Cladonia mitis* CM98, CM86, and *Usnea aurantiaco-atra*; and at $p/p_0 = 88\%$: *Himantormia lugubris*, *Umbilicaria antarctica* and *Caloplaca regalis*) were dehydrated in the atmosphere over silica gel ($p/p_0 = 0\%$), whereas the samples incubated at $p/p_0 = 100\%$ (used before for sorption isotherm at $p/p_0 = 93\%$: *Cladonia mitis* CM98, CM86, *Usnea aurantiaco-atra* and *Caloplaca regalis*; and at $p/p_0 = 76\%$: *Umbilicaria antarctica*, and *Caloplaca regalis*) were dehydrated over the surface of H_3PO_4 ($p/p_0 = 9\%$).

After completing the hydration or dehydration time courses, the dry mass of the sample was determined after heating in 70^0C for 72 h. Higher temperatures were not used as they may cause the decomposition of some organic constituents of thallus [224].

For all fruticose lichens (*Cladonia mitis*, *Himantormia lugubris* and *Usnea aurantiaco-atra*) the hydration kinetics from gaseous phase for relative humidity either $p/p_0 = 93\%$ or $p/p_0 = 100\%$ was well described by the double exponential function (Fig. 3–7a–h)

$$\Delta m / m_0 = C - A_1^h \exp\left(-t / t_1^h\right) - A_2^h \exp\left(-t / t_2^h\right), \tag{3.14}$$

where C is total saturation hydration level, A_1^h and A_2^h are the saturation hydration levels for fast and slow component, t_1^h and t_2^h are characteristic times for fast and slow component, respectively.

For foliose lichens, *Caloplaca regalis* and *Umbilicaria antarctica*, at both values of relative humidity, the hydration kinetics (Fig. 3–7i–l) is sufficiently well fitted by single exponent

$$\Delta m / m_0 = C - A^h \exp\left(-t / t^h\right), \tag{3.15}$$

where t^h is the hydration characteristic time, A^h is the saturation level of the hydration surplus over the equilibrium value, B^h, at the relative humidity of thallus incubation. The equilibrium value for incubation can be calculated from

$$B^h = C - A^h \tag{3.16a}$$

for single exponential process, and from

$$B^h = C - A_1^h - A_2^h \tag{3.16b}$$

for double exponential one. In Tab. 3–5 are set up the values of fitted parameters.

Similarly to hydration courses, the dehydration time-courses were performed at two differences between initial and actual values of relative humidity. Thalli incubated at $p/p_0 = 100\%$ were dehydrated at $p/p_0 = 0\%$, whereas thalli incubated at $p/p_0 = 93\%$ were dehydrated at $p/p_0 = 9\%$.

Similarly to hydration, the dehydration of fruticose thalli was well fitted by double exponential function (Fig. 3–7a–h)

$$\Delta m / m_0 = B^d + A_1^d \exp\left(-t / t_1^d\right) + A_2^d \exp\left(-t / t_2^d\right), \qquad (3.17)$$

where t_1^d and t_2^d are the characteristic times for the hydration of fast and slow component, respectively, A_1^d and A_2^d are the saturation hydration levels for fast and slow component, respectively, B^d was the equilibrium hydration at actual relative humidity (p/p_0 =0% or p/p_0 =9%).

In contrast to fruticose thalli, the dehydration time-courses of foliose thalli were sufficiently well fitted by single exponential dependency (Fig. 3–7i–l)

$$\Delta m / m_0 = B^d + A^d \exp\left(-t / t^d\right), \qquad (3.18)$$

where t^d is dehydration characteristic time and A^d is saturation hydration.

The values of fitted parameters are set up in Tab. 3–6.

Although fits of double exponential function also converged for some time-courses of foliose thalli, the obtained values varied accidentally and the contribution of second component did not exceed two per cent of total. That's why the single exponential approximation was chosen.

The hydration of fruticose thalli revealed the fast component, A_1^h, with minor amplitude and the slow component, A_2^h, with the contribution of more than 80% of total mass increase. Fast component is much slower than the extremely fast hydration component observed for hydration of lichen thallus performed from the aqueous phase [366].

Except *Cladonia mitis*, for which $t_2^h \approx 80$ h, the characteristic time constants for *Himantormia lugubris* and for *Usnea aurantiaco-atra* exceed 120 h, which is the value ~3 times longer than the values for foliose thalli. After very fast hydration to the certain level, the hydration process significantly slows down compared to hydration of foliose lichen. The overall hydration level, $Lh = B^h + A_1^h$, after the first step of hydration time-course seems not to depend on relative humidity, p/p_0, of external environment (see Tab. 3–7). Thus, this value, Lh, can be called "preferably low hydration level", and treated as a population of tightly bound water.

The mechanism of dehydration processes in fruticose thalli shows some analogies with hydration process. As the first one is removed the majority of bound water, the fraction with lesser affinity. Then, the second step takes place: the dehydration from the smaller fraction, which was bond as a first component during hydration process. The hydration level after the first, fast and effective step of dehydration process is equal to $Lh = B^d + A_2^d$ and on average does not depend on relative humidity of external environment (see Tab. 3–7).

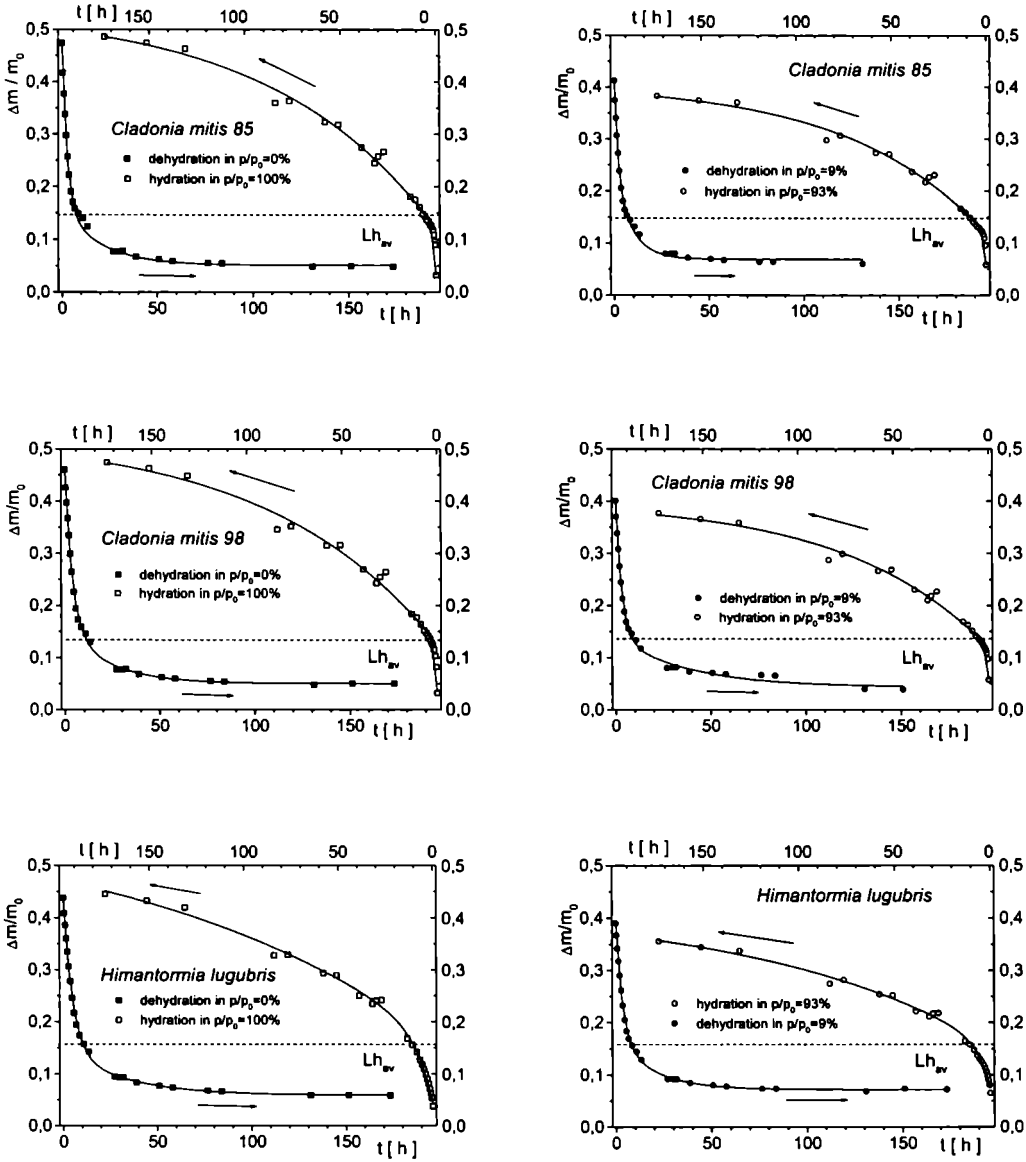

Fig. 3–7. Lichen thalli hydration (open symbols) and dehydration (close symbols) from gaseous phase recorded as relative mass increase, expressed in units of dry mass, $\Delta m/m_0$. Experimental cycles were performed between p/p_0 =100% and p/p_0 =0% (squares), and between p/p_0 =93% and p/p_0 =9% (circles). Prior to dehydration course thalli were incubated for 96h at p/p_0 =93% (thalli subsequently dehydrated at p/p_0 =9%), or at p/p_0 =100% (subsequently dehydrated at p/p_0 =0%). Fitted function is double exponential for (a,b) *Cladonia mitis* 86, (c,d) *Cladonia mitis* 98, (e,f) *Himantormia lugubris* and (g,h) *Usnea aurantiaco-atra* and single exponential for (i,j) *Caloplaca regalis* and (k,l) *Umbilicaria antarctica* (see text).

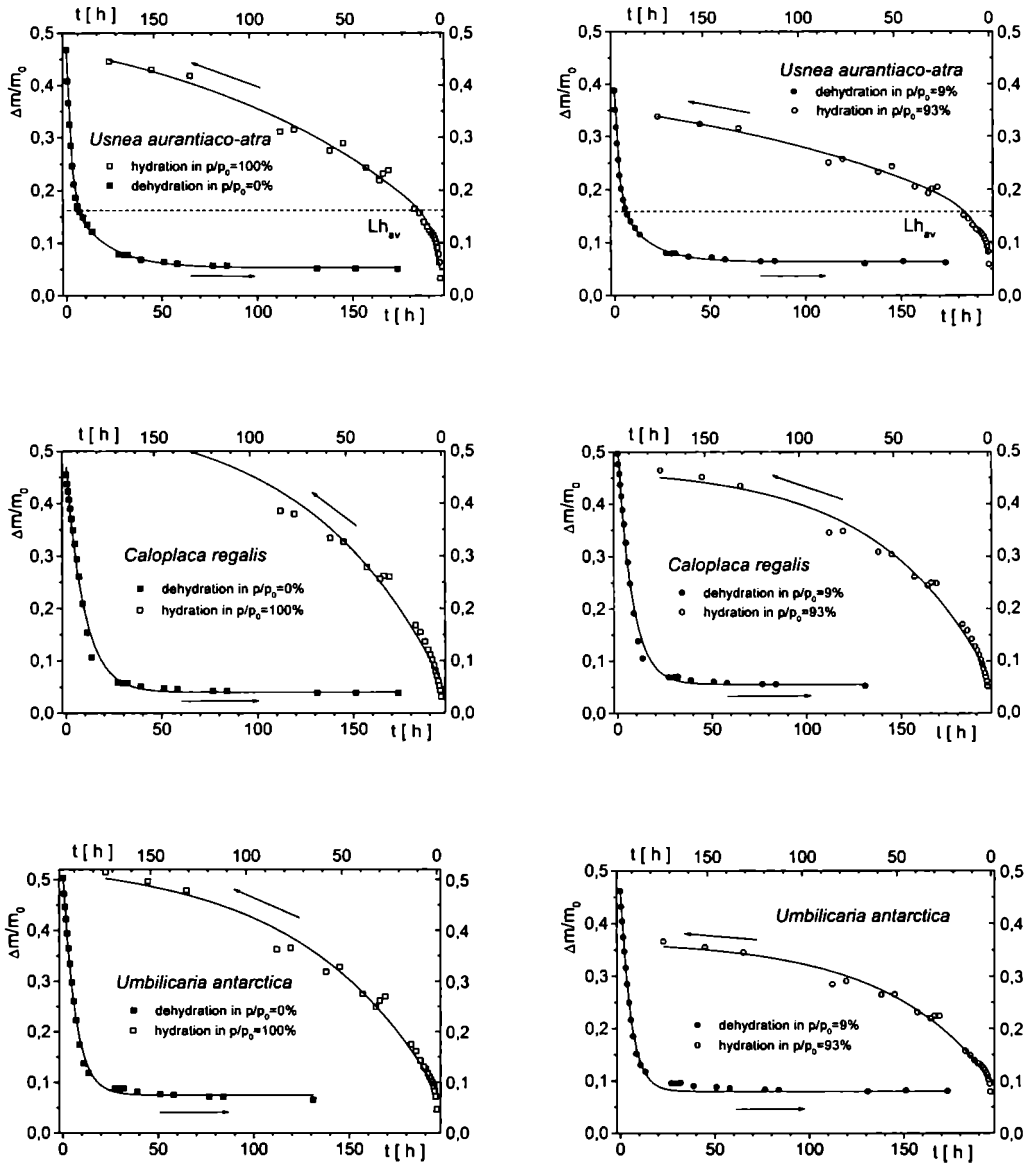

Fig. 3–7. Continuation: double exponential for (g,h) *Usnea aurantiaco-atra* and single exponential for (i,j) *Caloplaca regalis* and (k,l) *Umbilicaria antarctica* (see text).

Table 3–5. Lichen hydration kinetics performed from gaseous phase at $p/p_0 = 93\%$ and $p/p_0 = 100\%$, fitted from Eqs. (3.14) and (3.15) (see text). The errors are the standard errors of fitted parameters.

Table 3–5a.

$p/p_0 = 93\%$	C	A_1^h	t_1^h [h]	A_2^h	t_2^h [h]
Cladonia mitis CM86	0.406±0.010	0.059±0.009	0.47±0.17	0.291±0.009	70.4±5.7
Cladonia mitis CM 98	0.400±0.011	0.058±0.009	0.56±0.21	0.281±0.011	73.3±7.0
Himantormia lugubris	0.429±0.038	0.081±0.012	6.77±1.55	0.272±0.028	129.0±36.8
Usnea aurantiaco-atra	0.436±0.092	0.074±0.019	7.98±3.02	0.285±0.076	162.1±95.5
Caloplaca regalis	0.471±0.015	A^h = 0.396±0.014		t^h = 58.3±5.2	
Umbilicaria antarctica	0.368±0.009	A^h = 0.267±0.009		t^h = 55.9±4.8	

Table 3–5b.

$p/p_0 = 100\%$	C	A_1^h	t_1^h [h]	A_2^h	t_2^h [h]
Cladonia mitis CM86	0.538±0.018	0.088±0.012	0.59±0.18	0.420±0.016	83.8±7.5
Cladonia mitis CM 98	0.529±0.021	0.091±0.012	0.91±0.26	0.403±0.019	87.3±9.5
Himantormia lugubris	0.613±0.078	0.122±0.015	8.65±1.53	0.447±0.065	169.7±53.1
Usnea aurantiaco-atra	0.565±0.061	0.085±0.015	3.70±1.38	0.434±0.051	132.4±35.5
Caloplaca regalis	0.580±0.023	A^h = 0.519±0.022		t^h = 70.4±6.9	
Umbilicaria antarctica	0.541±0.023	A^h = 0.458±0.021		t^h = 70.4±7.6	

Table 3–6. Lichen dehydration kinetics performed from gaseous phase at $p/p_0 = 0\%$ (a) and $p/p_0 = 9\%$ (b), fitted from Eqs. (3.17) and (3.18) (see text). The errors are the standard errors of fitted parameters.

Table 3–6a.

$p/p_0 = 0\%$	B^d	A_1^d	t_1^d [h]	A_2^d	t_2^d [h]
Cladonia mitis CM86	0.050±0.003	0.294±0.011	2.42±0.15	0.132±0.011	20.15±2.52
Cladonia mitis CM 98	0.050±0.003	0.307±0.021	3.86±0.34	0.108±0.021	22.98±5.21
Himantormia lugubris	0.058±0.003	0.293±0.013	4.75±0.28	0.090±0.013	32.09±6.02
Usnea aurantiaco-atra	0.053±0.002	0.285±0.008	2.18±0.11	0.135±0.008	18.64±1.75
Caloplaca regalis	0.040±0.004	A^d = 0.434±0.008		t^d = 9.38±0.46	
Umbilicaria antarctica	0.073±0.003	A^d = 0.441±0.006		t^d = 6.44±0.21	

Table 3–6b.

$p/p_0 = 9\%$	B^d	A_1^d	t_1^d [h]	A_2^d	t_2^d [h]
Cladonia mitis CM86	0.062±0.003	0.233±0.012	2.35±0.17	0.117±0.011	16.4±2.43
Cladonia mitis CM 98	0.043±0.006	0.259±0.011	3.16±0.24	0.095±0.009	38.7±9.13
Himantormia lugubris	0.072±0.002	0.223±0.013	3.39±0.25	0.098±0.013	19.57±2.86
Usnea aurantiaco-atra	0.064±0.001	0.200±0.008	2.23±0.13	0.124±0.008	15.00±1.27
Caloplaca regalis	0.055±0.005	A^d = 0.458±0.009		t^d = 7.54±0.36	
Umbilicaria antarctica	0.086±0.002	A^d = 0.377±0.004		t^d = 5.21±0.12	

The Lh value, in general, is not connected with the relative humidity of air but it is a function of thallus structure. The relative mass increase at preferred low hydration level is below the one needed to formation ice crystallites inside the thallus [273, 274, 277, 278]. For foliose thalli the preferably low hydration level, Lh, cannot be distinguished from hydration courses.

Calculations of water clustering point for wood of klinki pine (*Araucaria klinkii* Lauterb.) gave the value $M/m_0 = 0.20–0.25$ [295], which exceeds the value of Lh for lichen thallus, however, it may be implied by different micro-structure of wood.

Table 3–7. The preferably low hydration level, Lh, for lichen thalli investigated.

	Dehydration: $Lh = B^d + A_2^d$		Hydration: $Lh = C - A_2^h$		Mean Lh
	$p/p_0 = 0\%$	$p/p_0 = 9\%$	$p/p_0 = 93\%$	$p/p_0 = 100\%$	
Cladonia mitis CM86	0.182±0.011	0.179±0.011	0.115±0.013	0.118±0.024	0.149±0.037
Cladonia mitis CM 98	0.158±0.021	0.138±0.011	0.119±0.016	0.126±0.028	0.135±0.017
Himantormia lugubris	0.148±0.133	0.170±0.013	0.157±0.047	0.166±0.102	0.160±0.010
Usnea aurantiaco-atra	0.188±0.008	0.188±0.008	0.151±0.119	0.131±0.080	0.165±0.028

The observed mechanism of hydration and dehydration in fruticose thalli may benefit in better adaptation to frost weather changes. At first, fast hydration step, the thallus is activated to "ready-to-function" low hydrated state, whereas further hydration is slow down, what can preserve the tissue during accidental fluctuations of local moisture and/or temperature. Very effective, fast dehydration may prevent against the ice crystallite formation inside thallus at rapid weather breakdowns, whereas the thallus still remains in "ready-to-function" state, which may benefit in the case, when the weather breakdown was short time event only.

There was no significant differences between two *Cladonia mitis* samples investigated. The overall hydration level and the ratio of the magnitudes of both components were not changed. The characteristic time, t^d, for dehydration of the fast component is longer for the sample CM98 than for the sample CM86. Short values of characteristic time constants could be caused either by decomposition of the thallus stored in herbary or by site differentiation of thallus (Iceland or Spitsbergen).

The mass of water bound to primary binding sites on thallus surfaces, $\Delta M/m_0$, show the values close for all six thalli (see Chpt. 3.4). As averaged over the lichen samples investigated $\Delta M/m_0 = 0.0675±0.0045$. This value is close to the average value of B^d constant at $p/p_0 = 0\%$, which is equal $B^d = 0{,}0540±0.0045$, and at $p/p_0 = 0\%$ equals $B^d = 0{,}0637±0.0147$. The values of B^h obtained from Eq.(3.16) for hydration to $p/p_0 = 93\%$ are equal $B^h = 0.056$ and 0.061, for *Cladonia mitis* CM85, and CM98, respectively, for *Himantormia lugubris* $B^h = 0.076$, for *Usnea aurantiaco-atra* $B^h = 0.077$, whereas for *Caloplaca regalis* $B^h = 0.075$, and for *Umbilicaria antarctica* $B^h = 0.101$. For hydration courses performed at $p/p_0 = 100\%$ fitted values of B^h are smaller (because thalli were dehydrated at

lower relative humidity – p/p_0 = 0%) and equal for *Cladonia mitis* CM85, and CM98, 0.03 and 0.035, respectively; for *Himantormia lugubris* B^h = 0.044, for *Usnea aurantiaco-atra* 0.046, for *Caloplaca regalis* 0.0061, and for *Umbilicaria antarctica* B^h = 0.083. The relative amount of water in pool B^h is to some extent controlled by the relative humidity of environment, however, it still reflects the elevated hydrophilicity of *Umbilicaria antarctica* thallus, as it was observed using sorption isotherm. The saturated value of this fraction is presented by B^d parameter, and agrees with the value of full coverage of primary binding sites, the number obtained from sorption isotherm.

"Hot" water binding sites reveal high affinity to water, as majority of them is occupied at low relative humidity. Moreover, it explains that primary water binding sites predicted by Dent model are in thallus "hot" binding sites, whereas hydration kinetics results point out another pool of bound water, the one defined as Lh.

3.6 Two-dimensional percolation of water bound in biological system observed using electric conductance

Static electric conductance, σ, as measured versus the hydration level of the dry biological structure is sensitive for water percolation threshold, p_c, occurring in dehydrated system. Water deposited on thallus surfaces is a conductive medium with the DC conductivity, σ, for hydration level just above and near the percolation threshold, p_c, [640]:

$$\sigma(p) \propto (p - p_c)^{\alpha}, \tag{3.19}$$

where p is the probability of site occupancy by the conducting medium, and α is a fractal exponent, which depends on the dimensionality of the system.

The probability of site occupacy is proportional to the hydration level of the system, the normalized value of conductivity: $(\sigma-\sigma_0)/\sigma_0$, where σ_0 is the DC conductivity value for a dehydrated system. Thus, from Eq. (3.19) one gets

$$\frac{\sigma - \sigma_0}{\sigma_0} = \left(\frac{\Delta m}{m_0} - \frac{M_c}{m_0} \right)^{\alpha}, \tag{3.20}$$

where m_0 is dry mass of thallus, Δm is a mass of water in the system, M_c/m_0 is hydration level at percolation threshold. The Eq. (3.20) can be easily applied to hydration data.

3.6.1 Percolation in a living system as observed using electric conductance

There are some early reports on dielectric techniques used to detect the water content in stored seeds [22] but specific mechanisms responsible for the observed dispersion were not reported [503].

Low-frequency χ–dispersion for nearly dry protein powders is of Maxwell-Wagner type [181].

The measurement of dielectric losses performed for lysozyme powders at varied hydration ($\Delta m/m_0 = 0.20–0.36$) showed an isotope effect for D_2O, strong pH dependency and an effect produced by complexion with a substrate, which together indicated proton conduction process involving ionizable side chain groups of the protein surface. The isotope effect strongly indicates that for lysozyme powders protonic conduction is the dominating contribution to the dielectric relaxation $\Delta\varepsilon_2$ in the frequency range studied (10 kHz to 10 MHz) [104]. The relaxation process is, thus, of Maxwell-Wagner type [529], and the σ values inferred from the τ_δ data, for frequencies higher than 10 kHz are assigned to a transport process that involves protons. Two conduction processes at two different frequency ranges are explained in terms of $\Delta\varepsilon_1$ relaxation assigned to proton transport through the bulk powder sample, and $\Delta\varepsilon_2$ relaxation attributed to proton displacements on a single macromolecule only. Thus, the resistivity of the intermolecular pathway in lysozyme powder must be considerably larger than the resistivity of the proton moving on the surface of the hydrated macromolecule [104].

In hydrated horse myoglobin ($\Delta m/m_0 = 0.36$) the dielectric response can be explained by fast reorientation of water dipoles and a frequency-dependent conductance of protons along threads of hydrogen-bonded water molecules [608].

For hydration below monolayer coverage for single molecules of lysozyme the hydration water is severly disordered [576]. The protonic conductivity of hydrated lysozyme powders revealed the percolation threshold at $M_c/m_0 = 0.15$, which value is independent on pH (for $3 \leq pH < 9$). As full coverage of the lysozyme surface requires the hydration level $M_m/m_0 = 0.38$ [576], the value of onset of hydration induced changes in dielectric properties gives the value of critical fractional coverage for protonic conduction as $\Delta M_c/\Delta M_m = 0.40$, which matches with percolation density equal $\rho_c = 0.45\pm0.03$ for 2-d networks [726]. Percolation through protein interior appears unlikely at least for hydration-dependent processes, such as proton conduction, when internal water in proteins is sparse and does not form interconnected threads. Moreover, internal water in proteins is generally structural and presumably more tightly bound than that at the hydration level M_c/m_0 [106].

Careri et al., 1988, reported for hydrated lysozyme powder $\alpha = 1.29$, which is within the theoretical ranges 1.1–1.3 for 2-d percolation [640, 726]. For hydration levels far from M_c/m_0, the critical exponent $\alpha = 2.08$, which is characteristic for 3-d process. It is possible that 3-d conduction pathways through the hydrated lysozyme powder layer appear at higher hydration level, as

intermolecular water bridges may be establish. There was no isotope effect on α value in hydrated lysozyme [107].

There are some early reports on dielectric techniques used to detect the water content in stored seeds [22] but specific mechanisms responsible for the observed dispersion were not reported [503].

Careri & Giansanti, [105], for wheat (*Triticum turgidum* L.) seeds (hydration range: $\Delta m/m_0 = 0.15–0.26$) suggested Maxwell-Wagner relaxation and that protons are major component of the moving charges. The hydration-sensitive d.c. conductivity displays an exponential increase with increasing hydration, as it was recorded for several biomacromolecules [529, 573].

Samples in form of pellets between 0.5 and 1.0 mm in diameter obtained from hand-dissected embryos and endosperms of maize seeds (*Zea mays* L.) show percolative behavior at dehydration to gaseous phase. Critical exponents $\alpha = 1.23$ (2-d process) were close in values for both samples, whereas hydration at percolation threshold was $M_c/m_0 = 0.082$ for embryo, and $M_c/m_0 = 0.127$ for endosperm [91].

In dehydrated purple membrane of *Halobacterium halobium* the capacitance and the derived conductivity show explosive growth above a threshold hydration level, $M_c/m_0 = 0.046$. Although there is no isotope effect neither on h_c nor on α, the conductivity is strongly affected by D_2O hydration suggesting protonic conductivity. The critical exponent $\alpha = 1.23$, which describes a 2-d percolative process. On the other hand, $\Delta M_c/\Delta M_m = 0.18$ for the full coverage of purple membrane, M_m/m_0, obtained from the sorption isotherm, which suggest the 3-d percolative process. Possibly, the long range proton conduction paths, reflected in the growth of the conductivity at the percolation threshold, may be localized in spatially separated regions of the membrane: (i) the lipid surfaces, (ii) the lipid-protein surfaces, or (iii) entirely within proteins. If such a region is preferentially hydrated relative to other regions of the membrane, the 2-d percolative process will show lower critical fractional coverage as expected for a process of higher dimensionality [577].

Cellular cysts of the brine shrimp *Artemia* show percolation behavior manifesting in sharp increase in conductivity at a critical threshold of hydration $M_c/m_0 = 0.35$. Critical exponent above h_c is equal $\alpha = 1.64$ for a 3-d infinite lattice. Cysts of the crustacean *Artemia* are early embryos covered by a chitinous shell and consist of about 4000 tightly packed, morphologically similar cells with virtually no extracellular space. Above $\Delta m/m_0 = 0.05$ the permittivity increases rapidly then reaches a near plateau up to hydration near $\Delta m/m_0 = 0.15$. This conductivity behaviour may be connected with the dissipative contribution of dipoles and charges which become mobile and/or polarizable only when in contact with number of water molecules, hydrogen bonded in three dimensions. An alternative explanation is the formation of functional biological structures in hydrated *Artemia* cysts. Model sample made from free isolated chitinous shells hydrates only up to $\Delta m/m_0 = 0.1$ (at which hydration they exhibit virtually no permittivity), showing

that the possible capillary condensation is not involved at the phenomena occurring at the higher hydration region. As D_2O affects the hydration of *Artemia* cysts, the isotope effect was here not investigated. At the hydration $\Delta m/m_0 = 0.35$ metabolism of a cyst is initiated suggesting that the establishment of random space connectivity of ionic pathways may facilitate formation and/or function of enzyme-enzyme and/or enzyme-cytomatrix associations [90].

Although bound water percolation threshold was recorded for several biological systems with increasing complexivity: protein powders, biological membranes, seed endosperm, these observation are not made on living creatures. The samples of isolated plant embryos dehydrated below percolation threshold, however, in a native seed even at very low total hydration level of seed, embryo remains in hydrated form [289]. The *Artemia* cysts seems to be an exception, however, percolation threshold in *Artemia* cysts is observed at relatively high hydration level significantly exceeding the hydration levels needed in other systems to cover the inner surfaces of tissue, suggesting that inside cyst there exist wet regions at dehydration. Moreover, *Artemia* cyst is an early embryo, which may not save its ability to survive the desiccation shock in its adult form.

Up to now the reversible dehydration below percolation threshold was not observed in a living organism *in vivo*, occurring at hydration level so low that all inner surfaces of the system take part in the process.

3.6.2 Percolation of water bound in lichens

To detect a percolation threshold in lichen thallus, this Author applied the static electric conductivity in a course of slow dehydration to the gaseous phase [282]. Disk-like electrodes (about 30 mm in diameter) of a parallel plate capacitor cell were cut out of a copper sheet and then randomly punctuated (25 holes 2 mm in diameter per electrode) to ensure sufficient gas exchange between the sample and the environment. The electrodes were then gold coated, and their outer surfaces insulated by Teflon mesh covers. To accommodate fragmented thalli samples the spacing between the electrodes was roughly 5mm, that produced the empty cell capacitance of about C_0 = 2.5 pF. Low-frequency dielectric spectra, $\varepsilon^*(\omega) = \varepsilon'(\omega) - i \cdot \varepsilon''(\omega)$; $\omega = 2\pi f$, were measured at a number of different frequencies between f = 100 Hz and 1 MHz, using the HP 4191A LF impedance analyzer. The dehydration was performed in dry gaseous nitrogen stream at room temperature. To monitor the sample hydration level, the cell was weighted continuously (every 3.5 min for about 16 h) to within 0.2 mg accuracy by a digital balance, WPS 72, RADWAG, Poland [282].

DC conductivity has been evaluated from the imaginary part (dielectric loss factor) of complex dielectric spectrum. The presence of three components in $\varepsilon''(\omega)$ was assumed

$$\varepsilon''(\omega) = \varepsilon_c''(\omega) + \varepsilon_{MW}''(\omega) + \varepsilon_p''(\omega) \tag{3.21}$$

$\varepsilon_c''(\omega) = \sigma/(\omega\varepsilon_0)$, where ε_0 is the permittivity constant, arises from the energy dissipation by the sample DC conductivity and is the contribution of principal interest. $\varepsilon_{MW}''(\omega)$ is a contribution from the Maxwell-Wagner relaxation effect that should be present in other biological samples [105]. For simple, regular structures the Maxwell-Wagner contribution has a Debye-like form with a single relaxation time [72]. For random in form and size structures like the thalli samples the distribution of relaxation times was expected. For simplicity, the effective Maxwell-Wagner contribution was described by the Cole-Cole formula

$$\varepsilon''_{MW}(\omega) = \Delta\varepsilon \cdot \frac{\cos(0.5\alpha\pi)}{\cosh\left((1-\alpha')\ln(\omega\tau_0)\right) + \sin(0.5\alpha\pi)} \tag{3.22}$$

with a symmetric distribution of relaxation times around τ_0, the width of which is parameterized by α', and $\Delta\varepsilon$ being the process strength. The third contribution, $\varepsilon_p''(\omega) \propto 1/f^2$, is due to electrode polarisation by free ions in the sample. The conductivity, σ was determined by fitting Eq. (3.21) to experimental dielectric loss spectrum.

Fig. 3–8 shows relative contribution to conductance coming from water bound on thallus surfaces versus hydration level above percolation threshold expressed in units of dry mass. The obtained hydration level, M_c/m_0, at percolation threshold and fractal exponent, α, are shown in Tab. 3–8.

For *Cladonia mitis* the value of fractal exponent $\alpha = 1.18$ fits well in the range of theoretical values for a 2-d system [640], whereas for *Himantormia lugubris* $\alpha = 1.42$ what slightly exceeds the value for two dimensions, signalizing the spatial curvature of inner thallus surfaces. For both lichens percolation threshold is observed at relative humidity often occurring in natural conditions and at storage in a herbary, namely, for *Himantormia lugubris* at $p/p_0 = 35\%$, and for *Cladonia mitis* at $p/p_0 = 34\%$ [271]. From anabiosis in herbary lichen easily returns to active life (see Chpt. 3.3).

Table 3–8. The hydration level at percolation threshold, M_c/m_0, fractal exponent, α, the intercept ot the logarithm of hydration dependent term of conductivity, $\log[(\sigma - \sigma_0)/\sigma_0]$, versus the logarithm of relative hydration excess over the percolation threshold, $\log(\Delta m/m_0 - M_c/m_0)$; and the relative humidity, h, at the percolation threshold [271].

	Site:	M_c/m_0	α	β	h
Himantormia lugubris	King George Island	0.099	1.46	8.02	0.35
Cladonia mitis	Northern Sweden	0.0926	1.18	5.70	0.34

(a)

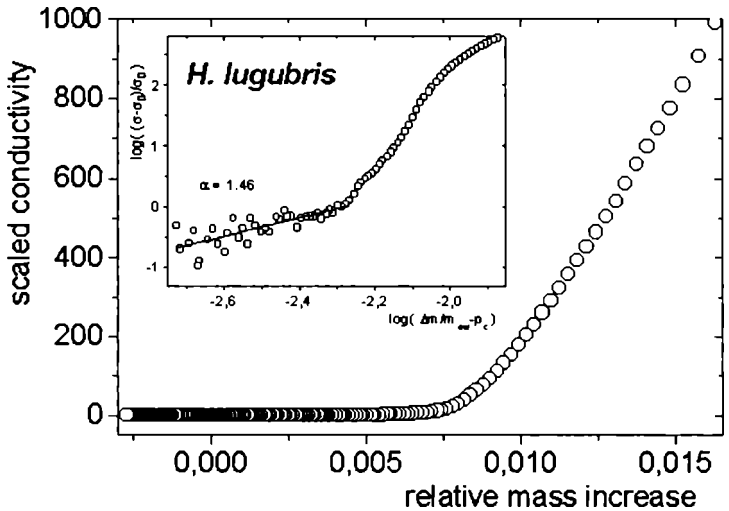

(b)

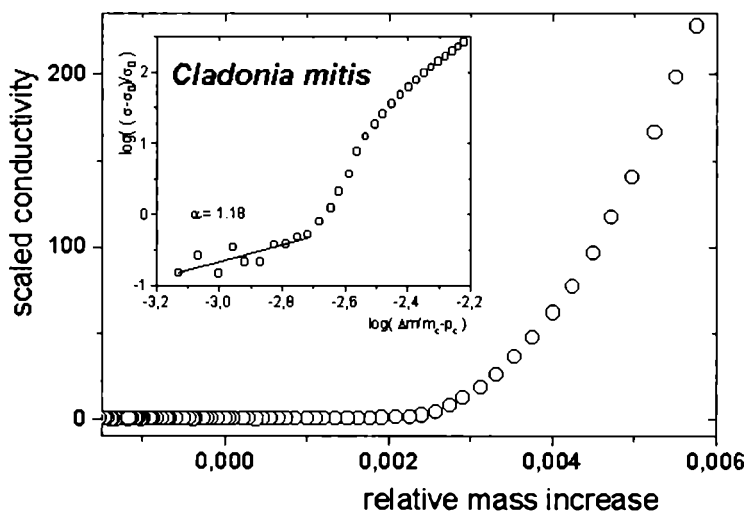

Fig. 3–8. The conductivity of lichen as a function of hydration level, $\Delta m/m_0$, in units of dry mass. Data shown were collected in the course of dehydration for *Himantormia lugubris* (a), and for *Cladonia mitis* (b). Data shown are of the percolation conductivity normalized to the background conductivity, $(\sigma - \sigma_0)/\sigma_0$. For better visualization of percolation phenomena, in the insets the new origin is set at the percolation threshold, and the data are plotted in a log–log scale (see Tab. 3–8).

3.7 Model of percolating lattice for water bound on the surface

The question arises, which lattice properly models the network of hydrogen bonds between water molecules bound on the surface of dry biological system, e.g. on lichen thallus.

One should first found the average number of hydrogen bonds binding waters on the surface. Stillinger, 1980, using molecular simulations found the distribution maximum number of hydrogen bonds per free water molecule equal $n_{HB} = 2.3$ at $t = +10^0$C. Other Monte Carlo simulations suggest the average value $\langle n_{HB} \rangle = 3.19$ at $T = 298$ K [345]. The X-ray experiment shows at $T = 300$ K the number of hydrogen bonded first neighbours $n_{HB} = 3.1$ (at $r = 2.87$ Å), whereas the number of first unbonded neighbours $n' = 1.3$ ($r = 3.41$ Å) [719]. As the unbounded neighbours were assigned by their proximity to a given water molecule only, the sum of $n_{HB}+n'$ should also be taken into account, as one of possible values of z. Although in liquid water many of hydrogen bonds may be distorted, the tetragonal arrangement of bonds is roughly saved, thus, majority of water molecules in bound water monolayer is bonded to the surface by one hydrogen bond. Also only negligible number of water molecules binds with more than four hydrogen bonds. Thus, with high dose of credibility one can assume that for free water the average number of hydrogen bound neighbours varies between 1.3 and 3. Only two types of 2-d lattice match to this range: Bethe lattices and honeycomb lattice. They have close values of site percolation threshold (see Tab. 3–3).

As for every water molecule the number of hydrogen bond varies with time, Bethe lattice with water molecules in its sites and hydrogen bonds in its branches, with the difference that there is no constant number of branches emanating from every given site of Bethe lattice should be considered. The process of breaking of hydrogen bonds and hydrogen binding is dynamic, thus, an averaged number of hydrogen bonds between neighboring water molecules is a good measure of the number of branches emanating from every given site, z. As an statistic average, z may not be an integer. As one of hydrogen bonds is already used for binding of water to the surface (assuming that this bond does not affect the protonic percolation process on the surface of solid system) the number of bonds, z, varies between 0 and 3.

Calculating the percolation threshold for Bethe lattice, one starts from the origin, then checks if there is a chance of finding of an infinite pathway of occupied sites starting from that origin. Walking along such a pathway, one finds (z–1) of new bonds emanating from every new site, except of the direction, from which we came. Every of these (z–1) bonds leads to the new neighboring site, which is occupied with the probability p. On average, we have now the p(z–1) new occupied neighbors, to which we may continue the

pathway. If this number $p(z-1)<1$, the averaged number of various pathways leading to the infinity decreases by the same factor at every generation of neighboring sites.

Thus, even assuming that z neighbors of occupied origin happen to be occupied, the probability of the finding of continuous pathway of occupied neighbors decreases to zero exponentially with the lengths of the pathway, if $p < 1/(z-1)$. Thus, the percolation threshold for Bethe lattice, with average number of neighbors equal z is

$$p_c = \frac{1}{z-1} . \tag{3.23}$$

The result is the same as for geometrical Bethe lattice, [640], where z is an integer.

If the geometric form of the lattice and, thus, threshold percolation probability, p_c, value is not known, Scher & Zallen, [H. Scher, R. Zallen, *J. Chem. Phys.*, **53**, 3759 (1970)], proposed the use of the critical percolation density, ρ_c, defined as

$$\rho_c = p_c \cdot f , \tag{3.24}$$

where f is a filling factor for the lattice, i.e., the fraction of space occupied by a set of circles centred in each site of the lattice, every circle of radius equal to the half the nearest-neighbour separation. So defined ρ_c is to a close approximation constant for several lattices tested, and equals $\rho_c = 0.44\pm0.02$ for 2-d lattice, and $\rho_c = 0.15\pm0.01$ for 3-d lattice. This value was then used for some authors in calculations of the system hydration [91, 106, 107, 577].

However, for water layer populating the surface of adsorbent, critical percolation density instead threshold percolation probability should not be applied, as the hydrogen-bond network of water molecules forms "puckered" structure with to the total area surface of the adsorbent closer to the definition of f than to the full coverage of the surface. As the mass of water layer fully covering the surface of the adsorbent is given the experimental value of the mass of water molecules covering this surface, but not the total geometric surface.

To explain the difference, for $t = 0^0C$ the critical percolation density for liquid water (assuming the percolation threshold value as for random Bethe lattice, $d_c = 0.917$ g cm^{-3} for ice, $d_c = 0.99987$ g cm^{-3} for liquid water, and the local tetrahedral structure in presence of distorted and stretched hydrogen bonds [642]) is calculated. The obtained values of ρ_c for $z = 2.5$ and for $z = 2.6$ noticeably differ from the values obtained for the lattices tested by Scher & Zallen (Tab. 3–9).

Table 3–9. The critical percolation density, ρ_c, calculated for water bound on the surface of adsorbent treated as a random Bethe lattice at t = 0°C, taking $d_c = 0.917$ g cm^{-3} for ice, $d_c = 0.99987$ g cm^{-3} for liquid water to recalculate the thermal compression of the network, and the local tetrahedral structure in presence of distorted and stretched hydrogen bonds; z = 2.3 is taken for free water [642] at t = +10°C; other values of z are calculated for water bound to lichen thallus.

	z	p_c	Ice, ρ_c	Liquid water, ρ_c
Free water	2.3	0.76923	0.3538	0.3748
Lichen thallus	2.5	0.68593	0.31553	0.3342
Lichen thallus	2.6	0.62148	0.28589	0.3028

3.8 Total water accessible surface of biological system

The obtained hydration level at percolation threshold, M_c/m_0, may be utilised to estimate the total water accessible surface of lichen thallus, including both outer as well as inner surfaces of the tissue. Tab. 3–10 shows thallus hydration levels at full coverage of water accessible surface calculated for several 2-d lattices with $n \leq 3$. The obtained values do not differ much from the values of preferably low hydration level, Lh, of lichen thallus obtained from hydration kinetics for *Cladonia mitis* (Lh = 0.149±0.037 and Lh = 0.135±0.017, for two different samples), and for *Himantormia lugubris*, Lh = 0.160±0.010 (see Chpt. 3.5, and [271]). This suggests that preferably low hydration level Lh is a hydration level needed for full coverage of all water accessible surfaces of lichen thallus.

Under the above assumption, the real value of percolation threshold is 0.61875 for *Himantormia lugubris*, and between 0.62148 and 0.68593 for *Cladonia mitis*. For Bethe lattice with varied number of branches, these values correspond to the average number of bonds equal n = 2.6 for *Himantormia lugubris* and n = 2.5 to 2.6 for *Cladonia mitis* (Tab. 3–10). They are also close to the percolation threshold for the honeycomb lattice (0.6046) [Scher & Zallen, 1970].

Bruni et al., [91], used the percolation density to describe the percolation phenomenon, however, for maize endosperm they reported the value of percolation threshold equal 0.7, which is close to results for lichens.

Table 3–10. The hydration level at full coverage of total water accessible surface in lichen thalli, as approximated using honeycomb and Bethe lattice for n = 2.3 [642], and for n = 3.1 [719], mean Lh [271], the value of percolation threshold, $p_{c,\,calc}$, calculated taking mean Lh as a full coverage, and respective value of n_{calc}.

	p_c	Honeycomb	Bethe n=2.3	Bethe n=3.1	Mean Lh	$p_{c,\,calc}$	n_{calc}
Himantormia lugubris	0.099	0.142	0.129	0.208	0.160±0.010	0.61875	2.6
Cladonia mitis	0.0926	0.133	0.120	0.194	0.149±0.037 0.135±0.017	0.62148 0.68593	2.6 2.5

Although water prefers layering conformation in restricted spaces between multilayered membranes obtained from frog sciatic nerves [490], water deposition on solid surface is not entirely a 2-d problem, as wetting angle may differ from zero [41, 392]. Thus, the calculated full coverage of inner thallus surface may not be the exact geometrical monolayer, but its thickness may slightly exceed the thickness of monolayer. However, at the hydration Lh the total water accessible surface of thallus is completely covered by water layer.

Taking into account this limitation, one may estimate the surface of water monolayer. Assuming the O–O distance r_{OO} = 2.76 Å, one gets for hexagonal ice I_h the surface per water molecule equal to s_{H_2O} = 8.85/100 Å^2 (which is 11.3 molecules/100 Å^2 on the surface of ice crystallite).

The surface of water monolayer per 1g, Σ, equals

$$\Sigma = \frac{s_{H_2O} \cdot n_A}{\mu}, \tag{3.26}$$

where n_A is the Avogadro number and μ is the mass of mole of water.

This number decreases with the increased density of liquid water compared with density of ice. The decrease is due to distorsion and breaking the regular lattice of hydrogen bonds, which results in better "packing" of molecule in liquid water [642]. The correction factor, ξ (at 0^{0}C ξ = 0.9439), is given by

$$\xi = \left(\frac{d_{ice}}{d_{H_2O}} \right)^{2/3}, \tag{3.27}$$

where d_{ice} is the density of ice (see Chpt. 1.2), and d_{H_2O} density of water. Thus, the surface of liquid water monolayer, Σ', is given by

$$\Sigma' = \xi \cdot \Sigma = 2795 \text{ m}^2\text{g}^{-1}, \tag{3.28}$$

and the water surface S per dry mass unit

$$\frac{S}{m_0} = \Sigma \cdot \frac{\Delta m}{m_0}, \tag{3.29}$$

where Δm is mass of water in thallus, and m_0 is dry mass.

As an upper limit of water accessible surface of thallus, one can take for fruticose thalli the preferred low hydration level, Lh. So obtained specific surface areas are shown in Tab. 3–11.

Thus, the Author showed that the combined measurements of static conductivity and hydration kinetics supply the method of non-invasive, *in vivo*, estimation of total water accessible surface of dry biological system.

Table 3–11. The estimated specific inner surface area of lichen thallus per dry mass unit as estimated from the number of water binding sites, S_{Dent}, (lower limit) and from the bound water layer and percolation threshold, S_{Lh}, (upper limit for fruticose thalli).

	S_{Dent} [m^2g^{-1}]	S_{Lh} [m^2g^{-1}]
Cladonia mitis 86	188.3	416.4
Cladonia mitis 98	191.7	377.3
Caloplaca regalis	171.7	–
Himantormia lugubris	199.4	447.2
Usnea aurantiaco-atra	176.5	461.2
Umbilicaria antarctica	203.8	–

There exist a model systems with very close value of specific surface area. In controlled pore glass CPG74, with pore diameter of 74 Å (pore distribution ±7%), the specific surface area is equal to 153 m^2g^{-1} [283]. Taking into account that the density of glass is ca. two and half times higher than the density of biological tissue (~1 g cm^{-1}), the specific surface area of lichen thallus per volume unit is close to the value for controlled pore glass (380–420 m^2cm^{-3}). Moreover, the specific pore volume of CPG74 equals 0.47 cm^3g^{-1} (porosity ~54%), which does not differ much from the data obtained for some lichen thalli (porosity 30% for *Lasallia hispanica* (Frey) Sancho & Crespo, and 28% for *Lasallia pustulata* (L.) Mérat, [678]).

3.9 Thallus hydration from gaseous phase as observed by proton magnetic relaxation

Proton relaxation observed for rehydrated lichen may differentiate tightly and loosely bound water pools. Several foliose lichens: *Xanthoria parietina*, and *Parmelia saxatilis* (samples P5 and P6); and others with fruticose thalli: *Cladonia mitis* (samples P1 and P2), *Cladonia bellidiflora*, and *Cetraria islandica* were investigated by this Author. Thalli were harvested in Northern Sweden in summer; except the sample P2 harvested in autumn. The samples were then stored at room temperature and humidity for 6 months. Before experiments thalli were incubated for 14 days over the supersaturated solution of H_3PO_4 (in $p/p_0 = 9\%$).

3.9.1 Hydration kinetics

We performed the hydration courses at p/p_0=93%. The relative mass increase, $\Delta m/m_0$, expressed in units of dry weigh was simplified by the single exponent

$$\Delta m / m_0 = A^h\left(1 - \exp\left(-t / t^h\right)\right) + B^h, \qquad (3.30)$$

where A^h is the saturation hydration at $p/p_0 = 93\%$, in case of fruticose thalli mostly the longer one of two components (see below), B^h is the hydration level in air-dry state ($p/p_0 = 9\%$), both expressed in units of dry weight; and t^h is the hydration time constant. After completing the hydration series, the dry mass of the sample was determined after heating in 70°C for 24 h. Higher temperatures were not used to avoid the decomposition of some thallus organic constituents [224].

Tab. 3–12 presents the fitted hydration parameters. Hydration times t^h vary from (33.4±3.7) h for *Cladonia mitis* (P2) up to (63.9±2.4) h for *Cladonia bellidiflora*. The obtained time constants are comparable with those obtained for maritime Antarctic lichens [366]. It should be noted that here the thallus was tightly packed in NMR tubes which might slow down the hydration process, compared to hydration in moist chamber.

The different values of hydration times t^h recorded for *Cetraria islandica* and *Cladonia mitis* at first and second hydration course reflect the history of the sample, i.e. the incubation (in $p/p_0 = 9\%$) before the second hydration was much longer (880 h) than that prior the first hydration run. Possibly, before the first hydration course the hydration of these samples was not in equilibrium and, thus, the second course presents the rehydration of thallus with better accuracy.

The equilibrium hydration value at $p/p_0 = 9\%$, B^h, varies only slightly for different lichen species investigated and its averaged value equals $B^h = (5.6\pm1.0)\%$.

The saturation hydration A_h is significantly lower than the value recorded for maritime Antarctic lichens [366], however, this may come from both the differences of hydration conditions and the difference between lichen species.

The dehydration courses were performed to $p/p_0 = 9\%$. Similarly to hydration, the dehydration of the thallus was fitted by single exponent

$$\Delta m / m_0 = A^d \exp\left(-t / t^d\right) + B^d \,, \tag{3.31}$$

where A^d the saturation hydration at initial conditions (p/p_0=93%) and B^d the final equilibrium hydration at p/p_0=9%, both expressed in units of dry weight; and t^d was the dehydration time.

For every lichen measured, the dehydration time T^d was shorter than the hydration time T^h. The non-removable equilibrium hydration at $p/p_0 = 9\%$ obtained for dehydration was in every case very close to the value obtained at hydration. The averaged value was $B^d = (5.6\pm1.0)\%$. The values of saturated hydration ($p/p_0 = 93\%$) are systematically higher than the values obtained at hydration [272].

To check the consistency of the data the supposed values of dry weight of the samples for initial and final stages of each hydration and dehydration course using the fitted values of A, B and t were calculated. In no case the overall increase of the sample dry weight was higher than 0.7% for the full series of gravimetric experiments. Thus, if the effect of growth was negligible, we came to the conclusion that the observed differences of parameters A for the same sample are most likely due to the history of the sample.

Table 3–12. The kinetics of hydration (and dehydration) performed from the gaseous phase at $p/p_0 = 93\%$ and $p/p_0 = 9\%$, respectively. The parameters fitted from Eqs. (3.30) and (3.31) (see text). Before the second course of hydration the short (interrupted after 54 h) hydration was performed after which the samples were incubated for 413 h in $p/p_0 = 9\%$ before the second hydration course. Character # denotes number of the hydration course.

	Hydration				Dehydration		
	#	A^h	B^h	T^h [h]	A^d	B^d	T^d [h]
Cladonia mitis P1	1st	0.175±0.003	0.055±0.001	59.5±2.5			
	2nd	0.183±0.004	0.048±0.002	43.2±2.4			
Cladonia mitis P2	2nd	0.172±0.007	0.046±0.004	63.7±6.4			
Cladonia bellidiflora		0.128±0.002	0.048±0.001	63.9±2.4	0.163±0.005	0.057±0.006	43.9±3.6
Cetraria islandica	1st	0.150±0.002	0.072±0.001	50.6±1.6			
	2nd	0.183±0.004	0.048±0.002	46.5±2.6			
Parmelia saxatilis P5		0.133±0.003	0.045±0.001	57.3±3.1	0.183±0.004	0.050±0.004	27.1±1.7
Parmelia saxatilis P6		0.145±0.003	0.074±0.002	36.0±2.4	0.182±0.010	0.076±0.009	21.4±3.7
Xanthoria parietina		0.187±0.004	0.050±0.002	51.6±3.0	0.260±0.005	0.047±0.004	19.6±1.1
Cladonia mitis P2 *	2nd	0.142±0.008	0.061±0.002	33.4±3.7	0.200±0.004	0.054±0.004	29.2±1.5

* *Cladonia mitis* loosely packed in the tube.

The conditions of hydration and dehydration runs were exactly the same (p/p_0 = 93% for hydration and p/p_0 = 9% for dehydration) but the storage period between both hydration courses was different, moreover, before the second series of hydration courses a short hydration experiment was performed (not presented here).

The obtained values of characteristic hydration time for hydration of *Cladonia mitis* $t^h \approx 60$ h (at $p/p_0 = 93\%$), and for dehydration $t^d \approx 30$ h (at $p/p_0 = 9\%$) are close to the values for the slow component of hydration process (see Chpt. 3.5). The short component was not observed, because the sampling times were to distant for initial stages of the hydration/dehydration process, thus the values for short times weakly affected the value of χ^2 function [272]. Although the absence of fast component for *Cladonia mitis* could be caused by the absence of two step freeze-protection mechanism in thallus from the sites of milder climat (Sweden), however, simple, numerical explanation is suggested.

3.9.2 Proton relaxation times

Proton spin-lattice relaxation time T_1 was recorded for *Cladonia mitis* (P2) at room temperature. The spin-lattice relaxation function was described by a single exponential function with $T_1 \approx 10$ ms for upper parts of thallus, and $T_1 \approx 15$ ms for lower parts of thallus, and did not vary much with the hydration, $\Delta m/m_0$, changed between 0.10 and 0.23. This suggests that the proton spin-lattice relaxation at room temperature is dominated by the electron paramagnetism of endogenous centers [716] present in thallus. Thus, the attention was focused on FID function characterized by T_2^* time constant (shorter than T_1), which here yields more information. FID experiment allows the analysis of the signal from solid and tightly bound water [272], whereas the resolution of loosely bound and/or free water subsystems requires an Carr-Purcell-Meiboom-Gill (CPMG) experiment [303].

3.9.3 Proton free induction decays

Fig. 3–9a,b shows proton FID for *Cladonia mitis* (P2) hydrated to $\Delta m/m_0 = 12.7\%$. The FID function is a superposition of a Gaussian component, coming from protons of the lichen solid matrix (a solid signal) and two exponential components (for some samples only one exponential is observed), L_1 and L_2, coming from the protons of water bound in thallus. These water fractions are differentiated by their dynamics, thus, by the proximity to the solid surface and/or type of chemical bonding. i.e. the protons of intracellular water contribute both to tightly and to loosely bound (or free) water fraction. The same is true for extracellular water protons. However, the T_2^* value for loosely bound water is strongly influenced by B_0 inhomogeneities, thus preventing the fine analysis of the loosely bound water pools differentiated by size or by paramagnetic ion content in micro-compartments of the thallus.

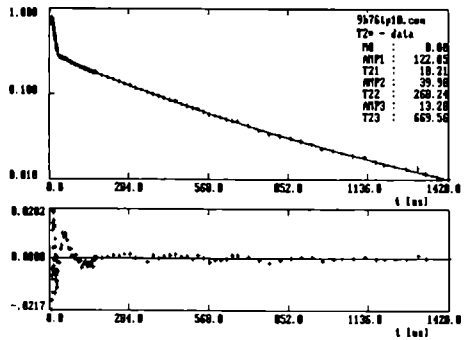

(a), (b)

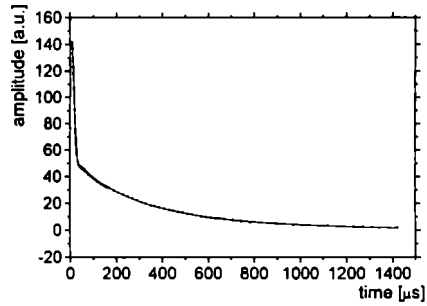

(c)

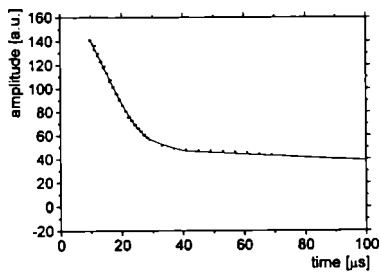

(d)

Fig. 3–9. Proton FID (crosses) recorded at room temperature for *Cladonia mitis*, sample P2, hydrated to $\Delta m/m_0$ = 15.7% (p/p_0 = 52%) with fitted superposition of Gaussian and two exponents (solid line) and the (b) the relative residual function. The fitted points differ less than 2% from the measured points; (c) fitted the moment expansion for solid signal (see Eq. (3.32) and two exponents for liquid signal, and (d) the extended time scale for the solid signal for fit (c).

The 1/e value of T_2^* [here (17.68±2.58) μs] for the solid matrix of *Cladonia mitis* is close to values obtained for other ultra-dry biological systems, as tooth enamel [221], dentine [222, 275], solid matrix of wheat seed [279, 289], horse chestnut bark and bast [290] or wood [296], and shell of molusc [280, 281]. The observed similarity between proton relaxation times T_2^* of the solid matrices for wide range of dry biological systems is most likely caused by the similarity of local proton environments in the range of single angstroems, which may be formed by only a limited number of different chemical groups of organic biological compounds [537].

To estimate the error made by Gaussian approximation, the moment expansion of the solid component of the FID signal was performed. The fitted function was

$$f(t) = S\left(1 - \frac{M_2}{2!}t^2 + \frac{M_4}{4!}t^4 - \frac{M_6}{6!}t^6\right), \tag{3.32}$$

where S was the amplitude of solid signal, M_i is the I-th moment of the absorption line, and t is the time starting from the final slope of $\pi/2$ pulse [1].

The detailed analysis of solid signal component, the moment expansion, gives $M_2 = 5.0 \cdot 10^9 s^{-2}$, $M_4 = 5.6 \cdot 10^{19} s^{-4}$ and $M_6 = 7.0 \cdot 10^{29} s^{-6}$, and the magnitude S = 114.1 (Fig. 3–9c, d). The solid line was nearly Gaussian ($\frac{M_4}{M_2^2} = 2.3$ [1]).

The 1/e value obtained from the moment expansion $T_2^* = 18.96$ μs differs from the value obtained from the Gaussian approximation by less than 4.0%, whereas the amplitude differs less than 6.5% from the value obtained from the Gaussian fit, thus, Gaussian approximation of solid components was used for all recorded FIDs.

The relaxation time T_2^* of solid matrix of thallus does not change with the sample hydration, suggesting that the solid matrix is not altered by water vicinity. For the whole hydration range, the value of T_2^* is significantly longer than the spectrometer dead time and can be evaluated with good accuracy. Thus, the amplitude of the solid component S has been used as a standard to scale the liquid signal.

3.9.4 Lichen hydration as observed by NMR

Fig. 3–10 shows the hydration dependence of T_2^* recorded for the lichen species studied. These species may be ordered in two groups: (i) samples with two liquid components, L_1 and L_2, and (ii) samples with only one liquid component. This may result from individual differences in thallus composition within the same lichen species collected from different sites, e.g. *Parmelia saxatilis*, samples P5 and P6, and *Cladonia mitis*, samples P1 and P2. On the other hand, the quality of the data may cause the difficulties in decomposition of liquid signal into two components (in the average value L_2 contribution dominates at high hydration and the L_1 contribution at low hydration level). To check whether for the same species the differences in signals are caused by the individual changes only, the FID's for *Cladonia mitis*, sample P2, were modeled taking the values of T_2^* for both components, and their amplitudes calculated from the linear dependencies of L/S. Then random noise was added. The single-exponential fit to such data gave the values of T_2^* matching with the averaged values obtained for *Cladonia mitis*, P1.

The amplitudes of liquid signals L_1 and L_2 in units of solid signal S (see Fig. 3–11) are expressed. For lichens, in which two liquid signal components may be resolved (see Tab. 3–13), the L_2 component (with much longer relaxation time T_2^*) appears for certain hydration M_2/m_0. Moreover, with increasing hydration level the amplitude of this component increases much faster than the amplitude of the L_1 component.

The amplitudes of solid S and liquid L_i signal are given by:

$$S = \alpha_S \rho_S m_0 \,, \tag{3.33a}$$

$$L_i = \alpha_{H_2O} \rho_{H_2O} \Delta m \,, \tag{3.33b}$$

where ρ_S and ρ_{H_2O} are the proton densities of the solid matrix and water, respectively; α_S and α_{H_2O} are the solid matrix and water effectiveness coefficients, which may be decreased in the vicinity of paramagnetic ions and, in case of solid signal, decreased if the spectrometer dead time is too long excluding proper estimation of S amplitude; m_0 is dry weight and Δm the mass of water present in the sample. From the L/S hydration dependence (see Tab. 3–13) a near-zero value of L/S for zero hydration is deduced, suggesting the absence of liquid pool in dry weight. From (3.33a,b) we get

$$\frac{L}{S} = \frac{1}{\beta}\frac{\Delta m}{m_0}, \tag{3.34}$$

where

$$\beta = \frac{\alpha_S \rho_S}{\alpha_{H_2O}\rho_{H_2O}}, \tag{3.35}$$

which is the effective (scaled to water) proton density of the solid matrix of thallus. It is worth mentioning that β is scaled to apparent water effective proton density in the system investigated, so if there are two different pools of water, which are influenced differently by paramagnetic centers, the obtained value of β will differ for both water fractions. If only one of water pools, say fraction "1", is influenced by paramagnetic ions, the ratio of partial slopes of L/S dependencies, η, is

$$\eta = \frac{\frac{1}{\beta^1}}{\frac{1}{\beta^2}} = \frac{\alpha^1_{H_2O}}{\alpha^2_{H_2O}}, \tag{3.36}$$

where the coefficients with superscript '1' refer to water fraction affected by paramagnetic species, and the ones denoted by '2' refer to the not affected fraction. Thus, η, quantifies the water signal switched off by relaxation in proximity of 'hot' paramagnetic centers.

The water fraction, L_1, comes from tightly bound water, because it appears as the first water subsystem during sample hydration and remains after the L_2 water subsystem is completely removed during thallus dehydration. The effective proton density of water in L_1 pool $\alpha^1_{H_2O}$ is much lower than $\alpha^2_{H_2O}$ for L_2, which means that the relaxation of L_1 fraction is under the influence of paramagnetic centers built in the solid matrix. This is observed for membranes of photobiont where the reaction centre of photosystem II contains manganese ions affecting strongly the proton relaxation process in the range of 30 MHz [54, 56, 254, 288, 381, 568, 569, 716, 717]. Thus, the signal of L_1 component is strongly reduced, whereas loosely bound water fraction, giving the signal L_2, is less (if at all) affected by paramagnetic impurities dissolved in bulk water.

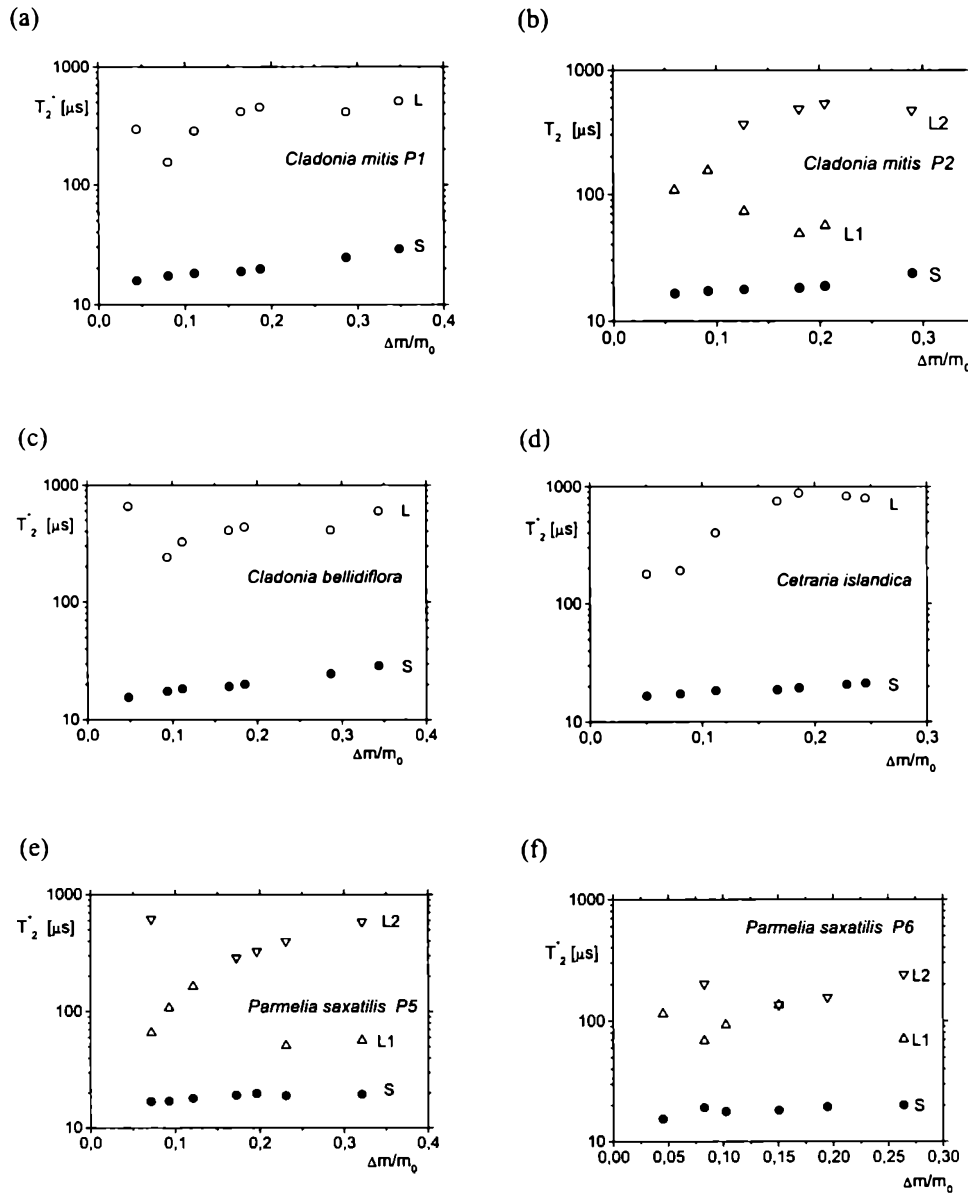

Fig. 3–10. The spin-spin relaxation time T_2^* (calculated from FID) versus hydration ($\Delta m/m_0$) for the lichens investigated. (a) *Cladonia mitis* P1. (b) *Cladonia mitis* P2. (c) *Cladonia bellidiflora*. (d) *Cetraria islandica*. (e) *Parmelia saxatilis* (P5). (f) *Parmelia saxatilis* (P6). (g) *Xanthoria parietina*.

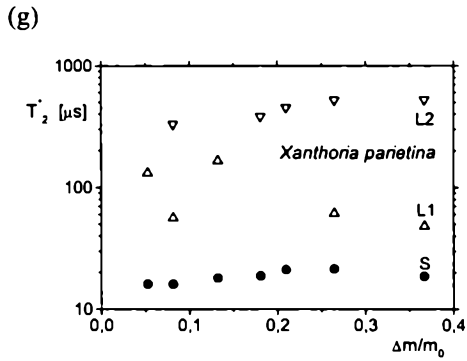

Fig. 3–10. Continuation: (g) *Xanthoria parietina.*

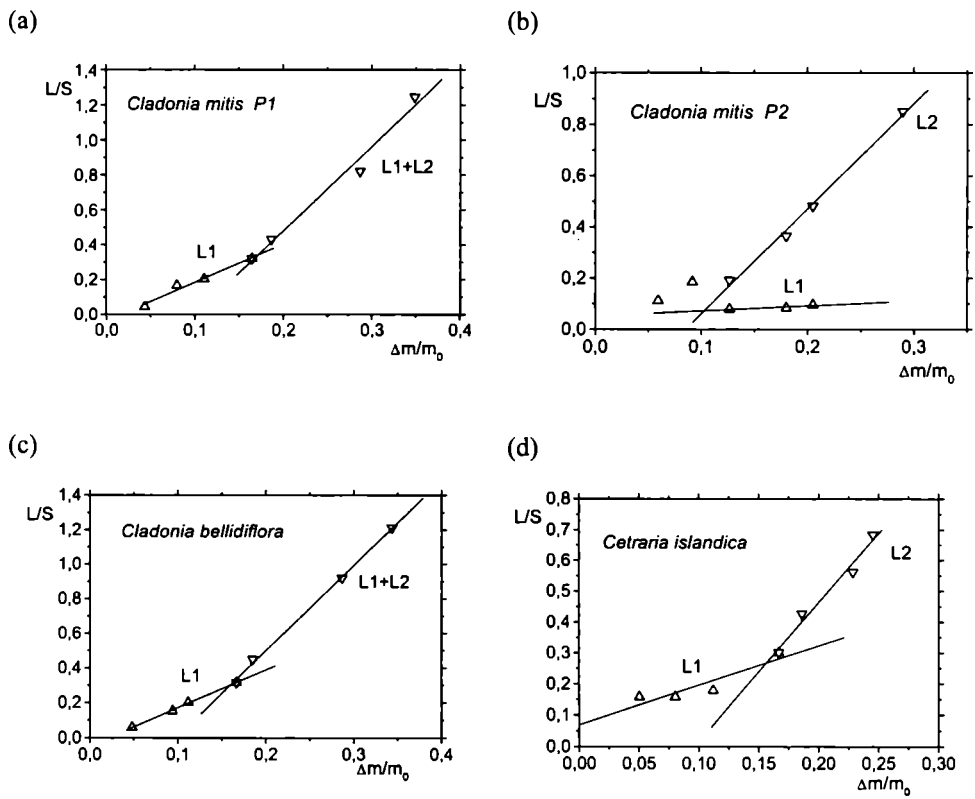

Fig. 3–11. The amplitude of liquid L_1 and L_2 components (or L if only one liquid component was recorded) of FID signal versus the hydration, $\Delta m/m_0$, for the lichens investigated. The amplitudes are expressed in units of the solid component amplitude. (a) *Cladonia mitis* P1. (b) *Cladonia mitis* P2. (c) *Cladonia bellidiflora.* (d) *Cetraria islandica.*

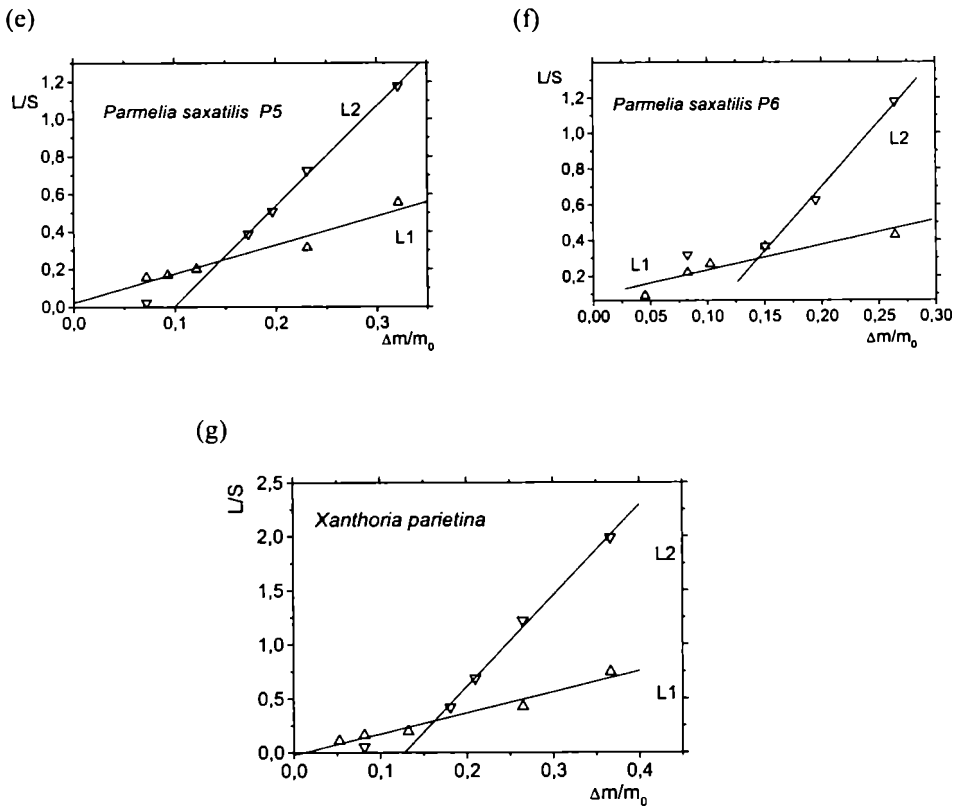

Fig. 3–11. Continuation: (e) *Parmelia saxatilis* (P5).
(f) *Parmelia saxatilis* (P6). (g) *Xanthoria parietina.*

It is possible that the partition of water between the two fractions is such that there are remnants of free water at very low hydration. However, the magnitudes of free water obtained at very low hydration level were so low that the simplest model may be proposed, based on abrupt vanishing of the loosely bound and free water fraction.

The tabulated (Tab. 3–13) values of η convince the statement that the effectiveness of the quenching of tightly bound water signal by paramagnetic species is high, as η (the detectable water signal) for several lichen species varies from 65.6% for *Cladonia mitis*, sample P2, to 23.1% for *Xantoria parietina*.

Assuming that the protons of solid and the protons of tightly bound water pool (most likely, one monolayer) are influenced by paramagnetic ions to the same extent (so the α values for solid and for L_1 are close), the β values should be near the stoichiometrical value of relative (scaled to water) mean proton density of thallus. Tab. 3–13 shows the obtained averaged proton densities which match with the ones calculated from the stoichiometry (Tabs. 3–14 and 3–14a).

Table 3–13. The hydration parameters found for investigated lichens: #L is the number of liquid components of proton FID (asterisk denotes calculations for initial and final slope of total liquid signal hydration dependence); L_0/S – the amplitude of the non-removable liquid signal (estimated for lichen dry weight), $L_{0.09}/S$ – fitted amplitude of liquid signal at $p/p_0 = 9\%$, both scaled in units of solid signal component; M_2/m_0 – the threshold hydration for loosely bound (free water appearance); β_S (= β_1) is the relative proton density of solid, scaled to L_1 fraction; η – part of L_1 water signal effectively observed.

Lichen/sample code	#L	L_0/S	$L_{0.09}/S$	M_2/m_0	η	β_S	$\Delta m/m_0$ (NMR)	$\Delta m/m_0$ (grav.)
Folliose thalli:								
Xanthoria parietina	2	0.002(±0.057)	0.111(±0.90)	0.128	0.222	0.53(±0.075)	0.059	0.0526
Parmelia saxatilis P5	2	0.033(±0.045)	0.118(±0.090)	0.099	0.28	0.67(±0.11)	0.079	0.0717
Parmelia saxatilis P6	1*	0.037(±0.100)	0.103(±0.143)	0.160	0.33	0.43(±0.18)	0.061	0.0452
Fruticose thalli:								
Cladonia mitis P2	2	0.053(±0.015)	0.111	0.085	0.047	5.21(±2.4)		0.0594
Cladonia mitis P2	2*	–0.066(±0.024)		~0.17	0.68	0.36(±0.03)		
Cladonia mitis P1	1*	–0.037(±0.028)	0.060(±0.04)	0.172	0.457	0.46(±0.05)	0.028	0.0438
Cladonia bellidiflora	1*	–0.047(±0.006)	0.058(±0.009)	0.160	0.443	0.46(±0.01)	0.027	0.0482
Cetraria islandica	1*	0.069(±0.043)	0.133(±0.062)	0.156	0.383	0.22(±0.03)	0.124	0.0505

It is worth mentioning that the hydration dependence of L/S for samples having only one liquid signal component also has a form with a step in derivative, suggesting that water bound to the surface of those lichens is organized in two pools, which are not distinguished for numerical reasons. Thus, based upon formulae given for the samples with two liquid signal components, the presumed effective proton density for solid matrix (from low hydration part of L/S dependence) and estimated the presumed percentage of detectable water signal of tightly bound water pool (from the ratio of initial and final slope) was calculated.

Table 3–14. The relative proton densities, β, (expressed in units of water) of major lichen constituents calculated directly from the chemical formulas [139, 551, 686].

Substance	β	Substance	β
chitine	0.576	celulose	0.556
Carothenoids			
β–carotene	0.940	β–cryptoxanthin	0.848
zeaxanthin	0.887	lutein	0.887
astaxanthin	0.785	lutein epoxide	0.863
mutatoxanthin	0.849		
Polyols			
erythritole	0.738	D–arabitole	0.711
ribitole	0.711	mannitole	0.692
volemitole	0.679	siphulitole	0.679
Secondary metabolic products consisting up to 10% of dry mass of lichen:			
caperatic acid (aliphatic)	0.835	diploschistesic acid (a depside)	0.377
alectoronic acid (a depsidone)	0.563	didymic acid (a dibenzofurane)	0.632
siphulin (a chromone)	0.589	lichexanthone (a xanthone)	0.441
partietin (an anthraquinone)	0.380	chiodectonic acid (a napthoquinone)	0.327

Table 3–14a. The proton density β calculated for the aminoacids mostly abundant in thalli.

Amino acids	β	Amino acid	β
alanine	0.708	asparagine	0.545
asparaginic acid	0.474	glutamine	0.616
glicyne	0.600	serine	0.600
treonine	0.681		

Effect of aging was tested on dehydrated *Cladonia mitis*, sample P2, stored for 20 months (12 months after all other experiments) at room temperature and at room humidity. The hydration courses were performed on the two samples obtained from upper and lower parts of thallus. The amplitude of liquid component present in dehydrated sample increased by factor 1.47 and 1.74 for lower and upper parts of thallus, respectively, which might be caused by changes of air hydration during sample storage. The tightly bound water component was not distinguished by numerical procedure, however, the change in slope of liquid signal hydration dependence appeared at the same value of M_2/m_0 (at 0.091 in comparison to 0.085

in the sample measured one year before). The proportion of the observed tightly bound water signal, was within the range of values measured for *Cladonia mitis* samples, however, it was decreased from 0.68 to 0.44 for the sample P2, reflecting the changes of paramagnetic centers localization during the storage of dehydrated thallus. The relative proton density of solid matrix was unchanged for the one year storage of *Cladonia mitis* thallus (see Tab. 3–15).

Table 3–15. Effect of 12 monts storage on *Cladonia mitis* thallus.

Sample	#L	L_0/S	$L_{0.09}/S$	M_2/m_0	η	β_S
Sample stored for 7 months:						
P2	2*	–0.066(±0.024)	–	0.12	0.68	0.36(±0.03)
P1	1*	–0.037(±0.028)	0.060	0.125	0.457	0.46(±0.05)
Sample stored for 19 months:						
P2 lower part	1	0.078(±0.007)	0.088	–	–	0.399(±0.020)
P2 upper part	1	0.092(±0.006)	0.084	0.10	0.443(±0.036)	0.329(±0.016)

3.9.5 NMR differentiation of bound water pools in thallus

The non-removable water fraction, B, detected in lichens gravimetrically did not vary significantly with lichen species either for hydration or for dehydration course. The average value for all gravimetric measurements was B = (5.6±1.0)%. The NMR hydration courses gave similar values, however, more scattered. In fact, the greatest discrepancy gave consequently the *Parmelia saxatilis*, sample P5, which might be caused by individual differences (much greater, however, than the difference between species). Fraction B observed by NMR may be assigned to water bound to "hot" binding sites on thallus surface, the fraction which was also distincted by sorption isotherm [271].

NMR showed that at lowest hydration level ($p/p_0 = 9\%$) only tightly bound water pool characterized by $T_2^* \approx 100$ μs remains. The value of T_2^* matches with that for water proton fraction bound to the pore surface of controlled pore glasses and recognized as 'solid' water [283].

The magnitude of 'tightly' bound water fraction suggest that this fraction is, indeed, identical with the full coverage of the thallus surface, denoted as Lh. NMR measurement allows to differentiate the Lh fraction by its dynamic properties manifested in nuclear magnetic relaxation.

Although the mild desiccation performed from gaseous phase (in conditions happening in nature) completely removes the loosely bound water fraction and significantly reduces the tightly bound water fraction, the values of hydration needed to re-initiate biotic activity in lichens are much higher ($\Delta m/m_0 = 0.3$ for *Cetraria nivalis* [373] and for *Usnea sulphurea* [357]).

3.10 Desiccation resistance of insects and Collembola

Plant desiccation resistance should be compared with the desiccation resistance of animals, among them some insect and Collembolan species may be treated as representative examples.

Arthropods must continually maintain their hydration level within physiologically tolerable limits. The terrestial species gain water from drinking, feeding and absorption from surrounding air, and from metabolism (metabolic water), whereas they loose water by cuticular transpiration, respiration, secretion from the mouth and anus, and by excretion [262]. Depending on their environment, physiological conditions and taxon, arthropods can withstand amount of body water loss between 17 to 89% of fresh mass [262], which is low value compared to respective values for plants.

3.10.1 Water in insects

Generally 95–99 out of 100 molecules in terrestial arthropods are water, and their hydration levels are between 65 and 75% of fresh mass (average 69±8%), with extremes: 40–90% [262]. There are three main compartments for fluids of arthropod body [63]: (i) the haemolymph and other body fluids; (ii) the cuticle and exoskeleton; (iii) other tissues, e.g. muscles, alimentary canal, fat deposits.

Body water in terrestial arthropods [63] is classified onto subsystems similarly to water in other biological systems:

(i) free or bulk water, which is lost by heating/drying;
(ii) structured or bound water, closely associated with membranes, proteins, nucleic acids [172];
(iii) vicinal water, which covers all structured water including that only transiently bound to molecular structures [193].

Enhanced complexity of the arthropod organism (compared with uniformity of lichen thallus) enforces the application of less-invasive methods of the determination of hydration level. The hydration level in arthropod samples is determined using the following methods [63]:

(i) gravimetric (fresh mass less that after drying to constant mass in air, e.g. for larvae of cranefly *Tipula paludosa* and eggs of grasshoppers dried at 60^0C for 72 h [62, 64]);
(ii) isotopic (dilution of injected labelled water);
(iii) calorimetric (using latent heat of fusion).

3.10.2 Characteristic of desiccation resistance of terrestial arthropods

High atmospheric humidity may cause the hygroscopic absorption of water onto the cuticle, may promote absorption of water vapor into the body, and may reduce amount of water lost via transpiration. Low atmospheric humidity increases evaporative loss of water to the surrounding air, and increases the transpiration rate.

Dry habitat species have slower rates of water loss than those living in moist environments, e.g. for East African carabids and curculionids from dry habitats as compared to similar species from *mesic* ("dry-air", [186]) or *hygric* ("humid-air") environments [724].

A factor of loss is of ~50 between the water loss rate of carabids from humid habitats and tenebrionids from dry habitats, for beetles of given size. In fact, these two families differ in ability to survive under dry conditions (in dry air at 20^0C those carabids survive a few days, whereas tenebrionids survive >2 months [6]).

Dessication resistance of arthropods is characterized by the following features [63]:

(i) water loss via respiration is a major pathway, (e.g. adult East African carabid and curculionid beetles living in dry habitats conserve water, beside reduction in cuticular water permeability, mostly by reduction in respiratory water loss by the development of a closed subelytral cavity and by lowered metabolic rate [724]);

(ii) haemolymph osmolality generally increases with dehydration (e.g. three alpine tenebrionid species, from 2600–3200m in the High Atlas Mountains in Morocco, tolerated >50% dehydration and did not osmoregulate [230]), but some species are osmoregulators (e.g. alpine chrysomelids *Timarcha* spp. maintain their haemolymph osmolality constant for body water losses up to 46% [230]);

(iii) cuticular conductance of water vapor varies with habitat dryness (e.g. in 4 mite and 3 Collembola species from Maritime Antarctic rates of water loss in dry air over the temperature range between -10^0C and $+45^0$C varied from 0 to ~30% fresh mass per hour [711]; for 16 Collembola species the cuticle conductances ranged from 0.6 mm min^{-1} for species from xeric habitats such as house dust to 159.0 mm min^{-1} for cave dwelling species, thus, the permeability is strongly correlated with humidity of the environment [294]);

(iv) amount of body water is critical for survival of desiccation (e.g. for two Antarctic springtails, *Paristoma octooculata* desiccates faster than *Cryptopygus antarcticus* under identical experimental conditions, with the difference that *Cryptopygus antarcticus* contained significantly more body water (~10 μg) [66];

(v) constant or changing temperatures influence measured water loss rates (e.g. the drying rates of some Collembola slow down as both ambient temperature and water content decrease [682]; the increase of the temperature from 5^0C to 20^0C of collembolan *Parisotoma octooculata* increases the cuticular conductance (or permeability to water vapor) by a factor 2.8 as recorded at each constant temperature, whereas the increase of drying temperature during

drying process retards the transpiration rate on the same level for the temperature range studied [294]).

3.10.3 Enormous desiccation resistance of *Polypedilum vanderplankii*

Larvae of an insect, a chironomid *Polypedilum vanderplanki* Hint., populating the temporary rock pools of tropical Africa, is the largest multicellular animal tolerating deep dehydration [306, 307]. During cryptobiosis (complete dehydration and metabolic activity on an undetected level) it survives the temperatures –270^{0}C (for 77 h), +106^{0}C (for 3 h), and 200^{0}C (for 5 min); the duration of cryptobyosis may prolonge for even up to 17 years [308, 309, 310].

In contrast to desiccation tolerant lichens, the process of desiccation for *Polypedilum vanderplanki* durates relatively long time (7 days), however, the special conditions of faster dehydration (48 h) are established [698]. During desiccation larva accumulates up to about 18% of dry body mass of trehalose (3 mg trehalose/mg proteins), whereas other sugars and polyols are not detected [698].

The rehydration, and also dehydration, of larvae occurs through the mouth and the anus. This differs the rehydration of larvae from the rehydration of lichen thalli, which occurs from gaseous phase through whole surface of thallus. The recovery to the active biotic state takes only 45 minutes.

The accumulation of trehalose may be induced by addition of sodium ions (1% of NaCl). The most popular chironomid in Japan, *Chironomus yoshimatsui*, which is enable to reach cryptobiosis, is characterized by much lower level of glycogen (precursor of trehalose), no enhanced synthesis of trehalose, and also much smaller level of lipids [T. Okuda, personal communication].

Decapitated, thus, deprived of brain, subesophageal ganglion, and thoracic ganglia, larvae completely dehydrate and recover, surviving for more than 2 weeks after recovery. They also accumulate trehalose although only about half as much as the intact larvae [698].

Almost unchanged effectiveness of freezing protection of decapitated larvae indicates that central nervous system is only to minor extent involved in freezing protection phenomena in *Polypedilum vanderplanki*. The cellular background of this mechanism suggests that there is a correspondence in freezing protection mechanism in this insect species and in lichen thalli.

4. Freezing protection mechanisms in dry biological system

Reversible desiccation of dry biological system may result in increased tolerance to low temperatures, if water amount in intra- or extra-cellular spaces is not sufficient to form ice crystallites. Thus, the resistance to acute water stress may be accompanied by chilling and/or freezing resistance of the system.

Indeed, there is a massive evidence that lichen reveal high tolerance to low temperature (see Chpts. 3.1.3 and 3.1.5), and/or biotic activity below 0^0C (Chpt. 3.1.4). These facts turn ones attention to the mechanism of lichen freezing resistance in correlation with varied hydration level.

4.1 Free and loosely bound water in lichen

This Author performed proton NMR experiment with the use of a very soft pulse ($\pi/2$ = 35 μs), which provides the information on the mobile fraction of water, consisting of loosely bound and free water pool, often defined as "freezable" water [277]. The contribution of tightly bound water signal is then significantly reduced, as it relaxes in lichen thallus with $T_2^* = 60–100$ μs; and solid signal with $T_2^* \approx 16$ μs is not observed at all [272, 273].

Thallus of *Cladonia mitis* Sandst. [= *C. arbuscula* (Wallr.) Flot ssp. *mitis* (Sandst.) Ruoss] was selected, because it populates habitats in a broad range of climatic conditions (samples harvested in Northern Sweden, in autumn, and then stored at room temperature in an air-dry state, but prior the hydration were dried for 14 days at p/p_0 = 9%). Slow (in equilibrium) cooling of the thallus was performed down to -45^0C, which is below the temperature range in habitats of *Cladonia mitis*.

To examine the effectiveness of freeze protecting mechanism at different hydration level, thalli were hydrated for 30 days from gaseous phase over the supersaturated solutions of Na_2SO_4 (p/p_0 = 93%), $Na_2S_2O_3$ (76%), or kept over the H_3PO_4 surface (9%). The obtained samples: "93", "76" and "09" contained $\Delta m/m_0$ = 0.193, 0.126 and 0.076 of water, where m_0 is dry mass measured after 48 h incubation in oven at 70^0C.

4.1.1 Line halfwidth

For thalli of *Cladonia mitis* hydrated to $\Delta m/m_0 = 0.193$ and to 0.126 (samples "93" and "76") proton NMR spectrum recorded at 300 MHz is well described by Lorentzian function in the temperature range investigated. For the Sample "09" ($\Delta m/m_0 = 0.076$) the NMR spectrum may be effectively approximated by Lorentzian function only at room temperature (T = 296 K), whereas at lower temperature it shows more complex structure with two pronounced peaks (Fig. 4–1a,b,c). Fitted peak positions, line widths and of areas under peak are presented in Tabs. 4–1a, 4–1b and 4–1c (Samples "93", "76", and "09", respectively).

For hydrated samples proton NMR spectrum is an average of free water and of loosely bound water contributions, whereas for dehydrated Sample "09" beside the signal of remaining mobile protons possibly manifests the contribution from tightly bound water partially excited by the soft NMR pulse.

Table 4–1. ^{1}H–NMR spectra vs. decreasing temperature recorded for *Cladonia mitis* hydrated at (a) $p/p_0 = 93\%$, at (b) $p/p_0 = 76\%$, and at (c) $p/p_0 = 9\%$. For Tab. 2c peak positions scaled to the middle of broad peak at room temperature. No external reference was used, so, the peak positions were scaled to the reference points defined in the scaling series of spectra recorded at T = 299 K.

Table 4–1a.

Temperature		Peak position		Halfwidth		Area
t[^{0}C]	T[K]	[Hz]	[ppm]	[Hz]	[ppm]	[a.u.]
26	299	500	1.7	1230	4.1	96.99
10	283	610	2.0	1210	4.0	77.63
3	276	650	2.2	1210	4.0	72.59
–5	268	650	2.2	1140	3.8	70.37
–20	253	680	2.3	1160	3.9	52.93
–35	238	900	3.0	2830	9.4	16.00
–45	228	1000	3.3	4120	13.7	10.26

Table 4–1b.

Temperature		Peak position		Halfwidth		Area
t[^{0}C]	T[K]	[Hz]	[ppm]	[Hz]	[ppm]	[a.u.]
20	293	540	1.8	1910	6.4	50.41
10	283	630	2.1	2140	7.1	48.48
3	276	680	2.3	2400	8.0	43.02
–5	268	750	2.5	2890	9.6	33.13
–20	253	1000	3.4	4350	14.5	18.04
–35	238	1150±200	3.8±2.6	6290±200	21.0±2.6	12.26
–45	228	1930±150	6.4±0.5	7790±250	26.0±0.8	4.83

Table 4–1c.

Temperature		Peak position		Halfwidth		Area
t[^{0}C]	T[K]	[Hz]	[ppm]	[Hz]	[ppm]	[a.u.]
23	296	–730	–2.4	1010±250	3.4±0.8	295.45
		1210±250	4.0±0.8	4380±170	14.6±0.6	
10	283	–1240	–4.1	1010±250	3.4±0.8	205.97
		1460±250	4.8±0.8	4960±250	16.5±0.8	
–5	268	–980	–3.3	1350±80	4.5±0.3	148.17
		1630±200	5.4±1.4	5050±420	16.8±1.4	
–20	253	–980	–3.3	1350±80	4.5±0.3	104.55
		1880±200	6.2±1.4	6310±670	21.0±2.2	
–35	238	–730±85	–2.6±0.3	1180±170	3.9±0.6	73.20
		1960±420	6.5±1.4	5890±590	19.6±2.0	
–45	228	2260±840	7.5±2.8	8580±840	28.6±2.8	69.68

(a)

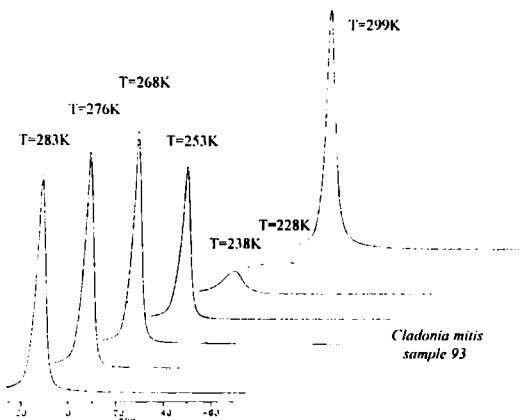

(b)

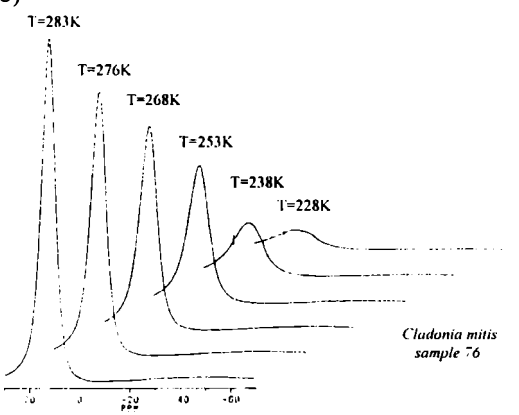

Fig. 4–1. Proton NMR spectrum recorded at 300 MHz for the thallus of *Cladonia mitis* as a function of temperature: (a) Sample "93" hydrated in $p/p_0 \approx 93\%$ ($\Delta m/m_0 = 0.193$); (b) Sample "76" hydrated in $p/p_0 = 76\%$ ($\Delta m/m_0 = 0.126$) and (c) Sample "09" hydrated in $p/p_0 = 9\%$ ($\Delta m/m_0 = 0.076$). The pulse length equals $\pi/2 = 35$ μs; the spectral widths 100 kHz; the spectra were processed without any line broadening except for the sample "09" (1 Hz Lorentzian line broadening). The temperature was stabilized in gaseous nitrogen flow with the accuracy of about 1 K. After the temperature of the stream was reached, there was at least 15' delay to allow the temperature of the sample to stabilize.

(c)

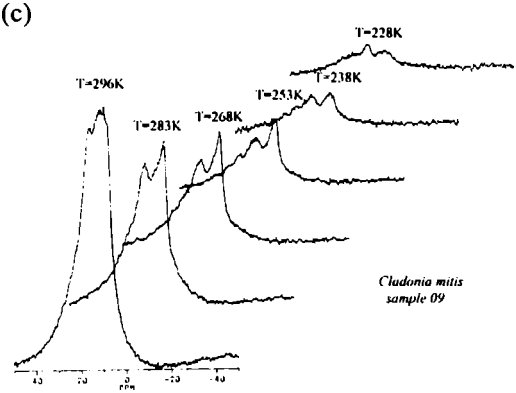

Fig. 4–1. Continuation.

Fig. 4–2 a,b shows the temperature dependency of the NMR line halfwidth for *Cladonia mitis* thallus hydrated to $\Delta m/m_0 = 0.193$ and to $\Delta m/m_0 = 0.126$ (Sample "93" and "76"), respectively. For the Sample "93" the halfwidth of proton line has a constant value $h_w = (3.98 \pm 0.08)$ ppm [(1190 ± 40) Hz] for $T > 253$ K. As the sample is solid, gently pressed lichen thallus, not forming a spatially uniform sample, linewidth measured for the Sample "93" resulted most likely from a distribution of magnetic fields (caused by local changes in susceptibility) experienced by the protons. In contrast, the halfwidth of proton NMR line observed for the Sample "76" continuously increases with decreasing temperature, which, assuming Lorentzian lineshape, gives a linear decrease of spin-spin relaxation time (calculated from the linewidth) on Arrhenius plot with activation energy equal to $E_a = (12.7 \pm 0.4)$ kJ mole^{-1}, which is close to lower limit of hydrogen bond energy [652]. However, it may be altered by the influence of paramagnetic ions present in aqueous medium in thallus.

(a) (b)

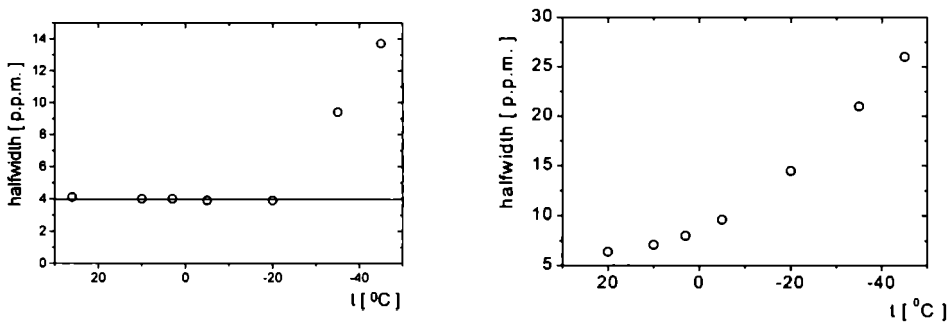

Fig. 4–2. The temperature dependency of proton NMR linewidth recorded at 300 MHz for the thallus of *Cladonia mitis* hydrated to (a) $\Delta m/m_0 = 0.193$ and to (b) $\Delta m/m_0 = 0.126$.

4.1.2 Peak positions

For all hydration levels, proton NMR peak position for *Cladonia mitis* shifts upwards with decreasing temperature, however, the slope of this function depends on hydration level of the sample. The chemical shift is a measure of the change in resonant magnetic field strength when the environment of a proton changes [187]. If an O–H group of a water molecule forms a hydrogen bond the magnetic resonant field strength decreases and the signal shifts downfield.

The temperature dependence of the chemical shift, δ, for liquid water is expressed by phenomenological formula [485, 592]

$$\delta = -4.58 + 0.0095\,t\,, \tag{4.1}$$

where temperature t is expressed in Celsius scale. The signal shifts downfield as steam is condensed and shifts further downfield as water is cooled. Similar shifts are observed for other substances forming hydrogen bonds. Usually shift is larger as hydrogen bond formed is stronger [187]. When O–H group enters into a hydrogen bond, the electronic environment of the proton changes in such a way that the screening constant, σ, is reduced. Thus, the local magnetic field acting on the hydrogen bond proton, B_{loc}, increases according to

$$B_{loc} = B_0(1-\sigma)\,, \tag{4.2}$$

where B_0 is applied magnetic field, and the resonance is observed at lower value of the applied magnetic field. This effect occurs because (a) the presence of oxygen O_B in the O_A — H .. O_B hydrogen bond changes the distribution of electronic charge in the O_A — H bond in such a way that it tends to draw the proton away from the electrons in the O_A — H bond, and reduces the electron density around the proton (resulting in reduction of σ and thus causing a chemical shift downfield); or (b) induced electron currents in O_B produce a magnetic field at the proton. Effect (b) is significant only if the magnetic susceptibility of O_B is anisotropic and can alter σ value [544].

The temperature dependency of the chemical shift of water has been interpreted both in terms of hydrogen-bond breaking and hydrogen-bond distortion. The interpretation in terms of bond breaking [304, 485] is based on the assumption that the chemical shift observed at given temperature, $\delta(T)$, is an average of the chemical shifts of hydrogen-bonded and non-hydrogen-bonded protons in the liquid (δ_{HB} and $\delta_{n\text{-}HB}$, respectively). In this model the observed chemical shift may be expressed as

$$\delta(T) = X_{HB}(T)\cdot\delta_{HB} + \left[1 - X_{HB}(T)\right]\cdot\delta_{n-HB} \tag{4.3}$$

where $X_{HB}(T)$ is the mole fraction of intact hydrogen bonds at the temperature T. As $X_{HB}(T)$ decreases with increasing temperature [642], $\delta(T)$ moves upfield with increasing temperature.

The temperature dependency of the chemical shift of hydrogen bonded substances may in part arise from distortion (the stretching) of hydrogen bonds [486]. Hindmann, [304], emphasized that either stretching or bending of hydrogen bonds can probably contribute to the chemical shift of water.

Fig. 4–3 shows the chemical shift for protons of water in thallus of *Cladonia mitis* at various hydration levels. For the temperature range below 0^0C, line shifts upfield with decreasing temperature. For a given hydration level the value $d\delta(T)/dT$ remains constant as the temperature is decreased, except for the Sample "93" ($\Delta m/m_0 = 0.193$) below -20^0C, where the freezing of the loosely bound water fraction occurs between -20^0C and -35^0C. (Also accompanied by a rapid decrease in the area under peak and the increase in the line halfwidths). The spectrum of the Sample "09" is a sum of two lines: a broad line and a narrow one. The linewidth of the narrow line is close to the one recorded for the sample "76" with the value $d\delta(T)/dT$ almost equal to the value for the Sample "76". This signal may come from isolated compartments containing remnants of water fraction dominating in more hydrated sample, whereas vast majority of water is in structural state characteristic for lower hydration level. Such a narrow peak was not observed in the experiments performed on other *Cladonia mitis* sample harvested from the same site [278].

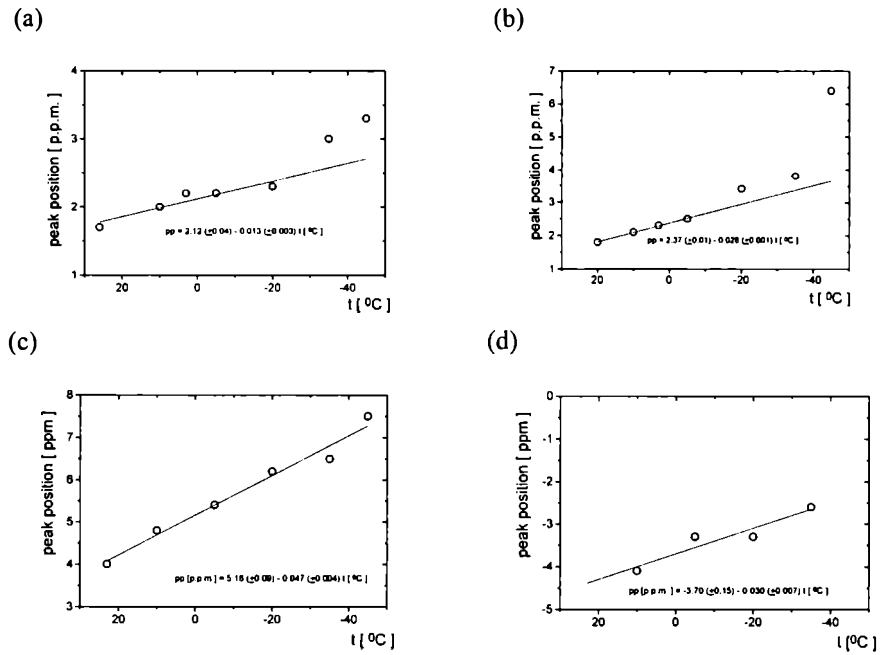

Fig. 4–3. The temperature dependency of the proton NMR line peak position recorded at 300 MHz for the thallus of *Cladonia mitis* hydrated to (a) $\Delta m/m_0 = 0.193$ and to (b) $\Delta m/m_0 = 0.126$. In the sample hydrated to $\Delta m/m_0 = 0.076$ a broad peak was observed (c) and a narrow one (d). Straight lines were fitted to the data recorded above -20^0C, whereas for the sample "09" to all recorded data. To emphasize the discrepancy caused by water immobilization, the fitted lines are extended to lower temperature.

The opposite tendency of chemical shift temperature dependence below 0^0C may be caused by the non-cooperative immobilization of water molecules: as they bound to inner surfaces of thallus, the average number of hydrogen bonds between the molecules in liquid water decreases (the layer of water loosely bound to the surface is relatively thin, thus, the relative number of hydrogen bonds between mobile water molecules decreases). If so, the $d\delta(T)/dT$ value should depend on the hydration level of the sample. Fig. 4–4 presents the slope of the chemical shift temperature dependence, $d\delta(T)/dT$, as a function of hydration level. For hydrated samples and for broad peak of the Sample "09" the value of $d\delta(T)/dT$ linearly depends on hydration level. The linear change suggests the contribution of two components: from water in bulk and from water in contact with the inner surface of thallus. As hydration level at low water amount is a linear function of the thickness of water layer, we may expect linear form of the dependency.

The linear function

$$\frac{d\delta(T)}{dT} = -(0.067 \pm 0.006) + (0.287 \pm 0.044)\frac{\Delta m}{m_0} \tag{4.4}$$

fits the data with the correlation coefficient equal to $\gamma = 0.989$.

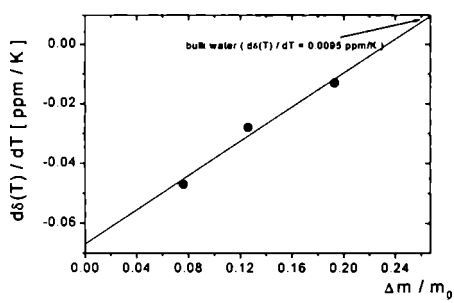

Fig. 4–4. The slope of the proton chemical shift temperature dependency, $d\delta(T)/dT$, for *Cladonia mitis* thallus hydrated to different levels ($\Delta m/m_0$).

If this is the case, from Eq. (4.4) one can get the hydration level needed for function $d\delta(T)/dT$ to reach the value for bulk water (Eq. 4.1). Free water limit is reached for $\Delta m/m_0 = 0.267$, which is well above the hydration level ($\Delta m/m_0 = 0.193$) at which water freezing in this series of *Cladonia mitis* samples is observed (see next Chapter).

4.1.3 Area under peaks

At all investigated hydration levels, the area under proton NMR line decreases with decreasing temperature. For the sample hydrated to $\Delta m/m_0 = 0.193$ (Fig. 4–5a), at temperatures above $t = -20^0$C the decrease is continuous, but for the spectra recorded at the lowest temperatures area under peak decreases to ~0.1 of the value

recorded at t = 26°C. The jump in area under peak at about t = –20°C is correlated with the rapid increase in proton linewidth (Fig. 4–2a) and reflects both the freezing of significant water fraction and the dramatic change in mobility of the remaining non-frozen water pool.

Fig. 4–5b shows the temperature dependence of the area under peak for *Cladonia mitis* thallus hydrated to $\Delta m/m_0 = 0.126$. The area under peak decreases with decreasing temperature, down to 0.096 of the value at t = 20°C. The decrease is continuous and there is no pronounced jump in area-under-peak temperature dependency. The decrease of more than 90% water signal is caused by freezing protection mechanism of water transfer from loosely to tightly bound water pool as it was reported elsewhere [273, 278]. As power of NMR pulse was not sufficient to excite the complete tightly bound water pool in *Cladonia mitis*, the decrease of proton signal caused by ice nucleation was not quantified (also reference [278]).

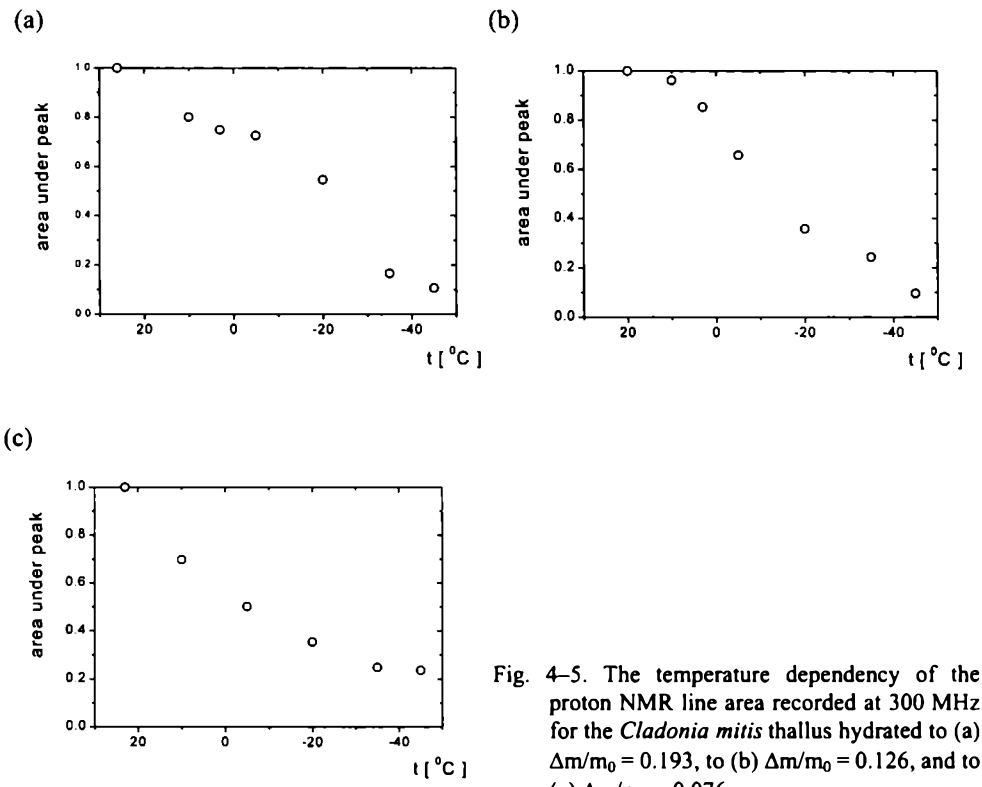

Fig. 4–5. The temperature dependency of the proton NMR line area recorded at 300 MHz for the *Cladonia mitis* thallus hydrated to (a) $\Delta m/m_0 = 0.193$, to (b) $\Delta m/m_0 = 0.126$, and to (c) $\Delta m/m_0 = 0.076$.

The temperature dependence of the area under line in *Cladonia mitis* hydrated to $\Delta m/m_0 = 0.076$ is shown in Fig. 4–5c. For this sample the proton NMR signal decreases smoothly with decreasing temperature and at t = –45°C reaches 0.236 of the value recorded at t = 23°C. Like in Sample "76", the decrease in area under peak with decreasing temperature is smooth. NMR line for the dehydrated thallus is significantly broader than for samples hydrated to

higher level. The amount of free water spread over the inner thallus surfaces in dehydrated *Cladonia mitis* is not sufficient to dominate in the NMR signal (and to activate the freezing protection transfer mechanism), thus, the more tightly bound water fraction present in the thallus is observed.

4.1.4 The mechanism of freezing protection in lichen

Although freezing protection of lichen thallus is extraordinarily effective, there is still very little known about its molecular mechanisms.

In the Sample "93" at temperature $t = -20^0C$ the freezing of the loosely bound water fraction causes the discontinuous decrease in the area under peak accompanied by the increase of the line halfwidths. The temperature of transition was lower than the one reported elsewhere [273]. It is possible that the temperature of thallus could be a little higher than the temperature recorded by sensor, because the air present in the sample tube may insulate pieces of thallus. For both Samples "76" and "09" the thermal changes of area under peak, peak halfwidths and the peak position vary continuously with decreasing temperature with no indication of the cooperative freezing. Cooperative freezing observed in the sample hydrated to $\Delta m/m_0 = 0.193$, occurs for hydration level lower then the value obtained from linear estimation of the freezing protection mechanism effectiveness ($\Delta m/m_0 = 0.26$ [273]). Also the estimation of the proton peak position temperature dependency showed that the free water limit is reached for the hydration level higher than the one needed for the ice crystallite formation in *Cladonia mitis* thallus.

Indeed, in thallus fluids ice nucleation takes place for the temperatures well above the lower limit of photosynthetic activity (see Chpt. 3.1.5). Among the 14 mycobiont species investigated by Kieft & Ahmadjian, [383], five showed the ice nucleation activity at -5^0C or higher, whereas none of photobionts investigated (*Nostoc*, *Trebouxia* nor *Coccomyxa peltigerae*) were active at this temperature. It seems that the ice nuclei are mainly produced by lichen mycobiont. The ice nucleation activity may appear for both symbionts in the same temperature range (as for *Cladonia cristatella* with its photobiont: *Trebouxia erici* or for *Acarosphora fuscata* with photobiont *Trebouxia*) or for the temperature much higher for mycobiont than for its photobiont (as for *Lecanora dispersa* with photobiont *Trebouxia incrustata*). For the several clones of the lichen fungus *Rhizoplaca chrysoleuca* no significant difference in ice nucleation temperature was recorded.

The ice nucleation temperature recorded in cellular fluids *in vitro* may differ from the temperature of the ice crystallite formation in lichen thallus, as there are other agents promoting ice nucleation.

In lichen thallus the ice nucleation might not necessarily be a destructive process. The ice crystallite formation in extracellular spaces may be promoted by the presence of proteinaceous nuclei [384]. It is thought that extracellular water freezing occurs in freezing tolerant plants and the lethal process of intracellular formation of hexagonal ice crystal is avoided [93]. Most likely, thallus acts not

only to protect it from ice crystallite growth in intra-cellular spaces during freezing, which otherwise might destroy the thallus microstructure; but also to promote ice crystallite formation in its extra-cellular spaces. The effect of the stimulation of the non-lethal growth of ice crystallites in extra-cellular space may result in accumulation of the increased water amount in form of ice crystallites, which can be advantageous during biotic activity periods for lichens living in sites with permanent moisture deficit.

4.2 Tightly bound water behavior

The increase in power of NMR pulse and, thus, decrease in its length allows the tightly bound water observation. Proton spectra recorded at the increased pulse power ($\pi/2$ = 8.3 μs) consist of the signal from either tightly or loosely bound water, whereas the signal from solid matrix of thallus ($T_2^* \approx 16$ μs) is significantly reduced [272].

Further increase in pulse power ($\pi/2$ = 1.3 μs) for high power relaxometry technique, yields full proton signal (including the signal from the solid matrix of thallus). If not reduced solid signal is recorded, water signal can be quantified in units of solid proton signal.

4.2.1 ^{1}H NMR spectra

To examine the influence of water content on the effectiveness of freeze-protection mechanism at varied water content, this Author selected three lichen species, two Antarctic ones: *Himantormia lugubris*, *Usnea aurantiaco-atra* and a cosmopolitan one: *Cladonia mitis* [278]. Thalli were cooled slowly (in equilibrium) from room temperature down to –45^{0}C on tightly bound water, The temperature courses at two different hydration levels of thallus were performed.

Himantormia lugubris and *Usnea aurantiaco-atra* were collected in King George Island, South Shetlands during the Antarctic summer, whereas *Cladonia mitis* was collected in Northern Sweden, in autumn. The thalli were stored at room temperature and at air-dry state. Prior to NMR measurements each type of thallus was divided into two samples: one was dehydrated for 48 hours over the surface of H_3PO_4 (p/p_0 = 9%) and the other hydrated over a supersaturated solution of Na_2SO_4 (93%).

4.2.1.1 Hydrated thalli

Proton spectra of dehydrated thalli consist of broad and narrow line component. For hydrated thalli the broad line component is hardly visible and only *Cladonia mitis* reveals the pronounced contribution of broad line (Fig.4–6). Fitted line widths and areas under peak are presented in Tab. 4–2a,b,c, for *Cladonia mitis*,

Himantormia lugubris, and *Usnea aurantiaco-atra*, respectively. The narrow line component comes from the free water or water loosely bound in the lichen thallus. The halfwidths of the broad line component equals 32–39 kHz. Except for *Cladonia mitis*, it was not possible to deconvolute the composite spectrum. For sake of consistency, the total areas under peaks and narrow peak positions are presented.

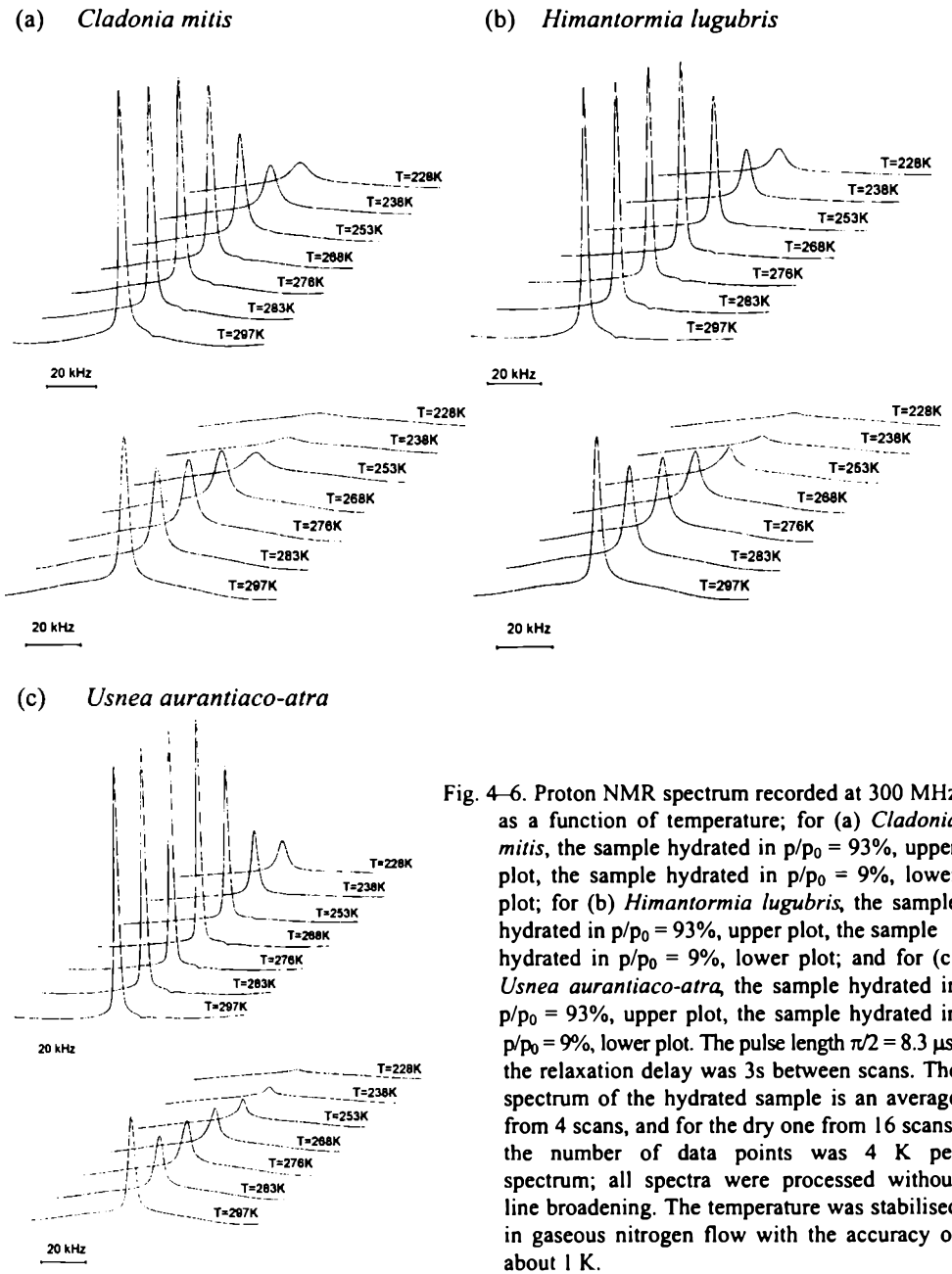

Fig. 4–6. Proton NMR spectrum recorded at 300 MHz as a function of temperature; for (a) *Cladonia mitis*, the sample hydrated in $p/p_0 = 93\%$, upper plot, the sample hydrated in $p/p_0 = 9\%$, lower plot; for (b) *Himantormia lugubris*, the sample hydrated in $p/p_0 = 93\%$, upper plot, the sample hydrated in $p/p_0 = 9\%$, lower plot; and for (c) *Usnea aurantiaco-atra*, the sample hydrated in $p/p_0 = 93\%$, upper plot, the sample hydrated in $p/p_0 = 9\%$, lower plot. The pulse length $\pi/2 = 8.3$ μs; the relaxation delay was 3s between scans. The spectrum of the hydrated sample is an average from 4 scans, and for the dry one from 16 scans; the number of data points was 4 K per spectrum; all spectra were processed without line broadening. The temperature was stabilised in gaseous nitrogen flow with the accuracy of about 1 K.

Table 4–2. The temperature course for *Cladonia mitis* (a), *Himantormia lugubris* (b), and *Usnea aurantiaco-atra* (c) hydrated at p/p_0 = 9% (dry samples) and at p/p_0 = 93% (wet samples). For dry samples line deconvolutions were performed using about 1200 data points per spectrum. Based on SIMPLEX procedure, the Bruker LINESIM program was used. The fits assuming individual Lorentzian line shape were good (RSS value between 1 and 1.6 per data point).

Table 4–2a.

Cladonia mitis		Dry sample (p/p_0 = 9%)			Wet sample (p/p_0 = 93%)		
Temperature		Area under peak			Halfwidth		Area under
t [C]	T [K]	[a.u.]	broad [%]	narrow [%]	[Hz]	[ppm]	peak [a.u.]
24	297	227.4	61.5	38.5	2028.7	6.76	240.6
10	283	215.5	77.2	22.8	1938.0	6.46	236.1
3	276	203.2	78.6	21.4	1996.8	6.65	237.8
–5	268	184.2	82.4	17.6	2171.5	7.23	232.2
–20	253	152.8	90.0	10.0	2983.5	9.95	212.8
–35	238	104.2	91.8	8.8	5307.7	17.69	167.0
–45	228	82.3	92.0	8.0	9073.8	30.22	139.5

Table 4–2b.

Himantormia lugubris		Dry sample (p/p_0 = 9%)			Wet sample (p/p_0 = 93%)		
Temperature		Area under peak			Halfwidth		Area under
t [C]	T [K]	[a.u.]	broad [%]	narrow [%]	[Hz]	[ppm]	peak [a.u.]
24	297	224.53	70.0	30.0	1622.5	5.41	137.0
10	283	226.20	75.0	25.0	1525.6	5.08	130.2
3	276	219.88	82.3	17.7	1634.8	5.45	126.6
–5	268	199.92	82.7	17.3	1684.4	5.61	119.2
–20	253	168.49	90.4	9.6	1901.8	6.33	94.7
–35	238	121.95	97.3	2.7	3152.6	10.5	65.4
–45	228	111.47	99.2	0.8	5721.7	19.1	53.3

Table 4–2c.

Usnea aurantiaco-atra		Dry sample (p/p_0 = 9%)			Wet sample (p/p_0 = 93%)		
Temperature		Area under peak			Halfwidth		Area under
t [C]	T [K]	[a.u.]	broad [%]	narrow [%]	[Hz]	[ppm]	peak [a.u.]
24	297	195.56	64.2	35.8	1606.0	5.35	145.32
10	283	189.39	76.2	23.8	1548.3	5.16	144.88
3	276	189.54	79.6	20.4	1516.7	5.05	148.79
–5	268	180.91	84.3	15.7	1517.6	5.05	144.42
–20	253	141.39	92.2	7.8	1625.1	5.41	132.21
–35	238	114.83	96.4	3.6	2515.4	8.38	97.75
–45	228	93.92	99.1	0.9	4024.2	13.4	79.34

Fig. 4–7a,c,d shows the halfwidths of the proton line for hydrated samples of investigated lichens. For the temperature range above -20^0C the line halfwidth is constant and equals 6.78 ppm for *Cladonia mitis*, 5.39 ppm for *Himantormia lugubris* and 5.20 ppm for *Usnea aurantiaco-atra*. As the sample is macro-heterogeneous, the measured value of linewidth is significantly broadened either by the non-uniformity of the effective magnetic field, B_{eff}, or by the magnetic susceptibility non-uniformity. For lower temperature the proton line broadens due to freezing of the loosely bound water fraction at -12^0C [273, 274].

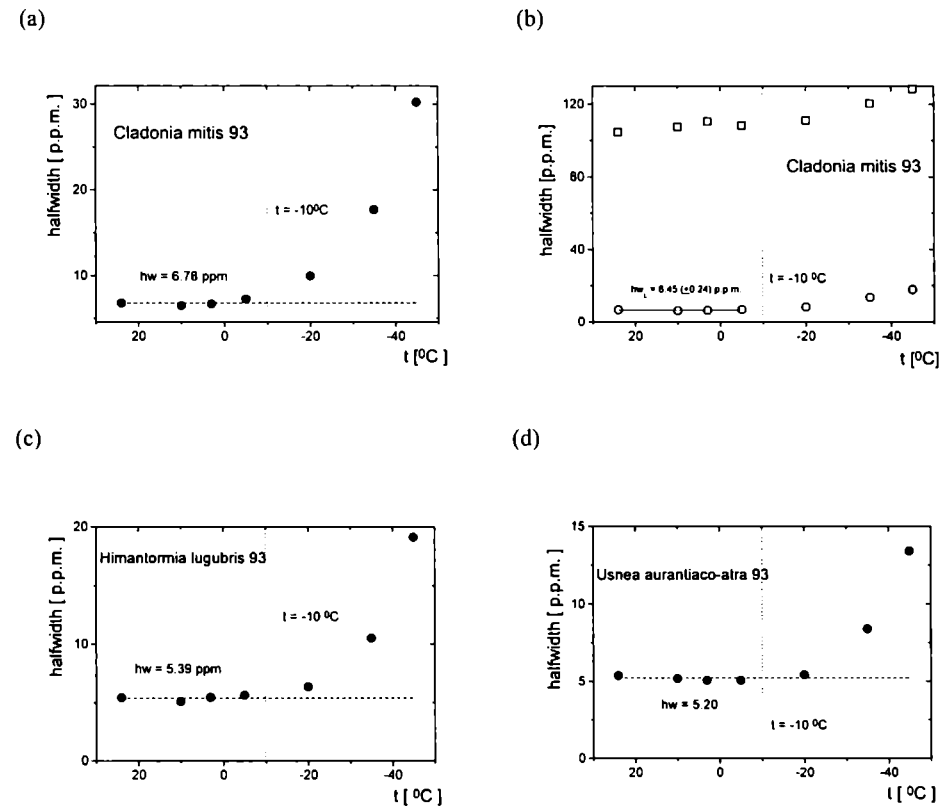

Fig. 4–7. The temperature dependence of the proton NMR linewidth recorded at 300 MHz for thallus hydrated in p/p_0 = 93%. (a) *Cladonia mitis*; (b) *Cladonia mitis* line decomposed into broad and narrow components; (c) *Himantormia lugubris*; (d) *Usnea aurantiaco-atra*.

For hydrated *Cladonia mitis* the spectrum may be deconvoluted into the sum of two components (Fig. 4–7b). For the temperatures above -20^0C the average Lorentzian line halfwidth (6.45±0.24 ppm) only slightly differs from the one (Fig. 4–7a) obtained using the single component analysis. The broad Gaussian line halfwidth equals ~100 ppm for the whole range of investigated temperatures. For the temperatures below -20^0C line broadens, which means that the structural change in loosely bound water fraction affects also the tightly bound water protons (Fig. 4–7b).

The total area under peak remains constant (or slightly decreases) with decreasing temperature down to t = -10^0C (Fig. 4–8), whereas, for further decreasing temperature the total area under peak rapidly decreases. A rapid decrease in the total area under peak below -10^0C is caused by the freezing of loosely bound water. This discontinuity was observed at -12^0C by high power proton relaxometry in the thallus of *Cladonia mitis* [273, 274]. At t = -40^0C the total area under line is 50% of its initial value. The decrease in area under line is correlated with the line halfwidth increase, suggesting that the free water pool at low temperatures may be transferred to a phase which differs from the free water observed at higher temperature.

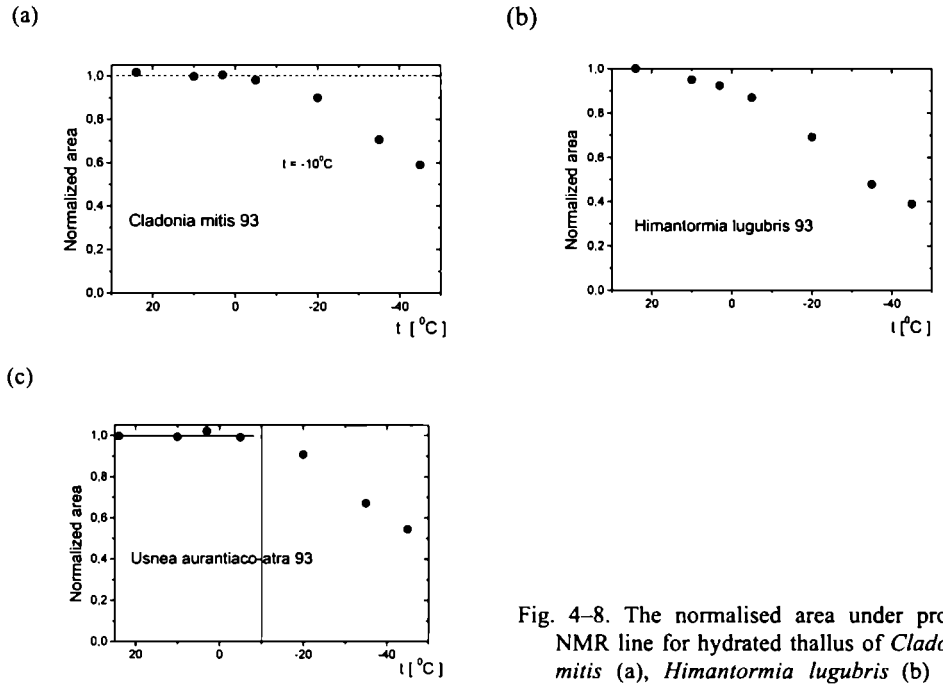

Fig. 4–8. The normalised area under proton NMR line for hydrated thallus of *Cladonia mitis* (a), *Himantormia lugubris* (b) and *Usnea aurantiaco-atra* (c) versus decreased temperature.

4.2.1.2 Dry thalli

For dehydrated samples, several functions were tested to fit the spectrum properly; namely, the superposition of Lorentzian and Gaussian line, two Lorentzians and two Gaussians. The narrow line component was well fitted using Lorentzian line in all samples investigated, whereas the broad line is fitted with sufficiently good quality using either Gaussian or Lorentzian function. (In the measurements in time-domain tightly bound water signal was fitted by an exponent [272, 273]).

Fig. 4–9 shows the temperature dependence of the area under broad and narrow component of the proton NMR line for the dehydrated thallus of the

investigated lichens. For *Himantormia lugubris* and for *Usnea aurantiaco-atra*, the total signal remains almost constant for temperatures above $t = -10^0C$, whereas for lower temperatures it smoothly decreases with decreasing temperatures. For *Cladonia mitis* the signal continuously decreases with decreasing temperature for the whole temperature range, which is the effect implied by the desorption isotherm requirements [78].

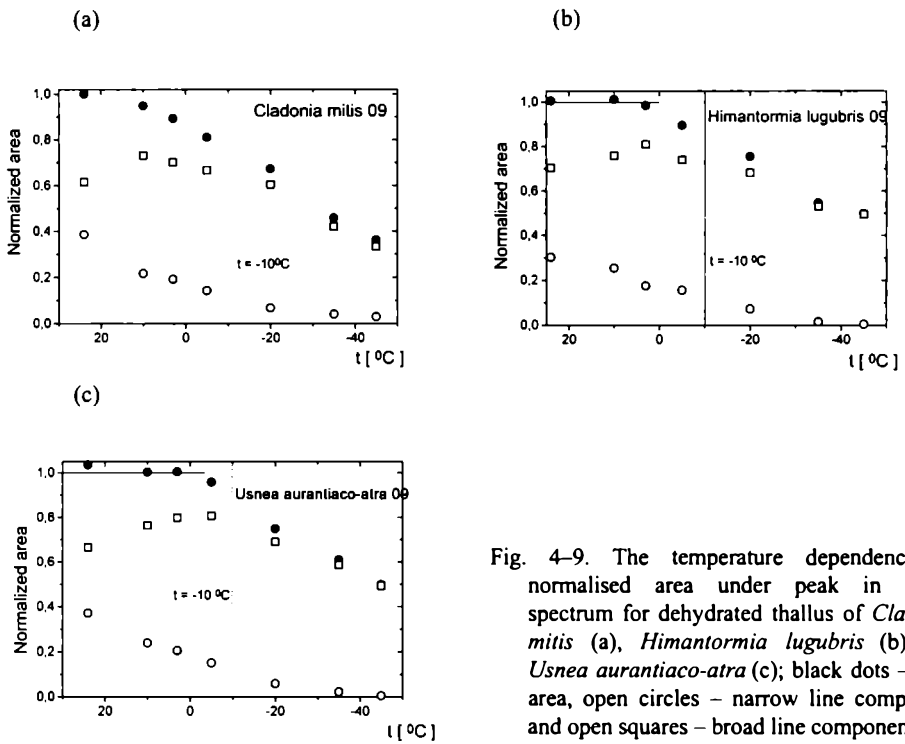

Fig. 4–9. The temperature dependence of normalised area under peak in NMR spectrum for dehydrated thallus of *Cladonia mitis* (a), *Himantormia lugubris* (b) and *Usnea aurantiaco-atra* (c); black dots – total area, open circles – narrow line component and open squares – broad line component.

The temperature behavior of the tightly bound and loosely bound water signal intensities are found to be similar for Antarctic and cosmopolitan lichen species. As the temperature is decreased, the loosely bound water signal significantly decreases. This decrease is compensated for by the increase in the tightly bound water signal.

The decrease in narrow line component is almost linear with temperature for *Himantormia lugubris* and for *Usnea aurantiaco-atra*, whereas for *Cladonia mitis* its magnitude stabilises at 8.7% of the total signal at $t = -20^0C$ and at lower temperatures. The process of the transfer of loosely water signal to the tightly bound water pool above $t = -10^0C$ occurs continuously with the temperature decrease. None of the samples show any discontinuities or breaks in the slope of temperature dependence of area under peak at $t = -35^0C$ (see Chpt. 4.4.2).

4.2.2 Proton relaxation

Proton high power relaxometry supplies information on the stoichiometry and the dynamic state of water protons, which can be used to assign the protons to several fractions: free and loosely bound water, tightly bound water, and protons of solid matrix of thallus. Gaussian signal coming from the solid matrix of the thallus structure is used as a standard to scale the signal from the different fractions of water present in the thallus.

This Author observed the behavior of tightly and loosely bound water during slow (in equilibrium) cooling (to -60^0C) of a thallus of *Cladonia mitis* [273]. The samples of *Cladonia mitis* were harvested in Northern Sweden in autumn. The air dry thallus was stored at room temperature for 6 months, then incubated for 14 days at $p/p_0 = 9\%$ (over the H_3PO_4 surface) prior to NMR experiments.

Thalli were hydrated from gaseous phase over a supersaturated solutions of either Na_2SO_4 ($p/p_0 = 93\%$), or $Na_2S_2O_3$ ($p/p_0 = 76\%$), or kept over H_3PO_4 ($p/p_0 = 9\%$); the obtained hydration levels in units of oven dry mass (24 h at 70^0C) equal $\Delta m/m_0 = 0.388$, 0.157 and 0.036, respectively.

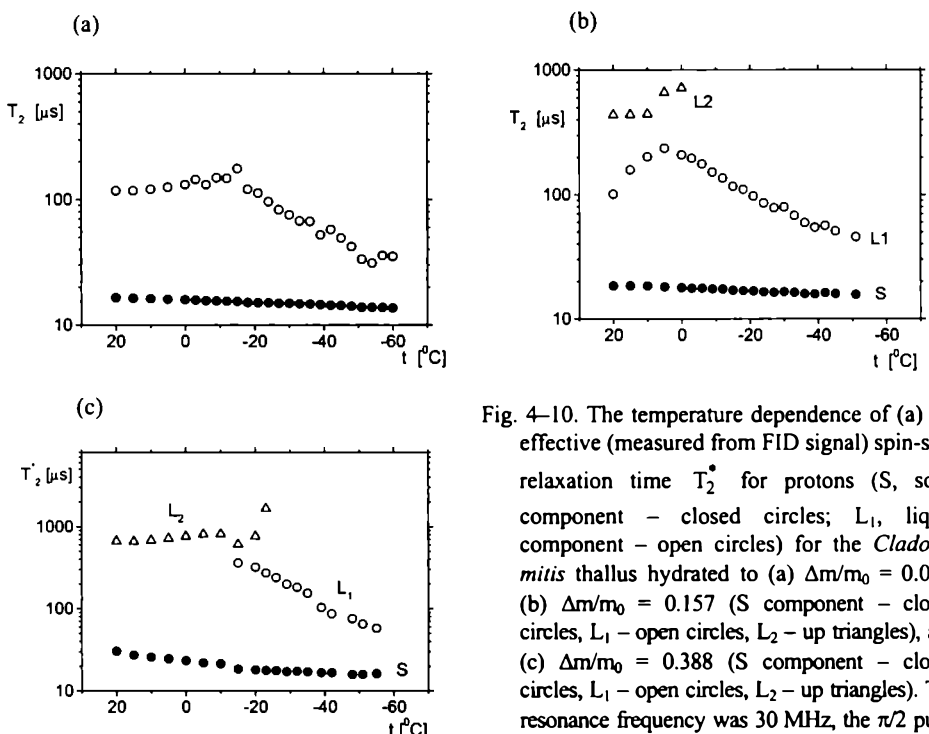

Fig. 4–10. The temperature dependence of (a) the effective (measured from FID signal) spin-spin relaxation time T_2^* for protons (S, solid component – closed circles; L_1, liquid component – open circles) for the *Cladonia mitis* thallus hydrated to (a) $\Delta m/m_0 = 0.036$, (b) $\Delta m/m_0 = 0.157$ (S component – closed circles, L_1 – open circles, L_2 – up triangles), and (c) $\Delta m/m_0 = 0.388$ (S component – closed circles, L_1 – open circles, L_2 – up triangles). The resonance frequency was 30 MHz, the $\pi/2$ pulse length 1.1 μs; the maximal output power was 400 W; the spectrometer dead time was of about 6 μs. Recording of all FIDs was started 10 μs after the $\pi/2$ pulse; the acquisition number was 500. The temperature varied in the range 20^0C to -60^0C and was stabilized in a gaseous nitrogen stream.

Fig. 4–10a,b,c shows the temperature dependence of T_2^* for the solid matrix of the thallus. For each hydration level the errors are less than the size of the symbol on the plot. The thermal T_2^* dependence is flat which means that the region of temperatures investigated for the solid matrix of the thallus reflects the rigid lattice approximation for spin-spin relaxation time versus molecular dynamics (correlation time) of the system. The amplitude of the solid (Gaussian) signal component was used as a standard to scale the liquid component intensity of recorded FID signal (T_2^* value much longer than the spectrometer dead time).

4.2.2.1 Dehydrated *Cladonia mitis*

At $\Delta m/m_0 = 0.036$, in *Cladonia mitis* only one liquid signal component coming from the tightly bound water on the thallus surface is detected [272]. The $T_2^* \approx 100$ μs for the temperature range between +20°C and –20°C then at temperatures below –20°C it shortens, still being observed at –60°C (Fig. 4–10a). In FID measurement the B_0 field inhomogeneities shorten the measured T_2^*, however, less effectively for very low temperature, where the real T_2 value is shorter [1]. Thus the observed break in slope of temperature dependence of T_2^* at ~–15°C may not reflect any structural change in water tightly bound to the thallus surface or of the thallus itself.

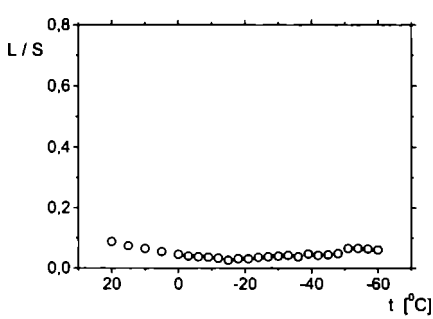

Fig. 4–11. The temperature dependence of the magnitude of liquid signal scaled in units of the solid signal L_l/S for the *Cladonia mitis* thallus hydrated to $\Delta m/m_0 = 0.036$.

Fig. 4–11 shows the temperature dependence of the magnitude of the liquid signal component, L_l, expressed in units of the solid component. The relative magnitude of the signal decreases for the overall temperature range between +20°C and –60°C (from 0.087 to 0.060). This may be caused both by the immobilization of the water layer tightly bound to the solid lichen matrix and by the effect implied by desorption isotherm [78]; the cooperative freezing of tightly bound water was not observed. Fluctuation in magnitude with decreased temperature most likely results from the numerical procedure.

4.2.2.2 Moderately hydrated *Cladonia mitis*

Cladonia mitis hydrated to an intermediate level ($\Delta m/m_0 = 0.157$) shows two liquid signal components coming from the tightly and loosely bound water

fractions (Fig. 4–10b). The averaged loosely bound water signal starts to decrease at $+10^0$C and vanishes completely between 0^0C and -3^0C as the thallus is cooled down. The T_2^* values for tightly bound water decrease smoothly with temperature decreasing below 0^0C (similarly to the pattern observed in thalli at the lower hydration level, $\Delta m/m_0 = 0.036$). The changes observed at temperatures $>0^0$C might be caused by transfer of water from the loosely bound to the tightly bound water pool which would modify the dynamics of this group of water protons.

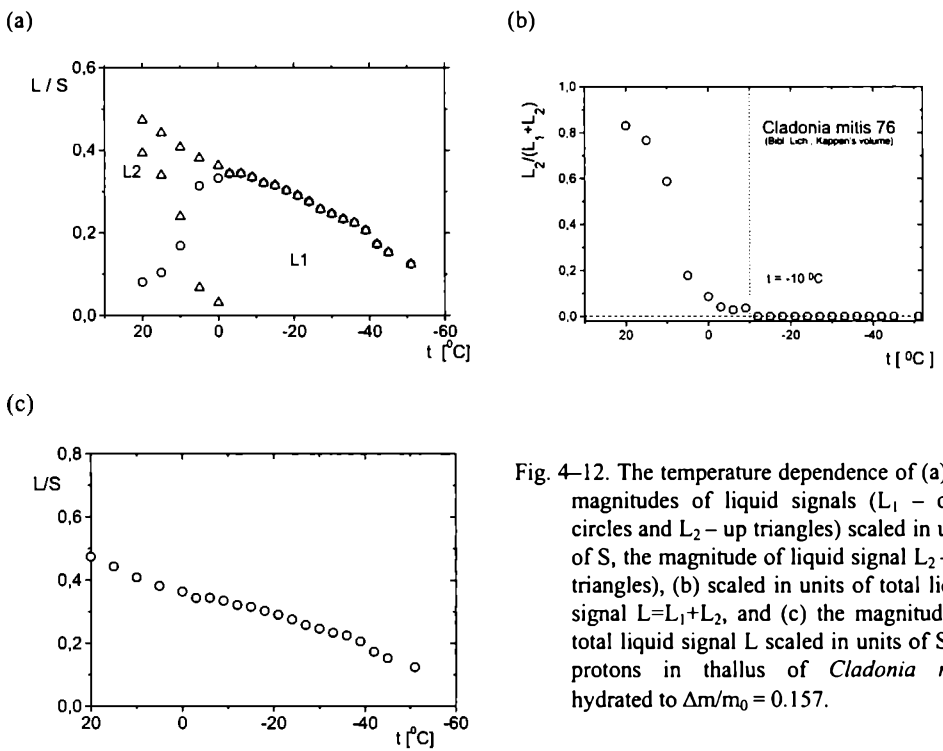

Fig. 4–12. The temperature dependence of (a) the magnitudes of liquid signals (L_1 – open circles and L_2 – up triangles) scaled in units of S, the magnitude of liquid signal L_2 – up triangles), (b) scaled in units of total liquid signal $L=L_1+L_2$, and (c) the magnitude of total liquid signal L scaled in units of S for protons in thallus of *Cladonia mitis* hydrated to $\Delta m/m_0 = 0.157$.

Fig. 4–12a presents the temperature dependence of the magnitudes of both liquid components scaled in units of the solid component for the thallus hydrated to $\Delta m/m_0 = 0.157$. The loosely bound water fraction, L_2, consists of the majority of total liquid signal at room temperature (83.0%). As the temperature is decreased, the magnitude of the L_2 signal decreases to 8.6% of the total liquid signal at 0^0C and vanishes at -3^0C (see Fig. 4–12b). Simultaneously, the tightly bound water component, L_1, increases, fully compensating the decrease in the loosely bound fraction. The transfer of water from the loosely bound to the tightly bound pool occurs at temperatures $> 0^0$C during slow cooling (6^0C / 60 min, then measurement at constant temperature).

As temperature decreases below 0^0C, the L_1 component decreases continuously but is still detectable (L/S = 0.123) at -50^0C. The transfer of the L_2

signal to the L_1 pool is not accompanied by a steep change in the total L/S temperature dependence (Fig. 4–12c), which means that the transfer process is not associated with an abrupt change of water structure and/or dynamics, but is a continuous process triggered by the decreasing temperature. The smooth decrease in total (L_1+L_2) liquid signal is the effect implied rather by the desorption isotherm requirements, then by non-cooperative water immobilization [78].

4.2.2.3 Highly hydrated *Cladonia mitis*

For the highly hydrated thallus, $\Delta m/m_0 = 0.388$, only one liquid component was recorded over almost the whole temperature range investigated (Fig. 4–10c). However, at temperatures above the loosely bound water freezing point (–12°C as demonstrated by the temperature dependence of the total liquid signal amplitude, L/S) T_2^* is the value for the loosely bound water pool, and at temperatures < –20°C the T_2^* value resembles that for the tightly bound water fraction in less hydrated thalli (Fig. 4–13a). Only between –12°C and –20°C were two liquid signal components simultaneously observed; first one, coming from the remnants of the loosely bound water pool and a second (dominating in magnitude) from the tightly bound water fraction. The tightly bound water fraction is not observed at temperatures > –12°C because the amplitude of its proton NMR signal is small in comparison to the loosely bound water signal in the highly hydrated thallus (see Fig. 4–13b) and the decomposing procedure did not distinguish its signal from the total liquid proton signal. The amplitude of the tightly bound water signal is the linear function of the water-system interface, so, after reaching the saturation level it does not increase. After saturation of the tightly bound water binding sites and locations, with further increasing sample hydration the loosely bound water fraction appears. For moderately hydrated thallus ($\Delta m/m_0 = 0.157$) the ratio of the tightly bound water to the loosely bound water fraction $L_1/L_2 \approx 0.205$ ($L_1/S = 0.08$, $L_2/S = 0.393$, at room temperature). In the hydrated sample $L_2/S = 1.54$, which means that the ratio L_1/L_2 for highly hydrated sample should be 0.052. Such a small contribution of the tightly bound water pool could not be distinguished by the numerical procedure, so long as the L_2 water pool gives rise to the overall signal. For this reason highly hydrated thallus ($\Delta m/m_0 = 0.388$) for which the contribution of the loosely bound water pool overwhelmed the amplitude of the tightly bound water fraction, only L_2 was observed at > –10°C.

At –12°C freezing of the loosely bound water fraction causes the decrease of 32.9% of the total liquid signal (Fig. 4–13c). At temperatures between –15°C and –23°C the loosely bound water fraction is still observed but rapidly decreases to zero. Respectively, the tightly bound water fraction increases reaching a maximal value at –23°C. As temperature is progressively decreased below freezing point, the total liquid component decreases smoothly as it did at lower hydration levels.

As $\Delta m/m_0 = 0.128$ of water freezes in –12°C, the rest gives the maximal amount of water which may be transferred to non-freezable water fraction

expressed in dry mass units, $\Delta M/m_0$, which in *Cladonia mitis* thallus is equal to 0.260.

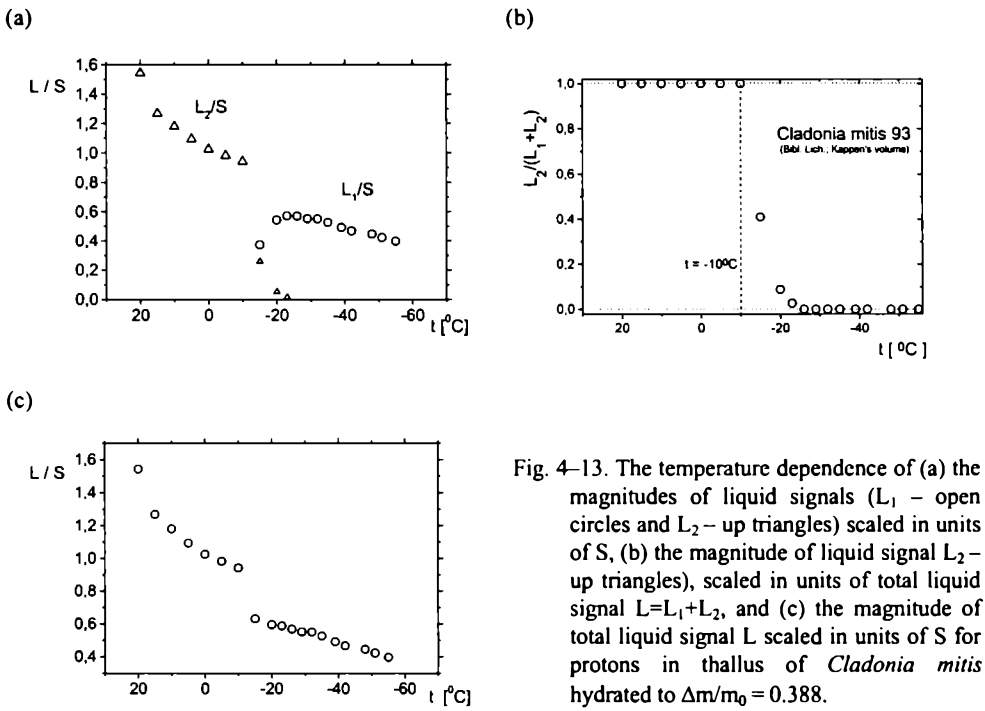

Fig. 4–13. The temperature dependence of (a) the magnitudes of liquid signals (L_1 – open circles and L_2 – up triangles) scaled in units of S, (b) the magnitude of liquid signal L_2 – up triangles), scaled in units of total liquid signal $L=L_1+L_2$, and (c) the magnitude of total liquid signal L scaled in units of S for protons in thallus of *Cladonia mitis* hydrated to $\Delta m/m_0 = 0.388$.

4.2.3 Cryoprotective mechanism of loosely bound to tightly bound water transfer

Freezing resistance of lichens should involve a mechanism that protects the thallus from the ice crystallite growth which might destroy the thallus microstructures.

Water freezing point decreases for liquid placed in small compartments, as the number of heterogeneous ice nuclei is proportional to liquid volume (see Chpt. 1.12.1). Thus, one could expect the decrease in temperature (or the absence) of cooperative freezing due to water-accessible compartment size in lichen thallus. Proton relaxation measurements of water filling pore system of controlled pore glass (CPG) revealed that no freezing was observed in CPG's with the average pore size of 24 and 40 Å, whereas freezing at about -16^0C in glasses with pore size of 196 Å and 252 Å was recorded [29]. The sizes of intra- and extracellular spaces in lichen thallus are significantly greater, which suggest that freezing protection mechanism in lichen thallus was not driven by a limited size of water-accessible thallus compartments.

Simultaneous observation of loosely bound and tightly bound water pool gives an insight in freezing protection mechanisms existing in the thallus. Indeed, the physical basis for such a freezing protection mechanism has not been established so far.

The observations of Antarctic arthropodes and variety of plants [26, 27, 68, 69, 173, 375, 425] suggest that polyhydric alcohols and simple sugars may act as cryoprotectants. Glycerol added to aqueous medium of wheat photosynthetic membrane protects the system from the ice crystallite formation [54, 288]. Although glucose and fructose were not found in *Evernia esorediosa* (Müll. Arg.) Du Rietz, in *Ramalina subbreviuscula* Asah., and in *Ramalina sublitoralis* Ash., in field conditions, and the significant content of monosugars was only forced by external osmotic conditions, the polyols (ribitol, mannitol, arabitol), as essential metabolites, were present in thalli on constant level (up to 3.4% w/w of arabitol in *Ramalina subbreviuscula*) [265] and may act as cryoprotective agents in thallus. Using ^{13}C–NMR, Chapman et al., [110], identified polyols and sugars, and quantified their abundance, in several Antarctic lichens. Polyol content varied between 17 mg g^{-1} for *Candelariella hallettenensis* (Murray) Ørsted [= *Candelariella flava* (Dodge & Baker) Castello & Nimis] and 65 mg g^{-1} for *Usnea antarctica* Du Rietz, with dominating contribution from arabitol, mannitol and ribitol, whereas sorbitol was not detected. Sugar content was approximately one order of magnitude smaller than the content of polyols. In Antarctic bryophytes the repeated freeze-thaw cycles (up to n = 16) increase rates of carbohydrate loss, which is not significantly correlated with the DSC-detected freezing temperature of tissue [472].

The cryoprotective action of polyols is based on blocking the formation of ice crystallites by steric mismatch of hydrogen bonds which may be formed between them and water. Although the overall concentration of polyols detected in the thallus is not sufficient to promote significant decrease of freezing point of cellular aqueous medium, if polyols are localized mainly in intracellular spaces, they may contribute to the freezing protection mechanism in lichens.

However, it is only partial explanation of the phenomena recorded using proton NMR. Proton relaxation [273] as well as proton spectra clearly suggest that during cooling the thallus down the amount of tightly bound (non-freezable) water increases very significantly. The increase in the total liquid proton signal upon cooling the thallus is not observed, as in case if liquid polyols were rapidly produced by dissolution of the water-soluble fraction of solid matrix, as it is seen for horse-chestnut bast at mild hydration [290]. In contrast to bast, the total liquid signal decreases with decreasing temperature.

The transformation of bulk water to less mobile fraction during the cooling of the thallus suggests that the steric mismatch is not the only effect responsible for the freezing resistance of lichens. If the freezing protection mechanism were based on steric effects alone, drastic changes in motional properties of bound water should not be observed. The immobilization of water suggests the presence of the active mechanism based on formation of a long range molecular network with a gel-like structure from liquid substances in the

liquid phase. This increases the area of liquid-solid interface, thus, increasing the tightly bound water amount.

The mechanism of water transfer from loosely bound ("freezable") to tightly bound ("non-freezable") pool may contribute to freezing protection of lichen thallus. Gel-like structure may form an „insulating shell" surrounding the ice crystallites as they are probably formed in inner spaces of lichen thallus and, thus, separating them from the direct contact with the membranes and other constituents of the thallus, which otherwise might be damaged by an ice crystallite. Such a "covering shell" may also hinder further growth of the ice crystallite. The detailed form of the water-tissue interface in lichen thallus is not known.

In "molecular scale", where the local curvatures of the organellae may be neglected, the thin [78] interfacial layer of water will have locally a planar form. Taking Lh = 0.149±0.037 (sample CM85) as a monolayer coverage [271] one gets the lower limit of the thickness of non-freezable water coverage as 1.85±0.45 monolayers for the threshold hydration $\Delta M/m_0 = 0.260$, or 1.40±0.35 taking as a threshold the value 0.193 or 0.195 [274, 277]. This seems to be the thickness sufficiently buffering the thallus structure from the ice crystallite growth.

Freezing protective transfer of loosely bound to tightly bound water pool (in intracellular spaces) is a complementary mechanism to the observed stimulation of ice crystallite growth in extracellular spaces of lichen thallus.

4.3 Freezing protection of D_2O-hydrated lichen

In the aim to observe the isotopic effect on hydration kinetics and freezing protection mechanism in lichen thallus, *Himantormia lugubris* thallus hydrated mainly by D_2O and investigated at slow (in equilibrium) cooling down to 223 K. Thalli of *Himantormia lugubris* were collected in King George Island, South Shetlands, during the Antarctic summer. The thallus was stored in air-dry state at room temperature.

In proton spectra ($\pi/2 = 8$ μs) the signal from solid matrix of thallus, from its movable groups and the decreased by isotope dilution signal coming from water protons still present in aqueous medium was observed.

4.3.1 D_2O-hydration kinetics

This Author performed the hydration of *Himantormia lugubris* from gaseous phase over the D_2O surface [276]. Prior to hydration time-courses the samples were dehydrated over the surface of H_3PO_4 ($p/p_0 = 9\%$).

The hydration kinetics, expressed as relative mass increase, $\Delta m/m_0$ (m_0 was the oven dry mass determined after 48 h at +70°C), is well fitted by the double-exponential function (Fig. 4–14)

$$\Delta m/m_0(t) = A_0 + A_1 \cdot \left[1 - \exp(-t/t_1)\right] + A_2 \cdot \left[1 - \exp(-t/t_2)\right], \qquad (4.5)$$

where fast component is denoted by indice '1', and slow one by indice '2'; $A_0 = 0.057$, is the non-removable water amount present in lichen thallus. The value obtained for A_0 in *Himantormia lugubris* matches with relative values for other lichen species investigated [271, 272]. Fast component hydrates to $A_1 = 0.045$ with the characteristic time constant $t_1 = (2.52 \pm 0.74)$ h, and slower component to $A_2 = 0.319$ with $t_2 = (55.9 \pm 5.7)$ h. The overall hydration level equals $A = 0.422 \pm 0.014$, which is four times lower than the hydration level at hydration from aqueous phase [599]. Two-step hydration kinetics discovered for hydration from gaseous phase in *Himantormia lugubris* [271] does not change at hydration in D_2O, however, the values of the constants are altered.

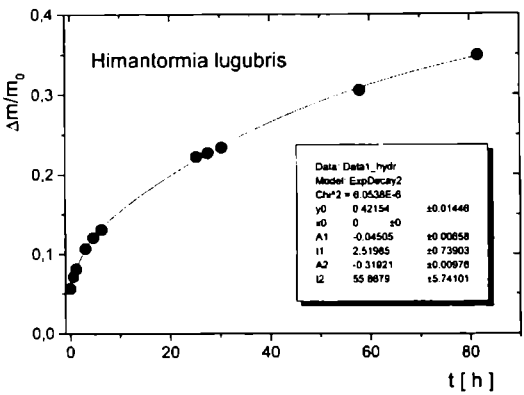

Fig. 4–14. Hydration time-course performed from gaseous phase, $p/p_0 = 100\%$, for *Himantormia lugubris* thallus recorded as $\Delta m/m_0(t)$. Inset presents the parameters of fitted curve.

4.3.2 NMR experiment

^{1}H–NMR spectra for D_2O-hydrated *Himantormia lugubris* thallus were recorded by this Author for the temperature range between 297 K and 223 K [276]. Isotope substitution of water protons enables more detailed observation of the signal from the non-exchangeable protons of solid matrix of thallus even at high hydration level of the thallus. Proton spectrum is a superposition of narrow, Lorentzian, component coming from free and/or loosely bound water fraction and broad, Gaussian, component from water tightly bound in thallus structure and reduced signal from solid matrix of thallus (Fig. 4–15). Peak positions of both line components do not change with decreasing temperature (see Tab. 4–3). Halfwidth of narrow line component, although almost unchanged down to 235 K, broadens for lower temperatures. This may be connected with the observed at 228 K in *Cladonia mitis* subtle structural change in water tightly bound on thallus [274]. In contrast, linewidth of Gaussian component increases from ~24 kHz at room temperature to 36 kHz at 261 K, and for lower temperatures remains unchanged (Fig. 4–16).

Narrow signal contribution smoothly decreases for the temperatures below 0^0C down to 253 K, reflecting the loosely bound-to-tightly bound water transfer observed by proton relaxometry and by ^{1}H–NMR spectra of H_2O hydrated *Cladonia mitis*, and by ^{1}H–NMR spectra of *Himantormia lugubris* [273, 278].

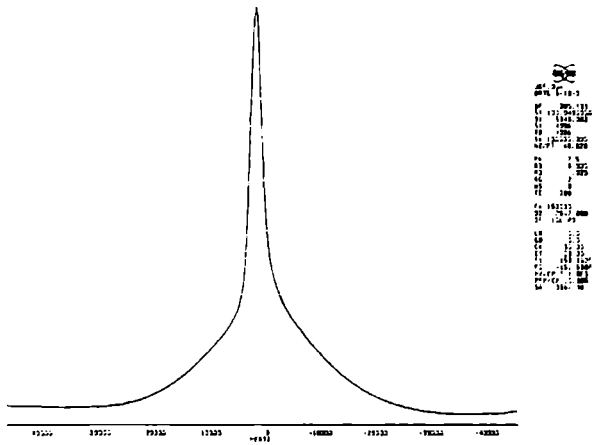

Fig. 4–15. ^{1}H–NMR spectrum for *Himantormia lugubris* thallus hydrated in D_2O at 300 MHz; number of scans NS = 8; repetition time was 3 s. Temperature T = 297 K. The pulse length was $\pi/2$=8 μs (7.5 μs pulse was used).

Table 4–3. ^{1}H–NMR line parameters for D_2O-hydrated thallus of *Himantormia lugubris*.

	Gaussian line component			Lorentzian line component		
T [K]	Position [kHz]	Linewidth [kHz]	Area under peak	Position [kHz]	Linewidth [kHz]	Area under peak
297	0,16	23,7	0,214	0,17	2,26	0,786
283	0,17	29,7	0,226	0,17	2,30	0,774
276	0,17	34,2	0,251	0,17	2,48	0,749
268	0,17	36,5	0,278	0,17	2,56	0,722
261	0,16	38,9	0,303	0,17	2,62	0,697
253	0,16	38,0	0,340	0,17	2,84	0,660
235	0,17	37,4	0,511	0,17	3,73	0,489
223	0,17	37,7	0,627	0,17	5,09	0,373

For lower temperatures the narrow line component decreases rapidly, which is correlated with broadening of the Lorentzian line (Fig. 4–17). This may reflect the structural change in bound water. Indeed, in this temperature range the water freezing was observed in hydrated *Cladonia mitis* thallus [273], however, overall area under ^{2}D–NMR line for *Himantormia lugubris* continuously decreases with the temperature decrease in the investigated range, reflecting rather slow non-cooperative immobilization of water versus decreased temperature, which is the background effect for the signal intensity changes observed for ^{1}H–NMR. No discontinuous decrease in ^{2}D–NMR line magnitude with temperature was observed, suggesting that the change observed for temperature 253 K in H_2O may not be caused by a cooperative water freezing.

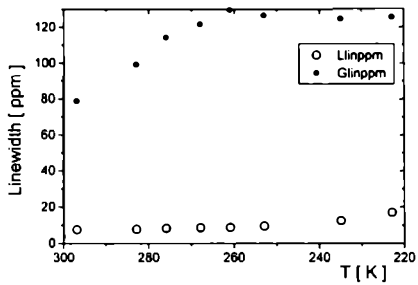

Fig. 4–16. Linewidth for Lorentzian (o) and Gaussian (+) line component in ^{1}H–NMR spectrum for *Himantormia lugubris* thallus hydrated in D_2O.

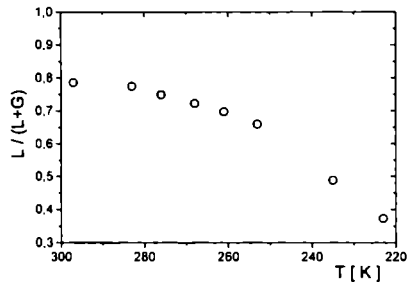

Fig. 4–17. Relative proportion of Lorentzian line component in ^{1}H–NMR spectrum for *Himantormia lugubris* thallus hydrated in D_2O.

4.4. Low temperature conformational transitions in lichen thallus as observed using proton spin-lattice relaxation

Proton spin-lattice relaxometry yields new information on the response of lichen thallus to decreased temperature. This Author performed the temperature courses of *Cladonia mitis* at different hydration level of the thallus, namely, $\Delta m/m_0$=0.046 (incubation over the surface of H_3PO_4, $p/p_0 = 9\%$), $\Delta m/m_0 = 0.195$ (over the surface of supersaturated $Na_2S_2O_3$, $p/p_0 = 76\%$), $\Delta m/m_0 = 0.448$ (Na_2SO_4, $p/p_0 = 93\%$), and $\Delta m/m_0 = 2.05$ (from aqueous phase) [274]. The dry mass m_0 was measured after heating the sample in oven in 70^{0}C for 24 h.

4.4.1 Proton spin-lattice relaxation function

The use of "spin-grouping" method [703] reveals the presence of three exponential components in spin-lattice relaxation function. The FID of each of the components was described by the same superposition of solid and liquid components [272, 273] This suggested the presence of three spin subsystems relaxing in regime of intermediate exchange. However, because of the low S/N ratio, the modelling of them by three subsystems in intermediate proton exchange is difficult. Thus, the single exponential approximation yields more information [274].

4.4.2 Proton spin-lattice relaxation time temperature dependencies

Fig. 4–18 shows the temperature dependence of the spin-lattice relaxation time for *Cladonia mitis* thalli at different hydration levels. For the samples hydrated to

$\Delta m/m_0$ = 0.046 and to $\Delta m/m_0$ = 0.195, T_1 increases with the decreasing temperature. For thallus hydrated to $\Delta m/m_0$ = 0.448 and to $\Delta m/m_0$ = 2.05 the minimum of T_1 at the temperatures between 0°C and −10°C is observed. Additionally in this temperature range the freezing of water free and/or loosely bound in both highly hydrated samples is observed, the temperature dependence of spin-lattice relaxation time was not fitted to these data.

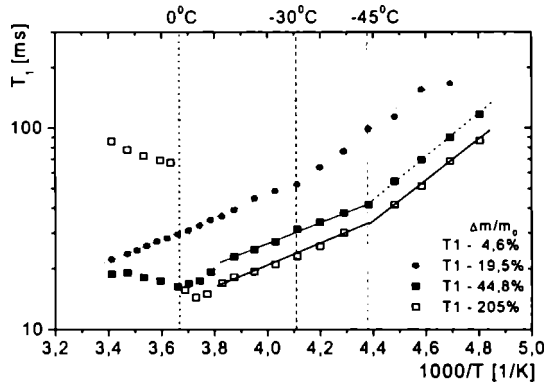

Fig. 4–18. The temperature dependency of proton spin-lattice relaxation time T_1 recorded at 30 MHz using inversion recovery method: π—τ—π/2—FID(t) for *Cladonia mitis* thallus at different hydration levels. The transmitter power 400 W, π/2 = 1.2 μs. For every pulse distance τ the FID function was averaged from 250 accumulations; the repetition time 2 s. Data were analyzed using the program CracSpin [703].

The activation energies calculated for the T_1 temperature dependencies for thallus of *Cladonia mitis* are presented in Tab. 4–4. Low values of activation energies suggest the presence of paramagnetic ions in *Cladonia mitis* thallus [272]. For the sample hydrated to $\Delta m/m_0 = 2.05$ the activation energy above the free water freezing point equals E_a=8.8 kJ mole^{-1}, which is the value close to the values for low temperature.

Table 4–4. The activation energies E_a [kJ mole^{-1}] for *Cladonia mitis* thallus at different hydration level, $\Delta m/m_0$, calculated either above or below the low temperature transition.

$\Delta m/m_0$	Above	Below
0.046	6.4	22.2
0.195	10.6	18.7
0.448	10.0	20.3
2.05	10.0	19.1

At the temperature −30°C for samples hydrated to $\Delta m/m_0$ = 0.046 and to $\Delta m/m_0$ = 0.195, and at the temperature −45°C for highly hydrated samples ($\Delta m/m_0 = 0.448$ and $\Delta m/m_0 = 2.05$) the Arrhenius dependencies of proton spin-lattice

relaxation time T_1 shows break in slope which may be caused by a conformational change.

Fig. 4–19 shows the temperature dependence of the liquid signal amplitude expressed in units of solid signal, L/S. *Cladonia mitis* hydrated to $\Delta m/m_0 = 0.448$ shows discrete decrease of liquid signal amplitude between -3^0C and -6^0C, which reflects the freezing of loosely bound and/or free water present in cellular fluids of thallus. For the sample hydrated to $\Delta m/m_0 = 2.05$ above -3^0C solid signal is very small compared to liquid and is not fitted [703]. The cooperative freezing of water is not observed in the samples hydrated to $\Delta m/m_0 = 0.195$ or lower.

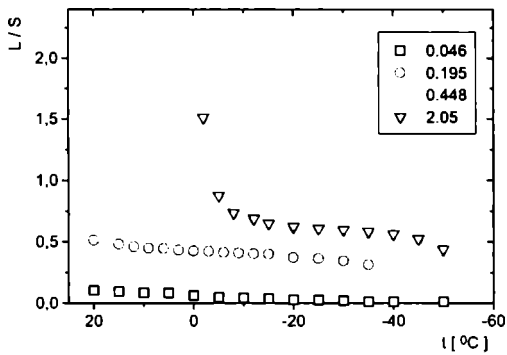

Fig. 4–19. The temperature dependency of proton liquid signal expressed in units of solid (L/S) vs. temperature for *Cladonia mitis* thallus at different levels of hydration.

The conformational change at -30^0C was not detected on the L/S temperature dependency, which means that it is not accompanied by the bound water freezing and/or its drastic change in mobility. This change did not manifest itself either in peak position or in peak halfwidth for low-power ($\pi/2 = 35$ μs) proton spectra of dehydrated *Cladonia mitis*; also the area under peak changes smoothly with decreasing temperature [277]. Moreover, the proton spectra at $\pi/2 = 8.3$ μs did not reveal any discontinuities in the area under peak at $t = -30^0$C for dehydrated thallus. As these experiments did not recorded the signal from solid matrix of thallus, but from bound water only, the above supports the hypothesis that the effect at $t = -30^0$C occurs in solid matrix of lichen thallus and, moreover, the tightly bound water layer is not involved in this process [274].

Indeed, there is no direct evidence on phase transitions in lichen thallus. However, there are some reports on lipid phase transitions occurring in liposomes from the extract of spinach lipids in -30^0 and -40^0C [339], in tomato chloroplast lipids in -29^0C [256]. In soya lecithine the temperature of transition was between -20^0C and -30^0C [549]. The observations made using different methods suggest that there is a liquid crystalline to gel phase transition occurring for some fractions of membrane lipids.

For thalli hydrated to higher level, at -45^0C the L/S and T_l temperature dependencies show the change in slope. This suggest a cooperative change in non-freezable water tightly bound on thallus surfaces. However, it may be also connected with the change in hydrophilic region of thallus membranes.

4.5 Freezing resistance of insects

The comparison of the freezing resistance mechanisms between different Kingdoms may allow to find very deep similarities in the response on frost among the creatures very distant in taxonomy. Insects reveal unusual abilities to survive the extreme desiccation, which suggest that they might develop the mechanisms of freezing resistance.

That some insect larvae survive being frozen, was for the first time reported by Réamur, 1734. During prolonged frost, when supercooling is terminated and the insect starts to freeze at its ice crystallization or spontaneous freezing temperature, heat is released exothermically and its body temperature rises momentarily and then decays; however, its maximum temperature never rises above the melting point of its body fluids [426]. Freezing-resistive insect species undertake two strategies to deal with frost: (a) freezing avoidance; (b) freezing tolerance.

4.5.1 Freezing avoidance

Freezing avoidance involves the ability to supercool by presence of freeze protectants as polyols, to depress the freezing point of the cellular fluids; or by other mechanisms to avoid ice nucleation and the formation of lethal ice. Freeze avoidant species cannot survive ice formation in their body fluids or in tissue. Some freezing avoidant species can supercool to around -60^0C [567]. Insect freezing protectants can be classified onto two classes: (a) polyhydric alcohols (polyols), and (b) antifreeze proteins. Freezing avoidance is a strategy very commonly undertaken by insects. It is characterized by the following features:

(i) ice formation inside body is lethal;
(ii) high degree of supercooling;
(iii) in most cases the minimal supercooling temperature is the lethal temperature at which insect is killed by cold;
(iv) the substance which promotes (stimulates) ice nucleation is absent or inactive;
(v) polyols act as antifreezers, depressing the freezing point;
(vi) antifreeze protein (AFP) which causes thermal hystheresis may be present stabilizing the temperature of freezing point.

Antifreezing polyols are glycerol (being the commonest), also sorbitol, mannitol, and several others. In association with polyols, the level of haemolymph sugars (mostly trehalose but also glucose and fructose) may be elevated in winter. Molar concentrations of glycerol and sorbitol have been reported reaching 4–5 M

[177, 478], also ethylene glycol (up to 2.7 M level) was recorded in an overwintering bark beetle (*Ips acuminatus*) [228]. Glycerol content in the larvae of the moth *Retinia* (*Petrova*) *resinella* seasonally increases up to ~28% of fresh mass, with the supercooling point about –47^{0}C [269].

AFP decreases the freezing point but not the melting point of water and aqueous solutions, thus, causing a thermal hystheresis in phase behavior of insect body fluids. Similarly acting proteins have been found in cold water marine fishes [165]. AFP of large molecular weight has been identified from more than thirty species of insects as well as from some spiders, centipedes and mites. The thermal hystheresis due to AFP action varies between 0.5^{0}C up to 8^{0}C [62]. The seasonal changes of thermal hystheresis are observed, indicating the seasonal changes in AFP in insects, e.g. in larval haemolymph of the darkling beetle (*Meracantha contracta*) the freezing and melting temperatures differ by 4^{0}C between December and March, whereas no thermal hystheresis was recorded between June and October [174]. Moreover, AFP inhibits the recrystallization of ice during thawing of frozen (or partially frozen) biological organism, by binding onto the surface of ice crystallite, preventing from the further crystal growth.

Endogeneous and exogeneous ice nucleating agents, e.g. mineral particles, ingested food materials, micro-organisms, proteins, lipoproteins, and intracellular supramolecular structures, occur in both freeze-avoiding and freeze tolerant insects, but their distribution in an insect body alters with the season of the year. In summer, all insect species deposit ice nucleating agents in intracellular or gut compartments. In winter freeze tolerant species deposit them either in intracellular or gut compartments or in haemolymph, whereas freeze-avoiding species reveal the absence of ice nucleating agents [722].

Some freeze-avoiding species cease feeding and void their guts at the onset of winter, to reduce the amount of exogeneous ice nucleating agents, with the reversal of the process during the following spring, e.g. Antarctic collembolan *Cryptopygus antarcticus* [94].

4.5.2 Freezing tolerance

Freezing tolerance is the ability to survive ice formation in tissues and in body fluids. It involves the promotion of non-lethal extracellular ice formation by proteinaceous ice nucleators, the use of freezing protectants, and the survival of partial ice formation. The extracellular freezing is promoted by ice nucleating agents of haemolymph (at relatively high, sub-zero temperatures), and in the same time body is prevented against intracellular ice formation.

Freezing tolerance is less commonly used strategy. There is about sixty species of insects belonging to this category. For instance, larvae of the cranefly *Tipula paludosa* (Diptera, Tipulidae) from an upland grassland in Northern England survive (96% survivality) freezing of their extracellular body fluids when

cooled at $0.1^0C\ min^{-1}$, with a mean crystallization temperature of -6.2^0C, whereas the lethal temperature was $\sim 7^0C$ lower [64].

Main features of freeze tolerant species are listed below [62]:

(i) they survive extracellular ice formation;

(ii) they have low supercooling ability;

(iii) the temperature, at which insect is killed by cold is usually lower than the temperature at which ice crystallization or spontaneous freezing begins;

(iv) active ice nucleating agents are present in haemolymph;

(v) polyols afford cryoprotection from ice;

(vi) thermal hystheresis proteins act as antifreezers.

The intracellular freezing causes that water enters the cell resulting in the swelling of the cell and, thus, subsequent membrane rupture. In contrast, at the extracellular ice formation water leaves the cell, which then shrinks causing the dehydration with the subsequent lowering of the freezing point of the intracellular fluids as the contained solutes are concentrated [723].

Nucleation occurs in extra-cellular spaces or possibly in the gut fluids of freeze tolerant insects, as isolated haemolymph usually nucleates 9^0C to 15^0C below the temperature of spontaneous ice growth of the whole insect. Ice nucleating agents of proteinaceous nature are synthetized by the insect and inactivated by proteases and heating above $+80^0C$. For instance, in adult form of maritime Antarctic perimylopid beetle, *Hydromedion sparsutum*, revealing the supercooling point at $-(3.0\pm1.0)^0C$, which is amongst the highest recorded for any terrestial arthropods, guts are probable site of nucleation, as the supercooling point [$-(3.9\pm0.6)^0C$] of the excised gut is close to the whole insect's supercooling point. Narrow range of supercooling points suggest the presence of an efficient ice nucleator. Gut contents of *Hydromedion* consists mostly of partly digested plant material, bacteria and fungi. Two potential food plants (mosses *Polytrichum alpinum* and *Andreaea* sp.) show ice nucleating activity at little lower temperatures (-4.0^0C and -5.0^0C, respectively; and -5.0^0C for possible lichen *Usnea fasciata*) suggesting that ingested plant material probably may not be directly responsible for ice nucleation. Heating to 75^0C significantly reduces the ice nucleation activity, suggesting the proteinaceous nature of ice nucleator [713].

Some freezing tolerant Arctic insects show lack of both endogeneous and exogeneous ice nucleating agents and reveal deep supercooling to -40^0C or lower [566]. The extremal example is here larval fruit fly (*Chymomyza costata*) exhibiting cold-induced freezing tolerance to the temperatures below -100^0C, which is accompanied by the accumulation of trehalose and proline [615].

The first insect proteinaceous ice nucleus was isolated from queens of the bald-faced hornet (*Vespula maculata*). It is a 74 kD protein, with pronounced hydrophilic amino acid composition, which promotes the ordering of water molecules into an embryo ice crystal on the protein surface [176].

Cryoprotectants (commonly glycerol, sorbitol and trehalose) are synthetized in most freezing tolerant insects to minimize or to prevent from

freezing damage, and high levels of amino acids (proline, glutamine, and glycine) are detected along with other organic compounds. Their action results in the reduction of the amount of ice formed when freeze-tolerant insects freeze, to buffer cells against ice crystals, and to protect proteins from freeze-thaw denaturation.

AFP are detected in some freeze-tolerant insect species. They may act as antifreezers in saeasons before freeze tolerance is fully developed. As they are potent inhibitors of ice recrystallization especially during the thawing process, they may promote freeze tolerance preventing from mechanical disruption.

Intracellular freezing is reported in cells isolated from several freeze-tolerant insect species, e.g. fat body cells from wintersized larvae of the golden rod gall fly *Eurosta solidaginis*, in which > 60% of such cells survive the intracellular freezing and the exposure to -80^0C, whereas no whole larvae survived [427]; also isolated fat body cells of freeze-tolerant larvae of the fly *Heliomyza borealis* from Swalbad reveal 85% viability when frozen at 0.1^0C min^{-1} to -40^0C, *in vivo*, and 45% viability, when frozen *in vitro* [62].

4.5.3 Adaptative switching between freeze-resistance strategies

In many species the mechanism of freeze tolerance is seasonal for overwintering, whereas they remain freeze avoidant at other times [62].

The most sophisticated mechanism of freezing tolerance was found in extremelly freeze tolerant larvae of long-lived (14 year life cycle) *Gynaephora groenlandica* ('wooly bear caterpillar') populating Canadian High Arctic Archipelago. The lowest supercooling temperature varies in the range -7 to -9^0C during whole year, whereas larva survives to -15^0C (in summer) and to -70^0C during winter. Larvae show two types of cold response:

(i) short-term (compensatory) responses: behavioral thermoregulation by sun basking which increases its energetic efficiency, and seeking shade near permafrost (voluntary hypothermia) which reduces metabolism and aids glycerol synthesis;

(ii) long-term (adaptative) responses: including mitochondrial degradation resulting in glycerol production and increased freezing tolerance.

Both types of response lead to similar results, but the larvae are thermoregulators in summer and thermoconformers during winter [401].

Two species of insects are reported that can switch from being freeze tolerant to freeze avoiding. The overwintering larvae of a beetle (*Dendroides canadensis*) initially freeze tolerant with supercooling point between -8^0C and -12^0C, and lowest lethal temperature ~ -28^0C, some years later in the same site (in Northern Indiana) showed supercooling point and lowest lethal temperature at ~ -26^0C [319]. In the same locality, larvae of beetle (*Cucujus clavipes*) changed from freeze tolerant (with mean supercooling point at -11^0C, high levels of two polyols, ice nucleation in haemolymph, and exhibiting thermal hystheresis) to freeze avoidant

(mean supercooling point at -30^0C, reduced polyol content, and similar thermal hystheresis); with the similar lowest lethal temperatures (-26^0C to -30^0C).

The almost simultaneous switch of two species was caused by a sequence of mild winters and probably occured between the winters 1979–80 and 1980–81, when ice nucleating agents were lost [175].

4.5.4 Freezing resistance of insect eggs

The egg is the principal overwintering stage of many insects and other terrestial arthropods. As liquid container it provides favorable conditions for supercooling. Indeed, eggs have a high capacity of supercooling compared with other life stages, and they are killed by freezing [67].

Mean supercooling points are -51^0C for tortricid *Zeiraphera diniana*, -42^0C for aphid *Pterocomma smithia*, -45^0C for tortricid *Alsophila pometaria* [632], -36^0C for *Neodiprion sertifer* (Hymenoptera, Tenthredinoidea) [16], -30^0C for not cold-adapted locust *Locusta migratoria* [445].

For three species of grasshoppers (Orthoptera, Acridoidea) from Inner Mongolia, Xilin River Basin, experiencing severe thermal conditions during winter (-30^0C), eggs of *Myrmeleotettix palpalis* contain 28% fresh mass of water, *Aeropedellus varigatus minutus* 46% of water, and eggs of *Dasyhippus barbipes* 52% fresh mass of water; which is equivalent to 0.3, 1.1, and 1.1 g g^{-1} of dry mass, respectively; whereas mean supercooling points are $-(24.5\pm2.2)^0$C (in the range -9.1 to -35.0^0C), $-(22.8\pm2.4)^0$C (-5.8 to -35.0), and $-(25.9\pm1.9)^0$C (in the range -5.1 to -30.5^0C), respectively. Potential cryoprotectants (glycerol, mannitol, and trehalose) occurred in the eggs in concentrations insufficient to influence the supercooling abilities (~0.1% of fresh mass) [67].

Indeed, egg of *Myrmeleotettix palpalis* contains 1.0×10^{-3}cm^3 of water, egg of *Aeropedellus varigatus minutus* $2.1\cdot10^{-3}$ cm^3, and egg of $2.2\cdot10^{-3}$ cm^3 *Dasyhippus barbipes* of water (calculated by this Author from [67]), which gives, in spherical approximation, the respective values of the water compartment diameters equal to 1.07 mm, 1.54 mm, and 1.56 mm.

Table 4–5. Ice nucleation temperatures for three species of grasshoppers from inner Mongolia. d is diameter of water compartment (in spherical approximation) (calculated from [67]); t_{mean} is mean nucleation temperature and t_{min} is minimal recorded nucleation temperature [67]; t_{het} is heterogeneous nucleation temperature for water droplets [43, 44]; t_{hom} is homogeneous nucleation temperature a) from [484], b) from [457].

Species	d [mm]	t_{mean} [^{0}C]	t_{min} [^{0}C]	t_{het} [^{0}C]	t_{hom} [^{0}C]
Myrmeleotettix palpalis	1.07	–(24.5±2.2)	–30.5	–24	–34[a], –33[b]
Aeropedellus varigatus minutus	1.54	–(22.8±2.4)	–35.0	–23	–33.5[a], –33[b]
Dasyhippus barbipes	1.56	–(25.9±1.9)	–35.0	–23	–33.5[a], –33[b]

Using the data from Tab. 4–5 this Author mentioned that the mean ice nucleation temperatures are in good agreement with the temperatures of heterogeneous ice nucleation for water droplets of the same size [43, 44]; whereas the lowest recorded ice nucleation temperatures well agree with the homogeneous ice nucleation temperatures estimated as minima for the set of water droplets of the same size [457, 484]. This coincidence shows that in grasshoppers' eggs there exist no specific freezing protection mechanism.

4.5.5 Influence of dessication tolerance on freezing tolerance of arthropods

The organisms populating both polar and alpine areas experience extreme cold, which is considered by a dominating constraint influencing survival and distribution of living species, but in the same time non-availability of moisture will limit their biological activity. Thus, question arises if there exist interference between cold adaptation and drought adaptation whether they are mutually exclusive to each other, antagonistic, or complementary processes.

Dessication tolerance may be pre-adaptation for freezing tolerance, e.g. in larvae of chironomid *Polypedilum vanderplancki* [309] being extremely cold resistant as dried, although they would never experience sub-zero temperatures in their natural habitat (see Chpt. 3.10.3).

Partial dehydration may significantly affect insect cold hardiness, whether the species of life stage is freeze tolerant or freeze avoiding, by increasing the production of polyols and by promoting the synthesis of antifreezers [63]. The following physiological features of partially dehydrated insects contribute to their cold hardiness [62]:

(i) body fluids are concentrated during the accumulation of polyols and other cryoprotectants;
(ii) individual supercooling points are depressed by loss of body water;
(iii) desiccation alters the ratio of freezable to unfreezable water;
(iv) ice nucleation agents may increase the amount of unfreezable water;
(v) unfreezable water does not act as a solvent for low molecular substances.

Additionally water influences cold hardiness by the following effects [63]:

(i) diet or food material influence cold hardiness by reducing supercooling, e.g. an access to water and algal food for 15 days both significantly reduced the supercooling ability of *Cryptopygus antarcticus* (field measurements, Signy Island, Maritime Antarctic) [102];
(ii) intake of water activates/unmasks ice nucleators, e.g. in laboratory measurements, the immediate and dramatic loss of supercooling ability for winter-acclimatised Collembola species doped with distilled water was observed [103];
(iii) potential cryoprotectants increase after water intake, e.g. the 5-day-availability experiment show significant increase of cryoprotectant in *Cryptopygus*

antarcticus fresh mass either in mannitol, sorbitol, glucose, and trehalose concentration or in total number of hydroxyl groups per water content [102];

(iv) supercooling ability related to body water content, e.g. for 15 species of coastal mites from Maritime Antarctic, the individual supercooling temperature linearly (correlation coefficient equal 0.814) increased from about -19^0C at body water 30 μg to -12^0C at 200 μg [548];

(v) seasonal changes in water content and supercooling point are correlated, e.g. field observations (Signy Island, maritime Antarctic) averaged over 4 to 8 years show that in *Cryptopygus antarcticus* mean monthly water content is correlated with supercooling temperature, from the minimal value ($\Delta m/m_0 = 1.2$, where m_0 is dry mass; supercooling temperature ~ -23^0C) in July, to maximal body water contents in September and February ($\Delta m/m_0 = 1.9$) and supercooling temperature -9^0C between November and March [65];

(vi) body water content decreased with polyol accumulation, e.g. the adult beetle *Ips acuminatus* Gyll. cultured at 3^0C during overwintering in Norway shows decline in body water to < 50% of fresh mass content correlated with lowering of the supercooling temperature to about -24^0C, and synthesis of major cryoprotectant (ethylene glycol) during November, with adult diapause terminated by the end of December [229]; during autumn in larvae of the goldenrod gall moth *Epibilema scudderiana* (Lepidoptera: Oletrheutidae) individual supercooling temperatures declined from -14^0C to -38^0C, water content decreased from 57 to 28% of fresh mass, glycerol concentration increased to ~19% of fresh mass [564];

(vii) about 25% of water is unfreezable, e.g. *Eleodes blanchardi* beetles (Tenebrionidae) tolerant to freezing at -6^0C to -7^0C contained ~25% unfreezable water, which proportion was not altered in freezing-avoidant specimens obtained by culturing at 20^0C [725];

(viii) three-fold increase in unfreezable water at onset of winter, e.g. freezing-tolerant larvae of *Eurosta solidaginis* (Diptera: Tephritidae) do not dehydrate during overwintering [26], but three times increases the proportion of freezable water in the period between early autumn and winter [645].

The features (i) up to (vi) characterize freeze-avoidant species, feature (vii) is common for freeze-avoidant and for freeze-tolerant arthropods, whereas (viii) was found for freeze-tolerant species only.

A reduced body water level in arthropodes helps to prevent freezing both directly (by reducing the amount of freezable water) and indirectly (by elevating the effective concentration of polyols present by enhancing the depression of the supercooling point) [646].

Freezing tolerant arthropods do not always reduce their water content by dehydration, but tend to increase the proportion of unfreezable water to ensure that the lethal limit (~65% of total water as ice) is not exceeded during the normal winter conditions [63].

4.6 Comparison of freezing protection mechanisms in lichens and in insects

Although lichens (lichenized fungi) being autotrophs are distant in taxomonical position from insects, e.g. with the structure of most tissues resembling that for vertebrates, including human tissues; freezing protective mechanisms of both groups reveal striking similarities.

(i) The stimulated growth of ice crystallite inside individual body occurs either in lichen or in insect. This strategy is less common for insects than for lichens, because the surplus of water enabling immediate start of active living processes is for plant more advantageous than it is for mobile insect. In lichens the ice crystallites are localized in extra-cellular spaces, whereas in insects beside extra-cellular spaces they may be deposited in guts.

(ii) Freezing avoidance in intra-cellular spaces based on the production of cryoprotectants (polyols or AFP's) characterizes either lichens or freezing resistant and freezing avoidant insects. The presence of cryoprotectant introduces the steric mismatch between water binding sites and, thus, prevents body from ice crystallite growth. The mechanism based on tightly bound water fraction increase (via gel-like structures formation) is detected only in lichens till now.

Beyond the stimulated increase of tightly bound water fraction, lichens show no exclusive freeze-protective mechanisms. In fact, there is no proof that similar mechanism does not exist in insects.

More composed freeze-protective strategies undertaken by insects, as two stage compensative-adaptative mechanism, or adaptative switching between freeze-tolerance to freeze-avoidance, do not essentially differ from the strategies common for both groups. Indeed, they are only combinations of both common freeze-protective mechanisms.

These signalizes that basic strategies of freeze protection were developed on very early stages of life evolution. More composed organisms use them just on more versatile way.

5. Summary. A droplet of philosophy

Better understanding of the resistance to acute water stress and the freezing protection mechanisms in extremophilous organisms give a hint in searching for the limits of life in dry environment and at decreased temperature.

Although the limits of desiccation and the mechanisms of freezing protection in lichens remained the main goal of the Thesis, the application of NMR forced the solution of the problems characteristic for this method (proper identification of proton subsystems) and the effects which exccedighly manifest in NMR measurements (paramagnetic ion and the presence of water soluble solid fraction effect).

Proton NMR is almost unique method giving an insight in the bound water behavior in dry biological system, which is not transparent. However, by the micro-heterogeneity of the system the recorded signal is superposition of the signals from the proton subsystems differentiated by their relaxation times. Thus, proton relaxation functions may be fitted by the superposition of the signals from different spin groups, or in case of high number of components, by distribution functions. The stretched exponential function (SE) is commonly applied, as it is "numerically capable" and, moreover, reflects the self-similar (fractal) distribution of pores in the system.

Two-dimensional analysis of relaxation matrixes helps to decompose the complex signals from micro-heterogeneous systems. Program CracSpin recognizes the spin groups differentiated by at least one of relaxation times recorded in a 2-d time-domain experiment, using two types of analyses of relaxation matrix cross-sections started alternatively from each of two time variables. It allows to decompose up to 7 exponents, two Gaussian components, and two different SE functions. Residual function help in proper assignment of fitted function. In some cases CracSpin resolves the components with the time constants different by less than factor of 3 (two short component, factor 2, for S/N > 100; two longest components in decay, factor < 2, S/N > 60, for the relative fraction of the long component exceeding 5%). CracSpin differentiates the data being the superposition of distinct exponents from the ones described by SE function.

The hydrocarbon fractions filling the pores of two different porous rocks were used as model systems to test the SE and the exponential fits, namely, Węglowicki sandstone and oil-containing limestone. In oil-containing limestone proton magnetization recovery is well fitted by single exponential function, whereas SE fits did not give satisfactory results. In contrast, the signal from Węglowicki sandstone is fitted by SE function and by modified stretched exponential (MSE) function, and the respective values of fitted parameters do not differ for SE and MSE fit. High quality of fits unambiguously determined the form of fitted function.

Commonly used SE function artificially enhances the amplitude of the spin fraction fitted by this function compared to the fraction described by exponent. However, the performed comparative analysis of the SE function and the MSE function (taking into account the presence the fraction with the shortest non-zero relaxation time) showed that the values of time constant of decay fitted by both functions not differ (within the experimental error), whereas the SE caused enhancement of the amplitude does not exceed $\delta = 3.5\%$ of the MSE fit.

Complex analysis of the bound water behavior in living organisms dehydrating to very low level, performed especially with the use of NMR, should be preceded by the proper recognition of some peculiarities revealed by ultra-dry biological systems, which are:

(i) paramagnetic ion behavior, and

(ii) the effects of the presence of water soluble solid fraction.

The use of a model system allows to exclude (or at least to diminish) the side effects.

To separate the paramagnetic impurity effect in limited amount of water, the effect of paramagnetic Fe contaminating water filled channels of controlled pore glasses (CPG) was investigated.

If the amount of water filling pores of CPG is comparable to the total volume of the pores, V_0, the concentration of Fe ions dissolved in water is constant, introducing the abnormal form of the proton relaxation time hydration dependence, showing two regions of linearity when plotted against V_0/V (the break between them sharply defined at $V_0/V = 1$). With the decrease of water level the surplus of ions is deposited on the surface of pore.

For further decrease of the hydration level of CPG pore, the following steps can be distinguished:

(i) the silica surface is fully covered by water;

(ii) bound water tends to form clusters, paramagnetic ions prefer the bound water clusters ($f_S = 1.71$, near full geometric coverage of the surface);

(iii) at the hydration level below the percolation threshold of bound water, the "apparent percolation transition" breaks the paths between clusters ($f_S = 0.34 \pm 0.02$);

(iv) bound water clusters decrease, water molecules gather around the paramagnetic ions;
(v) water cluster vanish, the remnant water molecules remain in vicinity of ions.

The NMR experiment is sensitive on the diffusion during the finite time of the experiment, thus, the "apparent percolation transition" detects the decrease in the size of water clusters below the percolation threshold.

The effect of the limited amount of the water soluble solid fraction was examined during the hydration of horse chestnut (*Aesculus hippocastanum* L.) bast, where the water soluble fraction makes up the meaningful fraction of the dry mass. As a reference, not containing the water soluble fraction bark of horse chestnut and of pine (*Pinus silvestris* L.) were measured.

Two alternative methods of *in situ* measurement of water soluble proton fraction present in bast or bark are proposed, however, the proposed equations are general, in sense, that they describe the soluble fraction influence on L/S ratio in any biological micro-heterogeneous system at low hydration.

First is based on the measurements of the absolute NMR signal, while the second one, simpler, requires the measurements of liquid amplitude expressed in units of solid fraction, L/S. The measurement of the absolute NMR signal yields for horse chestnut bast hydrophilic extractive fraction the upper dissolution threshold, $\Delta M/m_0 = 0.18$ (the amount of water necessary to dissolve the whole water-soluble fraction), saturation concentration of soluble fraction, $c_s = 0.643$ (little lower value than that for sucrose), thus, $\Delta M_c/m_0 = 0.325$, the content of solid soluble fraction, and effective (scaled to water) proton densities of bark solid and water soluble fractions of bark, *in situ*.

The measurement of relative L/S gives valid fits for most of these molecular parameters. For routine measurements, if one has only limited access to NMR spectrometer, the simpler measurements (not requiring constant conditions or at least an identical external reference) give satisfactory numbers for the majority of parameters considered.

During the initial phases of wheat (*Triticum aestivum* L.) seed imbibition, beside the dissolution, the enzyme action on starchy endosperm causes the increase in water soluble liquid fraction. Thus, the analysis of L/S shows the presence of unlimited amount of water soluble fraction, which is confirmed by S/(L+S) measurements of seed hydrated in D_2O. The initial hydration level of the investigated seed was $\Delta m/m_0 = 0.095 \pm 0.005$, however, the non-uniform moisture distribution in dry seed was observed (embryo was hydrated to higher level than endosperm).

Antarctic lichens were selected to the investigations of the dehydration resistance and the mechanisms of freezing protection, as a living organism experiencing in its natural habitat the extreme conditions of low temperature and

moisture deficit. Indeed, some lichen species survive extremely low temperatures (even below the temperature of liquid nitrogen); they can perform the active photosynthesis below 0^0C, and even below the temperature of ice crystallite nucleation in cellular fluids of thallus; they can take water directly from snow up to the level sufficient to initiate the photosynthesis.

Several test performed using proton relaxation and proton NMR spectra, hydration kinetics and adsorption isotherm, and the static conductance measurements, revealed the range of reversible dehydration of lichen thallus and gave an insight in molecular background of their freezing protection mechanisms.

Adsorption isotherms either for Antarctic lichens or cosmopolitan species (*Cladonia mitis*) showed the sigmoidal form, which was fitted using Dent model. The applied model classifies the water binding sites on the lichen thallus onto two groups: primary binding sites with high affinity to the thallus ($\Delta M/m_0$ varying from 0.063 for *Usnea aurantiaco-atra* to 0.073 for *Umbilicaria antarctica*, with an average value of 0.0675±0.0045), and secondary water binding sites (either to water bound on primary sites or to the thallus binding sites with the lesser affinity). Other parameters obtained from Dent model show that foliose *Umbilicaria antarctica* reveals elevated affinity of water binding sites, as at h = 1 the contribution of empty water binding sites equals here only 0.09%, whereas for fruticose species it varies from 2.44–2.06% for *Cladonia mitis* to 1.11% for *Himantormia lugubris*.

In hydration and dehydration runs the primary bound water fraction manifested as a component with an amplitude averaged over the lichen species investigated, equal 0.074 at hydration to $p/p_0 = 93\%$, 0.05 for hydration at $p/p_0 = 100\%$, 0.064 at dehydration to $p/p_0 = 9\%$, and 0.054 at dehydration to $p/p_0 = 0\%$. Due to high affinity of this water fraction, this component was almost constant for the hydration runs performed. In foliose *Umbilicaria antarctica* and in fruticose (but with thallus localized in vicinity of soil) *Caloplaca regalis* the hydration and dehydration kinetics is well described by the single exponential dependence with the hydration time constants 58 h and 56 h for hydration to $p/p_0 = 100\%$, respectively, and 70 h for $p/p_0 = 93\%$; the dehydration was described by the times 7.5 h and 5 h at $p/p_0 = 9\%$, and 9 h and 6.5 h at $p/p_0 = 0\%$, respectively. In other fruticose thalli either hydration or dehydration process were described by the superposition of two components. At hydration the fast component (except *Himantormia lugubris*, the hydration time less than 1 hour) with minor amplitude and the slow component with the contribution of more than 80% of total increase and the time constants ~3 times longer than those for foliose lichens are detected. At dehydration fast component consisted of majority of total amplitude, with the dehydration time 2–5 h, whereas the slow component was described by the time constant between 5 and 9 h. The dehydration process in fruticose thalli reveals some similarities with hydration process: as the first one is removed the majority of bound water, the fraction with lesser affinity. Then, in the second step the smaller fraction, which was bound as a first one, is removed.

The observed mechanism may benefit in better adaptation to frost weather changes. At first, fast hydration step the thallus is activated to the "ready-to-function" low hydration state, whereas further hydration is slow down, preserving the tissue during accidental fluctuations of local moisture and/or temperature. The hydration at the first, fast and effective step seems not to depend on relative humidity of the habitat. Thus, this value Lh varied from 0.135±0.017 for the fresh *Cladonia mitis* sample to 0.165±0.028 for *Usnea aurantiaco-atra* can be called "preferably low hydration level". This mechanism is not observed in lichen species with the thallus localized in the vicinity of soil, which stabilizes the hydration and dehydration process, sufficiently preventing the thallus from the effects of an accidental wetting.

Proton magnetic relaxation hydration experiments show that the tightly bound fraction (generally Lh) and the dominant, loosely bound water fraction differ in the degree of water molecule immobilization manifested by the spin-spin relaxation times (measured from FID) of the order of ~100 μs and ~1000 μs, respectively. Moreover, the signal from the tightly bound water pool is more significantly dumped than the loosely bound water fraction by the paramagnetic ions present in the system, presumably paramagnetic Mn in photosynthetic lamellae of lichen photobiont.

Static conductance measurement in dehydrated thallus of Antarctic *Himantormia lugubris* and in *Cladonia mitis* revealed that both lichens reversibly dehydrate below the percolation threshold of water bound on the thallus surfaces. It is the first observation of the mature living organism dehydrating to so low hydration level. The fractal exponent for *Cladonia mitis* $\alpha = 1.18$ fits well in the range of theoretical values for a two-dimensional system, whereas for *Himantormia lugubris* $\alpha = 1.42$ which slightly exceed the range for two-dimensional processes. The hydration threshold occurs at the hydration level $\Delta M_p/m_0 = 0.099$ for *Himantormia lugubris*, and at $\Delta M_p/m_0 = 0.096$ for *Cladonia mitis*, which are the values of hydration level often occurring in natural conditions and at the storage in a herbary, namely at $p/p_0 = 35\%$ and $p/p_0 = 34\%$, respectively. Full coverage of the thallus surface (slightly higher than mono-molecular) corresponds with the value of Lh, and, thus, yields the total water accessible surface of lichen thallus as equal 416 $m^2 g^{-1}$ and 377 $m^2 g^{-1}$ for *Cladonia mitis*, 447 $m^2 g^{-1}$ for *Himantormia lugubris*, and 461 $m^2 g^{-1}$ for *Usnea aurantiaco-atra*. Thus, the combined measurements of static conductivity and hydration kinetics supply the method of non-invasive, *in vivo*, estimation of total water accessible surface of dry biological system.

The freezing protection mechanisms were tested for cooled down lichen thalli using proton FID, and proton NMR spectra. Two complementary freezing protection mechanisms were recorded:

(i) Beside the observation of loosely bound water freezing in hydrated *Cladonia mitis* thallus, the analysis of the temperature dependence of the peak position of loosely bound water proton NMR line shows that

thallus stimulates non-lethal growth of ice crystallites (presumably in extra-cellular spaces).

(ii) Proton relaxation and spectra for both loosely bound and tightly bound water fraction show that with decreasing temperature the loosely bound water fraction decreases on a cost of a tightly bound (non-freezable) water pool. For *Cladonia mitis* thallus hydrated to $\Delta m/m_0 = 0.157$ this transition takes all water present in thallus, whereas for thallus hydrated to $\Delta m/m_0 = 0.388$ up to $\Delta M/m_0 = 0.260$ of water is transferred and the surplus freezes. The immobilization of water suggests the presence of the active mechanism based on formation of a long range molecular network with a gel-like structure increasing the liquid-solid interface and, thus, increasing the tightly bound water amount. The increase in non-freezable water fraction prevents the thallus from the lethal ice crystallite growth (presumably in intracellular spaces).

Proton spin-lattice measurements of the cooled down thallus of *Cladonia mitis* show, beside loosely bound water freezing in highly hydrated thallus, the presence of two conformational changes: first on at -30^0C, which is connected with the solid matrix of the thallus (presumably in membrane lipids), and the second on at -45^0C, which is probably the cooperative change in non-freezable water bound on thallus surfaces.

^{31}P–NMR spectra of the wheat photosynthetic membrane preparations, performed for different hydration level, for increased temperature, and for the membranes reconstituted from lyophilisate show that the lamellar structure of membranes is restored after the rehydration of lyophilizate. Although glycerol plays a cryoprotective role at low temperatures, its presence in aqueous medium (57 wt% of glycerol) at room and at elevated temperature destabilizes the membrane structure. The contribution of small membrane fragments increases on the cost of the large lammellar structures of thylakoid. Similarly acts the excess of water in the preparations of photosynthetic membranes.

Additional finding of these experiments was the first direct (not in thermally quenched preparations) observation of hexagonal phase in photosynthetic membrane occurring at the temperature 55^0C and at 60^0C. The lamellar-to-hexagonal liquid crystalline phase transition is correlated with the denaturation of PS II LHC and, thus, the irreversible lack of photosynthetic activity of thylakoid membrane. The presence of glycerol in aqueous medium promotes the direct formation of small micelles ('lipidic particles') omitting the intermediate stage of hexagonal phase cylinders.

The comparison of desiccation resistance of animals (insects and Collembola) shows that they do not dehydrate to so low level as lichens. There is, however, one exception, an African chironomid *Polypedilum vanderplankii*, which

deeply dehydrates to cryptobiosis stage, and analogically to lichens, in dehydrated state may survive extremely low temperatures.

In contrast, the freezing protection of insects and lichens reveals striking similarities. Both groups employ the strategy of stimulated non-lethal growth of ice crystallites inside body, and both groups use the strategy of freezing-avoidance by the use of cryoprotectants. The difference is that insects evolved more composed freeze-protective strategies, being, however, only the combinations of common two. Beyond the stimulated increase of tightly bound water fraction (not yet observed in insects), lichen show no exclusive freeze-protection mechanisms.

5.1 A droplet of philosophy

Let us finally note that in some textbooks there is an opinion expressed that there is a necessity for any living system to inherit at least the minimal part of the Pra-Ocean water structure and every living system is the spectacular manifestation of this general continuity.

A fragment of living system, as observed in molecular scale (~3 Å, size of the single water molecule), differs from the set of molecules taken, say, from the box in chemical shop only by the continuous network of hydrogen bonds (enabling the native conformation of biological macromolecules) between water molecules localized on- or at least interacting with the surface of the biological system.

Considering water surrounding the biological system as a dynamic network of relatively strong bindings, not as a passive medium, it is not meaningless whether or not the hydration of some of living systems may decrease below the percolation threshold, whether some of them can reversibly reach the state in which the infinite water cluster vanishes, or even reach the state in which separated water molecules exist. The continuous, long range network of bonds disappears at the percolation threshold, as the system is dehydrated. Knowing that at percolation the long range structure of water vanishes being replaced by short range structure of water clusters, one can conclude that their structure might be, in principle, copied by just a spatial setting up of the molecules. And subsequently only one Master Breath is needed (helping to pass the percolation threshold), which is an accidental increase of hydration level above the percolation threshold performed from gaseous phase.

So long, a spatial setting up of a large number of single molecules in a composed molecular system (with the complication comparable to the one for living organism) is realized during the molecular simulations, but it is not unthinkable that progress in nanotechnology will enable such an action in future. Although identical in results with origins of life, it should be rather called "clonning of lifes" or "clonning of life evolutions", as the arrangement of molecules in a living organism, although copied from a living entity, will not be a result of subsequent evolutionary steps, but will be installed (by the experimentator) in the system, *a priori*.

Dedication and Acknowledgments

I dedicate this book to the loving memory of my parents whom not enough time was given to see this manuscript completed.

Let me express my sincere gratitude to Professor Jerzy S. Blicharski who carefully supervised my scientific development since I was an Undergraduate and friendly motivated me during preparation of this manuscript, and to Professor Kazimierz Strzałka, who taught me biological routines of preparation and supplied wide variety of photosynthetic membranes.

I owe thanks to Professor Maria "Agnieszka" Olech, who assigned and supplied me best samples of Antarctic lichens from Arctowski Polish Antarctic Station situated in Admiralty Bay, King George Island, Southern Shetlands, Maritime Antarctic.

I would like to express my special thanks to Professor Mik M. Pintar who during my Post-Doctoral Fellowship in University of Waterloo taught me the spin-grouping, which showed its efficiency in my investigations and turned my attention to model porous systems.

It is a great pleasure to thank Professor Jean Grandjean for friendly cooperation and discussion during the measurements of lichen proton spectra, to Professor Wolfgang Dietrich during phosphorus measurements, and to Professor Józef Mościcki for valuable discussions on dielectric measurements, and to Professor Hartwig Peemoeller for critical reading of the significant part of this manuscript.

I would like to express my sincere thanks to Geoff Soga, Ph.D., Ron Rumm, Ph.D., Grzegorz Jasiński, Ph.D., Stefan Gaździński, Ph.D., Władysław Węglarz, Ph.D., Maciej Wnęk, Ph.D. who all helped in my NMR and dielectric measurements, and to Zbigniew Sojka, Ph.D. for EPR assignment of paramagnetic impurities, to Katarzyna Mosna-Bojarska, M.Sc. for tideous preparation of seed embryos, and to Marta Michalik, Ph.D., for lichen vitality tests.

I wish to thank Eng. Leszek Marszałek, M.Sc., for his constant encouragement and hours spent during repairing and adjusting of our relaxometer, to Professor Waldemar Nosel for friendly advises, and to Professor Gothard Klose, University of Leipzig, for valuable discussions on lipid bilayers,

and finally to my wife Ewa for help and patience.

Some of the research works presented were sponsored by the grants of the Committee of Scientific Research in Poland, by the Partnership Collaboration between the Jagiellonian University and the University of Liege, Liege, Belgium, and the Ruhr Universitaet, Bochum, Germany, and during my Post Doctoral Fellowship and further collaboration with the University of Waterloo, Waterloo, Ontario, Canada.

Abbreviations used

Comment: With the changes in lichen terminology, in recent years the names of several lichen species have been changed [512]. If the older synonymes of lichen species were used in quoted papers, the recent synonym is presented, whereas the older one appears in brackets.

1-d	one-dimensional
2-d	two-dimensional
3-d	three-dimensional
A_{jk}	spin dynamics matrix
AFM	atomic force microscopy
AFP	antifreeze protein
$\vec{B}_0$	external magnetic field
B_{loc}	local magnetic field
CCM	CO_2 concentrating mechanism
D	diffusion coefficient for isotropic diffusion ($D_{xx} = D_{yy} = D_{zz} = D$)
$\hat{D}$	diffusion tensor
DGDG	digalactosyl diacylglycerol
DPPC	dipalmitoyl phosphatidylcholine (1,2-dipalmitoyl-sn-glycero-3-phosphocholine)
DPPE	dipalmitoyl phosphatidylethanolamine
DPPG	dipalmitoyl phosphatidylglycerol
DPPS	dipalmitoyl phosphatidylserine
DSC	differential scanning calorimetry
DSPC	distearoyl phosphatidylcholine
E_{HB}	dissociation energy of the hydrogen bond
FID	free induction decay
H	Hamiltonian, Hamilton's operator
h	relative humidity (expressed in fraction)
H_{max}	maximal water content in thallus

INA ice nucleation activity
IRGA infrared gas analysis
J nucleation rate per unit of volume
$J_M^{(R)}(\omega)$ spectral density function for rotational diffusion
$J_M^{(T)}(\omega)$ spectral density function for translational diffusion
k' parameter characterizing the shape of the heterogeneous nucleation activity distribution
$\hat{L}$ Liouvillian, Liouville's operator
M molar mass
MGDG monogalactosyl diacylglycerol
MSE modified stretched exponential
n_{HB} number of hydrogen bonds per water molecule
NMR nuclear magnetic resonance
PC phosphatidylcholine
PE phosphatidylethanolamine
PG phosphatidylglycerol
PS phosphatidylserine
p/p_0 relative humidity (expressed in wt%)
Q spin operator
R_{jk} relaxation matrix
RDF radial distribution function
r.f. radio frequency
SE stretched exponential
S/N signal-to-noise ratio
SQDG sulphoquinovosyl diacylglycerol
S/V surface-to-volume ratio
$\hat{T}_k$ orthogonal and normalized operators in a n^2-dimensional Liouville space
T_1 spin-lattice relaxation time
T_2 spin-spin relaxation time
T_H homogeneous nucleation temperature
T_{jk} cross-relaxation times for multispin systems
T_m equilibrium freezing temperature
u_+ H^+ mobility
$X_{HB}(T)$ mole fraction of hydrogen bonds
$Z(a_i)$ ordinal number of atom a_i
γ nuclear gyromagnetic coefficient
ΔT supercooling
$\Delta T/T_m$ degree of supercooling
δ chemical shift
δ_{HB} chemical shift of hydrogen-bonded protons

δ_{n-HB} chemical shift of non-hydrogen-bonded protons
ε dielectric constant
χ isothermal compressibility
ρ density
σ density operator
σ screening constant
$\hat{\sigma}$ chemical shielding tensor
$\tau_{f-t}^{(EX)}$ exchange time between free water and trapped water
$\tau_{mh-tb}^{(EX)}$ exchange time between tightly bound water and main hydration shell
$\tau_{t-mh}^{(EX)}$ exchange time between main hydration shell and trapped water
τ_{HB} averaged hydrogen bond lifetime
$\tau_{f}^{(R)}$ rotational correlation time of free water
$\tau_{mh}^{(R)}$ rotational correlation time of main hydration shell
$\tau_{t}^{(R)}$ rotational correlation time of trapped water
$\tau_{tb}^{(R)}$ rotational correlation time of tightly bound water
$\xi_{\alpha\beta}$ frictional tensor

References

[1] A. Abragam, *The principles of nuclear magnetism*, Oxford University Press, London (1961).
[2] S.I. Aksyonov, E.A. Golovina, *studia biophysica*, **111**, 169 (1986).
[3] N. Albon, J.M. Sturtevant, *Proc. Natl. Acad. Sci. USA*, **75**, 2258 (1978).
[4] E. Almagor, G. Belfort, *J. Colloid Interface Sci.*, **66**, 146 (1978).
[5] O. Albrecht, N. Gruler, E. Sackmann, *Le Journal de Physique*, **39**, 301 (1978).
[6] J. Andersen, K.E. Zachariassen, G.M.O. Maloiy, J.M.Z. Kamau, *J. Trop. Ecol.*, **2**, 127 (1986).
[7] C.A. Angell, Supercooled water. In: *Water, a comprehensive treatise*, vol. 7: Water and aqueous solutions at subzero temperatures, Plenum Press, New York–London, pp. 1–81 (1982).
[8] C.A. Angell, E.J. Sare, *J. Chem. Phys.*, **52**, 1058 (1970).
[9] C.A. Angell, J.C. Shuppert, J.C. Tucker, *J. Phys. Chem.*, **77**, 3092 (1973).
[10] A.V. Anisimov, I.F. Ionenko, A.S. Evarestov, *studia biophysica*, **111**, 177 (1986).
[11] C.D. Araujo, A.L. MacKay, K.P. Whittal, J.R.T. Hailey, *J. Magn. Res.*, **B 101**, 248 (1993).
[12] P.A. Armond, O. Björkman, L.A. Staehlin, *Biochim. Biophys. Acta*, **601**, 433 (1978).
[13] L. Atanasiu, *Revue Roumaine de Biologie*, Series Botanica, **14**, 165 (1969).
[14] L. Atanasiu, *Revue Roumaine de Biologie*, Series Botanica, **16**, 105 (1971).
[15] M. Atoji, W.N. Lipscomb, *Acta Cryst.*, **7**, 173 (1954).
[16] Ö. Austrara, *Norsk. Ent. Tidsskr.*, **18**, 45 (1971).
[17] G. Bačič, S. Ratković, *Biophys. J.*, **45**, 767 (1984).
[18] M.R. Badger, G.D. Price, *Physiol. Plant*, **84**, 606 (1992).
[19] M.R. Badger, H. Pfanz, B. Büdel, U. Heber, O.L. Lange, *Planta*, **191**, 59 (1993).
[20] A.D. Bain, *J. Magn. Reson.*, **89**, 153 (1990).
[21] T.J. Baker, *Philos. Mag.*, **44**, 752 (1922).
[22] H.D. Barrs, *Water deficit and plant growth*, vol. 1, ed. by T.T. Kozlowski, Academic Press, London, New York, N.Y., p. 235 (1968).
[23] R.F. Bartholomew, J.W. Schreurs, *J. Non-Cryst. Solids*, **38/39**, 679 (1980).
[24] P.G. Barton, F.D. Gunstone, *J. Biol. Chem.*, **250**, 4470 (1975).
[25] J.G. Baust, *Cryobiology*, **20**, 357 (1981).
[26] J.G. Baust, R.E. Lee Jr., *Oikos*, **40**, 120 (1983).
[27] J.G. Baust, J.S. Edwards, R. Brown, *Antarctic J. United States*, **13**, 164 (1978).
[28] R.H. Beaumont, H. Chihara, J.A. Morrison, *J. Chem. Phys.*, **34**, 1456 (1961).
[29] G. Belfort, J. Scherig, D.O. Seevers, *J. Coll. Interface Sci.*, **47**, 106 (1974).
[30] J.D. Bell, R.W. Myatt, R.E. Richards, *Nature Phys. Sci.*, **230**, 91 (1971).

[31] J.B. Benedict, *Arctic and Alpine Research*, **22**, 81 (1990).
[32] J.B. Benedict, *Arctic and Alpine Research*, **23**, 189 (1991).
[33] W.S. Benedict, S.A. Clough, L. Frenkel, T.E. Sullivan, *J. Chem. Phys.*, **53**, 2565 (1970).
[34] W.S. Benedict, N. Gailar, E.K. Plyler, *J. Chem. Phys.*, **24**, 1139 (1956).
[35] J.E. Bertie, L.D. Calvert, E. Whalley, *J. Chem. Phys.*, **38**, 840 (1963).
[36] J.E. Bertie, L.D. Calvert, E. Whalley, *Can. J. Chem.*, **42**, 1373 (1964).
[37] A. Bertsch, *Planta (Berl.)*, **70**, 46 (1966).
[38] A. Bertsch, *Planta (Berl.)*, **68**, 157 (1966).
[39] P.R. Bevington, *Data Reduction and Error Analysis for the Physical Sciences*, McGraw-Hill Book Co., New York (1969).
[40] J.D. Bewley, M. Black, *Physiology and biochemistry of seeds in relation to germination*, Springer-Verlag, Berlin, Heidelberg (1978).
[41] D. Beysens, C.M. Knobler, *Phys. Rev. Lett.*, **57**, 1433 (1986).
[42] P. Bieble, *Amer. J. Bot.*, **51**, 697 (1964).
[43] E.K. Bigg, *Proc. Phys. Soc.*, **B66**, 688 (1953).
[44] E.K. Bigg, *Quart. L. Met. Soc.*, **79**, 510 (1953).
[45] D.G. Bishop, J.R. Kendrick, J.H. Bayston, A.S. MacPherson, S.R. Jones, *Biochim. Biophys. Acta*, **602**, 248 (1980).
[46] M. Blackman, N.D. Lisgarten, *Adv. Phys.*, **7**, 189 (1958).
[47] R.E. Blankenship, K. Sauer, *Biochim. Biophys. Acta*, **357**, 252 (1974).
[48] J.F. Blazyk, J.L. Newman, *Biochim. Biophys. Acta*, **600**, 1007 (1980).
[49] J.S. Blicharski, *Acta Phys. Polon.*, **24**, 817 (1963).
[50] J.S. Blicharski, *Phys. Letters*, **24A**, 608 (1967).
[51] J.S. Blicharski, *Acta Phys. Polon.*, **36**, 211 (1969).
[52] J.S. Blicharski, *Physica*, **39**, 161 (1968).
[53] J.S. Blicharski, *Acta Phys. Polon.*, **A38**, 19 (1970).
[54] J.S. Blicharski, H. Harańczyk, C. Jaeger, W. Jewko, K. Strzałka, *Acta Phys. Polon.*, **A62**, 151 (1982).
[55] J.S. Blicharski, H. Harańczyk, C. Jaeger, K. Strzałka, Phase transitions in photosynthetic membranes investigations using nuclear magnetic relaxation (in Polish). In: *Mat. XV Ogólnopol. Sem. MRJ, Kraków 1-2 grudzień 1982*, IFJ Raport No. 1206/PL, pp. 153–159 (1983).
[56] J.S. Blicharski, H. Harańczyk, K. Strzałka, *Polymer Bull.*, **5**, 285 (1981).
[57] J.S. Blicharski, W. Nosel, *Acta Phys. Polon.*, **A38**, 25 (1970).
[58] J.S. Blicharski, W. Nosel, *Acta Phys. Polon.*, **A42**, 223 (1972).
[59] J.S. Blicharski, W. Nosel, H. Schneider, *Ann. Phys.*, **27**, 17 (1971).
[60] J.S. Blicharski, H. Schneider, *Ann. Phys.* (Leipzig), **22**, 306 (1969).
[61] R. Blinc, J. Dolinsek, G. Lahajnar, A. Sepe, I. Zupancic, S. Zumer, F. Milia, M.M. Pintar, *Z. Naturforsch.*, **43a**, 1026 (1988).
[62] W. Block, *Science Progress*, **78**, 349 (1995).
[63] W. Block, *Eur. J. Entomol.*, **93**, 325 (1996).
[64] W. Block, G. Grubor-Lajsic, R. Worland, *Cryo-Letters*, **14**, 185 (1993).
[65] W. Block, P.M. Harrisson, *Glob. Chan. Biol.*, **1**, 347 (1995).
[66] W. Block, P.M. Harrisson, G. Vannier, *J. Insect Physiol.*, **36**, 181 (1990).
[67] W. Block, L. Hong-Chang, R. Worland, *Cryo-Letters*, **16**, 73 (1995).
[68] W. Block, L. Sømme, *Polar Biology*, **2**, 109 (1983).

[69] W. Block, L. Sømme, R. Ring, P. Ottesen, M.R. Worland, *British Antarctic Survey Bull.*, No 81, 65 (1988).
[70] G.C. Borgia, R.J.S. Brown, P. Fantazzini, *J. Magn. Reson.*, **132**, 65 (1998).
[71] E. Boroske, L. Trahms, *Biophys. J.*, **42**, 275 (1983).
[72] C.J.F. Böttcher, *Theory of Dielectric Polarization,* vol. II, Elsevier, Amsterdam (1973).
[73] W.H. Bragg, *Proc. Phys. Soc. London*, **34**, 98 (1922).
[74] P.W. Bridgman, *J. Chem. Phys.*, **3**, 597 (1935).
[75] P.W. Bridgman, *J. Chem. Phys.*, **5**, 964 (1937).
[76] R. Brill, *Angew. Chem. (Int. Edn.),* **1**, 563 (1962).
[77] C. Bronnimann, R. Zeigler, G. Maciel, *J. Am. Chem. Soc.*, **110**, 2023 (1988).
[78] V.L. Bronshteyn, P.L. Steponkus, *Bioph. J.*, **65**, 1853 (1993).
[79] E. Brosio, M. Delfini, A. di Nola, A. d'Ubaldo, C. Lintas, *Cell. Mol. Biol.*, **39**, 583 (1993).
[80] E. Brosio, A. Di Nola, M. Fracassi, E. Carnovale, E. Marconi, *Cell. Mol. Biol.*, **38**, 693 (1992).
[81] E. Brosio, A. Di Nola, B. Verzegnassi, *Cell. Mol. Biol.*, **39**, 193 (1993).
[82] E. Brosio, A. d'Ubaldo, E. Carnovale, A.M. Giusti, *Cell. Mol. Biol.*, **39**, 199 (1993).
[83] A.J. Brown, E. Whalley, *J. Chem. Phys.*, **45**, 4360 (1966).
[84] R.J.S. Brown, *J. Magn. Reson.*, **82**, 539 (1989).
[85] J.L. Browning, J. Seelig, *Biochemistry*, **19**, 1262 (1979).
[86] K.R. Brownstein, *J. Magn. Reson.*, **40**, 505 (1980).
[87] K.R. Brownstein, C.E. Tarr, *Phys. Rev.*, **A19**, 2446 (1979).
[88] T. Brumm, A. Möps, C. Dolainsky, S. Brückner, T. Bayerl, *Biophys. J.*, **61**, 1018 (1992).
[89] S. Brunauer, P.H. Emmett, E. Teller, *J. Am. Chem. Soc.*, **60**, 309 (1938).
[90] F. Bruni, G. Careri, J.S. Clegg, *Bioph. J.*, **55**, 331 (1989).
[91] F. Bruni, G. Careri, A.C. Leopold, *Phys. Rev.*, A**40**, 2803 (1989).
[92] S.G. Bruun, A. Hvidt, *Ber. Bunsenges. Phys. Chem.*, **81**, 930 (1977).
[93] M.J. Burke, L.V. Gusta, H.A. Quamme, C.J. Weiser, P.H. Li, *Ann. Rev. Plant Physiol.*, **27**, 507 (1976).
[94] A.J. Burn, *Com. Natn. Fr. Rech. Antarct.*, **51**, 209 (1981).
[95] E.E. Burnell, P.R. Cullis, B. de Kruijff, *Biochim. Biophys. Acta*, **603**, 63 (1980).
[96] G. Büldt, H.U. Gally, J. Seelig, G. Zaccai, *J. Mol. Biol.*, **134**, 673 (1979).
[97] G. Büldt, H.U. Gally, A. Seelig, J. Seelig, G. Zaccai, *Nature*, **271**, 182 (1978).
[98] E.F. Burton, W.F. Oliver, *Proc. Roy. Soc. (London),* **A153**, 166 (1935).
[99] D.A. Cadenhead, M.C. Phillips, *J. Coll. Interf. Sci.*, **24**, 491 (1967).
[100] P.T. Callaghan, K.W. Jolley, J. Lelievre, *Biophys. J.*, **28**, 133 (1979).
[101] C.G. Cannon, *Spectrochim. Acta*, **10**, 341 (1958).
[102] R.J. Cannon, *Br. Antarct. Surv. Bull.*, **71**, 19 (1986).
[103] R.J. Cannon, W. Block, G.D. Collett, *Cryo-Letters*, **6**, 73 (1985).
[104] G. Careri, M. Geraci, A. Giansanti, J.A. Rupley, *Proc. Natl. Acad. Sci. USA*, **82**, 5342 (1985).
[105] G. Careri, A. Giansanti, *Lettere al. Nuovo Cimento*, **40**, 193 (1984).
[106] G. Careri, A. Giansanti, J.A. Rupley, *Proc. Natl. Acad. Sci. USA*, **83**, 6810 (1986).
[107] G. Careri, A. Giansanti, J.A. Rupley, *Phys. Rev.*, **A 37**, 2703 (1988).
[108] H.Y. Carr, E.M. Purcell, *Phys. Rev.*, **94**, 630 (1954).

[109] R.S. Chahall, R.D. Miller, *Brit. J. Appl. Phys.*, **16**, 231 (1965).
[110] B.E. Chapman, D.J. Roser, R.D. Seppelt, *Antarctic Science*, **6**, 295 (1994).
[111] D. Chapman, R.M. Wiliams, B.D. Ladbrooke, *Chem. Phys. Lipids*, **1**, 445 (1967).
[112] J. Chappuis, In: *Multiphase Science and Technology*, eds. G.F. Hewitt, J. Delhaye, N. Zuber (Hemisphere, New York), p. 387 (1984).
[113] S.C. Chen, J.M. Sturtevant, B. Gaffney, *Proc. Natl. Acad. Sci. USA*, **77**, 5060 (1980).
[114] S.-H. Chen, J. Teixeira, *Adv. Chem. Phys.*, **64**, 1 (1985).
[115] G.M. Cheniae, I.F. Martin, *Biochem. Biophys. Res. Comm.*, **28**, 89 (1967).
[116] T.F. Child, N.G. Pryce, M.J. Tait, S. Ablett, *Chem. Commun.*, **1970**, 1214 (1970).
[117] C. Choi, H. Harańczyk, K.G. Soga, R.J. Rumm, M.M. Pintar, *J. Appl. Phys.*, **80**, 5861 (1996).
[118] D. Clausse, J.P. Dumas, F. Broto, *C. R. Acad. Sci. Paris*, **279B**, 415 (1974).
[119] W.F. Claussen, *J. Chem. Phys.*, **19**, 259 (1951).
[120] W.F. Claussen, *J. Chem. Phys.*, **19**, 662 (1951).
[121] W.F. Claussen, *J. Chem. Phys.*, **19**, 1425 (1951).
[122] N.J. Clayden, B.D. Hesler, *J. Magn. Reson.*, **98**, 271 (1992).
[123] M.H. Cohen, K.H. Mendelson, *J. Appl. Phys.*, **53**, 1127 (1982).
[124] A.W. Coleman, The role of resting spores and akinetes in chlorophyte survival. In: *Survival strategies of the algae*, ed. G.A. Fryxell, Cambridge University Press, Cambridge, pp. 1–21 (1983).
[125] J.R. Coleman, Plant, *Cell & Env.*, **14**, 861 (1991).
[126] C.H. Collie, J.B. Hasted, D.M. Riston, *Proc. phys. Soc.*, **60**, 145 (1948).
[127] M.L. Connolly, *J. Appl. Crystallogr.*, **16**, 548 (1983).
[128] C.A. Coulson, *Research (London)*, **10**, 149 (1957).
[129] C.A. Coulson, *Valence*, Oxford University Press (1961).
[130] C.A. Coulson, V. Danielsson, *Ark. Fys.*, **8**, 239 (1954).
[131] I.R. Cowan, O.L. Lange, T.G.A. Green, *Planta*, **187**, 282 (1992).
[132] R.P. Cox, D.S. Bendall, *Biochim. Biophys. Acta*, **347**, 49 (1974).
[133] W.A. Cramer, J. Whittmarsh, P.S. Low, *Biochemistry*, **20**, 157 (1981).
[134] P.R. Cullis, *FEBS Lett.*, **70**, 223 (1976).
[135] P.R. Cullis, Ch. Grathwohl, *Biochim. Biophys. Acta*, **471**, 213 (1977).
[136] P.R. Cullis, M.J. Hope, *Nature*, **271**, 672 (1978).
[137] B.M. Cwilong, *Proc. Roy. Soc. (London)*, **A190**, 137 (1947).
[138] T. Cybulko, *Kom. Nauk Roln. Poznań, Tow. Przyj. Nauk*, **46**, 7 (1978).
[139] B. Czeczuga, Carotenoids. In: *CRC Handbook of Lichenology*, vol. 1, ed. M. Galun, Boca Raton, CRC Press Inc., Florida, p. 25–34 (1988).
[140] J.F. Danielli, H. Davson, *J. Cell. Compar. Physiol.*, **5**, 495 (1935).
[141] R.B. Darling, E.I. Friedmann, P.A. Broady, *J. Phycol.*, **23**, 598 (1987).
[142] D.W. Davidson, Clathrate hydrates. In: *Water a comprehensive treatise, vol. 2: Water in crystalline hydrates, Aqueous solutions of simple nonelectrolytes*, ed. F. Franks, Plenum Press, New York–London, pp. 115–234 (1973).
[143] J.H. Davis, *Biophys. J.*, **27**, 339 (1979).
[144] J.H. Davis, C.P. Nichol, G. Weeks, M. Bloom, *Biochemistry*, **18**, 2103 (1979).
[145] S.S. Davis, T. Higuchi, J.H. Rytting, *J. Pharm. Pharmac.*, **24**, Suppl. 30P (1972).
[146] S.S. Davis, T. Higuchi, J.H. Rytting, *Adv. in Pharmaceutical Sci.*, **4**, 73 (1974).
[147] P. Debye, *Ann. N.Y. Acad. Sci.*, **51**, 575 (1949).
[148] L.C. de Coppet, *Ann. Chim. et Phys.*, **6**, 275 (1875).

[149] C. De Dominicis, H. Orland, F. Lainee, *J. Physique Lett.*, **46**, L463 (1985).
[150] P.-G. de Gennes, *Reviews of Modern Physics*, **57**, 827 (1985).
[151] B. de Kruijff, R.A. Demel, L.L.M. van Deenen, *Biochim. Biophys. Acta*, **255**, 331 (1972).
[152] B. de Kruijff, A.M.H.P. van den Besselaar, P.R. Cullis, H. van den Bosch, L.L.M. van Deenen, *Biochim. Biophys. Acta*, **514**, 1 (1976).
[153] B. de Kruijff, A.J. Verkleij, C.J.A. van Echteld, W.J. Gerritsen, C. Mombers, P.C. Noordam, J. de Gier, *Biochim. Biophys. Acta*, **555**, 200 (1979).
[154] J. Del Bene, J.A. Pople, *Chem. Phys. Letters*, **4**, 426 (1969).
[155] R. Del-Prado, L.G. Sancho, *Flora*, **195**, 51 (2000).
[156] R.A. Demel, B. de Kruijff, *Biochim. Biophys. Acta*, **457**, 109 (1976).
[157] R.A. Demel, W.S.M. Geuris van Kessel, R.F.A. Zwaal, B. Roelofsen, L.L.M. van Deenen, *Biochim. Biophys. Acta*, **406**, 97 (1975).
[158] R.W. Dent, *Textile Res. J.*, **47**, 145 (1977).
[159] W. Derbyshire, The dynamics of water in heterogeneous systems with emphasis on subzero temperatures. In: *Water, a comprehensive treatise, vol. 7: Water and aqueous solutions at subzero temperatures*, Plenum Press, New York, pp. 339–430 (1982).
[160] M. de Rosa, A. Gambacorta, A. Gliozzi, *Microbiol. Rev.*, **50**, 70 (1986).
[161] C. Despretz, *Ann. de Chemie et de Phys.*, **70**, 23 (1837).
[162] C. Despretz, *C.R. Acad. Sci. Paris*, **4**, 124 (1837).
[163] R. Dettre, R. Johnson. In: *Contact angle, wettability and adhesion*, ed. F.M. Fowkes, Advances in Chemistry Series, No. 143 (American Chemical Society, Washington, D.C.), p. 136 (1964).
[164] P. Devaux, H.M. McConnell, *J. Am. Chem. Soc.*, **94**, 4475 (1972).
[165] A.L. DeVries, *A. Rev. Physiol.*, **45**, 245 (1983).
[166] A. Di Nola, E. Carnovale, A. D'Ubaldo, M. Fracassi, E. Marconi, E. Brosio, NMR studies of seed hydration. In: *Recent Advances in cellular and molecular biology*, eds. R.J. Wegmann & M.A. Wegmann, Peeters Press, Leuven, Belgium, pp. 257–264 (1992).
[167] A. Di Nola, A. D'Ubaldo, M. Fracassi, E. Brosio, *Cell. Mol. Biol.*, **37**, 9 (1991).
[168] A.J. Dobbs, *Electron Spin Resonance Spec. Period. Rep.*, **2**, 281 (1974).
[169] F. D'Orazio, S. Bhattacharja, W. Halperin, K. Eguchi, T. Mizusaki, *Phys. Rev.*, **B42**, 9810 (1990).
[170] F. D'Orazio, J.C. Tarczon, W.P. Halperin, K. Eguchi, T. Mizusaki, *J. Appl. Phys.*, **65**, 742 (1989).
[171] L.G. Dowell, A.P. Rinfert, *Nature, Lond.*, **188**, 1144 (1960).
[172] W. Drost-Hansen, The occurrence and extent of vicinal water. In: *Biophysics of water*, eds. F. Franks & S. Mathias, Wiley, New York, pp. 163–169 (1982).
[173] J.G. Dudman, *J. Insects Physiol.*, **30**, 235 (1984).
[174] J.G. Duman, *J. Exp. Zool.*, **201**, 85 (1977).
[175] J.G. Duman, *J. Insect. Physiol.*, **30**, 235 (1984).
[176] J.G. Duman, J.P. Morris, F.J. Castellino, *J. Comp. Physiol.*, **B154**, 79 (1984).
[177] J.G. Duman, D.W. Wu, L. Xu, D. Tursman, T.M. Olsen, *Q. Rev. Biol.*, **66**, 387 (1991).
[178] T.R. Dyke, K.M. Mack, J.S. Muenter, *J. Chem. Phys.*, **66**, 498 (1977).
[179] K. Dyrek, Z. Sojka, W. Zabiński, *Mineral. Polon.*, **26**, 9 (1995).
[180] H. Eckert, J.P. Yesinowski, L.A. Silver, E.M. Stolper, *J. Phys. Chem.*, **92**, 2055 (1988).

[181] J. Eden, P.R. Gascoyne, R. Pethig, *J. Chem. Soc. Faraday Trans. I*, **76**, 426 (1980).
[182] O. Edholm, *Chem. Phys. Lipids*, **29**, 213 (1981).
[183] M. Eigen, *Angew. Chem. (Int. Edn.)*, **3**, 1 (1964).
[184] M. Eigen, L. De Maeyer, *Proc. R. Soc.*, **A 247**, 505 (1958).
[185] M. Eigen, L. De Maeyer, H.Ch. Spatz, *Ber. Bunsenges.*, **68**, 19 (1964).
[186] G. Eisenbeis, Kinetics of transpiration in soil arthropods. In: *New trends in soil biology*, eds. P. Lebrun, H.M. André, A. De Medts, C. Grégorie-Wibo, G. Wauthy, Dieu-Brichart, Louvain-la-Neuve, pp. 626–627 (1983).
[187] D. Eisenberg, W. Kauzmann, *The structure and properties of water*, Clarendon Press, Oxford (1969).
[188] J. Elster, J. Svobody, J. Komarek, P. Marvan, *Arch. Hydrobiol. Suppl.*, **119**, 57 (1997).
[189] M.F. Emerson, A. Holtzer, *J. Phys. Chem.*, **71**, 1898 (1967).
[190] S.C. Erfurth, P.J. Bond, W.I. Peticolas, *Biopolymers*, **14**, 1245 (1975).
[191] R.R. Ernst, G. Bodenhausen, A. Wokaun, *Principles of nuclear magnetic resonance in one and two dimensions*, Clarendon Press, Oxford (1987).
[192] W. Eschrich, Sealing systems in Phloem. In: *Encyclopedia of Plant Physiology, vol. 1*, eds. M.H. Zimmermann & J.A. Milburn, Springer-Verlag, Berlin–Heidelberg–New York, pp. 39–56 (1975).
[193] F.M. Etzler, W. Drost-Hansen, A role for water in biological rate processes. In: *Cell associated water*, eds. W. Drost-Hansen & J.S. Clegg, Academic Press, London, pp. 125–164 (1979).
[194] M. Falk, *Can. J. Chem.*, **44**, 1107 (1966).
[195] M. Falk, K.A. Hartmann Jr., R.C. Lord, *J. Am. Chem. Soc.*, **84**, 3843 (1962).
[196] M. Falk, K.A. Hartmann Jr., R.C. Lord, *J. Am. Chem. Soc.*, **85**, 387 (1963).
[197] M. Falk, K.A. Hartmann Jr., R.C. Lord, *J. Am. Chem. Soc.*, **85**, 391 (1963).
[198] M. Falk, A.G. Poole, C.G. Goymour, *Can. J. Chem.*, **48**, 1536 (1970).
[199] I. Farnan, S.C. Kohn, R. Dupree, *Geochim. Cosmochim. Acta*, **51**, 2869 (1987).
[200] F. Farron, *Biochemistry*, **9**, 3823 (1970).
[201] F. Farron, E. Racker, *Biochemistry*, **9**, 3829 (1970).
[202] D. Fengel, G. Wegener, *Wood – chemistry, ultrastructure, reactions*, W. de Gruyter, Berlin, pp. 240–267 (1984).
[203] E.J. Findlay, P.G. Barton, *Biochemistry*, **17**, 2400 (1978).
[204] E.G. Finer, D. Darke, *Chem. Phys. Lipids*, **12**, 1 (1974).
[205] N.H. Fletcher, *Phil. Mag.*, **7**, 255 (1962).
[206] N.H. Fletcher, *Phil. Mag.*, **18**, 1287 (1968).
[207] D.C. Fork, G. van Ginkel, G. Harvey, *Plant & Cell Physiol.*, **22**, 1035 (1981).
[208] H.S. Frank, M.W. Evans, *J. Chem. Phys.*, **13**, 507 (1945).
[209] R.E. Franklin, R.G. Gosling, *Acta crystallogr.*, **6**, 673 (1953).
[210] R.E. Franklin, R.G. Gosling, *Acta crystallogr.*, **6**, 678 (1953).
[211] F. Franks, Introduction – Water, the unique chemical. In: *Water, a comprehensive treatise, vol. 1: The physics and physical chemistry of water*, Plenum Press, New York–London, pp. 1–20 (1972).
[212] F. Franks, The properties of ice. In: *Water, a comprehensive treatise, vol. 1: The physics and physical chemistry of water*, Plenum Press, New York–London, pp. 115–149 (1972).
[213] F. Franks, H.T. Smith, *Trans. Faraday Soc.*, **64**, 2962 (1968).
[214] F. Franks, *Cryo-Letters*, **7**, 207 (1986).

[215] G. Friedel, *Ann. Phys.*, **18**, 273 (1922).
[216] M.E. Friedman, H.A. Scheraga, *J. Phys. Chem.*, **69**, 3795 (1965).
[217] L.D. Frye, M. Edidin, *J. Cell. Sci.*, **7**, 319 (1970).
[218] K. Fukuda, T. Kasuga, T. Mizusaki, *J. Phys. Soc. Japan*, **58**, 1662 (1989).
[219] E. Fukushima, S.B.W. Roeder, *Experimental Pulse NMR*, Addison-Wesley Publ. Co. Inc., Reading, MA (1981).
[220] M.E. Fuller, W.B. Brey, *J. Biol. Chem.*, **243**, 274 (1968).
[221] N. Funduk, D.W. Kydon, L.J. Schreiner, H. Peemoeller, L. Miljković, M.M. Pintar, *Magn. Res. in Medicine*, **1**, 66 (1984).
[222] N. Funduk, G. Lahajnar, L. Miljković, S. Skočajić, D.W. Kydon, L.J. Schreiner, M.M. Pintar, *Zobozdrav. Vestn.*, **41** (Suppl. 1), 139 (1986).
[223] K. Furuya, T. Mitsui, *J. Phys. Soc. Japan*, **46**, 611 (1979).
[224] D.F. Gaff, *Oecologia (Berl.)*, **31**, 95 (1977).
[225] K. Gawrisch, K. Arnold, T. Gottwald, G. Klose, F. Volke, *studia biophysica*, **74**, 13 (1978).
[226] K. Gawrisch, K. Arnold, H.-J. Rüger, P. Kertschner, P. Nuhn, *Chem. Phys. Lipids*, **20**, 285 (1977).
[227] C. Gebhardt, H. Gruler, E. Sackmann, *Z. Naturforsch.*, **32c**, 581 (1977).
[228] U. Gehrken, *J. Insect Physiol.*, **30**, 421 (1984).
[229] U. Gehrken, *J. Insect Physiol.*, **31**, 909 (1985).
[230] U. Gehrken, L. Sømme, *Comp. Biochem. Physiol.*, A **109**, 913 (1994).
[231] A. Geiger, A. Rahman, F.H. Stillinger, *J. Chem. Phys.*, **70**, 263 (1979).
[232] A. Geiger, F.H. Stillinger, A. Rahman, *J. Chem. Phys.*, **70**, 4185 (1979).
[233] N.L. Gershfeld, *J. Coll. Interf. Sci.*, **32**, 167 (1970).
[234] N.L. Gershfeld, R.E. Pagano, *J. Phys. Chem.*, **76**, 1231 (1972).
[235] J.A. Ghormley, *J. Chem. Phys.*, **25**, 599 (1956).
[236] J.A. Ghormley, *J. Am. Chem. Soc.*, **79**, 1862 (1957).
[237] W.F. Giauque, M. Ashley, *Phys. Rev.*, **43**, 81, (1933).
[238] W.F. Giauque, J.W. Stout, *J. Am. Chem. Soc.*, **58**, 1144 (1936).
[239] S.J. Gill, N.F. Nichols, I. Wadsö, *J. Chem. Thermodynamics*, **8**, 445 (1976).
[240] K.T. Gillen, D.C. Douglass, M.J.R. Hoch, *J. Chem. Phys.*, **57**, 5117 (1972).
[241] J.A. Glasel, *J. Am. Chem. Soc.*, **92**, 375 (1970).
[242] J.A. Glasel, K.H. Lee, *J. Am. Chem. Soc.*, **96**, 970 (1974).
[243] C.L. Glaves, P.J. Davis, D.M. Smith, *Powder Technol.*, **54**, 261 (1988).
[244] A. Goel, A.S.N. Murthy, C.N.R. Rao, *Indian J. Chem.*, **9**, 56 (1971).
[245] A. Goel, A.S.N. Murthy, C.N.R. Rao, *J. Chem. Soc. (London)*, **A1971**, 190 (1971).
[246] N.R. Gokhale, *J. Geophys. Res.*, **71**, 3351 (1966).
[247] E.A. Golovina, A.N. Tikhonov, *Biochem. Biophys. Acta*, **1190**, 385 (1994).
[248] D.S. Goodman, *J. Am. Chem. Soc.*, **80**, 3887 (1958).
[249] M.S. Gopinathan, M. Vijayakumar, N. Viaidehi, *Phys. Rev.*, **A40**, 6834 (1989).
[250] E. Gorter, F. Grendel, *J. Exp. Med.*, **41**, 439 (1925).
[251] K. Gounaris, A.P.R. Brain, P.J. Quinn, W.P. Williams, *FEBS Lett.*, **153**, 47 (1983).
[252] K. Gounaris, D.A. Mannock, A. Sen, A.P.R. Brain, W.P. Williams, P.J. Quinn, *Biochim. Biophys. Acta*, **732**, 229 (1983).
[253] K. Gounaris, A. Sen, A.P.R. Brain, P.J. Quinn, W.P. Williams, *Biochim. Biophys. Acta*, **728**, 129 (1983).
[254] Govindjee, *Nat. Acad. Sci. Letters*, **1**, 3 (1978).

[255] Govindjee, *Plant Bioch. J.*, S.M. Sircar Memorial Volume, 7 (1980).
[256] D. Graham, B.D. Patterson, *Ann. Rev. Plant Physiol.*, **33**, 347 (1982).
[257] H. Gränicher, C. Jaccard, P. Scherrer, A. Steinemann, *Discuss. Faraday Soc.*, **23**, 50 (1957).
[258] T.G.A. Green, O.L. Lange, I.R. Cowan, *Crypt. Bot.*, **4**, 166 (1994).
[259] W. Gründer, R. Göldner, H. Schneider, *Z. phys. Chemie*, **258**, 280 (1977).
[260] G. Gubelin, A. Boyd, *J. Petroleum Technol.*, **49**, 718 (1997).
[261] A. Gulik, V. Luzzati, *J. Mol. Biol.*, **182**, 131 (1985).
[262] N.F. Hadley, *Water relations of terrestial arthropods*, Academic Press, London (1994).
[263] A.J. Hailwood, S. Horrobin, *Trans. Faraday Soc.*, **42B**, 86 (1946).
[264] W.P. Halperin, F. D'Orazio, S. Bhattacharja, J.C. Tarczon, In: *Molecular Dynamics in Restricted Geometries*, eds. J. Klafter & J.M. Drake, New York: John Wiley & Sons, p. 311 (1989).
[265] N. Hamada, K. Okazaki, M. Shinozaki, *Bryologist*, **97**, 176 (1994).
[266] R.J. Hancock, R.D. Seppelt, *Polarforschung*, **58**, 171 (1988).
[267] D. Hankins, J.W. Moskowitz, F.H. Stillinger, *Chem. Phys. Lett.*, **4**, 527 (1970).
[268] S. Hanlon, B. Wolf, *Biochemistry*, **14**, 1661 (1975).
[269] T. Hansen, *Eesti NSV Tead. Akad. Toim. Biol.*, **22**, 105 (1973).
[270] F. Hanus, P. Gillis, *J. Magn. Reson.*, **59**, 437 (1984).
[271] H. Harańczyk, Water binding kinetics and sorption analysis in Antarctic and Cosmopolitan lichen thallus, submitted for publication (2003).
[272] H. Harańczyk, S. Gaździński, M.A. Olech, *New Phytologist*, **138**, 191 (1998).
[273] H. Harańczyk, S. Gaździński, M. Olech, Freezing protection mechanism in *Cladonia mitis* as observed by proton magnetic relaxation. In: *New Aspects in Cryptogamic Research, Contribution in Honour of Ludger Kappen. Bibl. Lichenol.*, vol. 75, pp. 265-274 (2000).
[274] H. Harańczyk, S. Gaździński, M. Olech, *Mol. Phys. Reps.*, **29**, 135 (2000).
[275] H. Harańczyk, H. Głąb, T. Róg, Human dentine degradation as observed by nuclear magnetic relaxation (in Polish). In: *Mat. XXVII Ogólnopol. Sem. MRJ, Kraków 1-2 grudnia 1994*, IFJ Raport Nr 1695/PL, pp. 425–428 (1995).
[276] H. Harańczyk, J. Grandjean, M. Olech, *Mol. Phys. Reps.*, **33**, 220 (2001).
[277] H. Harańczyk, J. Grandjean, M. Olech, Freezing of water bound in lichen thallus as observed by ^{1}H NMR. I. Freezing of loosely bound water in *Cladonia mitis* at different hydration levels, *Coll. Surf. B: Biointerfaces*, **28**/4, in press (2003).
[278] H. Harańczyk, J. Grandjean, M. Olech, M. Michalik, Freezing of water bound in lichen thallus as observed by ^{1}H NMR. II. Freezing protection mechanisms in a Cosmopolitan lichen *Cladonia mitis* and in Antarctic lichen species at different hydration levels, *Coll. Surf. B: Biointerfaces*, **28**/4, in press (2003).
[279] H. Harańczyk, G. Jasiński, K. Strzałka, Bound water freezing in wheat (*Triticum aestivum* L.) seed as observed using proton magnetic relaxation (in Polish). In: *Mat. XXVI Ogólnopol. Sem. MRJ, Kraków 1-2 grudnia 1993*, IFJ Raport Nr 1658/PL, pp. 151–156 (1994).
[280] H. Harańczyk, J. Kozub, A. Falniowski, Water bound in shells of *Unio pictorum* and *Anodonta cygnea* investigations using proton magnetic relaxation (in Polish). In: *Mat XXVIII Ogólnopol. Sem. MRJ, Kraków 1995*, Raport IFJ Nr 1717/PL, pp. 21–24 (1996).

[281] H. Harańczyk, J. Nizioł, A. Falniowski, The proton NMR investigations of water bound in shell of mussel (*Mytilius edulis*) (in Polish). In: *Mat. XXVI Ogólnopol. Sem. MRJ, Kraków 1-2 grudnia 1993*, IFJ Raport Nr 1658/PL, pp. 179–185 (1993).
[282] H. Harańczyk, M. Wnęk, M. Olech, J. Mościcki, Percolation threshold and molecular clustering point of water bound in *Cladonia mitis* and *Himantormia lugubris*, submitted for publication (2003).
[283] H. Harańczyk, K.G. Soga, R.J. Rumm, M.M. Pintar, *Mag. Res. Imag.*, **9**, 723, (1991).
[284] H. Harańczyk, K. Strzałka, *Zeszyty Naukowe UJ, Prace z Biol. Molek.*, **15**, 57 (1987).
[285] H. Harańczyk, K. Strzałka, T. Bayerl, G. Klose, J.S. Blicharski, Badania magnetycznego rezonansu jądrowego dla ^{31}P w błonach fotosyntetycznych chloroplastów. In: *Mat. XVI Ogólnopol. Sem. MRJ, Kraków 1-2 grudzień 1983*, Report IFJ No. 1237/PL, pp. 43–47 (1984).
[286] H. Harańczyk, K. Strzałka, T. Bayerl, G. Klose, J.S. Blicharski, *Photosynthetica*, **19**, 414 (1985).
[287] H. Harańczyk, K. Strzałka, W. Dietrich, J.S. Blicharski, *J. Biol. Phys.*, **21**, 125 (1995).
[288] H. Harańczyk, K. Strzałka, C. Jaeger, J.S. Blicharski, *Acta Phys. Polon.*, **A70**, 645 (1986).
[289] H. Harańczyk, K. Strzałka, G. Jasiński, K. Mosna-Bojarska, *Coll. Surf.*, **A115**, 47 (1996).
[290] H. Harańczyk, W.P. Węglarz, S. Sojka, *Holzforschung*, **53**, 299 (1999).
[291] H. Harańczyk, A. Wójcik, *Mol. Phys. Reps.*, **29**, 139 (2000).
[292] H. Harańczyk, A. Wójcik, *Acta Phys. Polon.*, **A 98**, 153 (2000).
[293] M.J. Harris, T. Higuchi, J.H. Rytting, *J. Phys. Chem.*, **77**, 2694 (1973).
[294] P.M. Harrisson, W. Block, M.R. Worland, *Rev. Ecol. Biol. Sol.*, **27**, 435 (1990).
[295] I.D. Hartley, S. Avramidis, *Holzforschung*, **47**, 163 (1993).
[296] I.D. Hartley, F.A. Kamke, H. Peemoeller, *Holzforschung*, **48**, 474 (1994).
[297] D.L. Hawksworth, Lichen components. IIa The fungal partner. In: *CRC Handbook of lichnology,* vol. 1, ed. M. Galun, CRC Press Inc., Boca Raton, Florida, pp. 35–38, *taken from:* D.L. Hawksworth, B.C. Sutton, G.C. Ainsworth, Ainsworth and Bisby's Dictionary of the Fungi, 7th ed., Commonwealth Mycological Institute, Kew, England, 1983 (1988).
[298] D.A. Haydon, F.H. Taylor, *Phil. Trans. Roy. Soc.*, **A252**, 225 (1960).
[299] D.A. Haydon, F.H. Taylor, *Trans. Faraday Soc.*, **58**, 1233 (1962).
[300] J.E. Hearst, *Biopolymers*, **3**, 57 (1965).
[301] R.B. Hermann, *J. Phys. Chem.*, **76**, 2754 (1972).
[302] D.W. Hilchie, *J. Petroleum Technology*, **40**, 273 (1988).
[303] B.P. Hills, S.L. Duce, *Magn. Res. Imaging*, **8**, 321 (1990).
[304] J.C. Hindmann, *J. Chem. Phys.*, **44**, 4582 (1966).
[305] J.C. Hindman, A. Svirmickas, *J. Phys. Chem.*, **77**, 2487 (1973).
[306] H.E. Hinton, *Proc. Zool. Soc. Lond.*, **121**, 371 (1951).
[307] H.E. Hinton, *J. Insect Physiol.*, **5**, 286 (1960).
[308] H.E. Hinton, *Nature*, **188**, 336 (1960).
[309] H.E. Hinton, *J. Insect Physiol.*, **5**, 286 (1960).
[310] H.E. Hinton, *Proc. Roy. Soc.*, B **171**, 43 (1968).
[311] H. Hinz, J.M. Sturtevant, *J. Biol. Chem.*, **247**, 6071 (1972).
[312] K. Hiraki, T. Hamanaka, T. Mitsui, Y. Kito, *Biochim. Biophys. Acta*, **647**, 18 (1981).

[313] M.M. Hoffmann, M.S. Conradi, *J. Am. Chem. Soc.*, **119**, 3811 (1997).
[314] R.W. Hoham, *Phycologia*, **14**, 213 (1975).
[315] Hon Nyok-Sai, *J. Polym. Sci.*, **13**, 1933 (1975).
[316] Hon Nyok-Sai, *J. Polym. Sci.*, **14**, 2497 (1976).
[317] R. Honegger, *Ann. Rev. Plant. Physiol.*, **42**, 553 (1991).
[318] G. Honjo, K. Shimaoka, *Acta crystallogr.*, **10**, 710 (1957).
[319] K.L. Horwath, J.G. Duman, *Physiol. Zool.*, **57**, 40 (1984).
[320] J. Hovenden, R.D. Seppelt, *Symbiosis*, **18**, 111 (1995).
[321] J.R. Hoyland, L.B. Kier, *Theor. Chim. Acta*, **15**, 1 (1969).
[322] E. Hsi, R. Hossfeld, R.G. Bryant, *J. Colloid Interface Sci.*, **62**, 389 (1977).
[323] J. Hu, X.-D. Xiao, D.F. Ogletree, M. Salmeron, *Science*, **268**, 267 (1995).
[324] P.S. Hubbard, *Rev. Mod. Phys.*, **33**, 249 (1961).
[325] A.H.L. Huiskes, N.J.M. Gremmen, J.W. Francke, *Circumpolar J.*, **1–2**, 77 (1996).
[326] A.H.L. Huiskes, N.J.M. Gremmen, J.W. Francke, *Antarctic Science*, **9**, 36 (1997).
[327] A. Hvidt, R. Moss, G. Nielsen, *Acta Chem. Scand.*, **B32**, 274 (1978).
[328] M. Ikeya, *New Applications of Electron Spin Resonance*, World Scientific, Singapore, p. 343 (1993).
[329] R.K. Iler, *The Chemistry of Silica*. John Wiley & Sons, New York–Chichester–Brisbane–Toronto (1979).
[330] Y. Inoko, T. Mitsui, *J. Phys. Soc. Japan*, **44**, 1918 (1978).
[331] H. Inoué, *Plant Cell Physiol.*, **19**, 355 (1978).
[332] T. Ioriya, *J. Tokyo Univ. Fish.*, **73**, 1 (1986).
[333] J.N. Israelachvili, D.J. Mitchell, B.W. Ninham, *J. Chem. Soc. Faraday*, II **72**, 1525 (1976).
[334] S. Itoh, *Plant Cell Physiol.*, **18**, 801 (1977).
[335] M.B. Jackson, J.M. Sturtevant, *Biochemistry*, **17**, 911 (1978).
[336] N. Jan, *Physica*, **A 266**, 72 (1999).
[337] H.H. Jellinek, *J. Colloid Interface Sci.*, **25**, 192 (1967).
[338] C.F. Jenner, Y. Xia, C.D. Eccles, P.T. Callaghan, *Nature*, **336**, 399 (1988).
[339] M. Jensen, U. Heber, W. Oettmeier, *Cryobiology*, **18**, 322 (1981).
[340] J.A. Jones, *J. Magn. Reson.*, **126**, 283 (1997).
[341] J.A. Jones, P. Hodgkinson, A.L. Barker, P.J. Hore, *J. Magn. Reson.*, **B 113**, 25 (1996).
[342] J.R. Jones, D.L.G. Rowlands, C.B. Monk, *Trans. Faraday Soc.*, **61**, 1384 (1965).
[343] P. Jursinic, Govindjee, *Photochem. Photobiol.*, **26**, 617 (1977).
[344] W. Kaemtz, *Traite de Meterologie*, **1**, 290 (1820).
[345] A.G. Kalinichev, J.D. Bass, *J. Chem. Phys.*, **101**, 9720 (1997).
[346] P. Kallio, S. Heinonen, *Reports on Kevo Subarctic Research Station*, **8**, 63 (1971).
[347] U. Kamat, R. Garg, C.B. Sharma, *Arch. Biochem. Biophys.*, **298**, 731 (1992).
[348] B. Kamb, *Acta crystallogr.*, **17**, 1437 (1964).
[349] B. Kamb, *Science*, **150**, 205 (1965).
[350] B. Kamb, *J. Chem. Phys.*, **43**, 3917 (1965).
[351] B. Kamb, S.K. Datta, *Nature, Lond.*, **187**, 140 (1960).
[352] B. Kamb, B.L. Davis, *Proc. Natl. Acad. Sci. USA*, **52**, 1433 (1964).
[353] B. Kamb, A. Prakash, C. Knobler, *Acta crystallogr.*, **22**, 706 (1967).
[354] H. Kanno, C.A. Angell, *J. Chem. Phys.*, **73**, 1940 (1980).
[355] H. Kanno, R.J. Speedy, C.A. Angell, *Science*, **189**, 880 (1975).

[356] A. Kaplan, R. Schwarz, J. Lieman-Hurwitz, I. Reinhold, *Plant Physiol.*, **97**, 851 (1991).
[357] L. Kappen, *Polar Biol.*, **1**, 249 (1983).
[358] L. Kappen, *Polarforschung*, **55**(1), 49 (1985a).
[359] L. Kappen, Water relations and net photosynthesis of *Usnea*. A comparison between *Usnea fasciata* (Maritime Antarctic) and *Usnea sulphurea* (Continental Antarctic). In: *Lichen Physiology and Cell Biology*, ed. D.H. Brown, Plenum Press, New York–London, pp. 41–56 (1985b).
[360] L. Kappen, Ecophysiological relationships in different climatic regions. In: *CRC handbook of lichenology*, vol. 2, ed. M. Galun, Boca Raton, CRC Press Inc., Florida, pp. 37–100 (1988).
[361] L. Kappen, *Antarctic Science*, **1**, 31 (1989).
[362] L. Kappen, *Arctic*, **46**, 297 (1993).
[363] L. Kappen, *Crypt. Bot.*, **4**, 193 (1994).
[364] L. Kappen, M. Breuer, *Antarctic Science*, **3**, 273 (1991).
[365] L. Kappen, E.I. Friedmann, *Polar Biol.*, **1**, 227 (1983).
[366] L. Kappen, J. Redon, *Flora*, **179**, 215 (1987).
[367] L. Kappen, M. Bölter, A. Kühn, *Polar Biol.*, **5**, 255 (1986).
[368] L. Kappen, M. Bölter, A. Kühn, *Progress and Problems in Lichenology in the Eighties. Bibl. Lichenol.*, vol. 25, J. Cramer in der Gebr. Borntraeger Verlagsbuchhandlg., Berlin–Stuttgart, pp. 297–312 (1987).
[369] L. Kappen, M. Breuer, M. Bölter, *Polar Biology*, **11**, 393 (1991).
[370] L. Kappen, B. Schroeter, G. Hestmark, J.B. Winkler, *Bot. Acta*, **109**, 292 (1996).
[371] L. Kappen, B. Schroeter, L.G. Sancho, *Oecologia*, **82**, 311, (1990).
[372] L. Kappen, B. Schroeter, C. Scheidegger, M. Sommerkorn, G. Hestmark, *Adv. Space Res.*, **18**, 119 (1996).
[373] L. Kappen, M. Sommerkorn, B. Schroeter, *Lichenologist*, **27**, 531 (1995).
[374] J. Karger, J. Lenzner, H. Pfeifer, H. Schwabe, W. Heyer, F. Janowski, F. Wolf, S.P. Zdanov, *J. Am. Ceram. Soc.*, **66**, 69 (1982).
[375] A. Kaurin, O. Juttila, J. Hansen, *Physiologia Plantarum*, **52**, 310 (1981).
[376] W. Kauzmann, *Adv. Protein Chem.*, **41**, 1 (1959).
[377] A.M. Kenwright, B.J. Say, Solid-state proton NMR studies of polymers. In: *NMR Spectroscopy of Polymers*, ed. R.N. Ibbett, Blackie Academic & Professional, Glasgow (1993).
[378] W.E. Kenyon, *Nucl. Geoph.*, **6**, 153 (1992).
[379] E. Kessler, *Planta*, **49**, 435 (1957).
[380] E. Kessler, W. Arthur, J.E. Brugger, *Arch. Biochem. Biophys.*, **71**, 326 (1957).
[381] Rita Khanna, S. Rajan, Govindjee, H.S. Gutowsky, *Biochim. Biophys. Acta*, **725**, 10 (1983).
[382] T.L. Kieft, *Appl. Environ. Microbiol.*, **54**, 1678 (1988).
[383] T.L. Kieft, V. Ahmadjian, *Lichenologist*, **21**, 355 (1989).
[384] T.L. Kieft, T. Ruscetti, *J. Bacteriol.*, **172**, 3519 (1990).
[385] J.A. Kilian, B. de Kruijff, *Biochemistry*, **24**, 7890 (1985).
[386] J.A. Kilian, B. de Kruijff, *Chem. Phys. Lipids*, **40**, 259 (1986).
[387] S.L. Kimball, F.B. Salisbury, *Botanical Gazette*, **135**, 147 (1974).
[388] K. Kinoshita, H. Ishikawa, K. Shinoda, *Bull. Chem. Soc. Japan*, **31**, 1081 (1958).
[389] R.L. Kleinberg, W.E. Kenyon, P.P. Mitra, *J. Magn. Reson.*, **A108**, 206 (1994).

[390] G. Klose, K. Gawrisch, *studia biophysica*, **84**, 22 (1981).
[391] G. Klose, F. Stelzner, *Biochim. Biophys. Acta*, **363**, 1 (1974).
[392] C.M. Knobler, *Physica*, **140A**, 198 (1986).
[393] S.C. Kohn, R. Dupree, M.E. Smith, *Nature*, **337**, 539 (1989).
[394] J.P. Korb, Shu Xu, J. Jonas, *J. Appl. Phys.*, **98**, 2411 (1993).
[395] C.B. Kretschmer, R. Wiebe, *J. Am. Chem. Soc.*, **74**, 1276 (1952).
[396] R.M. Kroeker, R.M. Henkelman, *J. Magn. Reson.*, **69**, 218 (1986).
[397] Z. Krupa, T. Baszyński, *Biochim. Biophys. Acta*, **408**, 26 (1975).
[398] M. Krzystyniak, H. Harańczyk, E. Baguet, *Mol. Phys. Reps.*, **33**, 235 (2001).
[399] M. Krzystyniak, H. Harańczyk, Z. Olejniczak, K. Strzałka, *Mol. Phys. Reps.*, **33**, 239 (2001).
[400] M. Krzystyniak, H. Harańczyk, D. le Botlan, K. Strzałka, *Mol. Phys. Reps.*, **33**, 230 (2001).
[401] O. Kukal, Behavioral and physiological adaptations to cold in a freeze tolerant Arctic insect. In: *Insects at low temperatures*, eds. R.E. Lee and D.L. Denlinger, Chapman and Hall, London, pp. 276–300 (1991).
[402] T. Kunitake, Y. Okahata, *J. Am. Chem. Soc.*, **99**, 3860 (1977).
[403] I.D. Kuntz, T.S. Brassfield, G.D. Law, G.V. Purcell, *Science, N.Y.*, **163**, 1329 (1969).
[404] A.-L. Kuo, C.G. Wade, *Biochemistry*, **18**, 2300 (1979).
[405] V.I. Kvivlidze, V.F. Kiselev, L.A. Ushakova, *Dokl. Akad. SSSR*, **191**, 1088 (1970).
[406] V.I. Kvivlidze, V.F. Kiselev, A.B. Kurzaev, L.A. Ushakova, *Surf. Sci.*, **44**, 60 (1974).
[407] B.D. Ladbrooke, R.M. Williams, D. Chapman, *Biochim. Biophys. Acta*, **150**, 333 (1968).
[408] B.D. Ladbrooke, T.J. Jenkinson, V.B. Kamat, D. Chapman, *Biochim. Biophys. Acta*, **164**, 101 (1968).
[409] C. Lafargue, *C. R. Acad. Sci. Paris*, **230**, 2022 (1950).
[410] O.L. Lange, *Planta*, **64**, 1 (1965).
[411] O.L. Lange, *Flora*, Abt. **B 156**, 500 (1966).
[412] O.L. Lange, *Flora*, Abt. **B 158**, 324 (1969).
[413] O.L. Lange, L. Kappen, Photosynthesis of lichens from Antarctica. In: *Antarctic Terrestial Biology*, ed. G.A. Llano, Antarctic Research Series, vol. **20**, pp. 83–95, Washington: American Geographical Union (1972).
[414] O.L. Lange, E. Kilian, *Flora*, **176**, 7 (1985).
[415] O.L. Lange, H. Metzner, *Naturwissenschaften*, **8**, 191 (1965).
[416] O.L. Lange, J.D. Tenhunen, *Oecologia*, **51**, 426 (1981).
[417] O.L. Lange, T.G.A. Green, H. Ziegler, *Oecologia*, **75**, 494 (1988).
[418] O.L. Lange, E. Kilian, H. Ziegler, *Oecologia*, **71**, 104 (1986).
[419] I. Langmuir, *J. Am. Chem. Soc.*, **39**, 1848 (1917).
[420] I. Langmuir, *J. Am. Chem. Soc.*, **40**, 1361 (1918).
[421] S.K. Larsen, C.G. Pierpont, *J. Am. Chem. Soc.*, **110**, 1827 (1988).
[422] D.W. Larson, *Can. J. Botany*, **56**, 2119 (1978).
[423] K. Larsson, *Chem. Phys. Lipids*, **20**, 225 (1977).
[424] W.M. Latimer, W.H. Rodebush, *J. Am. Chem. Soc.*, **42**, 1419 (1920).
[425] R. Lee, J.G. Baust, *Physiol. Zoology*, **60**, 499 (1987).
[426] R.E. Lee, *Bioscience*, **39**, 308 (1989).

[427] R.E. Lee, J.J. McGrath, R.T. Morason, R.M. Taddeo, *J. Insect Physiol.*, **39**, 445 (1993).
[428] J. Lennard-Jones, J.A. Pople, *Proc. Roy. Soc. (London)*, **A205**, 155 (1951).
[429] J. Levitt, *Responses of plants to environmental stresses, vol. 1: Chilling, freezing and high temperature stresses*, Academic Press, New York (1980).
[430] P. Levitz, G. Ehret, S.K. Sinha, J.M. Drake, *J. Chem. Phys.*, **95**, 6151 (1991).
[431] S.E. Lindow, Epiphytic ice nucleation active bacteria as incitants of frost-injury and plant disease. In: *Phytopathogenic prokaryotes*, eds. G. Lacy, M. Mount, Academic Press, New York, pp. 344–362 (1982).
[432] S.E. Lindow, Population dynamics of epiphytic ice nucleation active bacteria on frost sensitive plants and frost control by means of antagonistic bacteria. In: *Plant cold hardiness and freezing stress*, vol. 2, eds. P.H. Li, A. Sakai, Academic Press, New York, pp. 395–416 (1982).
[433] S.E. Lindow, *Ann. Rev. of Phytopathology*, **21**, 363 (1983).
[434] S.E. Lindow, D.C. Amy, C.D. Upper, *Appl. Environmental Microbiology*, **36**, 831 (1978).
[435] S.E. Lindow, S.S. Hirano, W.R. Barchet, D.C. Amy, C.D. Upper, *Plant Physiol.*, **70**, 1090 (1982).
[436] B.E. Lippert, *J. Phycol.*, **3**, 182 (1967).
[437] E.R. Lippincott, *J. Chem. Phys.*, **23**, 603 (1955).
[438] E.R. Lippincott, R. Schroeder, *J. Chem. Phys.*, **23**, 1099 (1955).
[439] J. Lisowski, A. Jezierski, E. Bylińska, *Appl. Magn. Res.*, **5**, 15 (1993).
[440] K. Londsale, *Proc. Roy. Soc.*, **A247**, 424 (1958).
[441] E.A. Long, J.D. Kemp, *J. Am. Chem. Soc.*, **58**, 1829 (1936).
[442] L.G. Longsworth, *J. phys. Chem. Ithaca*, **64**, 1914 (1960).
[443] J.D. Loren, *J. Petroleum Technol.*, **24**, 923 (1972).
[444] P.S. Low, D.R. Ort, W.A. Cramer, J. Whitmarsh, B. Martin, *Arch. Biochem. Biophys.*, **231**, 336 (1984).
[445] L.K. Lozina-Lozinskii, *Studies in cryobiology*, John Wiley, New York, pp. 69–84 (1974).
[446] V. Luzzati, X-ray diffraction studies of lipid-water systems. In: *Biological Membranes*, vol. **1**, ed. D. Chapman, Acad. Press, pp. 71–123 (1968).
[447] V. Luzzati, A. Tardieu, *Ann. Rev. Phys. Chem.*, **25**, 79 (1974).
[448] F.E. Mabbs, D. Collison, *Electron Paramagnetic Resonance of d Transition Metal Compounds*, Elsevier, Amsterdam, pp. 815–841 (1992).
[449] S. Mabrey, J.M. Sturtevant, *Biochim. Biophys. Acta*, **486**, 444 (1977).
[450] S. Mabrey, J.M. Sturtevant, In: *Methods in Membrane Biology*, vol. **9**, ed. E.D. Korn, Plenum Press, New York, p. 237 (1978).
[451] J.C. MacTavish, L. Miljkvic, M.M. Pintar, R. Blinc, G. Lahajnar, *Cem. Concr. Res.*, **15**, 367 (1985).
[452] P.J. Marchand, *Life in the cold, an introduction to winter ecology*. University Press of New England, Hanover (1987).
[453] E. Marconi, E. Carnovale, A. Di Nola, E. Brosio, *Int. J. Food Sci. Technol.*, **28**, 25 (1993).
[454] D.W. Marquardt, *J. Soc. Ind. Appl. Math.*, **11**, 431 (1963).
[455] S. Mashimo, N. Miura, T. Umehara, S. Yahigara, K. Higasi, *J. Chem. Phys.*, **96**, 6358 (1992).
[456] B.J. Mason, *The physics of clouds*, Clarendon Press, Oxford (1957).

[457] B.J. Mason, *Adv. Phys.*, **7**, 221 (1958).
[458] G. Mataloni, G. Tesolin, *Antarctic Sci.*, **9**, 250 (1997).
[459] C. McAuliffe, *J. Phys. Chem.*, **70**, 1267 (1966).
[460] J.W. McBain, C.S. Salmon, *J. Am. Chem. Soc.*, **42**, 426 (1920).
[461] K.R. McCall, D.L. Johnson, R.A. Guyer, *Phys. Rev.*, **B44**, 7344 (1991).
[462] H.M. McConnell, Lateral molecular motion in membranes: immune recognition and response. In: *Membranes and Intercellular Communication, Les Houches, Session XXXIII*, ed. R. Balian, M. Chabre, P.F. Devaux, North–Holland Publ. Co., Amsterdam–New York–Oxford, p. 267–292 (1981).
[463] R.N. McElhaney, *Chem. Phys. Lipids*, **30**, 229 (1982).
[464] B. R. McGarvey, *Transition Metal Chemistry*, **3**, 89 (1966).
[465] M.L. McGlashan, A.G. Williamson, *Trans. Faraday Soc.*, **57**, 588 (1961).
[466] T.J. McIntosh, C.R. Worthington, *Biophys. J.*, **14**, 363 (1974).
[467] H.L. McKague, J.R. Hearst, R.L. Ward, N.R. Burkhard, *Nuclear Geophysics*, **6**, 359 (1992).
[468] B.D. McKersie, J.E. Thompson, *Plant Physiol.*, **61**, 639 (1978).
[469] R.J. McLean, G.F. Pessoney, Formation and resistance of akinetes of *Zygnema*. In: *Contributions in Phycology*, eds. B. Parker and R.M. Brown, Allen Press, Lawrence, Kansas, pp. 145–152 (1971).
[470] J.A. McMillan, S.C. Los, *J. Chem. Phys.*, **42**, 829 (1956).
[471] J.A. McMillan, S.C. Los, *Nature, Lond.*, **206**, 806 (1965).
[472] D.R. Melick, R.D. Seppelt, *Antarctic Science*, **4**, 399 (1992).
[473] D.R. Melick, R.D. Seppelt, *Crypt. Bot.*, **4**, 212 (1994).
[474] R.S. Menon, A.L. Mackay, S. Flibotte, J.R.T. Hailey, *J. Magn. Res.*, **82**, 205 (1989).
[475] R.S. Menon, A.L. Mackay, J.R.T. Hailey, M. Bloom, A.E. Burgess, J.S. Swansson, *J. Appl. Polymer Sci.*, **33**, 1141 (1987).
[476] R. Merigoux, *Rev. Opt.*, **9**, 281 (1937).
[477] A.A. Miller, *Science*, **163**, 1325 (1969).
[478] L.K. Miller, R. Werner, *Cryobiology*, **17**, 621 (1980).
[479] T. Mizutani, A. Mizutani, *J. Non-Cryst. Solids*, **30**, 23 (1978).
[480] T. Mizutani, A. Mizutani, *Anal. Biochem.*, **83**, 216 (1977).
[481] J.F. Mohler, *Phys. Rev.*, **35**, 236 (1912).
[482] M.O. Morison, R.G. Sheath, *Phycologia*, **24**, 129 (1985).
[483] J.V. Moroney, H.D. Husic, N.E. Tolbert, *Plant Physiol.*, **79**, 177 (1985).
[484] S.C. Mossop, *Proc. Phys. Soc.*, **B68**, 193 (1955).
[485] N. Muller, *J. Chem. Phys.*, **43**, 2555 (1965).
[486] N. Muller, R.C. Reiter, *J. Chem. Phys.*, **42**, 3265 (1965).
[487] D.J. Murphy, *FEBS Lett.*, **150**, 19 (1982).
[488] D.J. Murphy, J.E. Woodrow, *Biochim. Biophys. Acta*, **725**, 104 (1983).
[489] A.S.N. Murthy, C.N.R. Rao, *Chem. Phys. Lett.*, **2**, 123 (1968).
[490] N.S. Murthy, C.R. Worthington, *Biochim. Biophys. Acta*, **1062**, 172 (1991).
[491] H.R. Müller, M. von Stackelberg, *Naturwiss.*, **39**, 20 (1952).
[492] F. Müller-Landau, D.A. Cadenhead, *Chem. Phys. Lipids*, **25**, 315 (1979).
[493] K. Mysels, L. Princen, *J. Phys. Chem.*, **63**, 1696 (1959).
[494] M. Nagao, K. Arakawa, D. Takezawa, S. Yoshida, S. Fujikawa, *J. Plant Res.*, **112**, 163 (1999).
[495] J.F. Nagle, *J. Math. Phys.*, **7**, 1484 (1966).

[496] J.F. Nagle, *J. Membr. Biol.*, **27**, 233 (1976).
[497] J.F. Nagle, H.L. Scott, *Phys. Today*, **31**, No. 2 (1978).
[498] K. Nakanishi, *Bull. Chem. Soc. Japan*, **33**, 703 (1960).
[499] A. Narayanan, J.S. Hartman, A.B. Bain, *J. Magn. Reson.*, **A112**, 58 (1995).
[500] T.H. Nash III, L. Kappen, R. Loesch, D.W. Larson, U. Matthes-Sears, *Flora*, **179**, 241 (1987).
[501] T.H. Nash III, L. Kappen, R. Loesch, U. Matthes-Sears, D.W. Larson, *Progress and Problems in Lichenology in the Eighties, Bibl. Lichenol.*, vol. 25, p. 313 (1987).
[502] T.H. Nash III, A. Reiner, B. Demmig-Adams, E. Kilian, W.M. Kaiser, O.L. Lange, *New Phytol.*, **116**, 269 (1990).
[503] S.O. Nelson, *Agri. Eng. Yearb.*, **293**, 352 (1971).
[504] G. Nemethy, H.A. Scheraga, *J. Chem. Phys.*, **36**, 3382 (1962).
[505] C.H. Neuman, R.J.S. Brown, *J. Petroleum Technology*, **34**, 2853 (1982).
[506] H.W. Nichols, S. Wong, J.S. Deacon, C.M. Thomas, M.S. Nichols, *Phytomorphology*, **42**, 15 (1992).
[507] W.G. Nolan, *Plant Physiol.*, **67**, 1259 (1981).
[508] W.G. Nolan, R.M. Smillie, *Biochim. Biophys. Acta*, **440**, 461 (1976).
[509] W.G. Nolan, R.M. Smillie, *Plant Physiol.*, **59**, 1141 (1977).
[510] A.C.T. North, A. Rich, *Nature Lond.*, **191**, 1242 (1961).
[511] M. Oguni, C.A. Angell, *J. Chem. Phys.*, **73**, 1948 (1980).
[512] M. Olech, *Annotated checklist of Antarctic lichens and lichenicolous fungi*, The Institute of Botany of the Jagellonian University, Cracow (2001).
[513] A. Oleinikova, I. Brovchenko, A. Geiger, B. Guillot, *J. Chem. Phys.*, **117**, 3296 (2002).
[514] I. Olovsson, D.H. Templeton, *Acta Cryst.*, **12**, 832 (1959).
[515] Yu.A. Osipov, B.V. Zheleznyi, N.F. Bondarenko, *Zh. Fiz. Khim.*, **51**, 1264 (1977).
[516] P. Overath, H. Träuble, *Biochemistry*, **12**, 2625 (1973).
[517] K. Overloop, L. Van Gerven, *J. Magn. Reson.*, **100**, 303 (1992).
[518] K. Palmqvist, *Planta*, **191**, 48 (1993).
[519] K. Palmqvist, C. Máguas, H.R. Badger, H. Griffiths, *Crypt. Bot.*, **4**, 218 (1994).
[520] L. Pauling, *J. Am. Chem. Soc.*, **57**, 2680 (1935).
[521] L. Pauling, *The nature of chemical bond*, Cornell University Press, Ithaca, New York (1960).
[522] L. Pauling, R.E. Marsh, *Proc. Natl. Acad. Sci. USA*, **38**, 112 (1952).
[523] H. Peemoeller, *Bull. Magn. Reson.*, **11**, 19 (1989).
[524] H. Peemoeller, M.M. Pintar, *Biophys. J.*, **28**, 339 (1979).
[525] H. Peemoeller, M.M. Pintar, *J. Magn. Reson.*, **41**, 358 (1980).
[526] H. Peemoeller, M.M. Pintar, D.W. Kydon, *Biophys J.*, **29**, 427 (1980).
[527] G. Peinel, W. Gründer, G. Kabisch, K. Arnold, *studia biophysica*, **59**, 37 (1976).
[528] S.W. Peterson, H.A. Levy, *Acta Crystallogr.*, **10**, 70 (1957).
[529] R. Pethig, *Dielectric and electronic properties of biological materials*, Wiley and Sons, New York (1979).
[530] M. Peyron, G.K. Pierens, A.J. Lucas, L.D. Hall, R.C. Stewart, *J. Magn. Reson.*, **A118**, 214 (1996).
[531] H. Pfeifer, Nuclear magnetic resonance and relaxation of molecules adsorbed on solids. In: *NMR Basic Principles and Progress, Grundlagen and Fortschritte*, vol. 7,

eds. P. Diehl & R. Kosfeld, Springer-Verlag, Berlin–Heidelberg–New York, pp. 65–153 (1972).
[532] P. Phelps, T.H. Giddings, M. Prochoda, R. Fall, *J. Bacteriol.*, **167**, 496 (1986).
[533] C.M. Phillips, R.M. Williams, D. Chapman, *Chem. Phys. Lipids*, **3**, 234 (1969).
[534] C.M. Phillips, H. Hauser, F. Paltauf, *Chem. Phys. Lipids*, **8**, 127 (1972).
[535] M.C. Phillips, D. Chapman, *Biochim. Biophys. Acta*, **163**, 301 (1968).
[536] S. Phung-Nhu-Hung, B. Houlier, A. Moyse, *Plant Sci. Lett.*, **6**, 243 (1976).
[537] M.M. Pintar, *Mag. Res. Imag.*, **9**, 753 (1991).
[538] A. Pirson, *Z. Bot.*, **31**, 193 (1937).
[539] D. Platikhanov, M. Nedyalkov, A. Schedulko, *J. Colloid Interface Sci.*, **75**, 612 (1980).
[540] D. Platikhanov, M. Nedyalkov, A. Schedulko, *J. Colloid Interface Sci.*, **75**, 620 (1980).
[541] M.-M. Poo, R.A. Cone, *Nature (London)*, **247**, 438 (1974).
[542] H. Popkie, H. Kistenmacher, E. Clementi, *J. Chem. Phys.*, **59**, 1325 (1973).
[543] J.A. Pople, *Proc. Roy. Soc.*, **A205**, 163 (1951).
[544] J.A. Pople, W.G. Shneider, H.J. Bernstein, *High-resolution nuclear magnetic resonance*, McGraw-Hill, New York (1959).
[545] M. Potts, *Microbiological Reviews*, **58**, 755 (1994).
[546] W.H. Press, B.P. Flannery, S.A. Teukolski, W.T. Vetterling, *Numerical Recipes in C: The Art of Scientific Computing*, Cambridge University Press, Cambridge (1992).
[547] H. Pruppacher, *J. Chem. Phys.*, **56**, 101 (1972).
[548] P.J.A. Pugh, *Acta Oecol.*, **15**, 71 (1994).
[549] P.J. Quinn, W.P. Williams, *Biochim. Biophys. Acta*, **737**, 223 (1983).
[550] A. Rahman, F.H. Stillinger, *J. Am. Chem. Soc.*, **95**, 7943 (1973).
[551] A.N. Rai, Nitrogen metabolism. In: *CRC Handbook of Lichenology*, vol. 1, ed. M. Galun, CRC Press Inc., Boca Raton, Florida, pp. 201–238 (1988).
[552] J.K. Raison, L.C. Wright, *Biochim. Biophys. Acta*, **731**, 69 (1983).
[553] A.K. Rajagopal, K.L. Ngai, R.W. Rendell, S. Teitler, *Physica*, **149A**, 358 (1986).
[554] C.N.R. Rao, Theory of hydrogen bonding in water. In: *Water, a comprehensive treatise, vol. 1: The physics and physical chemistry of water*, Plenum Press, New York–London, pp. 93–114 (1972).
[555] D.H. Rasmussen, A.P. MacKenzie, *J. Phys. Chem.*, **75**, 967 (1971).
[556] D.H. Rasmussen, A.P. MacKenzie, In: *Water structure at the water-polymer interface*, ed. H.H.G. Jellinek, Plenum Press, New York, p. 126 (1972).
[557] D.H. Rasmussen, A.P. MacKenzie, *J. Chem. Phys.*, **59**, 5003 (1973).
[558] R.A. Réamur, *Memoires pour servir à l'histoire des insects*, tome **2**, 170, d'Imprimerie Royal, Paris, pp. 141–147 (1734).
[559] A.G. Redfield, *IBM J. Res. Develop.*, **1**, 19 (1957).
[560] V. Regnault, *Ann. Chem. Phys.* 3e serie, **XI**, 273 (1844).
[561] V. Regnault, *Mem. Acad. Sci. Instr. Fr.*, **XXI**, 465 (1847).
[562] F. Reiss-Husson, V. Luzzati, *J. Phys. Chem.*, **68**, 3504 (1964).
[563] J.A. Reynolds, D.B. Gilbert, C. Tanford, *Proc. Natl. Acad. Sci. USA*, **71**, 2925 (1974).
[564] J. Rickards, M.J. Kelleher, K.B. Storey, *J. Insect Physiol.*, **33**, 443 (1987).
[565] M.T. Riggin, A.R. Sharp, R. Kaiser, *J. Appl. Polym. Sci.*, **23**, 3147 (1979).
[566] R.A. Ring, *Comp. Biochem. Physiol.*, **A73**, 605 (1982).

[567] R.A. Ring, D. Tcsar, *Cryobiology*, **18**, 199, (1981).
[568] H.H. Robinson, R.R. Sharp, C.F. Yocum, *Biochem. Biophys. Res. Comm.*, **93**, 755 (1980).
[569] H.H. Robinson, R.R. Sharp, C.F. Yocum, *Biochim. Biophys. Acta*, **593**, 414 (1980).
[570] H.H. Robinson, R.R. Sharp, C.F. Yocum, *Biochim. Biophys. Acta*, **636**, 144 (1981).
[571] J.D. Robinson, J.D. Loren, E.A. Vajnar, D.E. Hartman, *J. Petroleum Technol.*, **26**, 226 (1974).
[572] R.A. Robinson, R.H. Stokes, *Electrolytic solutions*, Butterworths, London (1959).
[573] B. Rosenberg, E. Postow, *Ann. N. Y. Acad. Sci.*, **158**, 161 (1969).
[574] R. Rumm, H. Harańczyk, H. Peemoeller, M.M. Pintar, *Cem. Concr. Res.*, **21**, 391 (1991).
[575] P.W. Rundel, Water relations. In: *CRC Handbook of Lichenology*, vol. 1, ed. M. Galun, CRC Press Inc., Boca Raton, Florida, pp. 17–37 (1988).
[576] J.A. Rupley, E. Gratton, G. Careri, *Trends Biochem. Sci.*, **8**, 18 (1983).
[577] J.A. Rupley, L. Siemiankowski, G. Careri, F. Bruni, *Proc. Natl. Acad. Sci. USA*, **85**, 9022 (1988).
[578] E. Sackmann, *Ber. Bunsenges. Phys. Chem.*, **82**, 891 (1978).
[579] W. Saenger, *Ann. Rev. Biophys. Biophys. Chem.*, **16**, 93 (1987).
[580] F.B. Salisbury, S.L. Kimball, B. Bennett, P. Rosen, M. Weidner, *Space Life Sciences*, **4**, 124 (1973).
[581] N.J. Salsbury, A. Darke, D. Chapman, *Chem. Phys. Lipids*, **8**, 142 (1972).
[582] L.G. Sancho, F. Valladares, B. Schroeter, L. Kappen, Ecophysiology of Antarctic versus temperate populations of a bipolar lichen: The key role of the photosynthetic partner. In: *Antarctic Ecosystems: Models for wider ecological understanding*, eds. W. Davison, C. Howard-Williams, P. Broady, The Caxton Press, Christchurch, p. 190–194 (2000).
[583] P.W. Sanderson, W.P. Williams, B.A. Cuningham, D.H. Wolfe, L.J. Lis, *Biochim. Biophys. Acta*, **1148**, 278 (1993).
[584] T. Sato, A. Chiba, R. Nozaki, *J. Chem. Phys.*, **110**, 2508 (1999).
[585] T. Sato, A. Chiba, R. Nozaki, *J. Chem. Phys.*, **112**, 2924 (2000).
[586] T. Sato, A. Chiba, R. Nozaki, *J. Chem. Phys.*, **113**, 9748 (2000).
[587] V.J. Schaefer, *Ind. Eng. Chem.*, **44**, 1300 (1952).
[588] H.U. Schairer, P. Overath, *J. Mol. Biol.*, **44**, 209 (1969).
[589] B. Schipperges, L. Kappen, M. Senesson, *Lichenologist*, **27**, 517 (1995).
[590] M. Schlensog, B. Schroeter, L.G. Sancho, A. Pintado, L. Kappen, Effect of strong irradiance on photosynthetic performance of the melt-water dependent cyanobacterial lichen *Leptogium puberulum* (Collemataceae) Hue from the maritime Antarctic. In: *New Species and Novel Aspects in Ecology and Physiology of Lichens. In honour of O.L. Lange. Bibl. Lichenol.*, vol. 76, ed. L. Kappen, pp. 235–246 (1997).
[591] E.J. Schmidt, K.K. Velasco, A.M. Nur, *J. Appl. Phys.*, **59**, 2788 (1986).
[592] W.G. Schneider, H.J. Bernstein, J.A. Pople, *J. Chem. Phys.*, **28**, 601 (1958).
[593] U. Schreiber, P.A. Armond, *Biochim. Biophys. Acta*, **502**, 138 (1978).
[594] L.J. Schreiner, J.C. MacTavish, L. Miljkovic, M.M. Pintar, R. Blinc, G. Lahajnar, D. Lasic, L.W. Reeves, *J. Am. Cer. Soc.*, **68**, 10 (1985).
[595] R. Schroeder, E.R. Lippincott, *J. Chem. Phys.*, **61**, 921 (1957).
[596] B. Schroeter, *Oecologia*, **98**, 212 (1994).
[597] B. Schroeter, T.G.A. Green, L. Kappen, R.D. Seppelt, *Crypt. Bot.*, **4**, 233 (1994).
[598] B. Schroeter, M. Olech, L. Kappen, W. Heitland, *Antarctic Sci.*, **7**, 251 (1995).

[599] B. Schroeter, Ch. Scheidegger, *New Phytol.*, **131**, 273 (1995).
[600] E.D. Schulze, O.L. Lange, *Flora.*, Abt. **B. 158**, 180 (1968)
[601] A. Seelig, J. Seelig, *Biochemistry*, **13**, 4839 (1974).
[602] V. Seewaldt, D.A. Priestley, A.C. Leopold, G.W. Feigenson, F. Goodsaid-Zalduondo, *Planta*, **152**, 19 (1981).
[603] A. Sen, A.P.R. Brain, P.J. Quinn, W.P. Williams, *Biochim. Biophys. Acta*, **686**, 215 (1982).
[604] A. Sen, W.P. Williams, P.J. Quinn, *Biochim. Biophys. Acta*, **663**, 380 (1981).
[605] A. Sen, W.P. Williams, A.P.R. Brain, P.J. Quinn, *Biochim. Biophys. Acta*, **685**, 297 (1982).
[606] P.N. Sen, C. Straley, W.E. Kenyon, M.S. Whittingham, *Geophysics*, **55**, 61 (1990).
[607] N. Senesi, *Humus, Its Structure and Role in Agriculture and Environment*, ed. J. Kubat, Elsevier (1992).
[608] M. Settles, W. Doster, F. Kremer, F. Post, W. Schirmacher, *Philosophical Magazine*, **B 65**, 861 (1992).
[609] R.R. Sharp, C.F. Yocum, *Biochim. Biophys. Acta*, **592**, 185 (1980).
[610] R.G. Sheath, M.L. Vis, J.A. Hambrook, K.M. Cole, *Hydrobiologia*, **336**, 67 (1996).
[611] J.R. Sheats, H.M. McConnell, *J. Am. Chem. Soc.*, **99**, 7091 (1977).
[612] J.R. Sheats, H.M. McConnell, *Proc. Natl. Acad. Sci. USA*, **75**, 4661 (1978).
[613] J.R. Sheats, H.M. McConnell, *J. Am. Chem. Soc.*, **101**, 3272 (1979).
[614] B.J. Shelp, D.T. Canvin, *Can. J. Bot.*, **62**, 1398 (1984).
[615] K. Shimada, A. Riihimaa, *Cryo-Letters*, **11**, 243 (1990).
[616] G.G. Shipley, J.P. Green, B.W. Nichols, *Biochim. Biophys. Acta*, **311**, 531 (1973).
[617] E.W. Simon, *New Phytol.*, **73**, 377 (1981).
[618] S.J. Singer, The cell membrane. In: *Membranes and Intercellular Communication, Les Houches, Session XXXIII*, ed. R. Balian, M. Chabre, P.F. Devaux, North-Holland Publ. Co., Amsterdam–New York–Oxford, p. 1–14 (1981).
[619] S.J. Singer, G.L. Nicholson, *Science*, **175**, 720 (1972).
[620] F.S. Sjöstrand, *The membranes*, Academic Press, New York–London (1968).
[621] E. Sjöström, *Wood chemistry*, Academic Press, Inc., Orlando (1981).
[622] Ch. Skaar, *Wood-water relations*, Springer-Verlag, Berlin, Heidelberg (1988).
[623] R.M. Smillie, C. Critchley, J.M. Bain, R. Nott, *Plant Physiol.*, **62**, 191 (1978).
[624] A.I. Smirnov, H.A. Golovina, O.E. Yakimchenko, S.I. Aksyonov, Y.S. Lebedev, *Plant Physiol.*, **140**, 447 (1992).
[625] A.I. Smirnov, O.E. Yakimchenko, H.A. Golovina, S.Kh. Bekova, Y.S. Lebedev, *J. Magnet. Reson.*, **91**, 386 (1992).
[626] B.A. Smith, H.M. McConnell, *Proc. Natl. Acad. Sci. USA*, **75**, 2759 (1978).
[627] R. Smith, C. Tanford, *Proc. Natl. Acad. Sci. USA*, **70**, 289 (1973).
[628] W.P. Snelgar, T.G.A. Green, A.L. Wilkins, *New Phytol.*, **88**, 353 (1981).
[629] W.T. Sobol, M.M. Pintar, *Mag. Res. Medicine*, **4**, 537 (1987).
[630] K.G. Soga, H. Harańczyk, R.J. Rumm, M.M. Pintar, *Mag. Res. Imag.*, **9**, 727 (1991).
[631] A.K. Soper, F. Bruni, M.A. Ricci, *J. Chem. Phys.*, **106**, 247 (1997).
[632] L. Sømme, *Comp. Biochem. Physiol.*, **73A**, 519 (1982).
[633] M.H. Spalding, W.L. Ogren, *FEBS Lett.*, **145**, 41 (1982).
[634] R.J. Speedy, C.A. Angell, *J. Chem. Phys.*, **65**, 851 (1976).
[635] S.G. Sprague, L.A. Staehlin, *Biochim. Biophys. Acta*, **777**, 306 (1984).

[636] J.B. Stamatoff, W.F. Graddick, L. Powers, D.E. Moncton, *Biophys. J.*, **25**, 253 (1979).
[637] S. Stapf, R. Kimmich, J. Niess, *J. Appl. Phys.*, **75**, 529 (1994).
[638] S. Stapf, R. Kimmich, R.O. Seitter, *Phys. Rev. Lett.*, **75**, 2855 (1995).
[639] F.W. Starr, J.K. Nielsen, H.E. Stanley, *Phys. Rev. Lett.*, **82**, 2294 (1999).
[640] D. Stauffer, A. Aharony, *Introduction to percolation theory*, Taylor & Francis, London, Washington DC (1991).
[641] J.M. Steim, M.E. Tourtellotte, J.C. Reinert, R.D. McElhaney, R.L. Rader, *Proc. Natl. Acad. Sci. USA*, **63**, 104 (1969).
[642] F.H.Stillinger, *Science*, **209**, 451 (1980).
[643] F.H. Stillinger, A. Rahman, *J. Chem. Phys.*, **60**, 1545 (1974).
[644] G.W. Stockton, K.G. Johnson, K.W. Butler, A.P. Tulloch, I. Boulanger, I.C.P. Smith, J.H. Davis, M. Bloom, *Nature*, **269**, 267 (1977).
[645] K.B. Storey, J.G. Baust, P. Buescher, *Cryobiology*, **18**, 315 (1981).
[646] K.B. Storey, J.M. Storey, *Physiol. Rev.*, **68**, 27 (1988).
[647] L. Stryer, *Biochemia*, PWN, Warszawa (1986).
[648] K. Strzałka, E. Machowicz, *Acta Physiol. Plant.*, **6**, 41 (1984).
[649] K. Strzałka, G. Majewska, E. Mędrela, *Acta Physiol. Plant.*, **11**, 49 (1980).
[650] W. Stumm, *Chemistry of the Solid-Water Interface*, J. Wiley, New York, p. 364 (1994).
[651] M. Sugisaki, H. Suga, S. Seki, *J. Chem. Soc. Japan*, **41**, 2591 (1968).
[652] S.J. Suresh, V.M. Naik, *J. Chem. Phys.*, **113**, 9727 (2000).
[653] K. Takala, H. Olkkonen, R. Salminen, *Environ. Pollut.*, **84**, 131 (1994).
[654] C. Tanford, *J. Phys. Chem.*, **76**, 3020 (1972).
[655] C. Tanford, *J. Phys. Chem.*, **78**, 2469 (1974).
[656] C. Tanford, *The hydrophobic effect: formation of micelles and biological membranes*, John Wiley & Sons, New York–Chichester–Brisbane–Toronto (1986).
[657] A. Tardieu, V. Luzzati, F.C. Reman, *J. Mol. Biol.*, **75**, 711 (1973).
[658] H.V. Tartar, *J. Phys. Chem.*, **59**, 1195 (1955).
[659] M.W. Tate, E.F. Eikenberry, D.C. Turner, E. Shyamsunder, S.M. Gruner, *Chem. Phys. Lipids*, **57**, 147 (1991).
[660] J. Texter, *Prog. Biophys. Molec. Biol.*, **33**, 83 (1978).
[661] L.L. Tieszen, *Arctic and Alpine Research*, **6**, 253 (1974).
[662] L.L. Tieszen, M.C. Lewis, P.C. Miller, J. Mayo, F.S. Chapin III, W. Oechel, An analysis of processes of primary production in tundra growth forms. In: *Tundra ecology: A comparative analysis*, eds. L.C. Bliss, O.W. Heal, I.J. Moore, pp. 285–356 (1981).
[663] A. Timur, *J. Petroleum Technol.*, **21**, 775 (1969).
[664] S. Torquato, M. Avellaneda, *J. Chem. Phys.*, **95**, 6477 (1991).
[665] J. Torres-Pereira, R. Mehlhorn, A.D. Keith, Lester Packer, *Arch. Biochem. Biophys.*, **160**, 90 (1974).
[666] H.C. Torrey, *Phys. Rev.*, **92**, 962 (1953).
[667] L. Trahms, W.D. Klabe, *Mol. Cryst. Liq. Cryst.*, **123**, 333 (1985).
[668] N.J. Trappeniers, C.J. Gerritsma, P.H. Oosting, *Phys. Lett.*, **18**, 256 (1965).
[669] J. Traube, *Ann.*, **265**, 27 (1891).
[670] J. Trillat, R. Fritz, *J. Chim. Phys.*, **35**, 45 (1937).
[671] M.-J.B. Tunis, J.E. Hearst, *Biopolymers*, **6**, 1345 (1968).

[672] J. Ulmius, H. Wennerström, G. Lindblom, G. Arvidson, *Biochemistry*, **16**, 5742 (1977).
[673] S. Utoh, T. Takemura, *Japanese J. Appl. Phys.*, **24**, 356 (1985).
[674] S. Utoh, T. Takemura, *Japanese J. Appl. Phys.*, **24**, 1404 (1985).
[675] S. Utoh, T. Takemura, *Japanese J. Appl. Phys.*, **25**, 730 (1986).
[676] S. Utoh, T. Takemura, *Japanese J. Appl. Phys.*, **26**, 801 (1987).
[677] G. Vali, E.J. Stansbury, *Can. J. Phys.*, **44**, 477 (1966).
[678] F. Valladares, L.G. Sancho, C. Ascaso, *Bot. Acta*, **111**, 99 (1997).
[679] V. Vambutas, E. Racker, *J. Biol. Chem.*, **240** (1965).
[680] P.W.M. van Dijck, B. de Kruijff, L.L.M. van Deenen, J. de Gier, R.A. Demel, *Biochim. Biophys. Acta*, **455**, 576 (1976).
[681] G. van Ginkel, D.C. Fork, *Photobiochem. Photobiophys.*, **2**, 239 (1981).
[682] G. Vannier, The importance of ecophysiology for both biotic and abiotic studies of the soil. In: *New trends in soil biology*, eds. P. Lebrun, H.M. André, A. De Medts, C. Grégorie-Wibo, G. Wauthy, Dieu-Brichart, Louvain-la-Neuve, pp. 289–314 (1983).
[683] A.J. Verkleij, C. Mombers, J. Leunissen-Bijvelt, P.H.J.Th. Ververgaert, *Nature*, **279**, 162 (1979).
[684] C.W. Vertucci, *Biophys. J.*, **58**, 1463 (1990).
[685] C.W. Vertucci, *Plant Physiol.*, **99**, 310 (1992).
[686] C. Vicente, M.E. Legaz, Lichen enzymology. In: *CRC Handbook of Lichenology*, vol. 1, ed. M. Galun, CRC Press Inc., Boca Raton, Florida, pp. 239–284 (1988).
[687] A. Vinocur, H. Pizarro, *Polar Biol.*, **15**, 401 (1995).
[688] M. von Stackelberg, W. Jahns, *Z. Elektrochem.*, **58**, 162 (1954).
[689] M. von Stackelberg, B. Meuthen, *Z. Elektrochem.*, **62**, 130 (1958).
[690] M. von Stackelberg, H.R. Müller, *Z. Elektrochem.*, **58**, 25 (1954).
[691] B. Vonnegut, *J. Colloid Sci.*, **3**, 563 (1948).
[692] K.L. Walther, A. Wokaun, A. Bailer, *Molecular Phys.*, **71**, 769 (1990).
[693] A. Walkenhorst, J. Hagemayer, S. Brackle, Passive Monitoring of Airborne Pollutants, Particularly Trace Metals with Tree Bark. In: *Plants Biomonit.*, pp. 523–540 (1993).
[694] J.H. Wang, *J. Phys. Chem. Ithaca*, **69**, 4412 (1965).
[695] J.H. Wang, C.V. Robinson, I.S. Edelman, *J. Am. Chem. Soc.*, **75**, 466 (1953).
[696] J.Y. Wang, T. Miyazawa, K. Fujimoto, Z.Y. Wang, T. Nozawa, *FEBS Letters*, **310**, 106 (1992).
[697] R.K. Wangsness, F. Bloch, *Phys. Rev.*, **89**, 728 (1953).
[698] M. Watanabe, T. Kikawada, N. Minagawa, F. Yukuhiro, T. Okuda, Mechanism allowing an insect to survive complete dehydration and extreme temperatures, *J. Exp. Biol.*, in press (2002).
[699] J.D.Watson, *The Double Helix*, New York (1968).
[700] R.C.Weast, *Handbook of Chemistry and Physics*, CRC Press Inc., 55-ed. (1974–75).
[701] W.A. Weyl, *J. Colloid Sci.*, **6**, 389 (1951).
[702] C. Weir, S. Block, G. Piermarini, *J. Res. Natl. Bur. Stand.*, **69C**, 275 (1965).
[703] W.Węglarz, H.Harańczyk, *J. Phys., D: Appl. Phys.*, **33**, 1909 (2000).
[704] E. Whalley, D.W. Davidson, *J. Chem. Phys.*, **43**, 2148 (1965).
[705] E. Whalley, J.B.R. Heath, *J. Chem. Phys.*, **45**, 3976 (1966).
[706] K.P. Whittal, A.L. MacKay, *J. Magn. Reson.*, **84**, 134 (1989).
[707] M.H.F. Wilkins, *Science, N.Y.*, **140**, 941 (1963).

[708] D.A. Wilkinson, J.F. Nagle, *Biochemistry*, **20**, 187 (1981).
[709] A. Wishnia, *J. Phys. Chem.*, **67**, 2079 (1963).
[710] E.J. Workman, F.K. Truby, W. Drost-Hansen, *Phys. Rev.*, **94**, 1073 (1954).
[711] M.R. Worland, W. Block, *J. Insect Physiol.*, **32**, 579 (1986).
[712] M.R. Worland, W. Block, H. Oldale, *Cryo-Letters*, **17**, 31 (1996).
[713] M.R. Worland, W. Block, P. Rothery, *Polar Biol.*, **13**, 105 (1993).
[714] C.R. Worthington, T.J. McIntosh, *Biophys. J.*, **14**, 703 (1974).
[715] F. Wunderlich, A. Ronai, V. Speth, J. Seelig, A. Blume, *Biochemistry*, **14**, 3730 (1975).
[716] T.J. Wydrzynski, S.B. Marks, P.G. Schmidt, Govindjee, H.S. Gutowsky, *Biochemistry*, **17**, 2155 (1978).
[717] T.J. Wydrzynski, N. Zumbulyadis, P.G. Schmidt, Govindjee, *Biochim. Biophys. Acta*, **408**, 349 (1975).
[718] R.G. Wylie, *Proc. Phys. Soc.*, **B66**, 241 (1953).
[719] K. Yamanaka, T. Yamaguchi, H. Wakita, *J. Chem. Phys.*, **101**, 9830 (1994).
[720] S.A. Yankofsky, Z. Levin, T. Bertold, N. Sandlerman, *J. Appl. Meteorology*, **20**, 1013 (1981).
[721] E. Young, F.T. Jones, *J. Phys. & Cell. Chem.*, **53**, 1334 (1949).
[722] K.E. Zachariassen, *J. comp. Physiol.*, **140**, 227 (1980).
[723] K.E. Zachariassen, Thermal adaptations to polar environments. In: *Thermal physiology*, ed. J.B. Mercer, Excerpta Medica, Amsterdam, pp. 23–34 (1989).
[724] K.E. Zachariassen, J. Andersen, M.O. Maloiy, M.Z. Kamau, *Comp. Biochem. Physiol.*, A **86**, 403 (1987).
[725] K.E. Zachariassen, H.T. Hammel, W. Schmidek, *Comp. Biochem. Physiol.*, A **63**, 203 (1979).
[726] R. Zallen, *The physics of amorphous solids*, Wiley, New York, Polish translation: "Fizyka ciał amorficznych", PWN (1994).
[727] B.V. Zheleznyi, *Russ. J. Phys. Chem.*, **42**, 950 (1968).
[728] B.V. Zheleznyi, *Russ. J. Phys. Chem.*, **43**, 1311 (1969).
[729] J.R. Zimmerman, W.E. Brittin, *J. Phys. Chem.*, **61**, 1328 (1957).
[730] R.F.A. Zwaal, R.A. Demel, B. Roelofsen, L.L.M. van Deenen, *TIBS*, **1**, 112 (1976).

Relevant papers of this Author

Chpt. 1.13.4 *water clustering in porous glass*

1. H. Harańczyk, K.G. Soga, R.J. Rumm, M.M. Pintar. Can we see, by proton spin relaxation, a percolation transition upon drying controlled pore size glass? *Mag. Res. Imag.*, **9**, 723–726 (1991).

Chpt. 1.21.4 *non-lamellar phases in photosynthetic membranes*

2. H. Harańczyk, K. Strzałka, W. Dietrich, J.S. Blicharski. ^{31}P-NMR observation of the temperature and glycerol induced non-lamellar phase formation in wheat thylakoid membranes. *J. Biol. Phys.*, **21**, 125–139 (1995).

Chpt. 2.3.1 *comparative analysis of SE and MSE model of relaxation function*

3. H. Harańczyk, A. Wójcik. Liquid phase contained in porous sandstone as observed by proton spin-lattice relaxation. *Molec. Phys. Reports*, **29**, 139–143 (2000).

Chpt. 2.3.2–7 *NMR relaxation function numerical analysis*

4. W.P. Węglarz, H. Harańczyk. Two-dimensional analysis of the nuclear relaxation function in the time domain: the program CracSpin. *J. Phys. D: Appl. Phys.*, **33**, 1909–1920 (2000).

Chpt. 2.4 *liquid phase in porous rock as a model of water in dry biological system*

5. H. Harańczyk, A. Wójcik. Liquid phase in porous rock as observed by proton magnetic relaxation. *Acta Phys. Polon.*, **A 98**, 153–161 (2000).

Chpt. 2.5 *ion concentration controll in wet porous glass*

6. K.G. Soga, H. Harańczyk, R.J. Rumm, M.M. Pintar. Self-regulation of metallic ion concentration in wet porous glass. *Mag. Res. Imag.*, **9**, 727–731 (1991).
7. C. Choi, H. Harańczyk, K.G. Soga, R.J. Rumm, M.M. Pintar. Self-regulation of iron ion concentration in hydrated porous glasses. *J. Appl. Phys.*, **80**, 5861–5865 (1996).

Chpt. 2.6.5–8 *presence of limited contribution of soluble solid fraction*

8. H. Harańczyk, W.P. Węglarz, Z. Sojka. The investigation of hydration processes in horse chestnut (*Aesculus hippocastanum* L.) and pine (*Pinus silvestris* L.) bark and bast using proton magnetic relaxation. *Holzforschung*, **53**, 299–310 (1999).

Chpt. 2.6.11–13 *presence of high amount of water soluble fraction*

9. H. Harańczyk, K. Strzałka, G. Jasiński, K. Mosna-Bojarska. The initial stages of wheat (*Triticum aestivum* L.) seed imbibition as observed by proton nuclear magnetic relaxation. *Colloids & Surfaces*, A:Physicochemical and Engineering Aspects, **115**, 47–54 (1996).

Chpt. 3.3–5 *sorption isotherm and hydration kinetics of lichens*

10. H. Harańczyk. "Water binding kinetics and sorption analysis in Antarctic and Cosmopolitan lichen thallus", submitted for publication.

Chpt. 3.6–8 *water percolation and total water accessible surface of lichen*

11. H. Harańczyk, M. Wnęk, M. Olech, J. Mościcki. "Percolation threshold and molecular clustering point of water bound in *Cladonia mitis* and *Himantormia lugubris*", submitted for publication.

Chpt. 3.9 *lichen hydration by NMR*

12. H. Harańczyk, S. Gaździński, M. Olech. The initial stages of lichen hydration as observed by proton magnetic relaxation. *New Phytologist*, **138**, 191–202 (1998).

Chpt. 4.1 *stimulated ice nucleation of free and loosely bound water in lichen*

13. H. Harańczyk, J. Grandjean, M. Olech. Freezing of water bound in lichen thallus as observed by ^{1}H NMR. I. Freezing of loosely bound water in *Cladonia mitis* at different hydration levels. *Colloids & Surfaces B: Biointerfaces*, **28/4**, in press (2003).

Chpt. 4.2 *loosely to tightly bound water transfer in lichen*

14. H. Harańczyk, J. Grandjean, M. Olech, M. Michalik 2002. Freezing of water bound in lichen thallus as observed by ^{1}H NMR. II. Freezing protection mechanisms in a Cosmopolitan lichen *Cladonia mitis* and in Antarctic lichen species at different hydration levels. *Colloids & Surfaces B: Biointerfaces*, **28/4**, in press (2003).
15. H. Harańczyk, S. Gaździński, M. Olech. Freezing protection mechanism in *Cladonia mitis* as observed by proton magnetic relaxation, In: *New Aspects in Cryptogamic Research, Contribution in Honour of Ludger Kappen. Bibl. Lichenol.*, **75**: 265–274 (2000).

Chpt. 4.3 *freezing protection of D_2O-hydrated lichen*

16. H. Harańczyk, J. Grandjean, M. Olech. Low temperature effect in D_2O-hydrated Antarctic lichen *Himantormia lugubris* as observed by ^{1}H NMR. *Molec. Phys. Reports*, **33**, 220–224 (2001).

Chpt. 4.4 *low temperature conformational transitions in lichen thallus*

17. H. Harańczyk, S. Gaździński, M. Olech. Low temperature effect on the thallus of *Cladonia mitis* as observed by proton spin-lattice relaxation. *Molec. Phys. Reports*, **29**, 135–138 (2000).

www.wuj.pl

ISSN 0239-782X
ISBN 83-233-1713-5